Measurement & prediction of key properties for novel refrigerant mixtures

Mirhadi Seyyedsadaghiani

Bachelor of Mechanical Engineering

Master of Renewable Energies Engineering

This thesis is presented for the degree of

Doctor of Philosophy

The University of Western Australia

Department of Chemical Engineering

23 February 2022

Thesis Declaration

I, Mirhadi Seyyedsadaghiani, certify that:

This thesis has been substantially accomplished during enrolment in the Doctor of Philosophy degree.

This thesis does not contain material that has been submitted for the award of any other degree or diploma in my name, in any university or other tertiary institution.

In the future, no part of this work will be used in a submission in my name, for any other degree or diploma in any university or other tertiary institution without the prior approval of The University of Western Australia and where applicable, any partner institution responsible for the joint-award of this degree.

This thesis does not contain any material previously published or written by another person, except where due reference has been made in the text and, where relevant, in the Authorship Declaration that follows.

This thesis does not violate or infringe any copyright, trademark, patent or other rights whatsoever of any person.

This research was supported an Australian Government Research Training Program (RTP) Scholarship along with additional financial support from Mitsubishi Heavy Industries and Woodside Energy Ltd.

This thesis contains published work and/or work prepared for publication, some of which has been co-authored.

Signature: 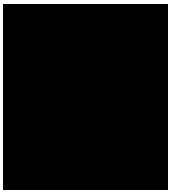

Date: 2022-02-23

Summary

This thesis explores the ignition hazards and thermophysical properties of alternative refrigerants with low global warming potential (GWP) and efficient heat transfer properties for domestic and cryogenic cooling systems. The high GWP of common refrigerants like Hydrofluorocarbons (HFCs) used in air-conditioners, like HFC-125 (GWP of 3170) and HFC-134a (GWP of 1300), make their replacement with low GWP working fluids an urgent task for industry to help tackle climate change. The new generation of synthetic refrigerants, called Hydrofluoroolefins (HFOs), presents a unique potential to address the adverse environmental impacts of the commonly used refrigerants. However, the mild flammability and limited available thermodynamic properties for these working fluids hinder their extensive employment in the air-conditioning systems. Additionally, the performance of gas liquefaction processes using mixed refrigerants (MRs) as working fluids of their cryogenic refrigeration cycles can be improved by adding heavy hydrocarbon components like iso-pentane to the MRs. However, the presence of such high-boiling compounds in the MRs inherently poses a potential risk of freeze-out and/or blockage in the cryogenic sections of heat exchangers.

Therefore, first, the minimum ignition energy (MIE) and laminar burning velocity (BV) for refrigerant/air mixtures of HFC-32 and HFO-1234yf and mixtures of HFC-32 and HFO-1234yf with non-flammable refrigerants of HFC-134a, HFC-125 and CO_2 were measured. Two pieces of new apparatus were designed, commissioned and deployed to measure these flammability characteristics of refrigerant mixtures. The measurement setups were successfully validated against the literature MIE and BV data for ammonia, which has similar flammability characteristics to the refrigerants. The results showed that by adding HFO-1234yf and CO_2 to HFC-32, the MIE needed to ignite the mixture increased by 40 times relative to the pure HFC-32. For the BV measurement, adding 5 vol% HFO-1234yf to HFC-32 decreased the BV of the mixture by 11 % relative to the pure HFC-32's BV of 7.4 m/s. Increasing the HFO-1234yf fraction to 10 vol% decreased the BV of the mixture below 5 m/s.

Among the HFO candidates to replace HFC-134a, HFO-1243zf has the lowest GWP of 0.3 that can help meet the objectives of the Montreal Protocol and the Kigali Amendment. Mixing HFO-1243zf with CO_2 can neutralise its flammability with minor reductions in the cooling performance of the mixture; however, no experimental data including vapour-liquid-equilibrium (VLE) were available for this binary system at the time of the thesis publication.

Therefore, the VLE of HFO-1243zf and CO_2 binary mixtures was measured along five isotherms at temperatures between (288 and 348) K and pressures between (0.68 and 7.69) MPa. The new VLE data are compared with the predictions of Helmholtz free energy and Peng Robinson thermodynamic models and the binary interaction parameters (BIPs) were adjusted by forcing agreement with the VLE data. These optimisations reduced the root-mean-square deviation (RMSD) of the data from the calculations by 45 % relative to the default BIPs.

The HFC-32 and CO_2 binary system presents as an eco-friendly and safe transitioning refrigerant blend that can help refrigeration industry reduce the GWP of their working fluids, while compatible systems with HFO refrigerants are being developed. However, the CO_2 fraction in the refrigerant mixture poses freeze-out risks at low-operating temperatures, which can block the cooling system and damage the equipment. Therefore, a visual high-pressure apparatus with chemical analysis capability was used to measure the VLE and solid-fluid equilibrium (SFE) of the binary system at low equilibrium temperatures between (132 and 273) K. A thermodynamic predictive model implemented in the ThermoFAST software was tuned to the measured SFE data by adjusting the BIP of the model. The optimisation reduced the RMSD of the data from the calculations by 60 % relative to the default model.

Furthermore, this thesis investigated the solid formation of high-boiling point components of MRs used in Liquefied Natural Gas (LNG) production. Adding these compounds to MRs can promote latent heat transfer from the gas to the coolant over wider ranges of temperature, resulting in smaller equipment size, higher gas liquefaction efficiency and reduced power consumption. Therefore, freezing and melting points of pure iso-pentane and methane + iso-pentane binary systems were measured. The iso-pentane melting data measured in this study, together with the reported literature data are used to optimise a thermodynamic model implemented in the ThermoFAST software package. The optimisation reduced the RMSD of the experimental data from the predictions by over 90 % relative to the default model.

Overall, this work improves the data situation and predictive capabilities of select thermodynamic models used to design modern refrigeration cycles across a wide range of applications. The results will help industry improve the safety aspects of employing eco-friendly refrigerants for public usage, aid in the development of new and efficient refrigeration systems for both domestic and industrial applications, and enhance solid freeze-out predictions in cryogenic refrigeration processes in LNG production and potentially pre-cooling stage of liquid hydrogen production.

Table of Contents

1 Contents

Dedication

To my Wife and Parents

Acknowledgements

To my principal supervisor, Prof Eric May, who guided and supported me in this PhD course. It was a great honour for me to work with you and enjoy your immense knowledge, enthusiasm, inspiration and patience. Thank you for providing me with the opportunity to study with the Fluid Science and Resources (FSR) research group, develop critical research and technical skills and grow. Working with you and the many great researchers in the FSR group has been the most rewarding experience for me.

To my co-supervisors, Prof Hui Tong Chua, Prof Dongke Zhang and Dr Arash Arami-Niya, who supported me with their extensive knowledge and patience. Thank you for standing by me every time that I needed your help and wisdom. I appreciate your vision, technical discussions and guidance with completing and publishing the papers included in this thesis.

To my friend and mentor, Dr Arman Siahvashi, for his endless support and valuable critique. I am grateful for your critical advice, technical insights, motivation and time you dedicated for me to support further development of my skills and overcome the research and life challenges.

To the researchers at the FSR group, particularly Dr Saif Al Ghafri and Dr Peter Metaxas, who were indispensable sources of technical knowledge and research experience. Thank you for your time, technical suggestions and lessons you provided for me to progress and grow.

To my parents, thank you for providing me with a fruitful life opportunity. I am forever indebted to you for sharing with me your love, wisdom and experiences that have made me who I am. To my brothers, Rahim and Heidar, thanks for being a great companionship and invaluable support.

To Sara, my wife and soul-mate, who stood by me through all my travails, my absences, my fits of pique and impatience; you bring endless love and happiness into my world. I am very grateful for being such a supportive life partner and could not be able to finish this work without your help.

I also acknowledge that this research was supported by the Australian Government Research Training Program (RTP), the University of Western Australia Top-up and Ad-Hoc Scholarships.

Authorship Declaration:

In accordance with the University of Western Australia's rules and regulations regarding Research High Degrees, this thesis has been organised as a series of publications.

The descriptions below summarise essential information regarding publications of which the candidate is the lead author in papers 1, 2 and 3. Chapters appear as published apart from style formatting and chapter referencing to ensure consistency and continuity throughout.

Paper 1

Seyyedsadaghiani, M., Arami-Niya, A., Zhang, D., Tsuji, T., Tanaka, Y., Seiki, Y., May, E. F. Minimum ignition energies and laminar burning velocities of ammonia, HFO-1234yf, HFC-32 and their mixtures with carbon dioxide, HFC-125 and HFC-134a. *Journal of Hazardous Materials*, 2021. https://doi.org/10.1016/j.jhazmat.2020.124781.

Details of work

This journal article appears as Chapter 2. The work presented relates to the ignition characteristics measurement for eco-friendly refrigerant mixtures with mild flammability and involved construction of new minimum ignition energy (MIE) and burning velocity (BV) measurement setups with a neutralisation system for toxic combustion products. A series of experimental MIE and BV data are reported for Ammonia and selected mixtures of Hydrofluorocarbons, Hydrofluoroolefins and Carbon dioxide.

Student's contribution to work

The student is the leading author of the publication. His contributions can be summarised as follows: Designed and constructed the measurement setup; Developed measurement methodology, safety protocols and toxic products neutralisation method; Executed experimental work; Data analysis; Drafting, redaction (with revisions from co-authors) and submission of the article.

Co-authors signature and dates

Arami-Niya, A		Date: 13 Dec 2021
Zhang, D.		Date: 12 Dec 2021
Tsuji, T.		Date: 15 Dec 2021
Tanaka, Y.		Date: 15 Dec 2021
Seiki, Y.		Date: 15 Dec 2021
May, E. F.		Date: 15 Dec 2021

Paper 2

Seyyedsadaghiani, M., Arami-Niya, A., Marsh, B., Al Ghafri, S. Z. S., May, E. F. Vapor–Liquid Equilibria for Carbon Dioxide+ 3, 3, 3-Trifluoropropene Binary Mixtures at Temperatures between (288 and 348) K. *Journal of Chemical & Engineering Data*, 2021. https://doi.org/10.1021/acs.jced.1c00297.

Details of work

This journal article appears as Chapter 3. This publication presents the vapour-liquid equilibrium (VLE) measurement of an eco-friendly binary system and involved commissioning a VLE measurement setup, executing experimental measurements and tuning two thermodynamic models. A series of experimental VLE data are reported for HFO-12343zf + CO_2 binary mixtures at temperatures between (288 and 348) K and the binary interaction parameters of Helmholtz free energy and Peng Robinson models are optimised.

Student's contribution to work

The student is the leading author of the publication. His contributions can be summarised as follows: Commissioned the measurement setup; Developed measurement procedures; Calibrated the Gas Chromatograph detector; Executed experimental work; Data analysis; Drafting, redaction (with revisions from co-authors) and submission of the article.

Co-authors signature and dates

Arami-Niya, A.	[redacted]	Date: 13 Dec 2021
Marsh, B.	[redacted]	Date: 17 Dec 2021
Al Ghafri, S. Z. S.	[redacted]	Date: 17 Dec 2021
May, E. F.	[redacted]	Date: 15 Dec 2021

Paper 3

Seyyedsadaghiani, M., Siahvashi, A., Norris, B. W. E., Al Ghafri, S. Z. S., Arami-Niya, A., May, E. F. Prediction of Solid Formation Conditions in Mixed Refrigerants with iso-Pentane and Methane at High Pressures and Cryogenic Temperatures. *International Journal of Energy*, 2022. https://doi.org/10.1016/j.energy.2022.123789.

Details of work

This journal article appears as Chapter 5. This publication presents freezing and melting temperatures of pure iso-pentane and (methane + iso-pentane) binary systems, measured at temperatures down to 87.5 K and pressures up to 13 MPa. The new melting data was used to optimise a predictive thermodynamic for the purpose of more accurately assessing freeze-out risk in mixed refrigerants that can be used in LNG production or potentially the pre-cooling stage of liquid hydrogen production.

Student's contribution to work

The student is the leading author of the publication. His contributions can be summarised as follows: Upgraded and maintained the measurement setup; Developed measurement procedures; Executed experimental work; Data analysis; Drafting, redaction (with revisions from co-authors) and submission of the article.

Co-authors signature and dates

Siahvashi, A.		Date: 17 Dec 2021
Norris, B. W. E.		Date: 17 Dec 2021
Al Ghafri, S. Z. S.		Date: 17 Dec 2021
Arami-Niya, A.		Date: 13 Dec 2021
May, E. F.		Date: 15 Dec 2021

Conference Proceedings During Candidature

Seyyedsadaghiani, M., Siahvashi, A., Norris, B., Al-Ghafri, S. Z. S., Metaxas, P. J., Arami-Niya, A., Aman, Z. M. and May, E. F. Visual Measurements of Water Solubility in Methane and Hydrate Equilibrium at Cryogenic Conditions with Implications for LNG Production, *Twenty-First Symposium on Thermophysical Properties*, Boulder, CO, USA, June 2021.

Seyyedsadaghiani, M., Arami-Niya, A., May, E. F. Isothermal vapour-liquid-equilibrium data for 3,3,3- Trifluoropropene (HFO-1243ZF) + carbon dioxide (CO_2) system, *The University of Western Australia Symposium on the Climate Change, Sustainability and Clean Energy*, Perth, Australia, Oct 2020.

Seyyedsadaghiani, M., Arami-Niya, A., May, E. F. Measurement of environmentally-friendly refrigerant mixture flammability properties, *The University of Western Australia Higher Degree Research Conference*, Perth, Australia, Oct 2019.

Student signature: [redacted] Date: 23 February 2022

I, Prof Eric F. May, certify that the student's statements regarding their contribution to each of the works listed above are correct.

Coordinating supervisor signature: [redacted] Date: 21 February 2022

List of Figures

List of Tables

1 Chapter 1 | Thesis Introduction

1.1 Introduction

Anthropogenic emissions of greenhouse gases (GHGs) in recent decades changed the earth-atmosphere energy balance and led to global warming as a threat to the world population and development [1]. Limiting global warming to less than 1.5 ℃ is a challenging task that requires a rapid reduction in GHG emissions across all sectors and regions. Despite constituting a minor fraction of the atmosphere, the GHGs absorb a significant portion of the upward flux of longwave solar radiations emitted by Earth's surface [2] and result in a global temperature rise. The GHGs emitted by increased industrial activities like refrigeration, power generation and steel production escalated global warming, causing shrinking Greenland and Antarctica ice sheets (over 420 billion tonnes of ice per year between 1993 and 2019 [3]) and increased ocean acidification by about 25 % since the beginning of the industrial revolution [4]. Figure 1.1 (a) shows the global warming potential (GWP) of the common GHGs over a time span of 100 years. The GWP is a measure of the amount of energy absorbed by the emissions of 1 ton of a gas relative to the emissions of 1 ton of Carbon Dioxide (CO_2) over a specific period [1]. Fluorinated gases (F-gases) used as working fluids (refrigerants) in current air-conditioning and cooling systems are considered the most detrimental GHGs with global warming potentials (GWPs) over 10,000 times that of carbon dioxide (CO_2) [5,6]. Eliminating the emissions of chemicals like F-gases with their high GWPs is an achievable objective that can significantly help mitigate climate change. Therefore, strict global regulations were set to control the emissions of high GWP refrigerants by replacing them with alternative and eco-friendly options [7].

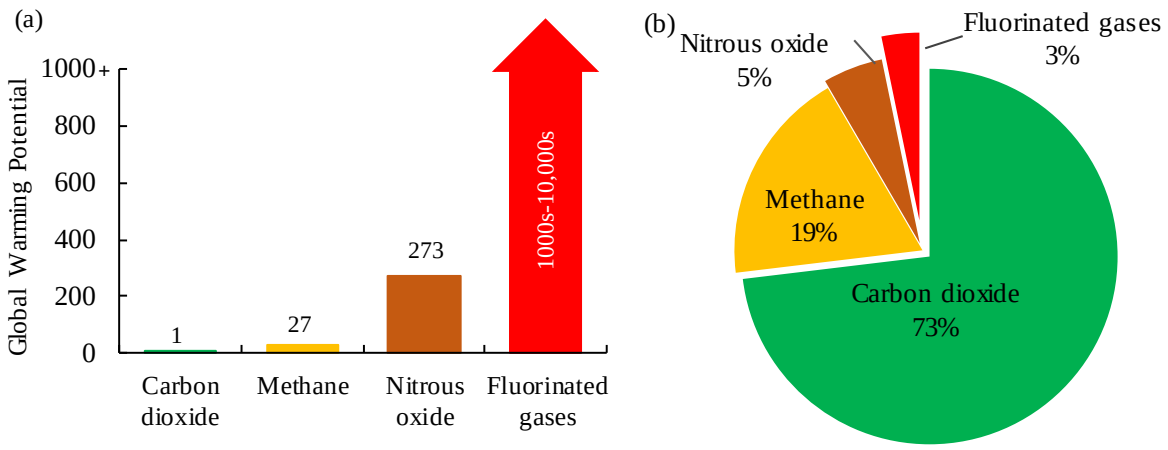

Figure 1.1: (a) The GWP of the common GHGs relative to carbon dioxide; the data were extracted from [8]. (b) The key contributors to the total anthropogenic GHG emissions of 52.4 Giga-tonnes of CO_2 equivalent ($GtCO_{2,eq}$) in 2019 (excluding land-use change and forestry); the data were extracted from [9].

Despite the lower GWP of CO_2, its high global emissions and long lifetime have a significant impact on climate change. Figure 1.1 (b) shows that CO_2 contributes to 73 % of the total anthropogenic GHG emissions of 52.4 $GtCO_2$ equivalent in 2019 compared with the 3 % contribution of the F-gases [10]. The CO_2 concentration in the atmosphere increased from around 277 ppm in 1750 (the pre-industrial era) to over 410 ppm in 2020, which is mostly caused by emissions from fossil fuel sources [11]. Among the top five common fuels, coal-originated CO_2 emissions account for 41 % of the total global emissions compared with the 21% contribution of natural gas, as shown in Figure 1.2. In addition, natural gas emits around (50-60) % less CO_2 compared with lignite coal for a similar energy unit [12], making it a better air-pollution-wise option. Because of its cleaner characteristics than other fossil fuels, natural gas is considered as a “bridge energy” to supply the global demand today while renewable and green technologies develop on a global scale. The liquefied form of natural gas (LNG) facilitated its global distribution from production wells to high demand locations when transporting through conventional pipelines is not feasible. However, the cryogenic refrigeration processes used in natural gas liquefaction facilities are energy-intensive and can undergo plant-shutdown periods, increasing the carbon footprint of LNG and blunting the long-term potential of the commodity. Reliable and uninterrupted supply of LNG with affordable prices can accelerate the transition from coal-fired systems to natural-gas-based power plants and iron, cement and steel production facilities. This affordability and reliability of natural gas supply will maintain a lasting decline in the demand for coal and help the global community tackle a key contributor to climate change.

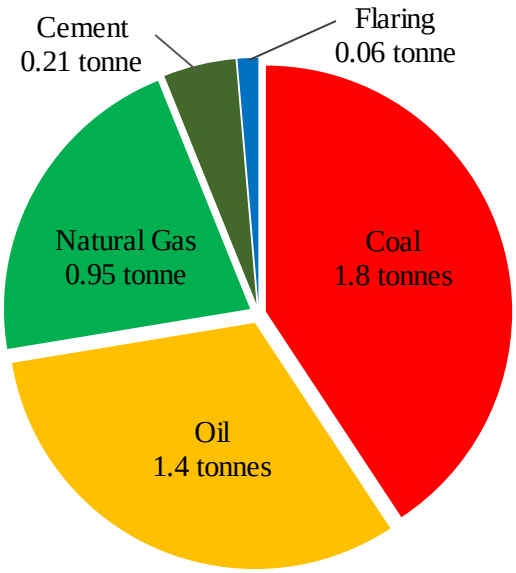

Figure 1.2: The average global CO_2 emissions per person from high-emission sources of coal, oil, gas, cement and flaring in 2020 [13].

1.2 Research focus

1.2.1 Low GWP refrigerant mixtures of HFOs, HFCs and CO_2

The first and second kinds of F-gases introduced to the refrigeration industry were Chlorofluorocarbons (CFCs) and Hydrochlorofluorocarbons (HCFCs). They were stable, efficient and safe-to-humankind working fluids that provided significant industrial and social development in their own time. However, their ozone layer depleting nature, substantial GWP and long lifetime in the atmosphere ended up their applications in the refrigeration system through a global ban by the Montreal Protocol (1987) [14,15]. To address the ozone depletion potential (ODP), a measure of damage a refrigerant causes to the ozone layer compared with an identical amount of trichlorofluoromethane (CFC-11) [1], the third generation of F-gases was introduced by substituting the chlorine component with hydrogen, called Hydrofluorocarbons (HFCs). Their acceptable heat transfer characteristics, stability over a wide operating temperature range, compatibility with the CFC equipment and lack of ODP promoted their applications in the domestic cooling systems [16]. Yet, the popular HFCs like HFC-143a, HFC-125 and HFC-134a have a GWP of 4470, 3170 and 1300 on a 100-year time scale, respectively [17]. Their extreme greenhouse effect and contributions to the total GHG

emissions of up to 20 % in the past 20 years urged the world community to reduce the global use of high-GWP fluids by 80 % by 2050 [18].

The fourth generation of fluorine-based gases is unsaturated HFCs called Hydrofluoroolefins (HFOs) [16]. The HFOs have zero ODP and much lower GWP than the HFCs and are excellent candidates to replace the commonly used refrigerants like HFC-134a and HFC-125 [19]. However, the popular HFOs like HFO-1243zf, HFO-1234yf and HFO-1234ze(E) are mildly flammable despite their GWP of less than 5 and their usage in mobile and stationary air-conditioning systems could be a potential risk [20–22]. The combustion products of the HFOs contain toxic and corrosive agents like Hydrogen Fluoride (HF) and Carbonyl Fluoride (COF_2) are other major safety risks. To mitigate these ignition hazards, HFOs can be blended with non-flammable refrigerants like carbon dioxide (CO_2), HFC-134a, HFC-125 and HFC-152a to neutralise their mild flammability characteristics [22]. Unfortunately, the thermodynamic property data for the HFO blends are scarce and predictive models perform poorly at simulating the cooling processes employing these refrigerant mixtures as their working fluid. Therefore, this thesis focused on filling the existing gap of knowledge for the thermophysical properties and flammability characteristics of eco-friendly HFO, HFC and CO_2 refrigerant mixtures listed in Table 1.1 that can contribute significantly to the phase-down of high GWP working fluids.

Table 1.1: Details of the refrigerants used in the mixtures for thermophysical and flammability characteristic studies.

ASHRAE Refrigerant Number	IUPAC name	Chemical formula	Referred convention	Refrigerant Type	GWP	Refs
R774	Carbon dioxide	CO_2	CO_2	Natural	1	[8]
R32	Difluoromethane	CH2F2	HFC-32	HFC	677	[15]
R134a	1,1,1,2-Tetrafluoroethane	CH2FCF3	HFC-134a	HFC	1300	[17]
R125	Pentafluoroethane	C2HF5	HFC-125	HFC	3170	[17]
R1234yf	2,3,3,3-Tetrafluoroprop-1-ene	C3H2F4	HFO-1234yf	HFO	4	[15]
R1243zf	3,3,3-Trifluoropropene	C3H3F3	HFO-1243zf	HFO	0.29	[23]

[a] ASHRAE stands for “American Society of Heating, Refrigerating and Air-Conditioning Engineers”.
[b] IUPAC stands for “International Union of Pure and Applied Chemistry”.

1.2.2 Cryogenic solid formation for high-boiling components in mixed refrigerants

A common refrigeration technology used in LNG production facilities is mixed refrigerant (MR) cryogenic cooling systems, where a blend of two or more components reduces the temperature of natural gas process feed down to 110 K. The advantages of MR cycles to pure fluid refrigeration cycles are improved heat transfer properties, adaptability of matching the system cooling curve and smaller and cheaper heat exchangers relative to other options. Adding high-boiling point components, like iso-pentane and iso-butane, to the refrigerant mixture will enhance the overall heat transfer properties of the mixture and promote the latent heat transfer from the gas to the coolant over wider ranges of temperature [24]. However, this improvement comes with a cost: the heavy components in the MR pose a potential risk of freeze-out and blockage that can result in equipment damage and unpredicted plant shutdowns. Such risks are similar to those caused by the freeze-out of trace impurities such as benzene, water and CO_2. [25–29], depositing in cryogenic heat exchangers and blocking the equipment. To understand and avoid these risks, this thesis investigates the solid formation and dissociation points for heavy components like iso-pentane in binary mixtures with methane (the component details are presented in Table 1.2) to mimic similar conditions in the MRs used in LNG production. These data sets are crucial to understanding the solidification properties of the concerned component and provide an optimised thermodynamic model capable of calculating freeze-out free refrigerant mixtures for safe and reliable cryogenic cooling systems.

Table 1.2: Details of the refrigerants used in the binary mixtures for solid formation studies.

ASHRAE Refrigerant Number	IUPAC name	Chemical formula	Referred convention	Refrigerant Type	GWP	Refs
R601a	2-methylbutane (iso-pentane)	C5H12	iso-Pentane	Natural	10	[30]
R50	Methane	CH4	Methane	Natural	25	[8]

1.3 Thesis Outline

This thesis is arranged as a series of three peer-reviewed published journal articles, and one manuscript under review with the industrial partner (Mitsubishi Heavy Industries) as the lead author, corresponding to Chapters 2, 3, 5, and 4, respectively. Also, Appendix B presents a peer-reviewed published journal article as a co-author. Each chapter represents a separate publication, and the combination of chapters follow the progression of work on thermophysical properties of refrigerant mixtures with applications for domestic and cryogenic cooling systems

completed during this doctoral research and embody a coherent narrative. This section provides a brief introduction to each chapter and how they are related.

The ignition hazards of mildly flammable eco-friendly refrigerant mixtures were investigated in Chapter 2. The minimum ignition energy (MIE) and laminar burning velocity (BV) measurement setups development and validation with the pure Ammonia (NH_3) were explained and the experimental MIE and BV data for refrigerant/air mixtures of HFC-32 and HFO-1234yf and mixtures of HFC-32 and HFO-1234yf with non-flammable refrigerants of HFC-134a, HFC-125 and CO_2 were reported. Chapter 3 presents the measured vapour-liquid equilibrium (VLE) data for binary mixtures of the HFO-1243zf and CO_2. The experimental VLE data were used to tune two thermodynamic models of Helmholtz free energy and Peng Robinson equations of state, which can help industry to design safe and efficient refrigeration systems employing this low GWP working fluid. Chapter 4 presents experimental phase equilibrium data including VLE and solid-fluid equilibrium (SFE) conditions for HFC-32 and CO_2 binary mixtures as an eco-friendly "bridge refrigerant mixture" to reduce the GWP of the working fluids in the cooling systems, while the HFO refrigerant mixtures are being developed.

In Chapter 5, experimental freezing and melting point data for pure iso-pentane and (methane + iso-pentane) binary systems were presented to investigate the solubility of this high-boiling point component in lighter compounds like methane for the purpose of more accurately assessing freeze-out risks in mixed refrigerants that can used in LNG production or the pre-cooling stage of liquid hydrogen production. The new experimental melting data for iso-pentane was used to optimise a thermodynamic model with the Peng-Robinson cubic equation of state implemented in the ThermoFAST software package.

Chapter 6 provides a summary of the main conclusions of the research outcomes and suggestions for future research to improve the accuracy of the thermodynamic models for refrigerant mixtures. Appendix B presents new thermodynamic data for mixtures of CO_2 with HFCs and HFO-1234yf refrigerant mixtures. The thermodynamic data include vapour-liquid equilibrium (VLE), density, and heat capacity properties. The accuracy of reference Helmholtz equations implemented in the NIST's REFPROP 10 software package was assessed for multi-component mixtures and their performance was optimised.

1.4 References

[1] Wang H, Zhao L, Cao R, Zeng W. Refrigerant alternative and optimization under the constraint of the greenhouse gas emissions reduction target. J Clean Prod 2021;296:126580. doi:10.1016/j.jclepro.2021.126580.

[2] Manabe S. Role of Greenhouse Gas in Climate Change. Tellus, Ser A Dyn Meteorol Oceanogr 2019;71:1–13. doi:10.1080/16000870.2019.1620078.

[3] Velicogna I, Mohajerani Y, Geruo A, Landerer F, Mouginot J, Noel B, et al. Continuity of Ice Sheet Mass Loss in Greenland and Antarctica From the GRACE and GRACE Follow-On Missions. Geophys Res Lett 2020;47:1–8. doi:10.1029/2020GL087291.

[4] Understanding the Science of Ocean and Coastal Acidification. United States Environ Prot Agency 2021. https://www.epa.gov/ocean-acidification/understanding-science-ocean-and-coastal-acidification.

[5] Abas N, Kalair AR, Khan N, Haider A, Saleem Z, Saleem MS. Natural and synthetic refrigerants, global warming: A review. Renew Sustain Energy Rev 2018;90:557–69. doi:10.1016/j.rser.2018.03.099.

[6] United Nation Climate Change. HFCs, Refrigeration and Air-conditioning: Minimising Climate Impact, Maximising Safety n.d.

[7] Leggett JA. The United Nations Framework Convention on Climate Change, the Kyoto Protocol, and the Paris Agreement: A Summary. Congr Res Serv 2020;1:11.

[8] The United States Environmental Protection Agency (EPA). Understanding Global Warming Potentials n.d. https://www.epa.gov/ghgemissions/understanding-global-warming-potentials.

[9] PBL Netherlands Environmental Assessment Agency. Trends in Global CO2 and Total Greenhouse Gas Emissions. 2020.

[10] Intergovernmental Panel on Climate Change. Climate Change 2014 Mitigation of Climate Change. 2014. doi:10.1017/cbo9781107415416.

[11] Friedlingstein P, O'Sullivan M, Jones MW, Andrew RM, Hauck J, Olsen A, et al. Global Carbon Budget 2020. Earth Syst Sci Data 2020;12:3269–340. doi:10.5194/essd-12-

3269-2020.

[12] Turner M, Iyengar A, Woods M. Cost and Performance Baseline for Fossil Energy Plants Supplement: Sensitivity To Co2 Capture Rate in Coal-Fired Power Plants. Natl Energy Technol Lab (NETL), United States Dep Energy 2019;1:36.

[13] Andrew RM, Peters GP. The Global Carbon Project's fossil CO2 emissions dataset (2021v34) [Data set]. Zenodo 2021. doi:https://doi.org/10.5281/zenodo.5569235.

[14] Buxton G. The Montreal protocol on substances that deplete the ozone layer. Int Negot 1988;1:231–46. doi:10.1163/15718069620847781.

[15] Ciconkov R. Refrigerants: There is still no vision for sustainable solutions. Int J Refrig 2018;86:441–8. doi:10.1016/J.IJREFRIG.2017.12.006.

[16] Ciconkov R. Refrigerants: There is still no vision for sustainable solutions. Int J Refrig 2018;86:441–8. doi:10.1016/j.ijrefrig.2017.12.006.

[17] Change IP on C. Anthropogenic and natural radiative forcing. In: Intergovernmental Panel on Climate Change, editor. Clim. Chang. 2013 Phys. Sci. Basis Work. Gr. I Contrib. to Fifth Assess. Rep. Intergov. Panel Clim. Chang., vol. 9781107057, Cambridge: Cambridge University Press; 2013, p. 659–740. doi:10.1017/CBO9781107415324.018.

[18] UNEP. The Kigali Amendment to the Montreal Protocol: HFC Phase-down. 28th Meet Parties to Montr Protoc 10-14 October, 2016, Kigali, Rwanda 2016:1–7.

[19] S. Sadaghiani M, Arami-Niya A, Marsh B, Z.S. Al Ghafri S, F. May E. Vapor–Liquid Equilibria for Carbon Dioxide + 3,3,3-Trifluoropropene Binary Mixtures at Temperatures between (288 and 348) K. J Chem & Eng Data 2021;0. doi:10.1021/acs.jced.1c00297.

[20] The Japan Society of Refrigerating and Air Conditioning Engineers. Risk Assessment of Mildly Flammable Refrigerants. 2014 Prog Rep 2015:132.

[21] Raabe G. Molecular simulation studies in hydrofluoroolefine (HFO) working fluids and their blends. Sci Technol Built Environ 2016;22:1077–89. doi:10.1080/23744731.2016.1206796.

[22] Bell IH, Domanski PA, McLinden MO, Linteris GT. The hunt for nonflammable refrigerant blends to replace R-134a. Int J Refrig 2019;104:484–95. doi:10.1016/j.ijrefrig.2019.05.035.

[23] González S, Jiménez E, Ballesteros B, Martínez E, Albaladejo J. Hydroxyl radical reaction rate coefficients as a function of temperature and IR absorption cross sections for CF3CH=CH2 (HFO-1243zf), potential replacement of CF3CH2F (HFC-134a). Environ Sci Pollut Res 2015;22:4793–805. doi:10.1007/s11356-014-3426-2.

[24] Khan MS, Lee S, Rangaiah GP, Lee M. Knowledge based decision making method for the selection of mixed refrigerant systems for energy efficient LNG processes. Appl Energy 2013;111:1018–31. doi:https://doi.org/10.1016/j.apenergy.2013.06.010.

[25] Hisazumi Y, Yamasaki Y, Sugiyama S. Proposal for a high efficiency LNG power-generation system utilizing waste heat from the combined cycle1Published in co-operation with the Japanese Society of Energy Resources.1. Appl Energy 1998;60:169–82. doi:https://doi.org/10.1016/S0306-2619(98)00034-8.

[26] Baccanelli M, Langé S, Rocco M V, Pellegrini LA, Colombo E. Low temperature techniques for natural gas purification and LNG production: An energy and exergy analysis. Appl Energy 2016;180:546–59. doi:https://doi.org/10.1016/j.apenergy.2016.07.119.

[27] Siahvashi A, Al Ghafri SZS, Yang X, Rowland D, May EF. Avoiding costly LNG plant freeze-out-induced shutdowns: Measurement and modelling for neopentane solubility at LNG conditions. Energy 2021;217:119331. doi:10.1016/j.energy.2020.119331.

[28] Sampson CC, Metaxas PJ, Siahvashi A, Stanwix PL, Graham BF, Johns ML, et al. Measurements of solidification kinetics for benzene in methane at high pressures and cryogenic temperatures. Chem Eng J 2020:127086. doi:https://doi.org/10.1016/j.cej.2020.127086.

[29] Siahvashi A, Al Ghafri SZ, May EF. Solid-fluid equilibrium measurements of benzene in methane and implications for freeze-out at LNG conditions. Fluid Phase Equilib 2020;519:112609. doi:10.1016/j.fluid.2020.112609.

[30] Garg P, Kumar P, Srinivasan K, Dutta P. Evaluation of isopentane, R-245fa and their mixtures as working fluids for organic Rankine cycles. Appl Therm Eng 2013;51:292

2 Chapter 2 │ Minimum ignition energies and laminar burning velocities of ammonia, HFO-1234yf, HFC-32 and their mixtures with carbon dioxide, HFC-125 and HFC-134a

Forward – The full text of this chapter has been published in the *Journal of Hazardous Materials* in 2021 (DOI: https://doi.org/10.1016/j.jhazmat.2020.124781). It has been reformatted with minor amendments to fit style and structure of this thesis.

2.1 Abstract

Given the safety issues associated with flammability characteristics of alternative environmentally-friendly refrigerants, it is vital to establish measurement systems to accurately analyse the flammability of these mildly flammable refrigerants. In this study, a customised Hartmann bomb analogue was used to measure the minimum ignition energy (MIE) and laminar burning velocity (BV) for refrigerant/air mixtures of pure ammonia (R717), R32, R1234yf and mixtures of R32 and R1234yf with non-flammable refrigerants of R134a, R125 and carbon dioxide (R744). The MIEs of R717, R32, and R1234yf were measured at an ambient temperature of 24 °C to be (18.0 ± 1.4), (8.0 ± 1.5) and (510 ± 130) mJ at equivalence ratios of 0.9, 1.27 and 1.33, respectively. Adding the non-flammable refrigerants R134a, R125 and R744 along with R32 at volumetric concentrations of 5% each to R1234yf reduced the latter compound's flammability and increased its MIE by one order of magnitude. The laminar burning velocities of pure R717 and R32 were measured at an equivalence ratio of 1.1 using the flat flame method and found to be 8.4 and 7.4 cm/s, respectively. Adding 5% R1234yf to R32 decreased the laminar burning velocity by 11%, while a further 5% addition of R1234yf resulted in a decrease of over 30% in the laminar burning velocity.

2.2 Introduction

Following the adoption of the Kyoto Protocol [1] and changes in the regulations of many countries to control the emissions of high global warming potential (GWP) refrigerants [2], substantial research has begun to replace the current high-GWP working fluids of the cooling systems with alternative refrigerants [3]. Hydrofluoroolefins (HFOs) are the latest generation of environmentally friendly refrigerants that can only survive in the atmosphere for merely a few days because of the weak double bonds in their structure. As a result, the GWP for HFOs is considerably lower (less than 1) than hydrofluorocarbons (HFCs); in contrast, R134a is one of the most popular refrigerants with a GWP of ~1330. However, the performance of HFOs in current refrigerators is inferior, as they consume larger amounts of energy to deliver a similar cooling power [4]. Besides, mild flammability of HFOs poses a risk for their domestic applications, such as air conditioning systems, potentially causing fire or emitting hazardous combustion products. Blending HFOs with non-flammable refrigerants – including HFCs and natural refrigerants – could boost their performance, decrease the mixtures' GWP, and minimise their flammability [5]. For example, R1234yf and R32 are two compounds compatible with conventional refrigeration systems, including new automobile air conditioners, that can be used to make low GWP refrigerant blends with a reasonable cooling performance [6].

The ASHRAE standard 34, "Designation and Safety Classification of Refrigerants" [7], categorises R32 and R1234yf as mildly flammable substances. Table 2.1 presents this classification in terms of safety and toxicity, where R32 and R1234yf fall into the A2L classification. Risks associated with these refrigerants include a high contribution to the accumulation of trifluoroacetic acid (TFA) in the atmosphere [6] and toxic combustion products such as hydrogen fluoride (HF) and carbonyl fluoride (COF_2) [8,9]. Therefore, the flammability characteristics of these refrigerants and their mixtures with non-flammable candidates must be addressed carefully and accurately.

Table 2.1: Safety classifications of refrigerants: (A) and (B) represent refrigerants with lower and higher toxicity, respectively [7].

	Safety Group	
Higher Flammability	A3	B3
Lower Flammability	A2	B2
	A2L*	B2L*
No Flammability	A1	B1
Toxicity	Lower	Higher

* A2L and B2L refrigerants have burning velocities lower than 10 cm/s.

The flammability characteristics of pure R32 and R1234yf in mixtures with air including their lower flammability limit (LFL), minimum ignition energy (MIE) and maximum laminar burning velocity (BV) have been investigated and reported in the literature [10–15]. Nevertheless, the reported results suffer from a paucity of consistency – caused by a wide variety of measurement approaches and procedures – that makes fire risk assessment demanding and potentially unreliable. Table 2.2 presents the different MIE values reported for refrigerant/air mixtures containing R32, R1234yf and R717. The reported MIE values of R32 in the literature range from 14 mJ [14] to 26,300 mJ [16]. Similarly, the reported MIE of R1234yf varies from (less than) 500 mJ [17] to 10,000 mJ [18]. The MIE of R717 was reported between 8 mJ [19] and 300 mJ [18]. Spark specifications were reported to be the main source of the variation in the MIE values [20]. Thus, the measured MIE values for a given refrigerant obtained with a specific measurement system can at least be compared with the values obtained for other compounds using the same apparatus under similar conditions.

Table 2.2: Reported minimum ignition energies for R717, R32, and R1234yf.

Compound	Ignition Method	Equivalence Ratio*	MIE/mJ	Ref.
R717	Spark Energy (Capacitive)	0.90	8	[19]
	Estimated	1.00	19	[14]
	Estimated	1.00	20	[18]
	Spark Energy (Capacitive)	1.00	50-100	[21]
	Spark Energy (Capacitive)	Not given	170	[21]
	Spark Energy (Capacitive)	1.00	100-300	[18]
R1234yf	Spark Energy (Capacitive)	1.32	<500	[9]
	Estimated	1.33	780	[14]
	Spark Energy	1.00	1500	[9]
	Estimated	1.00	2000	[18]
	Spark Energy (Capacitive)	Not given	5000-10000	[18]
R32	Estimated	1.27	14	[14]
	Estimated	1.27	20	[14]
	Estimated	1.00	20	[18]
	Spark Energy (Capacitive)	Not given	30-100	[18]

Bunsen burner, spherical vessel, and particularly vertical tube are the main laminar burning velocity measurement systems reported in the literature [13,22,23]. Jabour et al. [12,24] used a vertical tube to measure the BV of a series of refrigerants such as R32 and R717. They measured the BV at stoichiometric concentrations to be 6.5 cm/s and 7 cm/s for R32 and R717, respectively. Takizawa et al. [11] also measured the BV of R32 by the vertical tube method and found a maximum value of 6.2 cm/s for an R32 + air mixture at 19.2 vol%. Fuller et al. [23] proposed a new approach, known as the flat flame method, which enables a more direct measurement of the BV. In this arrangement, the effect of buoyancy on the flame was eliminated, and a one-dimensional flat flame was formed after ignition, which propagates downward at the mixture's BV. They used this method to measure the BV of propane + air mixture at 4 mol% to be 40 cm/s. For the same mixture and using a similar method, Bockhorn et al. [25] reported the BV to be 37 cm/s.

In this study, the flammability of pure R32, R1234yf, R717 and mixtures of R32 and R1234yf with non-flammable refrigerants such as R125, R134a and R774 (CO_2) was evaluated by measuring their MIE and Laminar BV. The MIE of the pure components of R32, R1234yf and R717 was measured using a customised Hartmann bomb analogue. To analyse the MIE of the refrigerants, the current and high voltage supplied to the discharge circuit to generate the spark were measured precisely during the ignition process. Furthermore, the effect of adding non-

flammable refrigerants on the MIEs of R32 and R1234yf was investigated. Finally, the laminar BV of pure R717, R32 and mixtures of R32 and R1234yf was measured directly with the flat flame method, and the results were compared with those in the literature.

2.3 Experimental

2.3.1 Minimum ignition energy

The details of the gases used in this work are presented in Table 2.3.

Table 2.3: Details of the pure refrigerants and air used in this study.

ASHRAE[a] refrigerant number	IUPAC[b] name	Chemical formula	CAS #	Supplier	Purity[c]
R32	Difluoromethane	CH_2F_2	75-10-5	Core gas	0.995
R125	Pentafluoroethane	C_2HF_5	354-33-6	Core gas	0.995
R134a	1,1,1,2-Tetrafluoroethane	$C_2H_2F_4$	811-97-2	Core gas	0.995
R1234yf	2,3,3,3-Tetrafluoropropene	$C_3H_2F_4$	754-12-1	Core gas	0.995
R744	Carbon Dioxide	CO_2	124-38-9	Core gas	0.99995
R717	Ammonia	NH_3	7664-41-7	BOC	0.9999
Air	Zero Grade Air	O_2 + N_2	132249-10-0	Core gas	0.21 ± 0.005 O_2

[a] ASHRAE stands for "American Society of Heating, Refrigerating and Air-Conditioning Engineers".
[b] IUPAC stands for "International Union of Pure and Applied Chemistry".
[c] Based on the supplier's specification (mole fraction).

The measurement of MIE for the selected refrigerants was conducted by the Hartmann bomb approach according to the British Standard EN 1839 [26]. The details of the original Hartman bomb setup were described in Appendix A (supplementary information - SI). To safely discharge the toxic combustion products, the existing Hartmann bomb setup was adapted to use a cylindrical tube vessel. As shown in Figure 2.1, the new setup had a similar configuration to the Hartmann bomb, but the ignition vessel is connected directly to a neutralising system, which is described in detail in Appendix A. The ignition vessel consisted of a transparent vertical tube with 40 mm ID and 1500 mm length, closed at both ends with two caps. The lower end cap (ignition cap) was equipped with two tungsten electrodes (3.2 mm OD) providing the spark for ignition. It also included a gas inlet connection and an inline pressure transducer (DJ Instruments thro-FLU DF2). Both caps had quenching plates to prevent the flame from transferring into the gas lines. The commissioned MIE measurement system was validated by

measuring pure R717 and R32 and comparing the results with the obtained values using the original Hartmann bomb apparatus.

A gas mixture preparation setup was applied to make mixtures of the refrigerants + air. The gas mixing setup consisted of several mass flow controllers (MFCs, Alicat Scientific MCS-1SLPM-D-IN-5M), where each MFC was connected to a pure gas cylinder. A small cylindrical container equipped with a stirrer was linked to the output of the MFCs to make the blends more homogenous. By setting the gas flow rates of the MFCs, it was possible to prepare a mixture with the desired composition. Before ignition, the prepared mixture flowed through the measurement system for 20 minutes, sufficient to purge the vessel's volume at least eight times. The temperature of the gas mixture was maintained constant at around 24 °C by using a heater inside the fume enclosure surrounding the ignition vessel and the gas mixing setup (Figure 2.1).

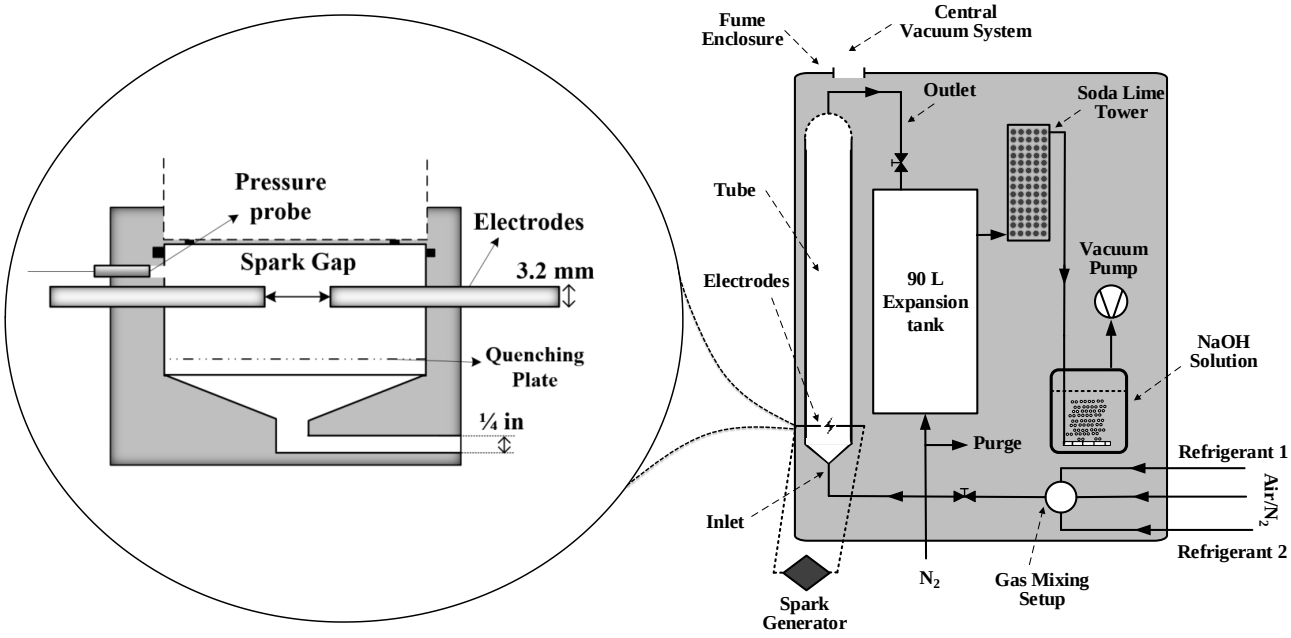

Figure 2.1: The schematic of the minimum ignition energy measurement system, including the effluent neutralisation and treatment components.

A high voltage spark generator – similar to that used by Lee and Shepherd et al. [27] – was connected to the electrodes in the measurement configuration to enable measurement of the minimum energy to ignite the flammable mixture. Further details are provided in Appendix A. The top-end cap of the ignition vessel was connected to a 90 L expansion tank to minimise the pressure rise in the vessel caused by the ignition. A vacuum pump (Varian SH-110) drew the

toxic and corrosive products through the neutralisation system, which included a sodium hydroxide solution and a soda-lime tower.

2.3.2 Laminar Burning Velocity

The flat flame approach was used for the laminar burning velocity measurements. The ignition vessel described in section 2.2 was modified slightly before being used for the BV measurements (Figure 2.2). The refrigerant + air mixture, prepared in the gas mixing setup, flowed through the ignition vessel from the bottom to purge the system (displacing at least eight times the vessel's volume). Then, the gas inlet and outlet were closed for two minutes to stabilise the fluid inside the vessel before opening the gas outlet to the expansion tank followed by the ignition of the mixture at the top cap (the ignition cap). The resulting flat flame propagated downward while a high-speed camera (Canon EOS M50 with 60 frames per second shooting speed) recorded the propagation. The BV of the mixture is equal to the lower luminous boundary of the flat flame's propagation speed [23]. The pressure inside the vessel was kept near atmospheric by opening the exhaust line to the expansion tank. The corrosive combustion products were neutralised by passing them through a soda-lime tower and NaOH solution in the neutralisation section (as described in Appendix A).

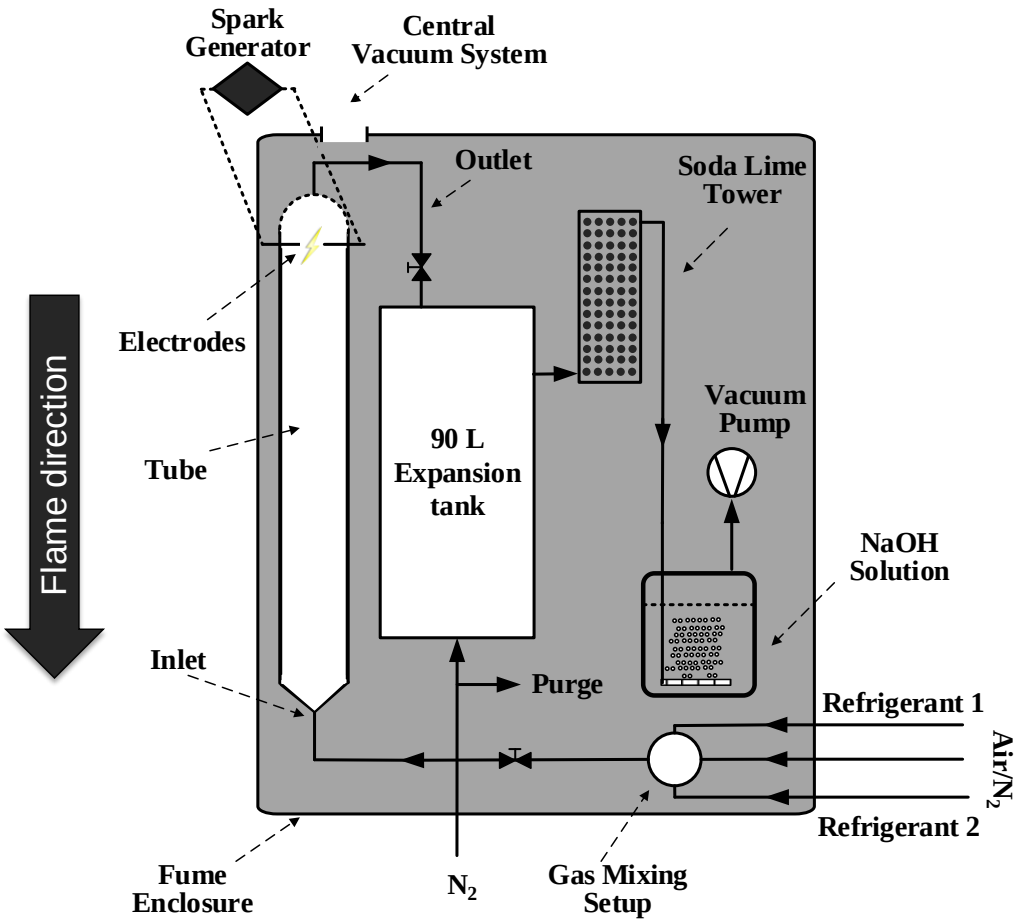

Figure 2.2: Schematic of the flat flame method configuration for the measurement of laminar burning velocity.

2.4 Results and Discussion

2.4.1 Minimum Ignition Energy

2.4.1.1 Pure Refrigerants

The MIE of the refrigerant/air mixtures was measured against the equivalence ratio to determine the lowest energy required to ignite the mixture, which the equivalence ratio is defined as follows:

$$\varphi = \frac{(\text{Refrigerant/Air})}{(\text{Refrigerant/Air})_{Stoichiometiric}} \qquad 2.1$$

The equivalence ratio is used to indicate whether the combustion is stoichiometric ($\varphi = 1$), lean with excess air ($\varphi < 1$) or rich with incomplete combustion ($\varphi > 1$). The uncertainty calculation methodologies for both minimum ignition energy and equivalence ratio are explained in Appendix A. Figure 2.3 (a) shows the measured MIE of R717 at equivalence ratios from 0.7 to 1.2. The lowest MIE was found to be (18.0 ± 1.4) mJ at an equivalence ratio of 0.9. The MIE values for R32 – measured at three equivalence ratios between 1 and 1.4 – are illustrated in Figure 2.3 (b), with the lowest ignition energy of (8.0 ± 1.5) mJ at an equivalence ratio of 1.27. As shown in Figure 2.3 (c), the MIE of R1234yf was measured to be (510 ± 130) mJ at an equivalence ratio of 1.33. The lower MIEs of R32 show that the risk of using it as the working fluid in the cooling systems is significantly higher than the HFO, R1234yF, or even R717 given the toxic combustion products. Figure 2.4 shows the propagating flame during the MIE measurement for refrigerant/air mixtures of R717, R32 and R1234yf.

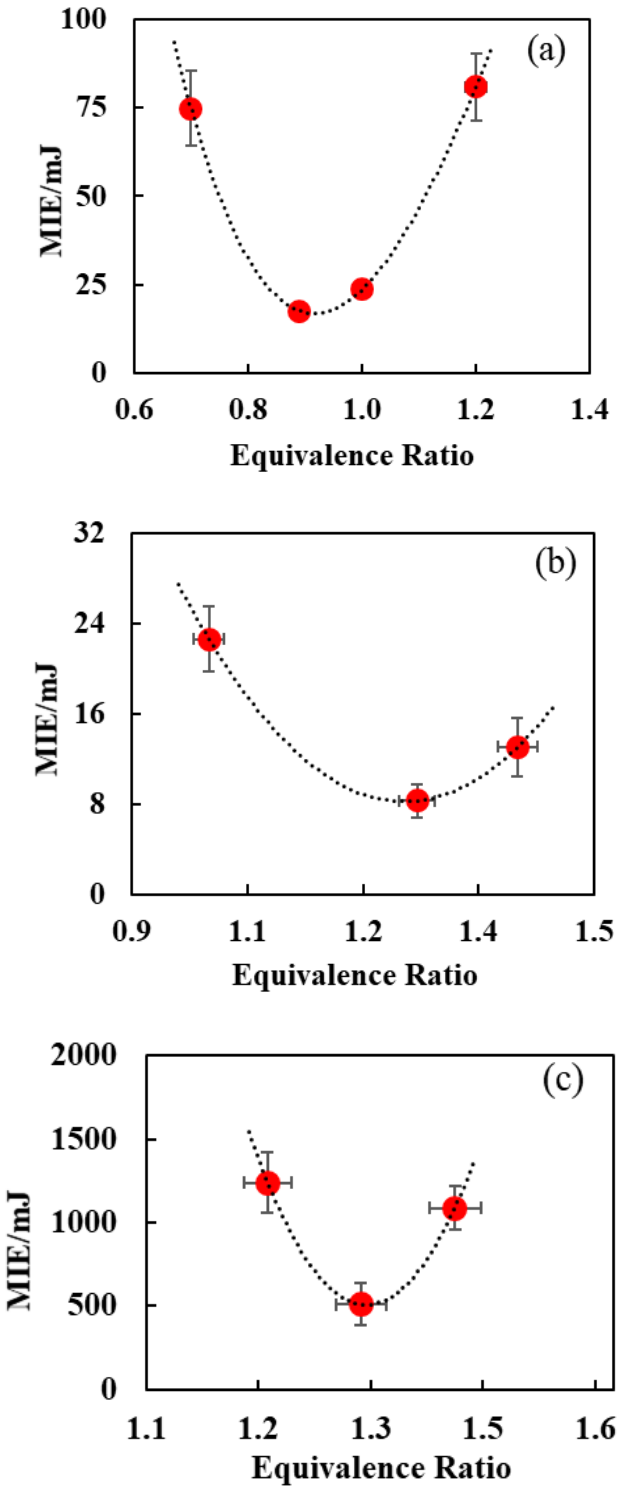

Figure 2.3: The MIE of R717 (a), R32 (b) and R1234yf (c) at different equivalence ratios. The dotted lines represent the trend line of the measured points.

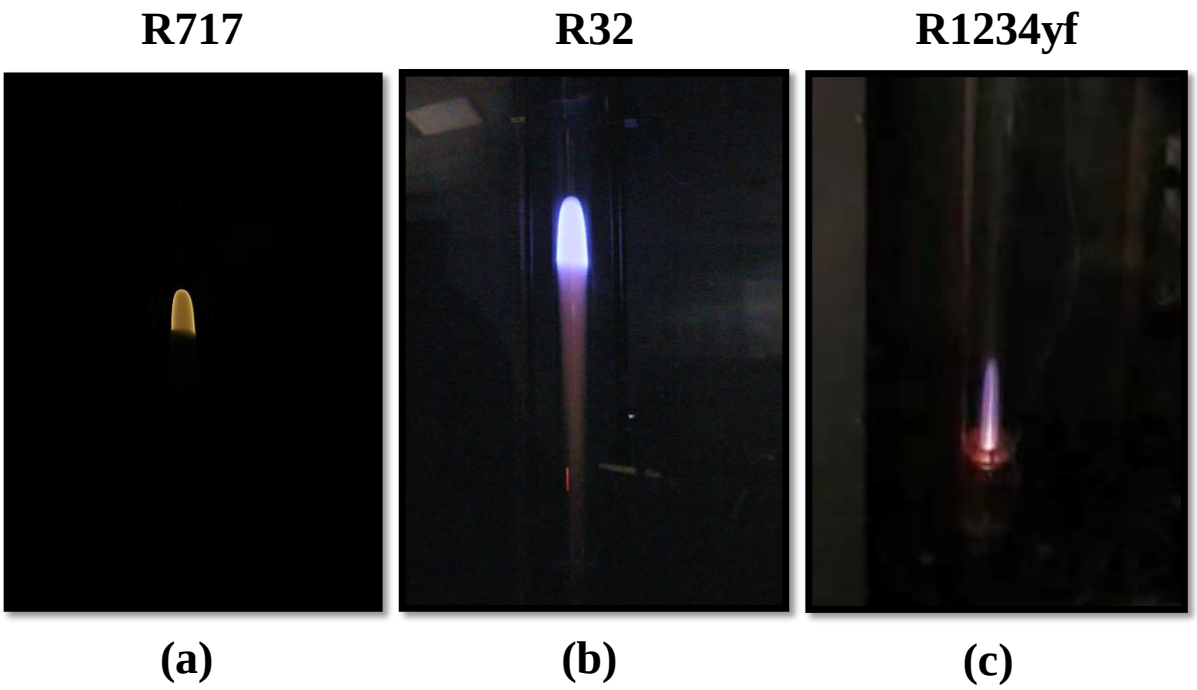

Figure 2.4: The propagating flame during MIE measurement of refrigerant/air mixtures for (a) R717, (b) R32 and (c) R1234yf.

A wide variation in reported MIEs for the refrigerants in the literature points to the dependency of this property on the measurement characteristics such as the spark gap and duration [20]. Takizawa et al. [14] conducted a comprehensive study of MIE measurements for mildly flammable mixtures. They used an alternative method based on quenching distance in which the minimum distance between two surfaces that allowed self-sustained flame propagation to take place was determined. Movileanu et al. [28,29] employed a similar approach to measuring the minimum ignition energies for hydrocarbon/air mixtures. Here, the MIEs measured in this work were compared with those reported by Takizawa et al.[14] by determining an equivalent quenching distance using the following equation:

$$E_{min} = \left(\frac{1}{6}\right)\pi d_{min}^3 \rho_b c_p (T_b - T_u) \qquad 2.2$$

Here d_{min}, ρ_b, c_p, T_b and T_u stand for the minimum quenching distance, the burned gas density, the burned gas heat capacity, the burned gas temperature, and the unburned gas temperature, respectively. T_b is considered equivalent to the adiabatic temperature of the flame, where the adiabatic flame temperature is determined by chemical and thermodynamic equilibrium reached in the burned gas. The values reported for ρ_b, c_p, T_b and T_u by Takizawa et al. [14] were used in Equation 2.2. for d_{min} is measured by reducing the flame thickness from the

measured quenching distance between two surfaces (quenching plates equipped on the electrodes), as expressed below:

$$d_{min} = (d_q - 2\delta) \quad 2.3$$

where d_q and δ denote the measured quenching distance and flame thickness, respectively. Takizawa et al. [14] estimated the MIE of R717 at an equivalence ratio of 1 to be 19 mJ, with a quenching distance of 7.45 mm. At the same equivalence ratio, the measured MIE for R717 (24 mJ) in this study corresponds to a quenching distance of (7.75 ± 0.15) mm, which is within 4% of the quenching distance reported by Takizawa et al. [14]. The corresponding quenching distance for the MIE of R32 measured in this work at an equivalence ratio of 1.27 (8 mJ) is (5.8 ± 0.2) mm. Takizawa et al. [14] reported the MIE for R32 at this equivalence ratio to be 14 mJ based on their measured quenching distance of 6.45 mm. Although this difference is larger than for R717, the agreement between the two independent determinations is reasonable.

The measured MIE for R1234yf – (510 ± 130) mJ – corresponds to a quenching distance of (23 ± 1) mm at 23 °C. Takizawa et al. [14] reported a quenching distance for R1234yf around 25 mm, corresponding to MIE of approximately 550 mJ. Again this level of agreement is encouraging. However, the MIE for R1234yf was also found in this work to be particularly sensitive to ambient temperature, with MIEs measured at 17 °C in the range of 3-4 J, six to eight times larger than MIEs at 23 °C. No dependence of the MIE on ambient temperature was observed for R32.

The sensitivity of the MIE to different spark gap sizes was also studied. Figure 2.5 shows the MIE of R32 at spark gaps of 5 and 6.5 mm. The MIE of R32 at the spark gap of 6.5 mm was measured to be 8 mJ at an equivalence ratio of 1.27. This increased to 31 mJ for a 5 mm spark gap because of the excessive flame heat loss to the electrodes and shortage of radicals, which increased the ignition energy by four times. Further increase in the spark gaps led to unsuccessful sparks, preventing from measuring the MIE with larger gaps. The increasing pattern of the MIE by reducing the spark gap is in consistent with trends reported in the literature [22].

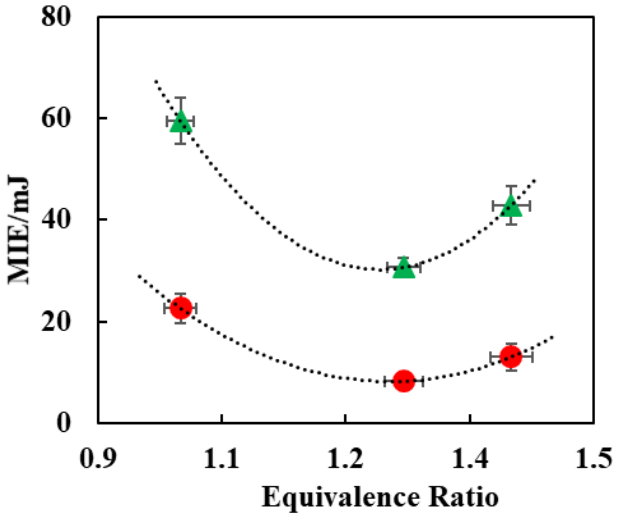

Figure 2.5: Effect of spark gap size on the MIE of R32: ● 6.5 mm gap and ▲ 5 mm gap. The dotted lines represent the trend line of the measured points.

2.4.1.2 Refrigerant mixtures

After validation of the measurement system by determining the MIEs of pure refrigerants, the effect of adding non-flammable refrigerants like R744, R125 and R134a on the MIE of mixtures of R32 and R1234yf was investigated. The minimum ignition energy of a ternary mixture of R32 + R1234yf + R744 (28:66:6 wt%) was measured at concentrations of 12, 14, and 16 vol% in air (Figure 2.6). The lowest value occurred at a concentration of 14 vol% with the corresponding MIE of (330 ± 60) mJ, which is 40 times higher than the MIE of pure R32. This mixture requires more energy to generate a self-sustaining flame kernel that would continue to propagate after the spark discharge.

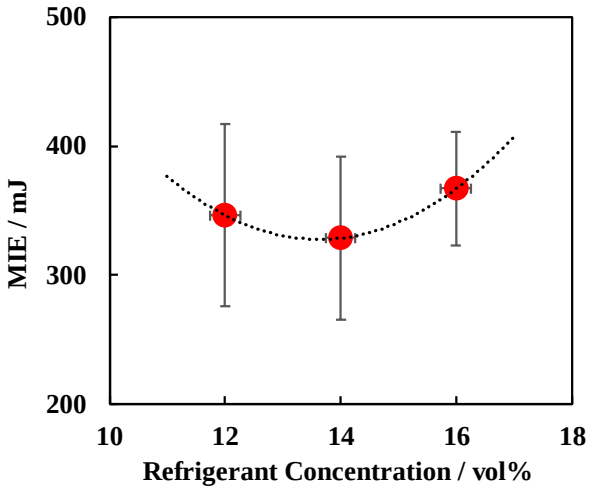

Figure 2.6: The MIE of R32 + R1234yf + R744 (28:66:6 %wt) mixture at different concentrations (vol%) in air. The dotted line represents the trend line of the measured points.

In this work, neither a four-component equimolar mixture of (R32 + R1234yf + R134a + R125) at refrigerant concentrations of 25, 27 and 29 vol% in air nor the equimolar five-component mixture of (R32 + R1234yf + R134a + R125 + R744) at similar concentrations could be ignited, even when the mixture was exposed to 8 J of spark energy. This shows the extinguishing effect of R134a, R125 and R744 on the R32 and R1234yf, which makes the mixture less risky to the ignition sources. For the five-component mixture, the ignition risk threshold concentration of R1234yf was found by increasing it sequentially to 80 vol%, with the other four components held at the same ratio (down to 5 vol%). At refrigerant concentrations of 12 and 15 vol% in air this mixture could be ignited with MIEs of (4.4 ± 0.8) J and (3.8 ± 0.8) J, respectively. Table 2.4 presents a summary of the MIEs measured for the multi-component mixtures. Also, the flames produced at these concentrations were weak and only propagated around 5 cm along the tube – less than the 30 cm threshold defined by EN1839 [26] as the minimum propagation distance required for a successful ignition. Such a high MIE and weak flame propagation emphasise the significance of blending refrigerants in alleviating the ignition hazards associated with cooling systems.

Table 2.4: The MIE of multi-component mixtures of refrigerants.

Mixture	Refrigerant/vol%	MIE/J
0.25 R1234yf + 0.25 R32 + 0.25 R134a + 0.25 R125	25, 27 and 29	No ignition (up to 8)
0.2 R1234yf + 0.2 R32 + 0.2 R134a + 0.2 R125 + 0.2 R744	25, 27 and 29	No ignition (up to 8)
0.8 R1234yf + 0.05 R32 + 0.05 R134a + 0.05 R125 + 0.05 R744	12	4.4 ± 0.8
0.8 R1234yf + 0.05 R32 + 0.05 R134a + 0.05 R125 + 0.05 R744	15	3.8 ± 0.8

2.4.2 Laminar Burning Velocity

2.4.3 Pure Refrigerants

Several attempts to measure the laminar burning velocity of R32 and R1234yf were also made using the Bunsen burner approach described in Appendix A. However, it was not possible to maintain a stable flame with the tested refrigerants unless the oxygen concentration of the air was increased to 28 % for R32 and 44.5 % for R1234yf. This confirms that the Bunsen burner is not applicable for measuring the burning velocities of 2L refrigerants such as R32 and R1234yf with air [21].

The vertical tube method was used for the BV measurements of R32 and R1234yf, as explained in Appendix A. However, based on Equation A-7 and Figure A.5, the calculation of the flame

area is one of the critical sources of uncertainty for a luminous flame, because the accurate determination of the flame boundary is a difficult task. Figure 2.7 shows the flame propagation of an R717/air mixture at an equivalence ratio of 1.1 in the vertical tube. The area of the flame varies by 50 % along the tube while the flame propagation speed was essentially constant (around 25 cm/s).

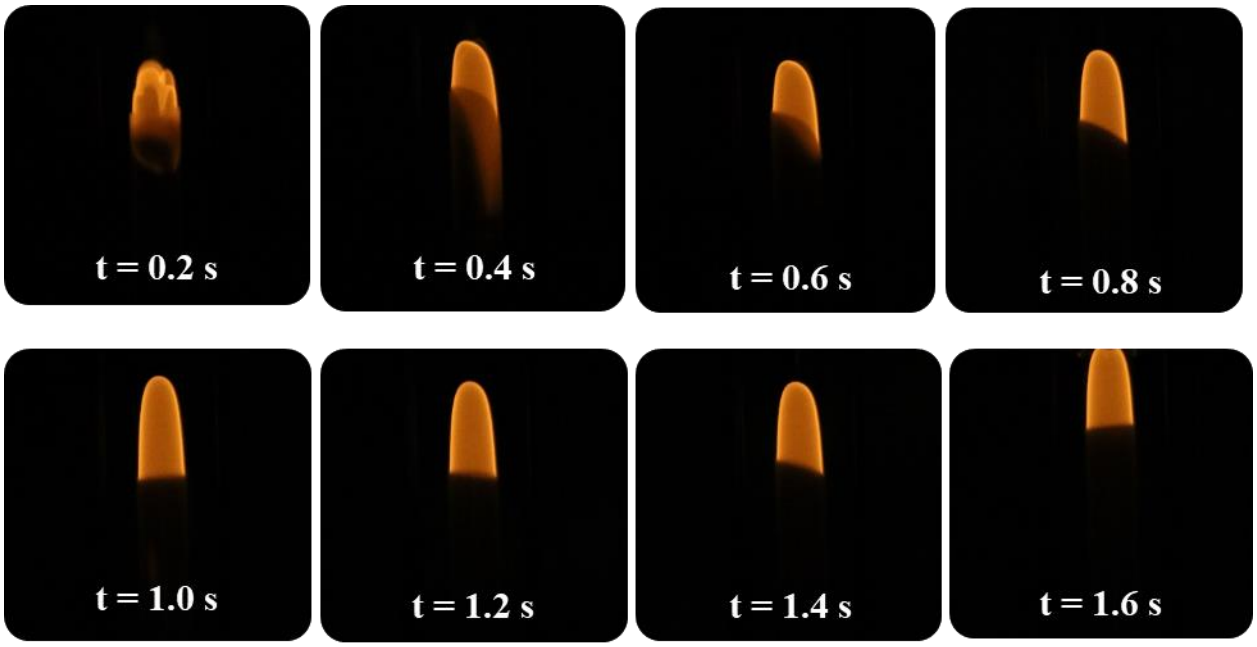

Figure 2.7: Flame propagation of R717 in the vertical tube method (equivalence ratio of 1.1).

Accordingly, the measurement system was modified by moving the ignition cap from the bottom to the top of the vessel to enable the use of the flat flame method and overcome problems associated with buoyancy. The flame produced in this approach was a one-dimensional surface that propagated downward with a velocity equal to the laminar burning velocity of the mixture [23]. Figure 2.8 illustrates the flame propagation achieved using the flat flame approach for a mixture of R32 + R1234yf (95:5 vol%) and pure R717.

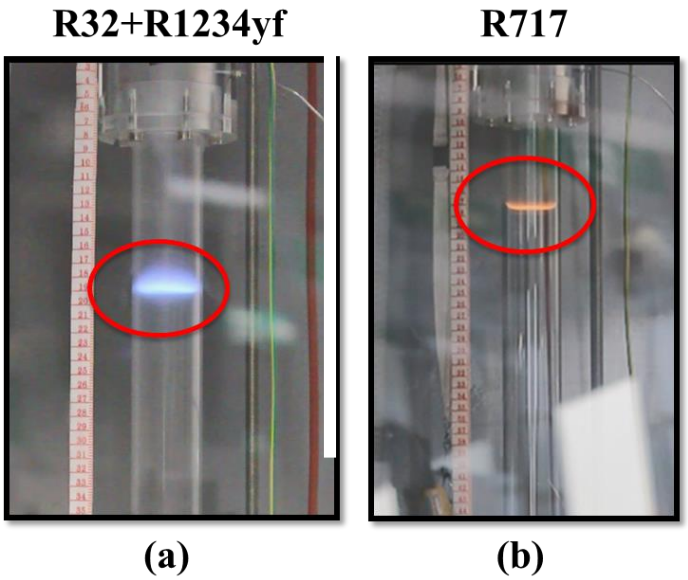

Figure 2.8: Flat flame propagation of (a) 0.95 R32 + 0.05 R1234yf and (b) pure R717.

Table 2.5 presents the measured BVs for R32 and R717 with the flat flame method, together with some results from the literature [10,11,13,24,30,31]. The laminar burning velocity of R717 at an equivalence ratio of 1.1 was measured to be (8.4 ± 0.4) cm/s using the flat flame method. At a similar equivalence ratio, the laminar burning velocity of R717 was reported to be between 6.7 cm/s [30] and 8 cm/s [31] based on measurements using the cylindrical bomb method. The laminar burning velocity for R32 at an equivalence ratio of 1.1 was measured in this work with a 50 mm diameter tube to be (7.4 ± 0.3) cm/s, which is in excellent agreement with the results of Takizawa et al. [10], where a value of 7.3 cm/s was reported using the vertical tube method. The results obtained via the flat flame method typically exhibit a dependence on the tube diameter; using a 40 mm diameter tube, a laminar burning velocity of (6.4 ± 0.3) cm/s was measured for R32 at an equivalence ratio of 1.1. Takizawa et al. [11] also used a vertical tube with a 40 mm diameter and measured the laminar burning velocity of 6.3 cm/s for R32 at a similar equivalence ratio.

The laminar burning velocity of R1234yf could not be measured because the flame was profoundly affected by buoyancy effects even in the flat flame method configuration: the induced convective currents in the tube prevented the flame from propagating downwards. Measuring the laminar burning velocity of R1234yf via the flat flame method might thus require microgravity conditions [13].

Table 2.5: Burning velocities of various pure components obtained with different methods and apparatus.

Refrigerant	Equivalence Ratio	Method	Tube ID/mm	BV/cm.s^{-1}	Ref.
R717	1.1	Heat Flux	-	6.3	[32]
	1.1	Cylindrical Bomb	-	6.7	[30]
	1.1	Vertical Tube	40	7.3	[24]
	1.1	Spherical Flame	-	7.5	[33]
	1.1	Cylindrical Bomb	-	8.1	[31,34,35]
	1.1	Flat Flame	50	8.4 ± 0.4	This work
R32	1.1	Vertical Tube	60	7.3	[10]
	1.1	Flat Flame	50	7.4 ± 0.3	This work
	1.1	Flat Flame	40	6.4 ± 0.3	This work
	1.1	Vertical Tube	40	6.3	[11]
R1234yf	1.33	Microgravity	-	1.5	[13]

2.4.3.1 Refrigerant mixtures

Determination of the laminar burning velocity of R32 + R1234yf and R32 + R1234yf + R744 mixtures was also attempted. No propagation could be established using the flat flame method for the R32 + R1234yf + R744 (28:66:6 wt%) mixture at refrigerant/air concentrations between 12 to 16 vol%. Even using the vertical tube method, no laminar flame propagation was observed. These results are consistent with the findings for pure R1234yf and are reasonable, considering R1234yf is the dominant component in these mixtures. Based on this, a BV value for R1234yf (1.5 cm/s) could be used as a rough estimate of the mixture's laminar burning velocity.

To cast light on the effect of adding R1234yf to R32 on the BV, binary mixtures of R32 + R1234yf at 19 vol% in air were studied. The laminar burning velocity of pure R32 at this refrigerant concentration in air was measured to be (7.4 ± 0.3) cm/s using the flat flame method with a 50 mm diameter tube. The laminar burning velocity for a mixture of R32 + R1234yf containing 5 vol% of R1234yf was then measured to be (6.6 ± 0.3) cm/s. No flat flame propagation could be maintained for a mixture containing 10 vol% R1234yf, indicating that the laminar burning velocity of such a mixture is below 5 cm/s. The minimum laminar burning velocity measured via the flat flame method in this work was 5 cm/s for an R717/air mixture at an equivalence ratio of 0.95), as summarised in Table 2.6.

Table 2.6: Measured burning velocities of refrigerant mixtures in air.

Mixture	Refrigerant/vol%	Method	BV/cm.s^{-1}
R32 + R1234yf + R744 (28:66:6 wt%)	12 to 16	Flat flame	< 5
R1234yf + R32 (5:95 vol%)	19	Flat flame	6.6
R1234yf + R32 (10:90 vol%)	19	Flat flame	< 5**

* The literature BV value for pure R1234yf (1.5 cm/s) provides a rough estimate of the mixture's BV.

** Lower limit of the measurable BV with the apparatus.

2.5 Conclusions

Two pieces of new apparatus were designed, commissioned and deployed to measure the minimum ignition energy and laminar burning velocity of environmentally-friendly refrigerant mixtures. The MIEs of R717, R32 and R1234yf were measured to be (18.0 ± 1.4) at an equivalence ratio of 0.9, (8.0 ± 1.5) mJ at an equivalence ratio of 1.27 and (510 ± 130) mJ at an equivalence ratio of 1.33, respectively.

To reduce the ignition risk, R1234yf and R744 were added to the R32/air mixture, which resulted in a substantial rise in the MIE to 0.33 ± 0.06 J at 14 vol% in air. Adding non-flammable refrigerants of R134a and R125 to R32 and R1234yf (an equimolar four-component mixture) removed the flammability of the blend. An equimolar five-component mixture of (R32 + R1234yf + R134a + R125 + R744) could not be ignited at concentrations from 25 to 29 vol% in air with spark energies up to 8 J. To ignite the mixtures, it was necessary to increase the amount of R1234yf in the five component mixture to 80 vol%, and then apply MIEs of (4.4 ± 0.8) J and (3.8 ± 0.8) J for concentrations of 12 vol% and 15 vol% in air, respectively.

The BV of R32 was measured to be 6.4 cm/s and 7.4 cm/s at an equivalence ratio of 1.1 with 40 and 50 cm tube IDs. No propagating flame could be established for R1234yf, precluding the determination of its BV. By adding 5 vol% of R1234yf to the R32/air mixture at 1.1 equivalence ratio, the laminar burning velocity decreased by 0.8 cm/s. However, no propagating flames could be established for R1234yf + R32 mixtures containing 10 vol% R1234yf, indicating that laminar BV for mixtures with 10 vol% or more R1234yf is below the measurable threshold of 5 cm/s.

Mixtures rich with R1234yf and R744 could provide more sustainable refrigerant solutions as both have very low global warming potential. This study provided the MIE of those mixtures at zero humidity level and room temperature. However, the flammability of R1234yf varies

significantly by temperature and humidity. As discussed in [13], the humidity decreases the MIE of R1234yf and increases its BV, worsening the overall flammability characterstristic of the refrigerant. In future work, a certain threshold value for R744 within a mixture of R1234yf/air at different humidity levels and temperatures needs to be determined; a concentration above which the MIE energy is high enough that the mixture is considered non-flammable at various weather conditions across the globe. Also, the rate of pressure rise and its maximum value caused by the explosion for different scales of refrigerant mixtures should be investigated to address the effect of the confinement as well as the extent of the hazards in case of ignition.

2.6 References

[1] Congressional Research Service. The United Nations Framework on Climate Change , the Kyoto Protocol , and the Paris Agreement : A Summary 2020.

[2] Regulation (EU) No 517/2014 of European Parliament and of the Council on Fluorinated Greenhouse Gases and Repealing Regulation (EC) No 842/2006. Off J Eur Union 2014:195–230.

[3] Bobbo S, Nicola G Di, Zilio C, Brown JS, Fedele L. Low GWP halocarbon refrigerants: A review of thermophysical properties. Int J Refrig 2018;90:181–201. doi:https://doi.org/10.1016/j.ijrefrig.2018.03.027.

[4] Bell IH, Domanski PA, McLinden MO, Linteris GT. The hunt for nonflammable refrigerant blends to replace R-134a. Int J Refrig 2019. doi:10.1016/j.ijrefrig.2019.05.035.

[5] Arami-Niya A, Xiong Xiao, Al Ghafri S, Jiao F, Khamphasith M, Sadeghi Pouya E, et al. Measurement and modelling of the thermodynamic properties of carbon dioxide mixtures with HFO-1234yf, HFC-125, HFC-134a, and HFC-32: vapour-liquid equilibrium, density, and heat capacity. Int J Refrig 2020;In Press.

[6] Ciconkov R. Refrigerants: There is still no vision for sustainable solutions. Int J Refrig 2018;86:441–8. doi:10.1016/J.IJREFRIG.2017.12.006.

[7] Wilson DP, Kujak S, Leary JMO, Kennoy DH, Kusmierz A, Patnaik V, et al. Designation and Safety Classification of Refrigerants. ANSI/ASHRAE Stand 34-2010

2010;4723:9.

[8] Askar E, Schröder V, Schmid T, Schwarze M. Explosion characteristics of mildly flammable refrigerants ignited with high-energy ignition sources in closed systems. Int J Refrig 2018;90:249–56. doi:10.1016/j.ijrefrig.2018.04.009.

[9] Kondo S, Takizawa K, Takahashi A, Tokuhashi K, Mizukado J, Sekiya A. Flammability limits of olefinic and saturated fluoro-compounds. J Hazard Mater 2009;171:613–8. doi:10.1016/j.jhazmat.2009.06.042.

[10] Takizawa K, Takagi S, Tokuhashi K, Kondo S, Mamiya M, Nagai H. Assessment of Burning Velocity Test Methods for Mildly Flammable Refrigerants, Part 1: Closed-Vessel Method (RP-1583) (DE-13-022). vol. 119. 2013.

[11] Takizawa K, Kondo S, Igarashi N, Mamiya M, Tokuhashi K, Nagai H. Assessment of burning velocity test methods for mildly flammable refrigerants, Part 2: Vertical-tube method. ASHRAE Trans 2013;119:255–64.

[12] Jabbour T, Clodic DF, Terry J, Kondo S. Burning velocity and refrigerant flammability classification. ASHRAE Trans 2004;110 PART I:522–33.

[13] Engineers AC. Risk Assessment of Mildly Flammable Refrigerants Final Report 2016 The Japan Society of Refrigerating and Air Conditioning Engineers 2017.

[14] Takizawa K, Igarashi N, Takagi S, Tokuhashi K, Kondo S. Quenching distance measurement of highly to mildly flammable compounds. Fire Saf J 2015;71:58–68. doi:10.1016/j.firesaf.2014.11.013.

[15] Feng B, Yang Z, Lv Z, Zhai R, Chen Y, Zhao W. Effect of gas disturbance on combustion characteristics of flammable refrigerants near LFLs. J Hazard Mater 2019;368:21–32. doi:10.1016/J.JHAZMAT.2018.12.119.

[16] Petersen D, Link R, Dean Smith N, Mitchell W, Tufts M. Determining Minimum Ignition Energies and Quenching Distances of Difficult-To-Ignite Compounds. J Test Eval 2003;31:11505. doi:10.1520/jte12425j.

[17] Takizawa K, Tokuhashi K, Kondo S. Flammability assessment of CH2{double bond, long}CFCF3: Comparison with fluoroalkenes and fluoroalkanes. J Hazard Mater 2009;172:1329–38. doi:10.1016/j.jhazmat.2009.08.001.

[18] Minor BH, Herrmann D, Gravell R. Flammability characteristics of HFO-1234yf. Process Saf Prog 2010;29:150–4. doi:10.1002/prs.10347.

[19] Verkamp FJ, Hardin MC, Williams JR. Ammonia combustion properties and performance in gas-turbine burners. Symp Combust 1967;11:985–92. doi:10.1016/S0082-0784(67)80225-X.

[20] Zhang Q, Li W, Zhang S. Effects of spark duration on minimum ignition energy for methane/air mixture. Process Saf Prog 2011;30:154–6. doi:10.1002/prs.10438.

[21] Harris GFP, Macdermott PE. Flammability and explosibility of ammonia. Inst Chem Eng Symp Ser No 49 1964:29–37.

[22] Rose JW, Cooper JR, Spiers HM. Technical data on fuel. London: British National Committee, World Energy Conference Edinburgh : Distributed by Scottish Academic Press; 1977.

[23] Fuller LE, Parks DJ, Fletcher EA. Flat flames in tubes—easy fundamental flame speed measurements. Combust Flame 1969;13:455–60. doi:https://doi.org/10.1016/0010-2180(69)90084-4.

[24] Clodic D, Jabbour T. Method of test for burning velocity measurement of flammable gases and results Method of test for burning velocity measurement of flammable gases and results. HVAC&R Res 2011;17:1:51–75. doi:10.1080/10789669.2011.543252.

[25] Bockhorn H, Fetting F, Mende JC. The laminar flame velocities of propane/ammonia mixtures. Combust Flame 1972;18:471–3. doi:https://doi.org/10.1016/S0010-2180(72)80199-8.

[26] EN 1839. Determination of Explosion Limits of Gases and Vapours. Eur Comm Stand 2003;Brussels.

[27] Lee JJ, Shepherd JE. Spark Ignition Measurements in Jet A : part II. Test 2000.

[28] Movileanu C, Mitu M, Giurcan V, Razus D, Oancea D. Quenching distances, minimum ignition energies and related properties of propane-air-diluent mixtures. Fuel 2020;274:117836. doi:https://doi.org/10.1016/j.fuel.2020.117836.

[29] Movileanu C, Razus D, Musuc A, Oancea D. Additive influence on quenching distances

and critical ignition energies of ethylene-air mixtures. Fuel 2017;193:401–10. doi:https://doi.org/10.1016/j.fuel.2016.12.065.

[30] Hayakawa A, Goto T, Mimoto R, Arakawa Y, Kudo T, Kobayashi H. Laminar burning velocity and Markstein length of ammonia/air premixed flames at various pressures. Fuel 2015;159:98–106. doi:10.1016/j.fuel.2015.06.070.

[31] Ronney PD. Effect of Chemistry and Transport Properties on Near-Limit Flames at Microgravity. Combust Sci Technol 1988;59:123–41. doi:10.1080/00102208808947092.

[32] Han X, Wang Z, Costa M, Sun Z, He Y, Cen K. Experimental and kinetic modeling study of laminar burning velocities of NH3/air, NH3/H2/air, NH3/CO/air and NH3/CH4/air premixed flames. Combust Flame 2019;206:214–26. doi:https://doi.org/10.1016/j.combustflame.2019.05.003.

[33] Lhuillier C, Brequigny P, Lamoureux N, Contino F, Mounaïm-Rousselle C. Experimental investigation on laminar burning velocities of ammonia/hydrogen/air mixtures at elevated temperatures. Fuel 2020;263:116653. doi:https://doi.org/10.1016/j.fuel.2019.116653.

[34] Shrestha KP, Lhuillier C, Barbosa AA, Brequigny P, Contino F, Mounaïm-Rousselle C, et al. An experimental and modeling study of ammonia with enriched oxygen content and ammonia/hydrogen laminar flame speed at elevated pressure and temperature. Proc Combust Inst 2020. doi:https://doi.org/10.1016/j.proci.2020.06.197.

[35] Mei B, Zhang X, Ma S, Cui M, Guo H, Cao Z, et al. Experimental and kinetic modeling investigation on the laminar flame propagation of ammonia under oxygen enrichment and elevated pressure conditions. Combust Flame 2019;210:236–46. doi:https://doi.org/10.1016/j.combustflame.2019.08.033.

[36] The Japan Society of Refrigerating and Air Conditioning Engineers. Risk Assessment of Mildly Flammable Refrigerants. 2014 Prog Rep 2015:132.

3 Chapter 3 │ Vapour-Liquid Equilibria for Carbon Dioxide (CO2) + 3,3,3-Trifluoropropene (HFO-1243zf) Binary Mixtures at Temperatures between (288 and 348) K

Forward – Reprinted with permission from the Journal of Chemical Engineering Data (J. Chem. Eng. Data 2021, 66, 11, 4044–4055, DOI: https://doi.org/10.1021/acs.jced.1c00297. Copyright 2021 American Chemical Society). It has been reformatted with minor amendments to fit style and structure of this thesis.

3.1 Abstract

Accurate property data for mixtures of hydrofluoroolefins with refrigerants like CO_2 are needed by industry to design safe and efficient refrigeration systems that employ low global warming potential working fluids. However, data available for these mixtures, particularly at conditions of vapour-liquid-equilibrium (VLE), are limited. In this work, the VLE of CO_2 and HFO-1243zf binary mixtures, which has not been studied previously, was measured along five isotherms at temperatures between (288 and 348) K and pressures between (0.68 and 7.69) MPa. The new VLE data are compared with the predictions of a Helmholtz free energy model that utilise GERG-2008 mixing rules. Adjusting the model's binary interaction parameters (BIPs) to force agreement with the new measurements reduced the root mean square deviation (RMSD) of the data from the model by 45 % relative to the default BIPs. Additionally, the data were compared with predictions from the Peng Robinson Advanced equation of state (PRA-EOS) with a one-fluid mixing rule and a fixed binary interaction parameter which was subsequently tuned to the experimental data. The tuned PRA-EOS could represent the experimental CO_2 mole fractions with an RMSD of 0.012, which is more than two times larger than the average experimental uncertainty, while the RMSD of the tuned Helmholtz free energy model from the experimental data was 0.009. The accurate data and improved model presented in this work will aid the development of environmentally friendly refrigerant mixtures.

3.2 Introduction

Hydrofluoroolefins (HFOs) are a new generation of refrigerants with much lower global warming potential (GWP) than the commonly used hydrofluorocarbons (HFCs). Three HFOs, namely HFO-1234yf, HFO-1234ze(E) and HFO-1243zf, are in particular excellent candidates to replace HFC-134a, which is widely used in domestic refrigeration systems but has a GWP of around 1300 and atmospheric lifetime of 13 years[1]. Of the three HFOs, HFO-1243zf has the lowest GWP of 0.29 with an atmospheric lifetime of about six days [2]; such a refrigerant could help meet the objectives of the Montreal Protocol [3] and the Kigali Amendment [4].

One barrier to the uptake of HFO replacement is the scarcity of the existing thermophysical property data available for HFOs blends. While the thermophysical properties of HFO-1234yf and HFO-1234ze(E) mixtures have been quite well studied [5–12], limited thermophysical property data are available for mixtures containing HFO-1243zf, including its binary systems with HFC-134a [1,13], iso-butane [14] and propane [15]. However, pure HFO-1243zf has demonstrated a higher coefficient of performance when used in an air conditioner than did HFC-134a, HFC-22 and HFC-32 [16]. Despite this potential, the experimental data available for pure HFO-1243zf and its binary mixtures are limited, as shown in Table 3.1.

In terms of thermophysical properties modelling, Akasaka and Lemmon [17,18] and Bobbo et al. [19] studied the performance of Helmholtz energy equations of state (EOS) for predicting the thermodynamic properties of HFO-1243zf. They showed that Helmholtz energy EOS was able to represent pure HFO-1243zf at temperatures between 234 K and 440 K and pressures up to 34 MPa with estimated uncertainties of 0.1 % for vapour pressure, 0.05 % for liquid density and 0.6% for vapour density.

Table 3.1: Summary of the open literature of thermodynamic property data for pure HFO-1243zf and its binary mixtures.

System	Properties	Range (T, p, z^*)	Reference
HFO-1243zf	T_c, p_c, ρ_c, ω, c_p	233-292 K, 0.1-10 MPa, pure	[20]
HFO-1243zf	p_{sat}	234-373 K; 0.1-3.2 MPa, pure	[21,22]
HFO-1243zf	p_{sat}	310-375 K, 0.8-3.4 MPa, pure	[23]
HFO-1243zf	p_{sat}	278-377 K, 0.8-4.5 MPa, pure	[24]
HFO-1243zf	pvT	279-368 K; 0.3-0.9 MPa, pure	[25]
HFO-1243zf	ρ_{sat}	240-370 K, Not Reported, pure	[26]
HFO-1243zf + HFC-134a	VLE	293-323 K, 0.5-1.3 MPa, 0-1.00	[1]
HFO-1243zf + HFC-134a	VLE	243-293 K, 0.08-0.5 MPa, 0-1.00	[13]
HFO-1243zf + iso-butane	VLE	253-293 K, 0.07-0.3 MPa, 0-1.00	[14]
HFO-1243zf + propane	VLE	243-288 K, 0.08-0.7 MPa, 0-1.00	[15]
HFO-1243zf + iso-butane	$pvTx$	308-383 K, 0.05-0.4 MPa, 0.1-0.78	[27]

* z represents the mole fraction of the first-named component in the binary mixtures.

On the other hand, HFOs' moderate flammability is another barrier to their widespread applications in domestic refrigeration systems because it may pose safety risks to users [28]. To mitigate this, HFOs can be blended with non-flammable refrigerants like HFC-134a, HFC-125 and carbon dioxide (CO_2) to neutralise their flammability with only minor cooling performance reductions. Carbon dioxide (CO_2) is an easily obtained non-flammable organic refrigerant with low GWP and zero ozone depletion potential (ODP). Mclinden et al. [29] conducted a comprehensive simulation-based study that ranked CO_2 next to HFO-1243zf as two of the most promising 62 refrigerants based on flammability, GWP and thermodynamic parameters. Bell et al. [30] carried out simulations that assessed the best replacements for HFC-134a, selecting HFO-1243zf and CO_2 as key targets of future work.

While data for binary mixtures of CO_2 with HFO-1234yf and HFO-1234ze have been reported [11,31,32], no experimental property data have been measured for the CO_2 + HFO-1243zf binary system. Vapour-liquid-equilibrium (VLE) data are particularly important to the design and optimisation of cooling systems that utilise alternative refrigerants [33]. In this work, the VLE of CO_2 + HFO-1243zf binary system was measured at five isotherms between (288 and 348) K. The analytical method was employed to generate new VLE data with quantitative uncertainty estimates to enable the development of improved models. The experimental set-up, materials, calibration and experimental procedures are discussed, and the data are compared with the predictions of two thermodynamics models for the mixture, one based on a Helmholtz free energy EOS and the other on the Peng Robinson Advanced (PRA)

EOS. Finally, both models are tuned based on the acquired experimental data, and their performance in properties predictions are compared with the original models.

3.3 Experimental

3.3.1 Apparatus

Two identical apparatus sharing one analysis system, as shown in Figure 3.1 and similar to those described in the previous studies [7,11,34], were used in this work to measure the VLE of the binary mixtures. Each apparatus consisted of an equilibrium cell machined from single stainless steel (SAE316L) billet with an internal volume of 65 ml and a pressure rating up to 30 MPa, shown in Figure 3.2. The outer surfaces of the equilibrium cells were coated with a 1 mm thickness of copper to enhance temperature uniformity and heat transfer. A quartz-crystal pressure transducer (Digiquartz, Paroscientific) with a full scale of 13.8 MPa and relative standard uncertainty of 0.01% of the full scale was used to measure the system's pressure. A magnetic stirrer was placed inside each equilibrium cell and used to ensure the mixture's homogeneity before sampling.

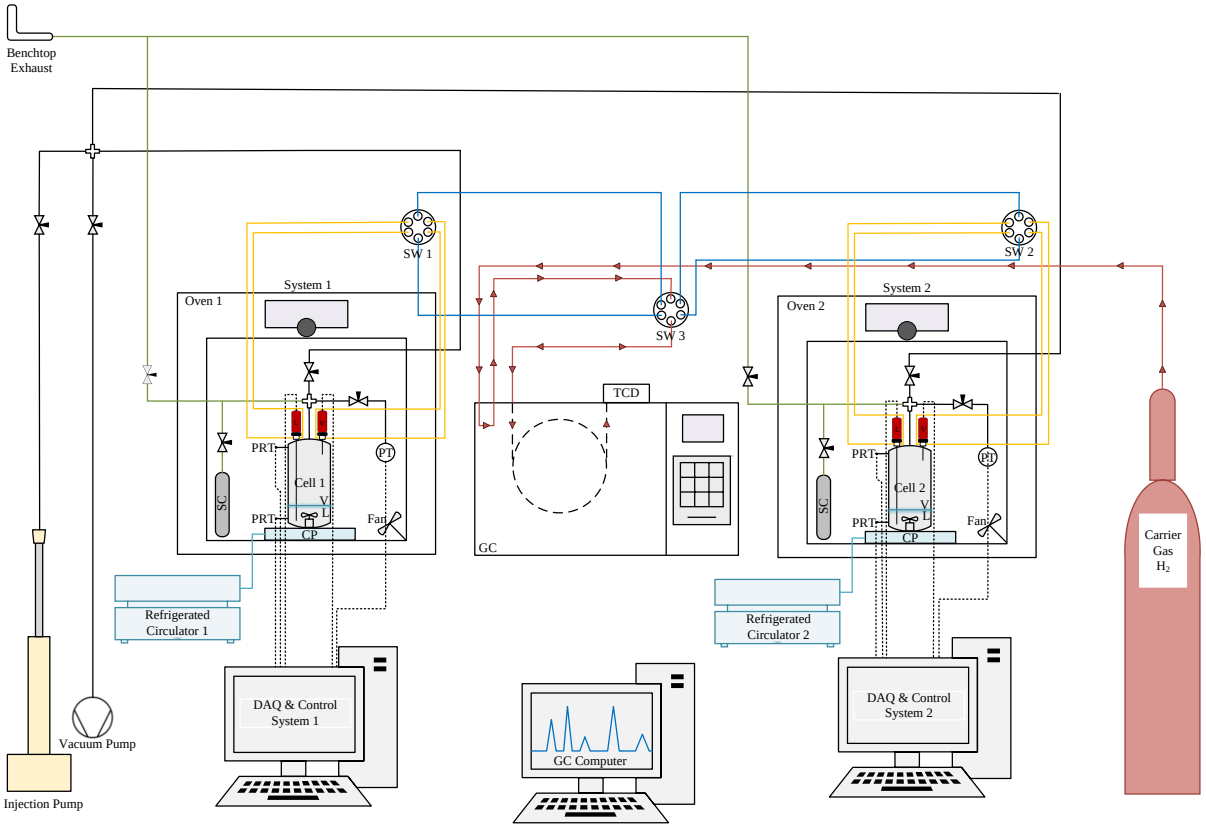

Figure 3.1: The schematic diagram of the VLE apparatus (CP: Cooling Plate; DAQ: Data Acquisition; GC: Gas Chromatograph, PRT: Platinum Resistance Thermometer; SC: Sample Cylinder; SW: Switch Valve; TCD: Thermal Conductivity Detector) [11].

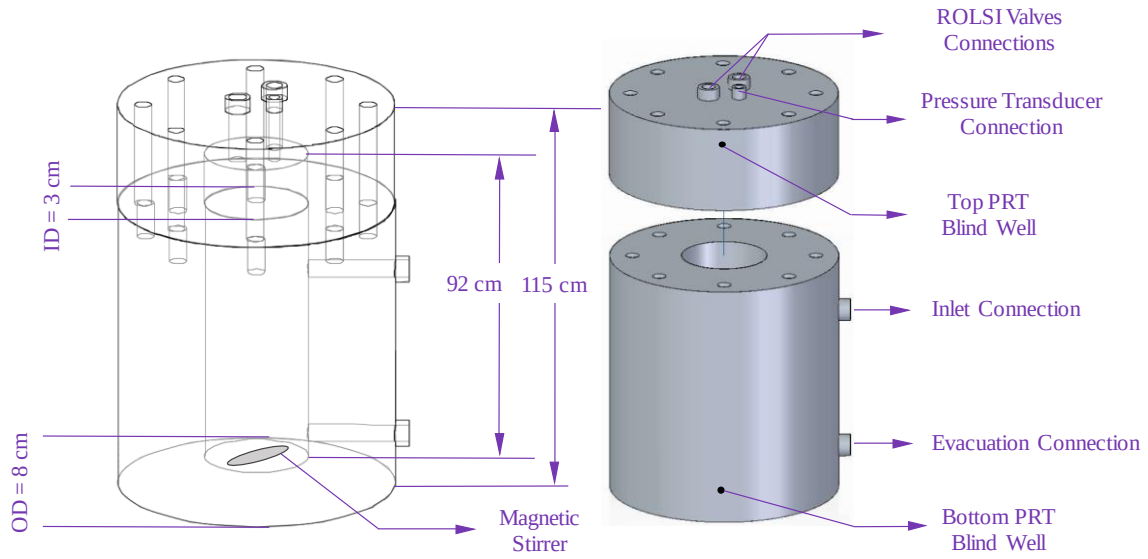

Figure 3.2: Visualisation showing an exploded view of the equilibrium cell.

Each equilibrium cell was housed inside its own incubator oven (Memmert-UN110) allowing it to be controlled at temperatures between (288 and 348) K with a temperature stability of

0.05 K over the duration of an isothermal VLE experiment (6 to 10 hours). Temperatures below ambient were achieved using a custom cooling system consisting of spiral copper tubes-plate placed inside the oven and connected to refrigerated circulators (PolyScience-9502A12E) using insulated PVC hoses, similar to the approach taken by Efika et al. [35]. The temperature was monitored using two platinum resistance thermometers (NR-141-100S, Netsushin) with a standard uncertainty of 0.05 K. These PRTs were calibrated against a standard PRT (ASL-WIKA) in a constant temperature bath between 273.15 K and 398.15 K. The average temperature difference between these PRTs during the VLE measurement was less than 0.1 K.

Two remotely controlled electromagnetic sampling (Rapid On-Line Sampling Injectors – ROLSI^{TM}) [36,37] valves were used to sample the vapour and liquid phases. A stainless steel (SAE316L) capillary tube with an ID of 0.1 mm, OD of 1 mm and operating pressure up to 30 MPa was connected to each ROLSI valve and suspended down into the cell. Samples were analysed using an Agilent 7890A GC coupled with a capillary column (Agilent J&W HP/PLOT-U) and a thermal conductivity detector.

3.3.2 GC detector calibration procedure

The pure fluids used in the VLE measurements were received directly from the suppliers listed in Table 3.2 and were used without further purification.

Table 3.2: Details of chemicals used.

ASHRAE Refrigerant Number	IUPAC name	Chemical formula	CAS #	Supplier	Mole Fraction Purity*
R744	Carbon Dioxide	CO_2	124-38-9	Coregas	0.99995
R1243zf	3,3,3-Trifluoropropene	$C_3H_3F_3$	677-21-4	SynQuest Labs	0.99
N/A	Hydrogen	H_2	1333-74-0	BOC	0.99999

* Based on the supplier reports.
** Referred as HFO-1243zf in this chapter.
*** The carrier gas of the gas chromatograph (GC).

Mixtures were made for two purposes: (1) GC detector calibration and (2) VLE measurements. For the GC detector calibration, five binary mixtures of CO_2 and HFO-1243zf were prepared volumetrically, and the exact compositions were determined gravimetrically. The procedure began with weighing evacuated 300 mL Swagelok stainless steel cylinders ten times on an electronic scale with precision up to 0.01 g. Two separate pressure, temperature and relative humidity sensors were used to capture the average ambient conditions of the measuring environment before and after weighing the cylinders to correct the measured mass for the

buoyancy effect of air [38]. This process was repeated 6 hours after the first measurement to obtain an averaged value of the initial cylinder mass. The volumes of HFO-1243zf and CO_2 needed to prepare 10, 30, 50, 70, & 90 mol% of CO_2 were calculated according to the Helmholtz free energy EOS [17,39] for the respective pure components. The HFO-1243zf was first pressurised using a syringe pump (Teledyne ISCO pump 260D) to 2 MPa, where it was held for 12 hours to ensure the sample was in a compressed liquid state. This well-known amount of HFO-1243zf was then injected into the empty cylinder, as shown in Figure 3.3. Similarly, pure CO_2 was then loaded into the (evacuated) syringe pump and pressurised to 9 MPa before being injected into the cylinder to produce the required mixture. Each cylinder was weighted after each injection, as described earlier.

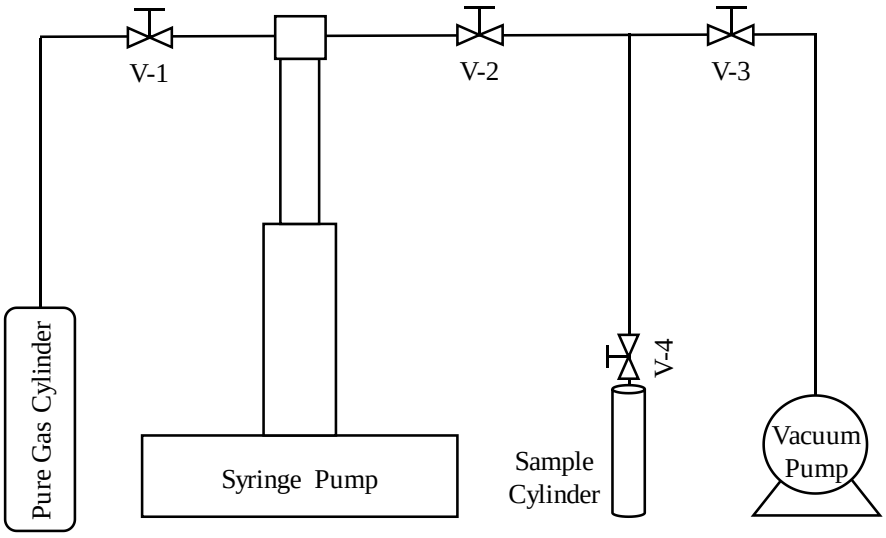

Figure 3.3: The calibration mixture preparation set-up.

The mixtures prepared for GC detector calibration were transferred into the VLE measurement cell for sampling according to the following procedure: after connecting the cylinder to the equilibrium cell, all the lines were evacuated via a vacuum pump (RZ6 Vacuubrand). Then the temperature of the entire system (cell + cylinder) was increased up to 10 K higher than the cricondentherm temperature of the synthetically prepared binary mixture to ensure the mixture was in a single-phase condition during the transfer. The bottom part of the cylinder was heated using a heating pad up to 10 K higher than the incubator temperature to ensure the homogeneity of the prepared mixture by inducing convective mixing inside the cylinder. Additionally, ball bearings were placed within the cylinder to mix the prepared binary mixture by shaking the cylinder manually 20 times before transferring the mixture into the cell.

Table 3.3 presents the prepared mixtures' calculated cricondentherm temperatures using REFPROP 10 software package developed by NIST [40]. Then the connecting valve between the cylinder and the cell was opened to release the one-phase mixture into the cell. After injection, the cylinder was disconnected, and the mixture in the cell was left to stabilise for about 3 h under continuous stirring before any sampling commenced.

Table 3.3: Gravimetrically prepared mixtures' composition, molar ratio, critical and cricondentherm temperatures calculated using REFPROP 10.

z_{CO2}	$u(z_{CO2})$	$\frac{z_{CO2}}{z_{HFO-1243zf}}$	$u(\frac{z_{CO2}}{z_{HFO-1243zf}})$	T_c /K	$T_{cricondentherm}$ /K
0.0952	0.0007	0.1062	0.0007	378.9	378.9
0.1909	0.0007	0.2383	0.0007	377.4	377.5
0.4939	0.0006	0.9858	0.0012	367.9	368.6
0.6937	0.0003	2.284	0.0016	349.1	350.8
0.8799	0.0001	7.400	0.0038	321.7	322.6

Once the calibration mixture was at a stable pressure and temperature, at least 30 samples were acquired and analysed using three different opening times of the ROLSI valves. For a given binary mixture and within the linear range of the TCD detector, the mole fraction, z_i, can be determined by solving the following system of equations:

$$(\frac{z_i}{z_j}) = k(\frac{A_i}{A_j}) \quad 3.1$$

$$z_i = 1 - \frac{1}{1 + k(\frac{A_i}{A_j})} \quad 3.2$$

Where A_i and A_j represent the integrated area for components *i* and *j* of the binary mixture, respectively, and *k* stands for the calibration response factor of the TCD detector. Figure 3.4 shows the relationships obtained between the sample's molar ratios and their corresponding area ratios ($A_{CO2}/A_{HFO\text{-}1243zf}$). Table 3.4 presents the optimised GC method conditions used during the measurement to separate the CO_2 from HFO-1243zf peaks sufficiently.

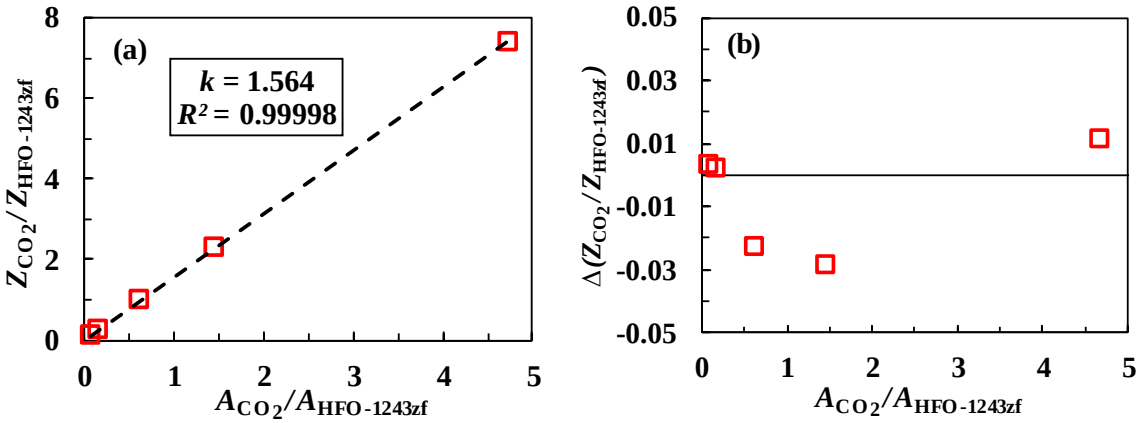

Figure 3.4: Thermal-conductivity detector (TCD) gravimetric calibration data for CO_2 + HFO-1243zf binary system: (a) gravimetric molar ratios of CO_2 to HFO-1243zf against GC area response ratios of CO_2 to HFO-1243zf, (b) deviation of the calculated molar ratios ($z_{CO2}/z_{HFO-1243zf}$) based on the calibration equation (Equation 3.1) from the gravimetrically measured values against GC area response ratios; □ experimental data, (---) Equation 3.1.

Table 3.4: The optimised GC conditions for the separation of CO_2 from HFO-1243zf.

Gas Chromatograph Parameter	**Optimised Condition**
Detector Conditions	
TCD temperature	443.15 K
Carrier gas	H_2
Carrier gas flow rate	15 mL/min
Makeup gas flow rate	3 mL/min
Column Conditions	
Separations column	Agilent J&W HP/PLOT-U, 320 µm D, 30 m
Oven temperature	373.15 K
Injector temperature	423.15 K
Split Ratio	100/1
CO_2 retention time	1.5 min
HFO-1243zf retention time	2.8 min

3.3.3 VLE measurement procedure

For the VLE measurements, the equilibrium cell and all connections were vented and evacuated before mixture preparation. A predetermined volume of HFO-1243zf was injected into the cell. The mixture's composition was then adjusted by injecting CO_2 in increments of 5 to 10% by volume to enable the majority of the phase envelope at each temperature to be covered. After each injection of CO_2, the mixture was stirred for 3 hours at the desired temperature to ensure homogeneity. When the sample's pressure and temperature were stable over a three-hour period within 0.005 MPa and 0.05 K, respectively – indicating equilibrium between vapour

and liquid phases within the cell – the GC lines were flushed, and the mixture was sampled. Sampling was performed 20 times for each phase.

3.3.4 Uncertainty analysis and validation

The uncertainty analysis was carried out in accordance with the "Guide to the Expression of Uncertainty in Measurement (GUM)" method developed by NIST [41]. Because this study is focused on a binary system, the mole fractions *x* and *y* are defined here to represent the mole fraction of CO_2 in the liquid and vapour phases, respectively. The quantities of *T*, *p*, *x* and *y* were determined through the average of *N* independent samples acquired under almost identical measurement conditions. The standard uncertainty of the mole fraction *z* (representing either *x* or *y*) is given as follows:

$$u(z) = \sqrt{\left[\left(\frac{\partial z}{\partial T}\right)u(T)\right]^2 + \left[\left(\frac{\partial z}{\partial p}\right)u(p)\right]^2 + \left[\left(\frac{\partial z}{\partial k}\right)u(k)\right]^2 + \left[\left(\frac{\partial z}{\partial R}\right)u(R)\right]^2} \quad 3.3$$

The symbols *u(T), u(p), u(k),* and *u(R)* stand for the standard uncertainty of temperature, pressure, calibration coefficient and measured peak area ratios of two components, respectively. The temperature and pressure sensors' standard uncertainties, including the uncertainties of temperature and pressure measurements, were considered to be 0.1 K and 0.005 MPa, respectively. The uncertainty arising from the GC detector calibration can be expressed as follows:

$$u(k) = \sqrt{\left[\left(\frac{\partial k}{\partial Z_R}\right)u(Z_R)\right]^2 + \left[\left(\frac{\partial k}{\partial R}\right)u(R)\right]^2} \quad 3.4$$

In Equation 3.4, $u(Z_R)$ and *u(R)* represent the uncertainties associated with the gravimetric mixture preparation (the mole ratio of CO_2 to HFO-1243zf in each calibration mixture) and measured peak area response ratios during the calibration process, respectively. In Equations 3.3 and 3.4, *u(R)* is considered to be equal to the standard deviation of the measured area ratios during the VLE and calibration measurements, respectively. The term $u(Z_R)$ consists of the uncertainties associated with the injected masses of CO_2 and HFO-1243zf into the cylinders during gravimetric mixture preparation. The standard uncertainty of the mass change recorded at each weighing is based on the resolution of the scale (0.01 g). Table 3.3 presents

the standard uncertainties of the CO_2 mole fraction in the gravimetrically prepared mixtures, calculated according to the method described by Arami-Niya et al. [11], which vary between 0.0001 and 0.0007. The mole fraction uncertainties associated with the VLE measurements are reported in Table 3.5 and range from 0.001 to 0.008.

As a validation of the apparatus readings, the vapour pressures of the pure components injected into the equilibrium cell during the sample loading procedure were checked regularly against the values expected using the measured temperature and the reference EOS for that compound. The differences observed were always smaller than the standard experimental uncertainty in pressure. Additional results obtained with this set-up also served to validate the measurement technique. Measurements made for binary mixtures containing CO_2 and HFC-32, HFC-125, HFC-134a or HFC-1234yf [11], as well as for the binary system HFO-1234ze(E) + HFC-134a[7] were consistent with VLE data reported in the literature for the same systems within the combined experimental uncertainties.

3.4 Thermodynamic modelling

The predictions of two equations of state used commonly for refrigerant mixtures, namely a Helmholtz energy model and the cubic PRA EOS, were tested against the obtained experimental results. The PRA EOS correlates pressure, temperature and volume as follows [42]:

$$p = \frac{RT}{v-b} - \frac{a}{v^2 + 2bv - b^2} \qquad 3.5$$

The symbol *R* is the universal gas constant, and v is the molar volume. Furthermore, a and b stand for temperature-dependent energy and co-volume parameters, respectively. The PR-EOS can be used for pure fluids as well as mixtures by employing, for example, the van der Waals one-fluid mixing rules that incorporate a single binary interaction parameter (BIP). A temperature-independent BIP (k_{ij}) was used in this study since the measurement temperature range was limited.

$$a = \sum_i \sum_j x_i x_j (1 - k_{ij}) \sqrt{a_i a_j} \qquad 3.6$$

$$b = \sum_i x_i b_i \qquad 3.7$$

The PRA-EOS implemented in the MultiFlash software package version 7.0 was used in this study to predict the VLE property data. The PRA-EOS describes the pure substance parameters a_i and a_j in Equation 3.6 in terms of each components' vapour pressure curve over a range of reduced temperatures proposed by Mathias and Copeman [43]:

$$a_i = a_{ci}(1 + \kappa_{i1} t_i + \kappa_{i2} t_i^2 + \kappa_{i3} t_i^3 + \kappa_{i4} t_i^4 + \kappa_{i5} t_i^5 \qquad 3.8$$

$$t_i = 1 - \sqrt{\frac{T}{T_{ci}}} \qquad 3.9$$

Here the constants κ_{i1} to κ_{i5} are determined by the linear regression to the vapour pressure of component *i* over a range of reduced temperatures. Further information can be found in the MultiFlash user manual [44].

The BIP in Equation 3.6 was adjusted by regression to the experimental results measured in this work. The best-fit value k_{ij} was found by minimising the objective function of (*S*) defined as [45]:

$$S = \sqrt{\frac{1}{2N} \sum_{i=1}^{N} \left[(x_{2,i} - x_{2,i,calc})^2 + (y_{2,i} - y_{2,i,calc})^2 \right]} \qquad 3.10$$

The symbol *N* represents the total number of VLE data points used in the fitting of the EOS. The parameters $x_{2,i}$ and $x_{2,i,calc}$ stand for the experimental and predicted bubble point mole fractions of HFO-1243zf for the VLE data point "*i*". The parameters $y_{2,i}$ and $y_{2,i,calc}$ correspond to the experimental and predicted dew point mole fractions of HFO-1243zf for the VLE data point "*i*".

On the other hand, the Helmholtz free energy EOS are considered state-of-the-art models for predicting the thermodynamic properties of refrigerant mixtures, particularly if sufficient data are available at the time of their development. The default GERG-2008 EOS mixing rules [46], implemented in the software package NIST REFPROP 10, are shown below: these represent

the reducing functions which contain BIPs used to improve the agreement between properties measured for binary mixtures and those predicted using the Helmholtz model:

$$\frac{1}{\rho_r(\bar{x})} = \sum_{i=1}^{N} x_i^2 \frac{1}{\rho_{c,i}} + \sum_{i=1}^{N-1} \sum_{j=i+1}^{N} 2x_i x_j \, \beta_{v,ij}\gamma_{v,ij} \cdot \frac{x_i + x_j}{\beta_{v,ij}^2 x_i + x_j} \cdot \frac{1}{8}\left(\frac{1}{\rho_{c,i}^{1/3}} + \frac{1}{\rho_{c,j}^{1/3}}\right)^3 \qquad 3.11$$

$$T_r(\bar{x}) = \sum_{i=1}^{N} x_i^2 T_{c,i} + \sum_{i=1}^{N-1} \sum_{j=i+1}^{N} 2x_i x_j \, \beta_{T,ij}\gamma_{T,ij} \cdot \frac{x_i + x_j}{\beta_{T,ij}^2 x_i + x_j} \cdot (T_{c,i} \cdot T_{c,j})^{1/2} \qquad 3.12$$

here $\bar{x}$, ρ_r and T_r are the molar composition vector, the reducing functions of the mixture density and temperature; and parameters $\rho_{c,i}$, $\rho_{c,j}$, $T_{c,i}$, $T_{c,j}$, x_i and x_j are the critical density, critical temperature and mole fraction of components *i* and *j*. The constants $\beta_{T,ij}$, $\gamma_{T,ij}$, $\beta_{v,ij}$, and $\gamma_{v,ij}$ are four independent BIPs that can be adjusted if sufficient experimental data spanning a wide range of conditions are available. If the experimental data for the binary mixture are limited, the BIPs are set to unity. In this work, only two parameters $\beta_{T,ij}$, and $\gamma_{T,ij}$ included within Equations 3.11 and 3.12 were adjusted to minimise the objective function shown in Equation 3.10, while the other BIPs ($\beta_{v,ij}$, and $\gamma_{v,ij}$) were set to unity. The two tuned parameters are the most appropriate factors for fitting Helmholtz free energy EOS to VLE data, as discussed by Bell and Lemmon [47].

3.5 Results and discussion

3.5.1 VLE data

The VLE of the CO_2 + HFO-1243zf binary system was measured at five temperatures between (288 and 348) K and pressures from (0.68 to 7.69) MPa. Table 3.5 presents the average of the measured temperature, pressure, relative volatility and composition of the liquid and vapour phases at each equilibrium condition. Figure 3.5 shows the experimental pressure and composition data, together with values calculated using the two tuned models.

Table 3.5: The experimental liquid (x) and vapour (y) phase mole fractions of CO_2 in binary mixtures with HFO-1243zf mixtures at equilibrium temperatures (T) and pressures (p)*.

T/K	p/MPa	x	y	α_{12}**	$u(x)$	$u(y)$	$u(\alpha_{12})$
289.6	0.680	0.0606	0.3226	7.39	0.0020	0.0080	0.38
288.9	0.861	0.1134	0.4875	7.44	0.0030	0.0074	0.31
289.3	1.127	0.1820	0.6138	7.14	0.0041	0.0066	0.28
289.2	1.428	0.2589	0.7063	6.88	0.0052	0.0057	0.27
288.9	1.851	0.3638	0.7879	6.49	0.0062	0.0045	0.25
288.7	2.305	0.4688	0.8434	6.10	0.0067	0.0036	0.23
288.5	3.146	0.6460	0.9070	5.34	0.0063	0.0023	0.21
288.5	3.612	0.7364	0.9305	4.79	0.0054	0.0018	0.19
288.5	4.012	0.8044	0.9499	4.62	0.0045	0.0014	0.19
288.9	4.291	0.8576	0.9619	4.19	0.0037	0.0011	0.18
298.1	0.820	0.0569	0.2834	6.56	0.0015	0.0071	0.29
297.1	0.938	0.0898	0.3914	6.52	0.0025	0.0073	0.28
298.2	1.276	0.1616	0.5473	6.27	0.0038	0.0069	0.25
298.2	1.669	0.2467	0.6631	6.01	0.0050	0.0061	0.23
297.3	2.099	0.3437	0.7499	5.73	0.0060	0.0050	0.22
297.3	2.665	0.4515	0.8147	5.34	0.0067	0.0040	0.20
298.2	3.398	0.5738	0.8639	4.72	0.0066	0.0032	0.18
297.3	4.205	0.7167	0.9117	4.08	0.0056	0.0022	0.16
297.3	5.151	0.8493	0.9501	3.38	0.0039	0.0014	0.14
297.2	5.660	0.9018	0.9704	3.57	0.0029	0.0010	0.17
317.7	1.140	0.0281	0.1228	4.84	0.0012	0.0051	0.32
317.8	1.514	0.0950	0.3339	4.78	0.0025	0.0064	0.19
317.8	1.804	0.1455	0.4413	4.64	0.0034	0.0068	0.18
317.8	2.257	0.2205	0.5549	4.41	0.0046	0.0066	0.17
317.7	2.876	0.3166	0.6558	4.11	0.0058	0.0060	0.16
317.7	3.604	0.4193	0.7307	3.76	0.0065	0.0053	0.14
317.8	4.392	0.5241	0.7906	3.43	0.0066	0.0045	0.13
317.7	5.647	0.6724	0.8491	2.74	0.0060	0.0035	0.10
317.8	6.927	0.8037	0.8809	1.81	0.0043	0.0028	0.07
318.2	7.651	0.8611	0.8688	1.07	0.0078	0.0030	0.08
333.4	1.905	0.0706	0.2185	3.68	0.0019	0.0052	0.16
333.5	2.239	0.1174	0.3202	3.54	0.0029	0.0061	0.14
333.4	2.666	0.1766	0.4251	3.45	0.0039	0.0066	0.13
333.5	3.197	0.2460	0.5088	3.17	0.0049	0.0067	0.12
333.4	3.724	0.3128	0.5760	2.98	0.0057	0.0065	0.11
333.6	4.380	0.3898	0.6297	2.66	0.0063	0.0062	0.10
333.6	5.357	0.4987	0.6928	2.27	0.0066	0.0057	0.09
333.4	6.437	0.6129	0.7573	1.97	0.0063	0.0049	0.07

333.3	7.693	0.7353	0.8016	1.44	0.0052	0.0043	0.06
348.3	2.307	0.0423	0.1113	2.84	0.0014	0.0035	0.14
348.2	2.228	0.0324	0.0885	2.90	0.0012	0.0032	0.16
348.2	2.863	0.1127	0.2602	2.77	0.0028	0.0054	0.11
348.2	4.031	0.2550	0.4389	2.29	0.0050	0.0067	0.09
348.1	4.644	0.3218	0.5008	2.11	0.0058	0.0067	0.08
348.1	5.326	0.3930	0.5536	1.92	0.0063	0.0066	0.07
348.2	6.145	0.4864	0.5704	1.40	0.0066	0.0065	0.05
348.5	7.112	0.6128	0.6198	1.03	0.0062	0.0061	0.04

* The standard uncertainties in temperature, *u(T)*, and pressure, *u(p)*, are 0.1 K and 0.005 MPa, respectively.

** The relative volatility of CO_2 (1) to HFO-1243zf (2) in their binary system.

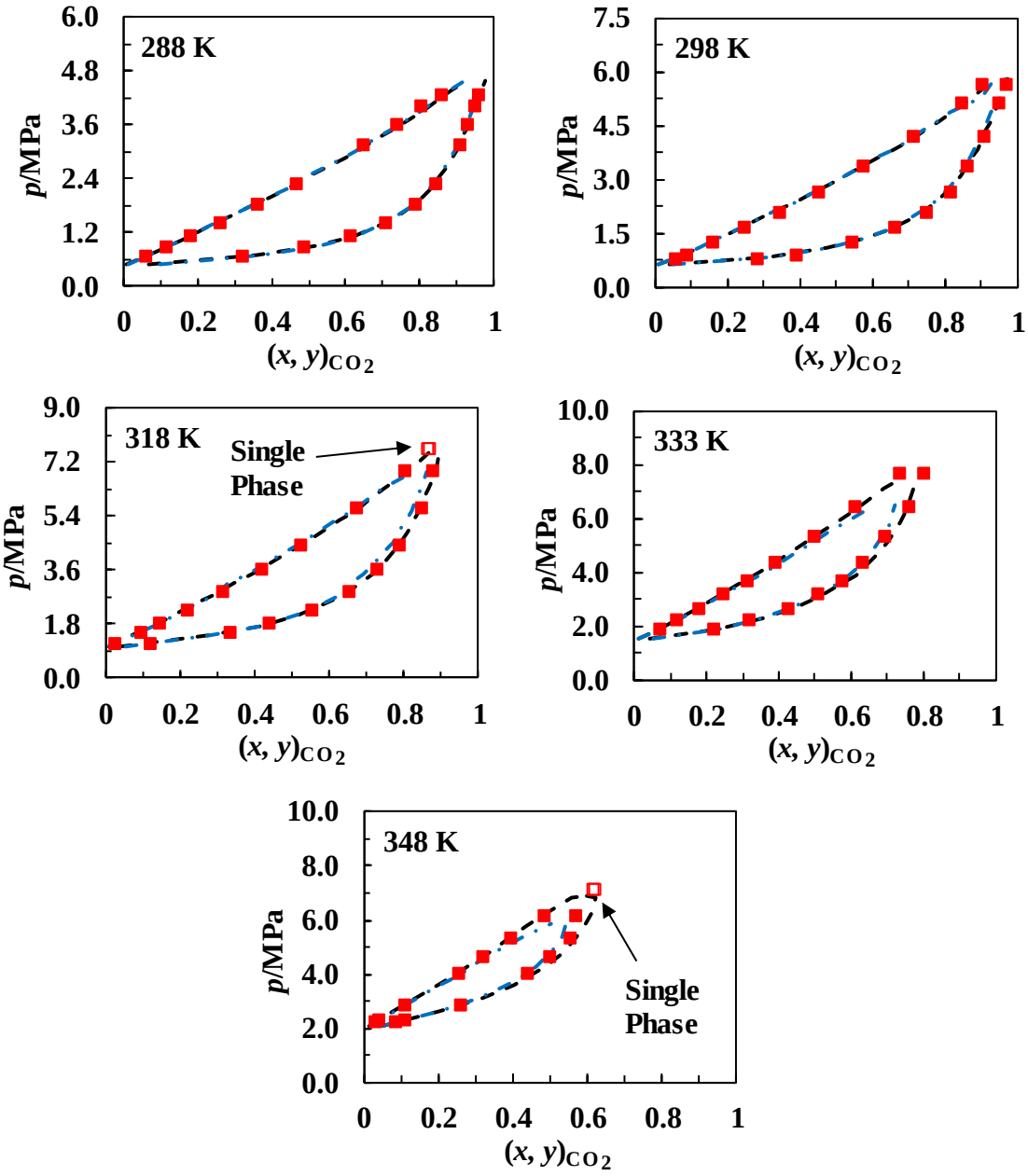

Figure 3.5: VLE data and calculated phase envelopes for the CO_2 + HFO-1243zf system at 288 K, 298 K, 318 K, 333 K and 348 K: (blue - · -) PRA-EOS (tuned); (---) Helmholtz free energy EOS (tuned); ■ this work (hollow symbols show the measured compositions in the dense phase region, acquired to check the Helmholtz energy EOS prediction of a two-phase condition).

3.5.2 Relative volatility and thermodynamic consistency

The relative volatility of a binary mixture at a certain temperature is defined as the ratio of K factors for the two components as follows:

$$\alpha_{ij} = \frac{K_i}{K_j} = \frac{y_i}{x_i} \Big/ \frac{y_j}{x_j} = \frac{y_i x_j}{x_i y_j} \qquad 3.13$$

Here, y_i and x_i are the mole fractions of component i in the vapour and liquid phases of the mixture. Figure 3.6 shows experimental and predicted relative volatilities (α_{12}) of CO_2 (1) to HFO-1243zf (2) at the five temperatures between (288 and 348) K. The relative volatility (α_{12}) decreased with increasing overall CO_2 mole fraction and temperature.

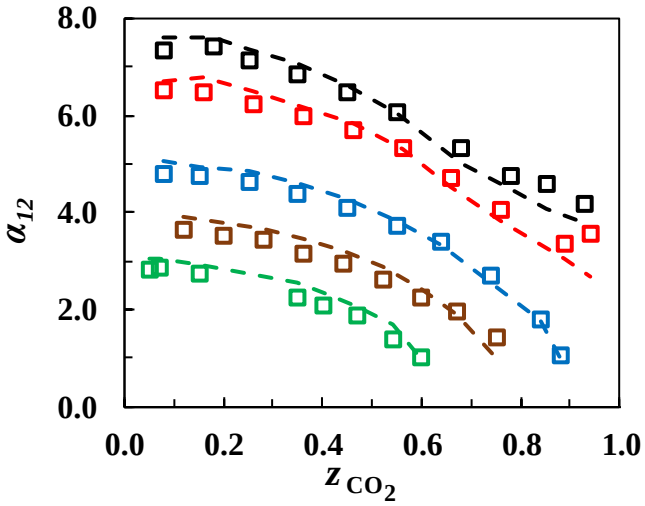

Figure 3.6: The relative volatility (α_{12}) of CO_2 (1) to HFO-1243zf (2) for experimental equilibrium points (□) and the values predicted using the tuned Helmholtz Energy EOS (---); black , T = 288 K; red, T = 298 K; blue, T = 318 K; brown, T = 333 K and green, T = 348 K.

The measured VLE data were assessed for thermodynamic consistency by the point test method presented by Fredenslund et al. [48–50]. To determine the data's consistency, the following statistics were calculated:

$$\Delta y_i = (y_{exp,i} - y_{calc,i}) \qquad 3.14$$

$$\overline{\Delta y_i} = \frac{1}{N}\sum_{i=1}^{N} \Delta y_i \qquad 3.15$$

$$AAD y_i = \frac{1}{N}\sum_{i=1}^{N} |\Delta y_i| \qquad 3.16$$

$$STD \Delta y_i = \sqrt{\frac{1}{N}\sum_{i=1}^{N} [\Delta y_i - \overline{\Delta y_i}]^2} \qquad 3.17$$

Each value of y_{calc} was calculated using the untuned Helmholtz energy model implemented in REFPROP 10, with the measured temperature and liquid phase composition as inputs. According to Fredenslund et al. [49,50], the VLE data set is considered consistent if the average absolute deviation of the dew points (AADy_i) is less than or equal to 0.01 mole fraction. They also recommended the use of polynomial expansions to determine activity coefficients needed to estimate y_{calc}. However, an EOS was used in this work because at (318, 333, and 348) K, pure CO_2 is supercritical. Table 3.6 presents the values of the statistics calculated for each isotherm of the measured VLE data. For the (318, 333 and 348) K isotherms, the closest point to the critical pressure was excluded. More important than the average absolute deviation (AAD), however, is the degree of scatter present in the trend of the deviations with pressure; the AAD will necessarily have a finite value if the untuned EOS is used to determine $y_{calc,}$ but if the data are thermodynamically consistent, they will deviate from the y_{calc} in a smooth trend with pressure. The $\mathrm{STD}\Delta y_i$ quantifies how scattered the data follow that smooth trend; in all cases its value is less than or comparable with the estimated experimental uncertainties.

Table 3.6: The thermodynamic consistency test results for the CO_2 + HFO-1243zf binary systems.

	Helmholtz energy EOS	
T/K	$\mathrm{STD}\Delta y_{CO2}$	$\mathrm{AAD}y_{CO2}$
288	0.003	0.003
298	0.004	0.004
313	0.004	0.003
333	0.005	0.009
348	0.005	0.010
Average (all VLE data)	0.004	0.006

Additionally, the measured VLE data's thermodynamic consistency was assessed further by analysing the vapour enhancement factors of HFO-1243zf in the CO_2 + HFO-1243zf binary systems. The enhancement factor is equal to the quotient of the experimental partial pressure of HFO-1243zf and the saturation vapour pressure of pure HFO-1243zf at the same equilibrium temperature, which is as calculated as follow:

$$f = \frac{y_{\mathrm{HFO-1243zf}} p_{exp}}{p^{sat}_{\mathrm{HFO-1243zf}}} \qquad 3.18$$

Here, the parameters $y_{\text{HFO-1243zf}}$ and p_{exp} are the measured mole fraction of HFO-1243zf in the vapour phase and the pressure of the equilibrium mixture, while $p^{sat}_{\text{HFO}-1243\text{zf}}$ is the saturation vapour pressure of HFO-1243zf at the equilibrium temperature calculated using the reference EOS in REFPROP 10. For each isotherm, the enhancement factor will approach unity in the limit of zero equilibrium pressure. Figure 3.7 shows the enhancement factor for the measured VLE data. It can be seen that the enhancement factor approaches unity at low pressures for all the VLE data and varies smoothly with pressure at a constant temperature, indicating that the data quality is reasonable.

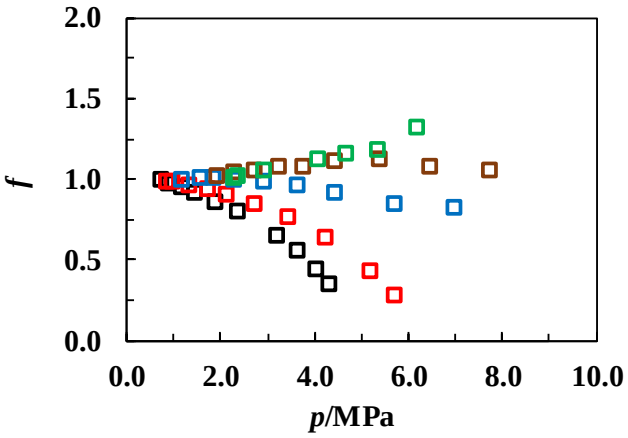

Figure 3.7: The enhancement factor for HFO-1243zf in the CO_2 + HFO-1243zf binary systems on five isotherms of 288 K (black), 298 K (red), 318 K (blue), 333 K (brown) and 348 K (green).

3.5.3 Model tuning

Figure 3.8 (a), (b) shows the differences between the experimental results and the liquid and vapour compositions predicted by the original (un-tuned) Helmholtz energy and PRA EOS. In these plots, the abscissa is the measured saturation pressure, and the ordinates are the differences between the measured and predicted mole fractions of CO_2. The mole fractions for each phase were computed by performing a flash calculation at the corresponding experimental pressure and temperature. The bulk (overall) composition of the binary mixture used as input to the flash calculation was taken to be the experimental value. Generally, the Helmholtz energy EOS provided a better representation of the VLE data than the PRA-EOS, with the deviations of both models being about 3 to 4 times larger than the experimental uncertainty. The variation between the experimental and predicted data for the bubble points increased with pressure for both models. The Helmholtz EOS provided a better representation of the dew points data at low pressure than the PRA EOS, but at high pressure, the performance of the two models in predicting the dew point condition was reversed.

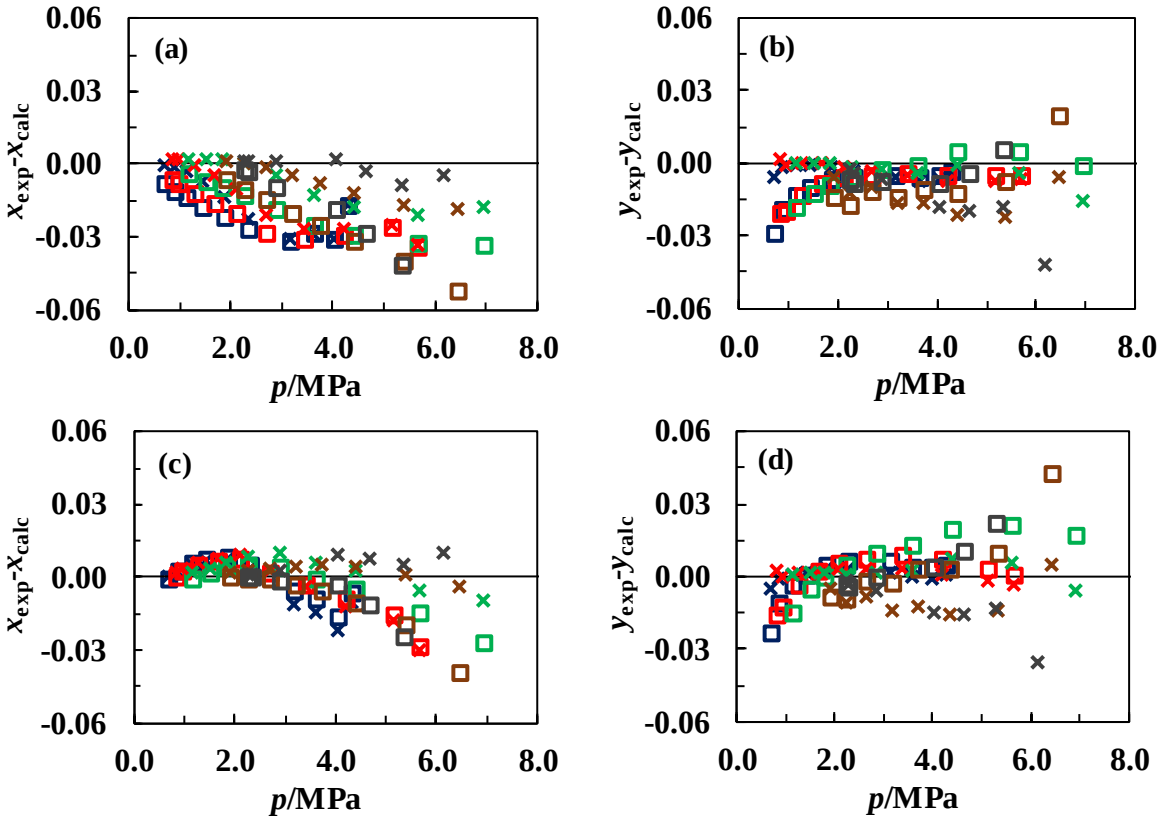

Figure 3.8: Absolute differences between the measured mole fraction (x_{exp}, y_{exp}) and the predicted values (x_{calc}, y_{calc}) by the original and tuned PRA-EOS (□) and Helmholtz Energy EOS (×) for the first component (CO_2); (a) bubble points – original models; (b) dew points – original models; (c) bubble point – tuned models and (d) dew points – tuned models; navy blue, T = 288 K; red, T = 298 K; green, T = 318 K; brown, T = 333 K and dark grey, T = 348 K. The average experimental uncertainty for all the experimental VLE data was a CO_2 mole fraction of 0.005.

When fitting the PRA-EOS and Helmholtz EOS binary interaction parameters, the four experimental data points acquired closest to the critical point at 318, 333 and 348 K were omitted from the regression as the models failed to follow the measured phase envelopes at those conditions. Tuning the PRA-EOS (with an initial BIP of zero) to the experimental data allowed the root mean square deviation (RMSD) – equivalent to the objective function in Equation 3.10 – to be decreased from 0.019 to 0.012 with an optimised BIP of k_{ij} = 0.0254. For the Helmholtz EOS, the fitted binary interaction parameters of ($\beta_{T,ij}$ = 1.009 and $\gamma_{T,ij}$ = 0.992) decreased the objective function from 0.013 to 0.009. The RMSD of the experimental phase compositions from those predicted by the model was significantly improved for both models by this optimisation. For the tuned Helmholtz EOS, the RMSD is less than two times the average experimental uncertainty (CO_2 mole fraction of 0.005), indicating that the fitted model represents the data reasonably well considering their uncertainty.

Figure 3.8 (c), (d) shows the differences between the experimental and predicted liquid and vapour compositions by the tuned Helmholtz EOS and PRA-EOS. The deviations of the bubble points decreased significantly for both models after tuning, particularly at lower pressures.

Table 3.7 presents RMSD and maximum deviation values for the original and tuned EOS. The tuned Helmholtz energy model represents dew and bubble points with lower RMSDs (0.009 for each phase) than the tuned PRA-EOS (0.012 for each phase). The maximum deviation between the experimental and predicted dew and bubble points by the Helmholtz free energy EOS decreased from 0.042 and 0.034 to 0.034 and 0.030, respectively, after tuning the model. The tuned PRA-EOS represents the mole fractions for the liquid phases better than the original PRA-EOS, where the RMSDs decreased from 0.024 to 0.012. It was noted that the RMSD for the vapour phase increased from 0.011 to 0.012 after tuning the PRA-EOS, even though the total RMSD decreased from 0.019 to 0.012. Further optimisation of Helmholtz energy EOS would require more extensive experimental data for other properties such as density and heat capacity.

Table 3.7: Model deviations for the original and tuned PRA-EOS and Helmholtz free energy EOS*

Error	PRA-EOS (original)	PRA-EOS (tuned)	Helmholtz Free energy EOS (original)	Helmholtz Free energy EOS (tuned)
Total RMSD	0.019	0.012	0.013	0.009
RMSD (y)	0.011	0.012	0.011	0.009
RMSD (x)	0.024	0.012	0.015	0.009
Max. Deviation (y)	0.029	0.042	0.042	0.036
Max. Deviation (x)	0.052	0.039	0.034	0.030

* The average experimental uncertainty for all the VLE data was a CO2 mole fraction of 0.005.

3.5.4 Comparison between HFO-1234yf, HFO-1234ze(E) and HFO-1243zf

In this section, the phase behaviour of three HFO candidates of replacing HFC-134a in equimolar mixtures with CO_2 is compared. Figure 3.9 (a) shows the phase diagrams for the binary mixtures predicted by optimised Helmholtz Energy EOS. The optimised model for the HFO-1243zf + CO_2 binary system was based on this work, while for the binary systems HFO-1234yf + CO_2 and HFO-1234ze(E) + CO_2 were based on Arami-Niya et al. [11] and Lemmon et al. [51]. The HFO-1234yf and HFO-1243zf binary mixtures with CO_2 have almost

identical bubble point pressures, while the bubble and dew point curves of the latter mixture are separated by between (0.4 and 4.2) K more in the pressure range (5.7 to 0.3) MPa. Figure 3.9 (b) shows the calculated *p-H* diagrams for the binary mixtures with the HFO-1243zf + CO_2 equimolar binary system being (0.7 to 1.4) kJ/mole wider than the other two binaries in the pressure range (5.7 to 0.3) MPa.

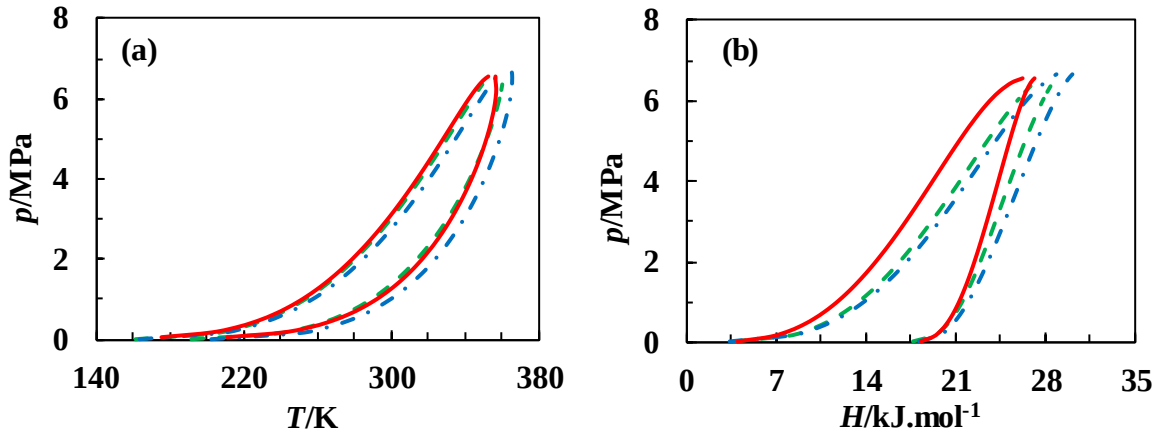

Figure 3.9: (a) *p-T* and (b) *p-H* diagrams of three equimolar binary mixtures of CO_2 + HFO-1243zf (red −), CO_2 + HFO1234yf (green ---) and CO_2 + HFO-1234ze(E) (blue - · -), predicted by the optimised Helmholtz energy EOS.

3.6 Conclusions

New experimental vapour-liquid equilibrium data for CO_2 + HFO-1243zf binary mixtures are reported at temperatures from (288 to 348) K, and pressures between (0.68 and 7.69) MPa. Data presented in this work were compared with the predictions of a Helmholtz free energy model that utilises the GERG-2008 mixing rule and the Peng-Robinson Advanced EOS with van der Waals one-fluid mixing rules. Both models' binary interaction parameters were determined by fitting to the experimental data. The PRA-EOS with the tuned binary interaction parameter provided a slightly better representation of the data than the original untuned Helmholtz free energy EOS. However, the tuned Helmholtz free energy EOS represented the experimental bubble and dew points with an RMSD of 0.009, 33 % better than the tuned PRA-EOS and 45 % better than the un-tuned Helmholtz free energy EOS. The phase behaviour of three popular HFO-1234yf, HFO-1234ze(E) and HFO-1243zf in equimolar mixtures with CO_2 were compared. The binary mixture studied in this work has (0.7 to 1.4) kJ/mole wider enthalpy difference between bubble and dew point curves in the pressure range (5.7 to 0.3) MPa. This work provides new accurate VLE data that will aid in designing and simulating refrigeration processes utilising working fluids with low global warming potential. Further experimental

thermophysical data, in particular density, should be acquired to enable further improvements in the performance of engineering models.

3.7 References

[1] Yang Z, Tang X, Wu J, Lu J. Experimental measurements of saturated vapor pressure and isothermal vapor-liquid equilibria for 1,1,1,2-Tetrafluoroethane (HFC-134a) + 3,3,3-trifluoropropene (HFO-1243zf) binary system. Fluid Phase Equilib 2019;498:86–93. doi:10.1016/J.FLUID.2019.06.020.

[2] González S, Jiménez E, Ballesteros B, Martínez E, Albaladejo J. Hydroxyl radical reaction rate coefficients as a function of temperature and IR absorption cross sections for CF3CH=CH2 (HFO-1243zf), potential replacement of CF3CH2F (HFC-134a). Environ Sci Pollut Res 2015;22:4793–805. doi:10.1007/s11356-014-3426-2.

[3] No. 26369. Montreal Protocol on Substances that Deplete the Ozone Layer. Concluded at Montreal on 16 September 1987 2000;1522:422–47. doi:10.18356/df488915-en-fr.

[4] UNEP. The Kigali Amendment to the Montreal Protocol: HFC Phase-down. 28th Meet Parties to Montr Protoc 10-14 October, 2016, Kigali, Rwanda 2016:1–7.

[5] Mylona SK, Hughes TJ, Saeed AA, Rowland D, Park J, Tsuji T, et al. Thermal conductivity data for refrigerant mixtures containing R1234yf and R1234ze(E). J Chem Thermodyn 2019;133:135–42. doi:10.1016/j.jct.2019.01.028.

[6] Akhfash M, Al Ghafri SZS, Rowland D, Hughes TJ, Tsuji T, Tanaka Y, et al. Liquid and Vapor Viscosities of Binary Refrigerant Mixtures Containing R1234yf or R1234ze(E). J Chem Eng Data 2019;64:1122–30. doi:10.1021/acs.jced.8b01039.

[7] Al Ghafri SZ, Rowland D, Akhfash M, Arami-Niya A, Khamphasith M, Xiao X, et al. Thermodynamic properties of hydrofluoroolefin (R1234yf and R1234ze(E)) refrigerant mixtures: Density, vapour-liquid equilibrium, and heat capacity data and modelling. Int J Refrig 2019;98:249–60. doi:10.1016/j.ijrefrig.2018.10.027.

[8] Sampson CC, Kamson M, Hopkins MG, Stanwix PL, May EF. Dielectric permittivity, polarizability and dipole moment of refrigerants R1234ze(E) and R1234yf determined using a microwave re-entrant cavity resonator. J Chem Thermodyn 2019;128:148–58. doi:10.1016/j.jct.2018.07.011.

[9] Kim D, Yang X, Arami-Niya A, Rowland D, Xiao X, Al Ghafri SZS, et al. Thermal conductivity measurements of refrigerant mixtures containing hydrofluorocarbons (HFC-32, HFC-125, HFC-134a), hydrofluoroolefins (HFO-1234yf), and carbon dioxide (CO2). J Chem Thermodyn 2020;151:106248. doi:10.1016/j.jct.2020.106248.

[10] Yang X, Arami-Niya A, Xiao X, Kim D, Al Ghafri SZS, Tsuji T, et al. Viscosity Measurements of Binary and Multicomponent Refrigerant Mixtures Containing HFC-32, HFC-125, HFC-134a, HFO-1234yf, and CO2. J Chem Eng Data 2020;65:4252–62. doi:10.1021/acs.jced.0c00228.

[11] Arami-Niya A, Xiao X, Al Ghafri SZS, Jiao F, Khamphasith M, Sadeghi Pouya E, et al. Measurement and modelling of the thermodynamic properties of carbon dioxide mixtures with HFO-1234yf, HFC-125, HFC-134a, and HFC-32: vapour-liquid equilibrium, density, and heat capacity. Int J Refrig 2020;118:514–28. doi:10.1016/j.ijrefrig.2020.05.009.

[12] Di Nicola G, Di Nicola C, Arteconi A, Stryjek R. PVTx measurements of the carbon dioxide +

2,3,3,3-tetrafluoroprop-1-ene binary system. J Chem Eng Data 2012;57:450–5. doi:10.1021/je201051q.

[13] Yao X, Ding L, Dong X, Zhao Y, Wang X, Shen J, et al. Experimental measurement of vapor-liquid equilibrium for 3,3,3-trifluoropropene(R1243zf) + 1,1,1,2-tetrafluoroethane(R134a) at temperatures from 243.150 to 293.150 K. Int J Refrig 2020;120:97–103. doi:10.1016/j.ijrefrig.2020.09.008.

[14] Deng Z, Xu G, Sun S, Zhao Y, Dong X, Gong M. Isothermal (vapour-liquid) equilibrium for the binary {isobutane (R600a) + 3,3,3-trifluoropropene (R1243zf)}cc system at temperatures from 253.150 to 293.150 K. J Chem Thermodyn 2020;150:106177. doi:10.1016/j.jct.2020.106177.

[15] Ding L, Yao X, Hou Y, Zhao Y, Dong X, Gong M. Isothermal (vapour-liquid) equilibrium for the binary {3,3,3-trifluoropropene (R1243zf) + propane(R290)} system at temperatures from 243.150 K to 288.150 K. J Chem Thermodyn 2020;144:106091. doi:10.1016/j.jct.2020.106091.

[16] Lai NA. Thermodynamic properties of HFO-1243zf and their application in study on a refrigeration cycle. Appl Therm Eng 2014;70:1–6. doi:10.1016/j.applthermaleng.2014.04.042.

[17] Akasaka R. Recent trends in the development of Helmholtz energy equations of state and their application to 3,3,3-trifluoroprop-1-ene (R-1243zf). Sci Technol Built Environ 2016;22:1136–44. doi:10.1080/23744731.2016.1208000.

[18] Akasaka R, Lemmon EW. Fundamental Equations of State for *cis* -1,3,3,3-Tetrafluoropropene [R-1234ze(Z)] and 3,3,3-Trifluoropropene (R-1243zf). J Chem Eng Data 2019;64:4679–91. doi:10.1021/acs.jced.9b00007.

[19] Bobbo S, Nicola G Di, Zilio C, Brown JS, Fedele L. Low GWP halocarbon refrigerants: A review of thermophysical properties. Int J Refrig 2018;90:181–201. doi:10.1016/j.ijrefrig.2018.03.027.

[20] Brown JS, Zilio C, Cavallini A. Thermodynamic properties of eight fluorinated olefins. Int J Refrig 2010;33:235–41. doi:10.1016/j.ijrefrig.2009.04.005.

[21] Daubert TE, Hutchison G. Vapor pressure of 18 pure industrial chemicals. AIChE Symp Ser 1990;86:93–114.

[22] Brown JS, Di Nicola G, Fedele L, Bobbo S, Zilio C. Saturated pressure measurements of 3,3,3-trifluoroprop-1-ene (R1243zf) for reduced temperatures ranging from 0.62 to 0.98. Fluid Phase Equilib 2013;351:48–52. doi:10.1016/J.FLUID.2012.09.036.

[23] Higashi Y, Sakoda N, Islam MA, Takata Y, Koyama S, Akasaka R. Measurements of Saturation Pressures for Trifluoroethene (R1123) and 3,3,3-Trifluoropropene (R1243zf). J Chem Eng Data 2018;63:417–21. doi:10.1021/acs.jced.7b00818.

[24] Higashi Y, Sakoda N, Islam MA, Takata Y, Koyama S, Akasaka R. Measurements of Saturation Pressures for Trifluoroethene (R1123) and 3,3,3-Trifluoropropene (R1243zf). J Chem Eng Data 2018;63:417–21. doi:10.1021/acs.jced.7b00818.

[25] Di Nicola G, Steven Brown J, Fedele L, Securo M, Bobbo S, Zilio C. Subcooled liquid density measurements and PvT measurements in the vapor phase for 3,3,3-trifluoroprop-1-ene (R1243zf). Int J Refrig 2013;36:2209–15. doi:10.1016/j.ijrefrig.2013.08.004.

[26] Raabe G. Molecular simulation studies in hydrofluoroolefine (HFO) working fluids and their blends. Sci Technol Built Environ 2016;22:1077–89. doi:10.1080/23744731.2016.1206796.

[27] Tomassetti S, Pierantozzi M, Di Nicola G, Polonara F, Brown JS. Vapor-Phase PvTx Measurements of Binary Blends of cis-1,2,3,3,3-Pentafluoroprop-1-ene + Isobutane and 3,3,3-

Trifluoropropene + Isobutane. J Chem Eng Data 2019;64:688–95. doi:10.1021/acs.jced.8b00921.

[28] Sadaghiani MS, Arami-Niya A, Zhang D, Tsuji T, Tanaka Y, Seiki Y, et al. Minimum ignition energies and laminar burning velocities of ammonia, HFO-1234yf, HFC-32 and their mixtures with carbon dioxide, HFC-125 and HFC-134a. J Hazard Mater 2021;407:124781. doi:10.1016/j.jhazmat.2020.124781.

[29] McLinden MO, Kazakov AF, Steven Brown J, Domanski PA. A thermodynamic analysis of refrigerants: Possibilities and tradeoffs for Low-GWP refrigerants. Int J Refrig 2014;38:80–92. doi:10.1016/j.ijrefrig.2013.09.032.

[30] Bell IH, Domanski PA, McLinden MO, Linteris GT. The hunt for nonflammable refrigerant blends to replace R-134a. Int J Refrig 2019;104:484–95. doi:10.1016/j.ijrefrig.2019.05.035.

[31] Wang S, Fauve R, Coquelet C, Valtz A, Houriez C, Artola PA, et al. Vapor–liquid equilibrium and molecular simulation data for carbon dioxide (CO 2) + trans-1,3,3,3-tetrafluoroprop-1-ene (R-1234ze(E)) mixture at temperatures from 283.32 to 353.02 K and pressures up to 7.6 MPa. Int J Refrig 2019. doi:10.1016/j.ijrefrig.2018.10.032.

[32] Juntarachat N, Valtz A, Coquelet C, Privat R, Jaubert JN. Experimental measurements and correlation of vapor-liquid equilibrium and critical data for the CO 2 + R1234yf and CO 2 + R1234ze(E) binary mixtures. Int J Refrig 2014. doi:10.1016/j.ijrefrig.2014.09.001.

[33] Qin Y, Wang Z, Zhang H, Wu Y. Investigation on vapor liquid equilibrium for strongly-zeotropic ternary mixture of 2,3,3,3-tetrafluoroprop-1-ene (R1234yf) + trifluoromethane (R23) + tetrafluoromethane (R14). Int J Heat Mass Transf 2017;114:1135–45. doi:10.1016/j.ijheatmasstransfer.2017.06.014.

[34] May EF, Guo JY, Oakley JH, Hughes TJ, Graham BF, Marsh KN, et al. Reference quality vapor-liquid equilibrium data for the binary systems methane + ethane, + propane, + butane, and + 2-methylpropane, at temperatures from (203 to 273) K and pressures to 9 MPa. J Chem Eng Data 2015;60:3606–20. doi:10.1021/acs.jced.5b00610.

[35] Efika EC, Hoballah R, Li X, May EF, Nania M, Sanchez-Vicente Y, et al. Saturated phase densities of (CO2 + H2O) at temperatures from (293 to 450) K and pressures up to 64 MPa. J Chem Thermodyn 2016;93:347–59. doi:10.1016/j.jct.2015.06.034.

[36] Guilbot P, Valtz A, Legendre H, Richon D. Rapid on-line sampler-injector: A reliable tool for HT-HP sampling and on-line GC analysis. Analusis 2000;28:426–31. doi:10.1051/analusis:2000128.

[37] Richon D. Method and device for taking micro samples from a pressurized fluid contained in a container. Organisation Mondiale De La Propriete Intellectuelle (Bureau International), Publication No FR2853414B1, 2003.

[38] Davis RS. Equation for the determination of the density of moist air (1981/91). Metrologia 1992;29:67–70. doi:10.1088/0026-1394/29/1/008.

[39] Span R, Wagner W. A new equation of state for carbon dioxide covering the fluid region from the triple-point temperature to 1100 K at pressures up to 800 MPa. J Phys Chem Ref Data 1996;25:1509–96. doi:10.1063/1.555991.

[40] Lemmon EW, Bell I, Huber ML, McLinden MO. NIST Standard Reference Database 23: Reference Fluid Thermodynamic and Transport Properties-REFPROP, Version 10.0 n.d.

[41] Joint Committee for Guides in Metrology. Evaluation of measurement data - Guide to the expression of uncertainty in measurement. JCGM 2008;100:1–116.

[42] Peng D-Y, Robinson DB. A New Two-Constant Equation of State. Ind Eng Chem Fundam 1976;15:59–64. doi:10.1021/i160057a011.

[43] Mathias PM, Copeman TW. Extension of the Peng-Robinson equation of state to complex mixtures: Evaluation of the various forms of the local composition concept. Fluid Phase Equilib 1983;13:91–108. doi:10.1016/0378-3812(83)80084-3.

[44] Infochem / KBC Advanced Technologies Ltd. MultiFlash User Guide for Models and Physical Properties. 2017.

[45] Souza LFS, Al Ghafri SZS, Trusler JPM. Measurement and modelling of the vapor–liquid equilibrium of (CO2 + CO) at temperatures between (218.15 and 302.93) K at pressures up to 15 MPa. J Chem Thermodyn 2018;126:63–73. doi:10.1016/J.JCT.2018.06.022.

[46] Kunz O, Wagner W. The GERG-2008 Wide-Range Equation of State for Natural Gases and Other Mixtures: An Expansion of GERG-2004. J Chem Eng Data 2012;57:3032–91. doi:10.1021/je300655b.

[47] Bell IH, Lemmon EW. Automatic Fitting of Binary Interaction Parameters for Multi-fluid Helmholtz-Energy-Explicit Mixture Models. J Chem Eng Data 2016;61:3752–60. doi:10.1021/acs.jced.6b00257.

[48] Wisniak J, Ortega J, Fernández L. A fresh look at the thermodynamic consistency of vapour-liquid equilibria data. J Chem Thermodyn 2017;105:385–95. doi:10.1016/J.JCT.2016.10.038.

[49] Fredenslund A, Gmehling J, Rasmussen P. Vapor-liquid Equilibria Using UNIFAC. Elsevier Ltd; 1977. doi:https://doi.org/10.1016/B978-0-444-41621-6.50009-0.

[50] Christiansen LJ, Fredenslund A. Thermodynamic consistency using orthogonal collocation or computation of equilibrium vapor compositions at high pressures. AIChE J 1975;21:49–57. doi:10.1002/aic.690210105.

[51] Lemmon EW, Huber ML, McLinden MO. NIST Standard Reference Database 23: Reference Fluid Thermodynamic and Transport Properties-REFPROP, Version 9.0 2013.

4 Chapter 4 │ Cryogenic Vapour and Solid Solubility Measurements for CO_2 + HFC-32 Binary Mixtures at Temperatures between (132 and 273) K

4.1 Abstract

Accurate phase equilibrium data for mixtures of eco-friendly but mildly-flammable refrigerants with inert components like CO_2 will help industry safely employ working fluids with 80 % less global warming potential than the current options. In this work, a visual high-pressure measurement setup with analytic capability was used to measure the vapour-liquid equilibrium (VLE) and solid-fluid equilibrium (SFE) of HFC-32 + CO_2 binary systems at temperatures between (132 and 273) K. The measured VLE data in this study together with the literature data are compared with values calculated using a previously optimised Helmholtz energy model. The model represented the VLE data with a root mean square deviation (RMSD) of 0.02 CO_2 mole fraction for the liquid and vapour phases. The solid-liquid-vapour equilibrium (SLVE) and solid-liquid equilibrium (SLE) data were used to tune a thermodynamic model implemented in the ThermoFAST software package by adjusting the BIP in the Peng-Robinson equation of state. The tuned model represents the measured melting points for binary mixtures with an RMSD of 3 K, which is 60 % less than when the model used the default BIP. The accurate property data and improved model presented in this work will help avoid solid deposition risk in cryogenic applications of the HFC-32 + CO_2 binary system and promote widespread applications of environmentally-friendly refrigerant mixtures.

4.2 Introduction

The hydrofluorocarbons (HFCs) of HFC-32, HFC-134a and HFC-125 are refrigerants commonly used as working fluids in domestic air-conditioning systems, with global warming potentials (GWPs) of 677, 1300 and 3170 over a 100-year time scale, respectively [1]. Of the three HFCs, HFC-32 has the lowest atmospheric lifetime of 5.2 years (80% less than the other HFCs) and better heat transfer properties [1]. However, its moderate flammability and toxic combustion products pose safety hazards to public users and are barriers to its widespread

replacement [2]. Therefore, HFC-32 is often blended with non-flammable HFC-125 in binary mixtures of HFC-410A (HFC-32/HFC-125: 50/50 wt%) and HFC-410B (HFC-32/HFC-125: 45/55 wt%) to neutralise its flammability and be safely used in the domestic refrigeration systems [3]. These blends, however, have GWPs of 2235 (HFC-410A) and 2328 (HFC-410B) that does not satisfy the refrigerant regulation objectives of the Montreal Protocol and the Kigali Amendment [4].

Carbon dioxide (CO_2), as a natural refrigerant, can be blended with HFC-32 to neutralise its flammability and significantly reduce the overall GWP of the mixture with minor reductions in HFC-32's cooling performance. To efficiently use the HFC-32 + CO_2 binary system as the working fluid of the refrigeration systems, reliable predictions of its thermophysical properties in a wide range of working temperatures and pressures are necessary. The thermophysical properties of this binary mixture have been well studied at relatively high operating temperatures, as shown in Table 4.1. However, limited studies have been conducted at low temperatures, which hinders the ability to assess thermodynamic model predictions at these conditions. Additionally, CO_2 with a triple point of 216.55 K at 0.518 MPa [5] poses a freeze-out risk at low temperatures, with solid crystals potentially damaging equipment or blocking flow [6]. Therefore, solid formation at low temperatures needs to be investigated. Although some solid-fluid equilibrium (SFE) data for HFC-32 + CO_2 binary mixtures has been reported at the vapour pressure of the binary mixture [7], no experimental SFE data have been reported at elevated pressures for this system.

Table 4.1: Summary of the thermodynamic property data available for HFC-32 + CO_2 binary mixtures

Properties	Range (T, p, z)[a]	Ref.
pvTx	303-343 K, 0.14-4.6 MPa, 0.17-0.8	[8]
VLE	289-290 K, 1.4-3.6 MPa, 0.04-0.8	[9]
VLE	280-310 K, 1.7-6.4 MPa, 0.21-0.8	[10]
VLE	222-283 K, 0.1-4.5 MPa, 0-1.0	[11]
VLE	283-343 K, 1.1-6.6 MPa, 0-1.0	[12]
VLE	293 K, 1.8-4.8 MPa, 0.09-0.89	[13]
SLVE	137-217 K, 0.03-0.5 MPa, 0-1.0	[7]

[a] z represents the mole fraction of CO_2 in the binary mixtures.

In this work, the VLE of the HFC-32 + CO_2 binary system was measured along three isotherms of (273, 238 and 223) K using an analytical method similar to that described previously in Chapter 3 [14]. The new VLE data, together with their quantitative uncertainty estimates, are used to check the reliability of a Helmholtz energy equation of state (EOS) [15] tuned by

Arami-Niya et al. [13] (Appendix B) to thermodynamic data measured at higher temperatures for phase equilibrium predictions at the low-temperature conditions. The SFE of the HFC-32 + CO_2 binary mixtures were also measured at CO_2 concentrations between (0 and 100) mol% at pressures up to 11 MPa using the synthetic method [16,17]. A thermodynamic model consisting of a Peng-Robinson EOS for the fluid phase and a reference Helmholtz energy EOS for the CO_2 solid phase (I) [18] implemented in the ThermoFAST software package [19] was tuned to the SFE data.

4.3 Experimental

4.3.1 Apparatus overview

The measurement setup, shown in Figure 4.1 (a)-(b) and described previously [20–23], was upgraded to incorporate an analytic measurement capability to the equilibrium cell, augmenting the synthetic technique previously used for SFE determinations at cryogenic conditions. The experimental setup consists of a visual equilibrium cell that includes a transparent sapphire tube and two stainless steel (SAE316L) flanges, as shown in Figure 4.2 (a)-(b). The cell has an internal volume of 75 mL and a pressure rating of 31 MPa. A Digiquartz Paroscientific pressure transducer with a full scale of 41 MPa and relative standard uncertainty of 0.01 % of the full scale is used to measure the system's pressure. A magnetic stirrer, driven by a stepper motor (Arun Microelectronics), is placed inside the cell to ensure the mixture homogeneity during the phase equilibrium measurements.

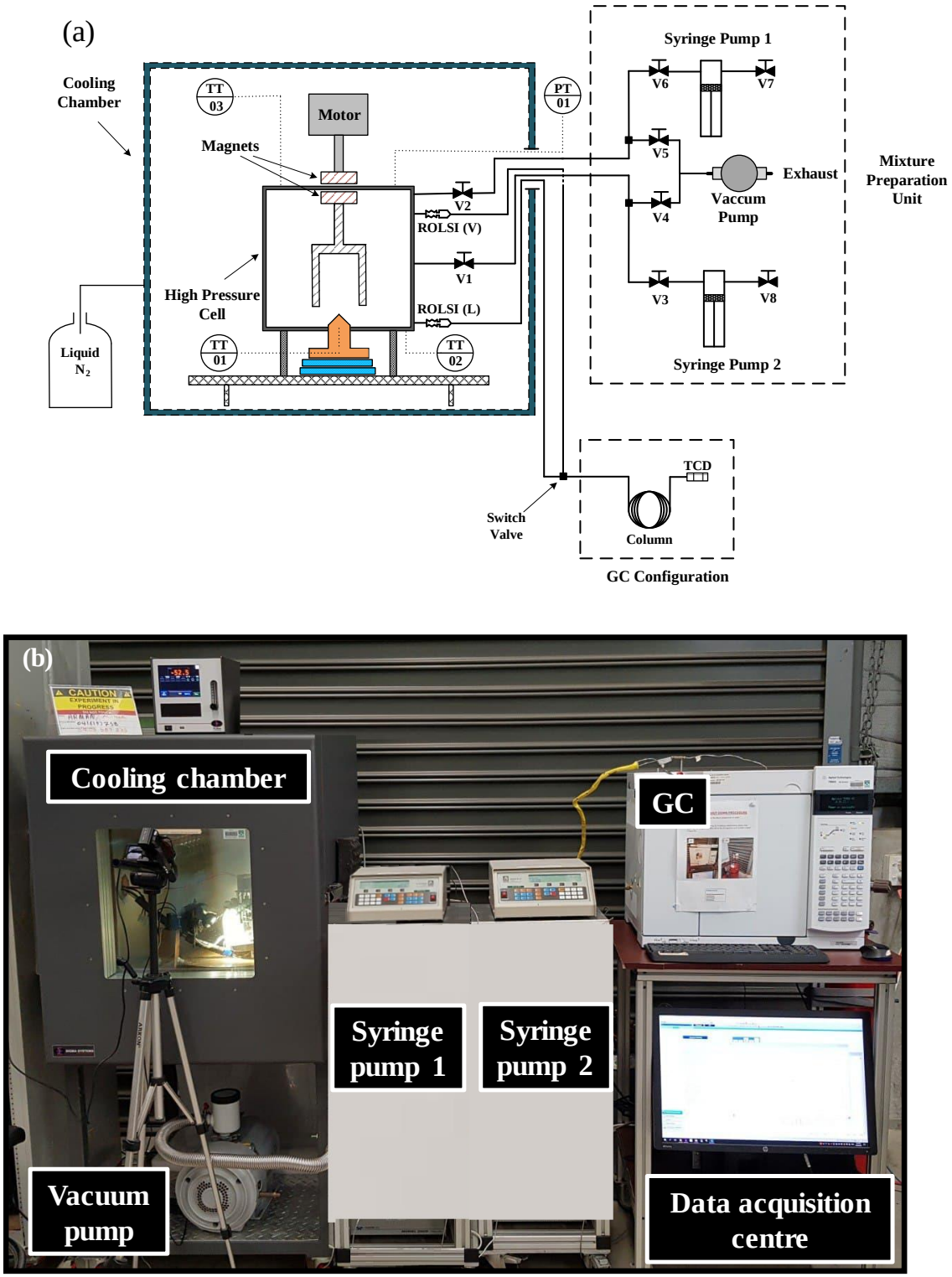

Figure 4.1: (a) Schematic diagram of the VLE & SFE apparatus; (b) photograph of the measurement setup.

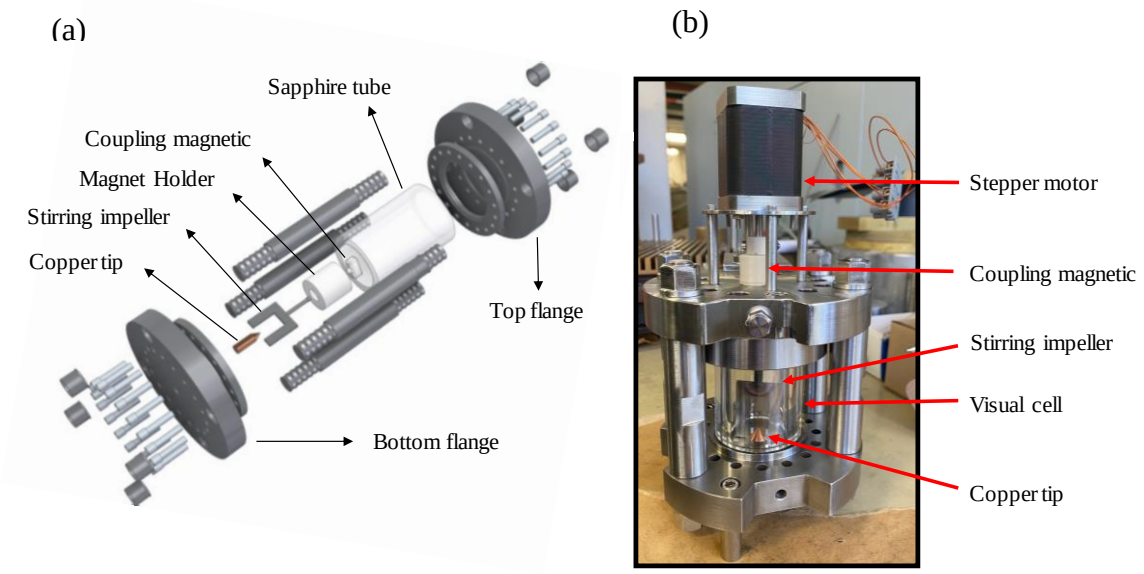

Figure 4.2: (a) Visualisation of the equilibrium cell showing an exploded view and (b) a photograph.

A cryogenic environmental chamber (M170J-13100) with an operating temperature range of (87 to 473) K housed the visual cell and controlled bulk fluid temperature (Thermal Solution Series - KTS6310AB). To minimise thermal shock risk for the sapphire tube, the cooling and heating rates of the chamber were controlled to a maximum of 1 $K \cdot min^{-1}$ by adjusting the liquid nitrogen flow from a high-pressure Dewar. Three fast-response 100 Ω platinum resistance thermometers (PRT NR-14, Netsushin) were employed to measure the cell temperature and were placed into holes bored on the top and bottom flanges and the copper tip inside the cell. The PRTs were calibrated against a reference standard temperature sensor (ASL-WIKA) with 0.02 K standard uncertainty over temperatures between (100 and 273) K. The mean temperature difference between these PRTs at the top and bottom of the cell was less than 0.1 K during the equilibrium condition. For the SFE measurements, the copper tip temperature was taken as the measure of the observed freezing and melting points. A Panasonic high-definition (HD) camcorder (HCV 180) captured and recorded observations of solid freezing and melting.

Two remotely controlled rapid online sampling injector (ROLSI) [24,25] valves were used to take samples from the vapour and liquid phases during the VLE measurements. Two stainless steel (SAE316L) capillary tubes with an i.d. of 0.13 mm, o.d. of 1.6 mm and length of 250 mm, connected the ROLSI valves to the top and bottom flanges of the cell. The taken samples were analysed using an Agilent 7890A Gas Chromatograph (GC) with a thermal conductivity detector (TCD) and a capillary column (Agilent J&W HP/PLOT-U).

4.3.2 GC detector calibration procedure for VLE measurement

The pure fluids used in the VLE and SFE measurements were received directly from the suppliers listed in Table 4.2 and were used without further purification.

Table 4.2: Details of chemicals used.

ASHRAE Refrigerant Number	IUPAC name	Chemical formula	CAS #	Supplier	Mole Fraction Purity*
R744	Carbon Dioxide	CO_2	124-38-9	Coregas	0.99995
R32**	Difluoromethane	CH_2F_2	75-10-5	Coregas	0.995
N/A	Hydrogen***	H_2	1333-74-0	BOC	0.99999

* As stated by the supplier.
** Referred as HFC-32 in this chapter.
*** The carrier gas of the Gas chromatograph (GC).

The GC detector calibration procedure used in this study is similar to the one described previously in Chapter 3 [14], so only a brief explanation was provided here. Four binary mixtures of HFC-32 + CO_2 were volumetrically prepared with CO_2 fractions of 20, 40, 60 and 80 mol% in sample cylinders (300 mL Swagelok stainless steel) using the mixture preparation setup described in [14]. The composition of the prepared calibration mixtures was gravimetrically determined.

For this purpose, the evacuated sample cylinders were weighed 20 times over six hours on an electronic scale with a precision of 0.01 g to obtain an averaged value of the initial cylinder mass. The average ambient conditions of the measuring environment before and after weighing were captured by two separate temperature, pressure and relative humidity sensors and used to correct the apparent mass for the effect of air buoyancy [26]. The CO_2 and HFC-32 volumes needed to prepare binary mixtures of (20, 40, 60 and 80) mol% CO_2 were determined from the pure fluid densities calculated using each component's reference Helmholtz energy EOS [21,22]. The pure HFC-32 and CO_2 samples were pressurised by high precision syringe pumps (Teledyne ISCO 260D) at (6 and 9) MPa, respectively, and were held for 12 hours to ensure the samples were in a compressed liquid state. Then, each component was injected into the cylinders, and the cylinder was weighed after each injection to determine the mass of the injected samples.

The prepared mixture for the GC detector calibration was transferred into the equilibrium cell for sampling as a single-phase mixture. For this purpose, the cylinder was placed inside the chamber and connected to the VLE cell, and all lines were evacuated using the vacuum pump (RZ6 Vacuubrand). Then, the temperature of the entire system (cylinder + VLE cell) was

maintained at 10 K higher than the cricondentherm temperature of the prepared binary mixture to ensure the mixture remained in a single-phase condition during the transfer. Table 4.3 presents the prepared mixtures' composition, molar ratio and calculated critical and cricondentherm temperatures using the REFPROP 10 software package developed by NIST [27]. The cylinder was disconnected from the cell after transferring the mixture, and the mixture in the cell was left to stabilise for about 3 hours under continuous stirring before sampling the mixture.

Table 4.3: Gravimetrically prepared mixtures' composition, molar ratio and cricondentherm temperatures calculated using REFPROP 10.

z_{CO2}	$u(z_{CO2})$	$\frac{z_{CO2}}{z_{HFC\text{-}32}}$	$T_{cricondentherm}$ /K
0.214	0.0004	0.272	344.6
0.397	0.0002	0.658	337.5
0.592	0.0002	1.451	328.3
0.796	0.0001	3.892	317.2

Once the transferred mixture was stabilised, at least 30 samples were taken from the top and bottom part of the VLE cell and analysed using different opening times of the ROLSI valves. Within the linear range of the TCD detector, the mole fraction, z_i, for a given binary mixture can be determined by using the following equations:

$$\left(\frac{z_i}{z_j}\right) = k\left(\frac{A_i}{A_j}\right) \tag{4.1}$$

$$z_i = 1 - \frac{1}{1 + k\left(\frac{A_i}{A_j}\right)} \tag{4.2}$$

Here, A_i and A_j stand for the peaks' areas for components *i* and *j* of the binary mixture, respectively. The parameter *k* represents the calibration factor for the GC TCD detector. Figure 4.3 shows the relationships between the sample's molar ratios ($z_{CO2}/z_{HFC\text{-}32}$) and the corresponding area ratios ($A_{CO2}/A_{HFC\text{-}32}$). Table 4.4 presents the GC method used during the measurement, which was able to sufficiently separate the HFC-32 and CO_2 peaks in each sample.

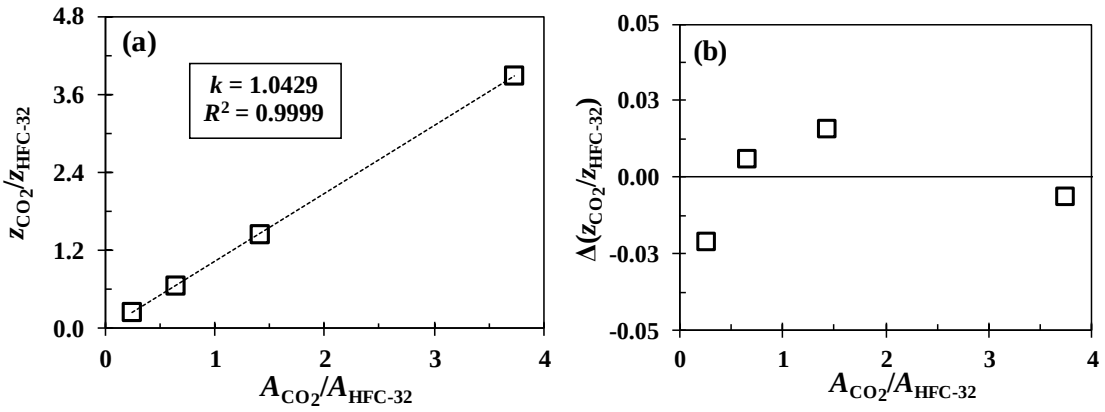

Figure 4.3: Thermal-conductivity detector (TCD) gravimetric calibration data for HFC-32 + CO_2 binary mixtures: (a) gravimetric molar ratios of CO_2 to HFC-32 against GC area response ratios of CO_2 to HFC-32, (b) deviation of the calculated molar ratios (z_{CO2}/z_{HFC-32}) based on Eq. 4.11 from the gravimetrically measured values against GC area response ratios; □ experimental data, (---) Equation 4.1.

Table 4.4: The GC method used for separating CO_2 and HFC-32 peaks.

Gas Chromatograph Parameter	Optimised Condition
Detector Conditions	
TCD temperature	453.15 K
Carrier gas	H_2
Carrier gas flow rate	15 mL·min^{-1}
Makeup gas flow rate	3 mL·min^{-1}
Column Conditions	
Separations column	Agilent J&W HP/PLOT-U, 320 µm D, 30 m
Chamber temperature	323.15 K
Split Ratio	100/1
CO_2 retention time	2 min
HFC-32 retention time	3.5 min

4.3.3 VLE measurement procedure

Before preparing a mixture for the VLE measurement, the visual cell and all connections were cleaned and evacuated using the vacuum pump (Varian SH-110). Predetermined HFC-32 and CO_2 volumes were injected into the cell using two high-precision syringe pumps (Teledyne ISCO 260D) at ambient temperature (measured by an independent 100 Ω PRT) for an in-situ mixture preparation. After the injection, the mixture was stirred for 3 hours at the desired temperature to ensure the mixture was homogenous. The pressure and temperature fluctuations

of the sample within 0.008 MPa and 0.1 K over three hours indicated equilibrium between vapour and liquid phases within the cell. Then, the GC lines were flushed, and both vapour and liquid phases were sampled 20 times.

4.3.4 Mixture preparation for SFE measurements

For the SFE measurements, the HFC-32 + CO_2 binary mixtures were prepared in two different approaches. For binary mixtures of (80 to 95) mol% CO_2, a predetermined volume of pure HFC-32 was injected into the cell, and the mixture composition was then adjusted by injecting CO_2 in increments of 5 mol%. Additionally, the mixtures with CO_2 compositions of (11, 28, 51 and 72) mol% were prepared by injecting the predetermined amounts of HFC-32 and CO_2 into a high-precision syringe pump. The prepared mixtures were pressurised at (8 and 11) MPa, higher than the mixture's cricondenbar pressure (calculated using REFPROP 10 [27]), to ensure the samples were in a single-phase condition during the storage and transfer to the cell. The bottom section of the syringe pump's cylinder was also heated at 328 K to ensure the mixture's homogeneity by allowing convective mixing inside the syringe pump. The cell was connected to the syringe pump and the single-phase mixture was injected into the cell while the syringe pump remained pressurised at 8 MPa at all times. Once the pressure in the equilibrium cell had reached 8 MPa, it was left to stabilise at constant pressure for 6 hours while being stirred. At this high pressure, samples taken using the ROLSI valves would saturate the GC column, meaning that the analytical method could not be used to verify the overall mixture. Instead, the bubble point of the sample was measured and compared with the prediction of the tuned Helmholtz energy EOS [13] to confirm that the mixture was well-mixed and sample composition is close to the volumetrically determined value. To synthetically measure the sample's bubble point, the cell was isolated, and the mixture was cooled down at a controlled rate of 0.8 $K \cdot min^{-1}$ as shown in Figure 4.4. The measured bubble points corresponded to CO_2 mole fractions that were consistent with the values determined volumetrically within the combined uncertainty in the overall composition of the synthetic binary mixtures (0.01 CO_2 mole fraction).

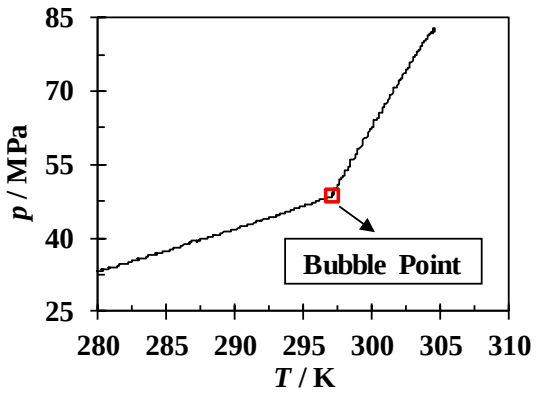

Figure 4.4: The pressure-temperature (PT) diagram during the isochoric cooling of the HFC-32 + CO_2 (28:72 mol%) binary mixture to synthetically determine the bubble point. The red square corresponds to the predicted bubble point.

4.3.5 Melting and freezing measurement procedures

After loading the cell, the cooling chamber temperature was reduced with a cooling rate of 0.8 $K \cdot min^{-1}$ until stabilised by control algorithms at the desired set-points. Then, the cell temperature gradually reduced at a rate between (0.1 and 0.25) $K \cdot min^{-1}$ until the solid crystals were formed. The observed temperature and pressure of this point were recorded as the freezing point (T_f and p_f) of the sample. After forming the solids in the cell, the temperature was increased at steps of (0.1 to 1) K every 20 minutes (corresponding to a heating rate between (0.005 and 0.05) $K \cdot min^{-1}$ due to the thermal lag of the system) until complete melting was observed. The temperature and pressure of this point were recorded as the melting point (T_m and p_m) of the sample. Each melting point measurement was repeated three times.

4.3.6 Uncertainty analysis

The uncertainty analysis for the VLE and SFE measurements was conducted based on the "Guide to the Expression of Uncertainty in Measurement (GUM)" method described by National Institution of Standards and Technology (NIST) [28]. For the VLE measurement, the mole fractions x and y are defined here to represent the CO_2 mole fractions in the liquid and vapour phases, respectively. Each of the quantities T, p, x and y used are the average of N independent samples obtained under similar measurement conditions. The standard uncertainty of the mole fraction z (which represents either x or y) is given as follows:

$$u(z) = \sqrt{\left[\left(\frac{\partial z}{\partial T}\right)u(T)\right]^2 + \left[\left(\frac{\partial z}{\partial p}\right)u(p)\right]^2 + \left[\left(\frac{\partial z}{\partial k}\right)u(k)\right]^2 + \left[\left(\frac{\partial z}{\partial R}\right)u(R)\right]^2} \quad 4.3$$

The symbols $u(T)$, $u(p)$, $u(k)$, and $u(R)$ represented the standard uncertainty of temperature, pressure, GC detector calibration response factor, and measured GC response peaks area ratios of two components, respectively. The standard uncertainties of the temperature and pressure sensors were estimated to be 0.1 K and 0.008 MPa, respectively, based on both the standard uncertainties of the sensors and the stability of temperature and pressure under equilibrium conditions. The uncertainty of the GC detector calibration response factor can be expressed as follows:

$$u(k) = \sqrt{\left[\left(\frac{\partial k}{\partial Z_R}\right)u(Z_R)\right]^2 + \left[\left(\frac{\partial k}{\partial R}\right)u(R)\right]^2} \quad 4.4$$

In Equations 4.3 and 4.4, $u(R)$ is determined through calculating the standard deviation of the measured area ratios during the VLE measurement and calibration process, respectively. The parameter $u(Z_R)$ represents the uncertainty in the molar ratio of CO_2 to HFC-32 for each gravimetrically prepared mixture used to calibrate the GC detector. The combined uncertainties associated with the injected masses of HFC-32 and CO_2 into the sample cylinders during gravimetric mixture preparation were also considered in $u(Z_R)$. Table 4.3 presents the standard uncertainty of the CO_2 mole fraction for the gravimetrically prepared mixtures, determined based on the method explained by Arami-Niya et al. [29], which varies between 0.0001 and 0.0004 CO_2 mole fraction. As reported in Table 4.5, the mole fraction uncertainties of the VLE data measured analytically range from 0.002 to 0.02 CO_2 mole fraction.

For the SFE measurement, the temperature and pressure measurements' experimental uncertainty assessment was detailed by Siahvashi et al. [16,17]. The standard uncertainties in the measured melting and freezing temperatures were estimated to be the standard deviation of the repeated measurements (in the range of ± 0.3 K) covering the standard uncertainty of the PRT sensors (0.05 K). The estimated standard uncertainty in pressure measurements was 0.02 MPa, calculated by taking temperature and pressure fluctuations into account. The standard uncertainty in the overall composition of the synthetic binary mixtures is mainly affected by the uncertainties in the injected volumes from the syringe pumps and the pure fluid densities under the syringe pumps' conditions. The standard uncertainties in the densities of the

pure samples in the syringe pumps' conditions were estimated to be around 1 % considering the temperature and pressure measurement uncertainties for the syringe pumps and using the Helmholtz energy equations of state implemented in REFPROP 10 [5,30]. The overall relative standard uncertainty associated with the syringe pumps' injected volumes was 0.3 % [22]. Considering all the mentioned uncertainties, the combined uncertainty in the overall composition of the mixtures used for the SFE measurements had an average of 0.01 CO_2 mole fraction.

4.3.7 Apparatus validation

The Paroscientific pressure sensor's readings for the pure N_2 gas at pressures between (0.1 and 23) MPa were validated against the values measured by a reference pressure transmitter (Mensor/Wika CPT9000). The Mensor CPT9000 pressure transmitter was calibrated and certified by the accredited Australian Pressure Laboratory over a pressure range of (0.1 and 41) MPa with a standard uncertainty of 0.004 MPa. The difference in the reading of the two pressure sensors for the investigated pressure range was within the standard uncertainties of the sensors.

Further validations of the apparatus involved comparing the measured vapour pressure of pure CO_2 at a temperature range of (240 to 300) K with those predicted by the CO_2 reference EOS developed by Span and Wagner [5]. Figure 4.5 shows the deviations between the measured pressure (p_{exp}) and the predicted pressure (p_{calc}) by the EOS while the measured temperatures were the input to the EOS. The deviations did not exceed the standard uncertainty of the experimental data.

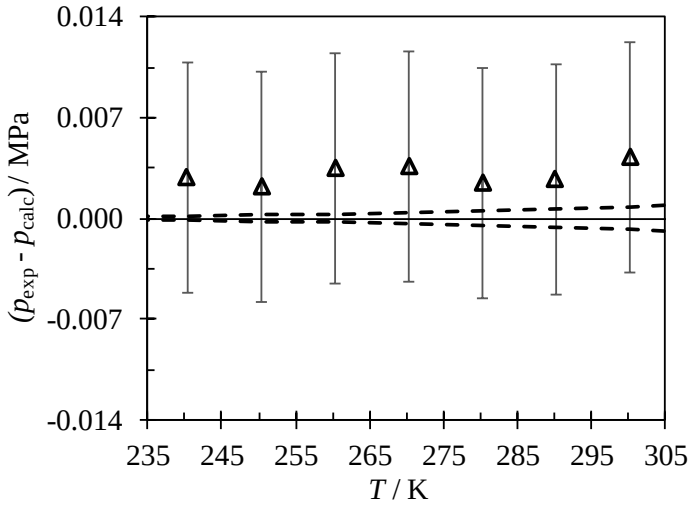

Figure 4.5: Deviation $\Delta p = (p_{exp} - p_{calc})$ between the experimental vapour pressure of pure CO_2 (p_{exp}) and the reference values (p_{calc}) from the Helmholtz EOS [5] as a function of the observed temperature (T): Δ, this work. The error bars show the standard uncertainty of the experimental data, while the dashed lines represent the uncertainty of the calculated CO_2 vapour pressures as specified by Span and Wagner [5].

To validate the visual melting point measurement method, the triple point of the pure CO_2 was measured to be 216.6 K at 0.53 MPa, which is in good agreement with the reference triple point temperature of 216.55 K at 0.518 MPa reported by Span and Wagner [5]. Additionally, the triple point temperature of pure HFC-32 was measured to be 135.3 K, around 1 K lower than the reported triple point temperatures by Di Nicola et al. [36] and Lüddecke and Magee [37]. Those studies used a visual evaluation of the experimental pressure-temperature profile for the fluid to locate the triple point of HFC-32 by noting a sharp break in the temperature rise rate, assuming the solid melting process was started. However, in this study, the triple points of the pure CO_2 and HFC-32 were measured visually when complete melting was observed, as shown in Figure 4.6.

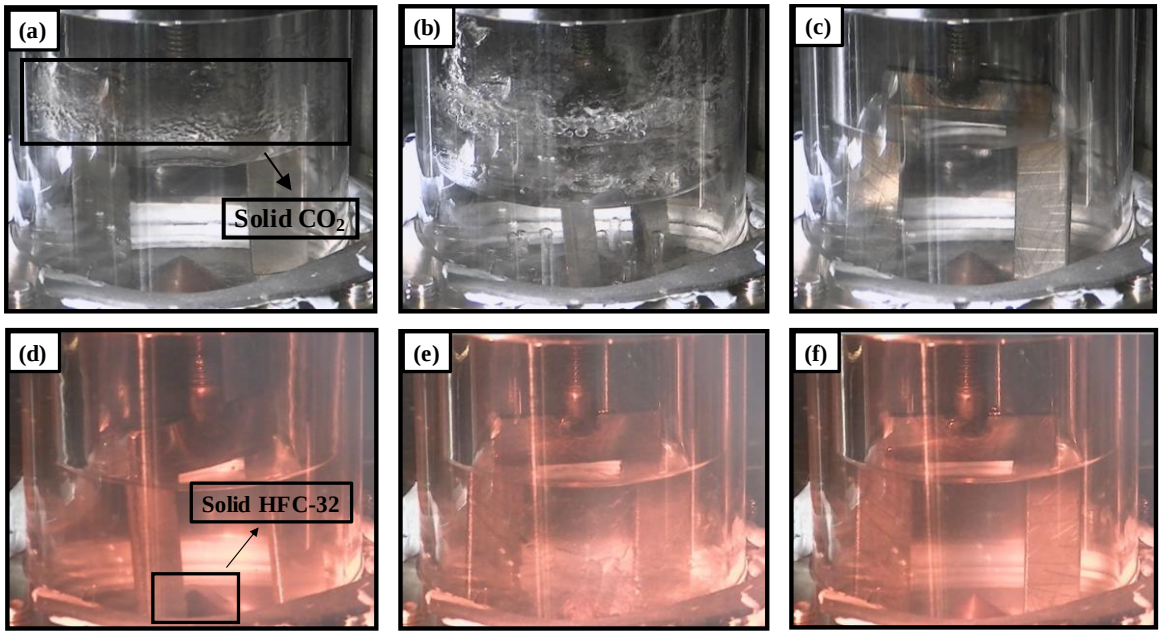

Figure 4.6: The triple point measurement procedure for pure CO_2 (a-c) and HFC-32 (d-f): (a) freezing point of CO_2 (p = 0.518 MPa, T = 215.7 K), (b) sub-freezing point (p = 0.48 MPa, T = 215.6 K), (c) melting point of CO_2 (p = 0.526 MPa, T = 216.6 K); (d) freezing point of HFC-32 (p = 0.02 MPa, T = 134.4 K), (e) sub-freezing point (p = 0.02 MPa, T = 134 K), (f) melting point of HFC-32 (p = 0.02 MPa, T = 135.3 K).

4.4 Thermodynamic modelling

In this work, the measured VLE data are compared with predictions of the Helmholtz energy EOS implemented in REFPROP 10 as these are the state-of-the-art models available for representing the thermodynamic properties of refrigerant mixtures. The Helmholtz EOS uses a multi-fluid Helmholtz-energy approximation to express the dimensionless reduced Helmholtz free energy ($\alpha = \frac{A}{(RT)}$) as a function of temperature (T), molar density (ρ) and molar composition vector ($\bar{x}$) [31]:

$$\alpha(\tau, \delta, \bar{x}) = \left[\sum_{i=1}^{N} x_i \{\alpha_i^{id}(T, \rho) + \ln x_i\}\right] + \left[\sum_{i=1}^{N} x_i \alpha_i^{r}(T, \delta) + \Delta\alpha^{r}(\tau, \delta, \bar{x})\right] \quad 4.5$$

$$\tau = \frac{T_r}{T} \text{ and } \delta = \frac{\rho}{\rho_r} \quad 4.6$$

Here, τ and δ represent the inverse reduced mixture temperature and density, respectively. The terms $\alpha_i^{id}(T, \rho)$, $\alpha_i^{r}(T, \delta)$ are the ideal-gas and residual parts of the reduced Helmholtz energy for the component i, and $\Delta\alpha^{r}(\tau, \delta, \bar{x})$ is the departure function. The reference Helmholtz EOSs

of Span and Wagner [5] for CO_2 and Tillner-Roth and Yokozeki [30] for HFC-32 were used to describe the thermodynamic properties of the pure components. The quantities T_r and ρ_r are determined from the composition-dependent reducing functions for the temperature and density of the mixture, which can be expressed as follows:

$$T_r(\bar{x}) = \sum_{i=1}^{N} x_i^2 T_{c,i} + \sum_{i=1}^{N-1} \sum_{j=i+1}^{N} 2x_i x_j \beta_{T,ij}\gamma_{T,ij} \cdot \frac{x_i + x_j}{\beta_{T,ij}^2 x_i + x_j} \cdot (T_{c,i} \cdot T_{c,j})^{1/2} \quad 4.7$$

$$\frac{1}{\rho_r(\bar{x})} = \sum_{i=1}^{N} x_i^2 \frac{1}{\rho_{c,i}} + \sum_{i=1}^{N-1} \sum_{j=i+1}^{N} 2x_i x_j \beta_{v,ij}\gamma_{v,ij} \cdot \frac{x_i + x_j}{\beta_{v,ij}^2 x_i + x_j} \cdot \frac{1}{8}\left(\frac{1}{\rho_{c,i}^{1/3}} + \frac{1}{\rho_{c,j}^{1/3}}\right)^3 \quad 4.8$$

Here $T_{c,i}$, $T_{c,j}$, $\rho_{c,i}$, $\rho_{c,j}$, x_i and x_j stand for the critical temperature, critical density and mole fractions of components *i* and *j*. The constants of $\beta_{T,ij}$, $\gamma_{T,ij}$, $\beta_{v,ij}$, and $\gamma_{v,ij}$ are four independent binary interaction parameters (BIPs) that can be adjusted if sufficient sets of experimental data for a wide range of conditions are available; otherwise, they are set to unity. In this work, a Helmholtz EOS for the HFC-32 + CO_2 binary system, tuned by Arami-Niya et al. [13] to the available experimental thermodynamic data (mostly at atmospheric or higher temperatures), was used to represent the VLE data measured in this work at cryogenic conditions.

At SFE the fugacity of the CO_2 fraction in the fluid mixture is equal to the fugacity of CO_2 in the solid phase:

$$f_{CO2}^{S}(p,T) = f_{CO2}^{\text{fluid}}(p,T,z_{CO2}) \quad 4.9$$

Here, z_{CO2} is the CO_2 mole fraction in the fluid mixture. The fugacity of pure solid CO_2 may be calculated the reference Helmholtz EOS for the CO_2 solid phase (I) developed by Trusler [18] as follows:

$$f_{CO2}^{S}(p,T) = f_{CO2}^{\text{fluid}}\left(p_{eq},T,z_{CO2}\right) \cdot Exp\left(\frac{G(p,T) - G\left(p_{eq},T\right)}{RT}\right) \quad 4.10$$

$$G(p,T) = A(p,T) + pv \quad 4.11$$

where R is the universal gas constant, p_{eq} is equilibrium pressure for CO_2 solid at the experimental temperature T, and $G(p,T)$ represents the molar Gibbs energy of the pure solid

CO_2 at the melting point of p and T. The molar Helmholtz energy, $A(p,T)$, can be used to calculate the molar Gibbs energy by Equation 4.11, where v and p are the molar volume and pressure at the melting point. The term f_{CO2}^{fluid} is calculated using the cubic equation of state proposed by Peng and Robinson [32] in 1976 (PR-EOS). The PR-EOS correlated pressure, temperature and volume as follows [32]:

$$p = \frac{RT}{v-b} - \frac{a}{v^2 + 2bv - b^2} \qquad 4.12$$

Here, v is the molar volume and parameters a and b represent the temperature-dependent energy and co-volume parameters, respectively. The van der Waals one-fluid mixing rules that incorporate a single temperature-independent BIP (k_{ij}) can be used to correlate the mixtures' thermodynamic properties.

$$a = \sum_i \sum_j x_i x_j (1 - k_{ij}) \sqrt{a_i a_j} \qquad 4.13$$

$$b = \sum_i x_i b_i \qquad 4.14$$

This SFE model was implemented in the software package ThermoFAST, which has a default BIP (k_{ij}) of zero for the HFC-32 + CO_2 binary systems. This BIP was adjusted by regression to the experimental SFE data measured in this work. The best-fit value of the BIP was determined by minimising the root mean square deviation (RMSD) of the experimental (T_{exp}) and calculated (T_{calc}) melting temperatures as follows:

$$RMSD_T = \sqrt{\frac{\sum_{i=1}^{N} \left[T_{exp,i} - T_{calc,i}\right]}{N}} \qquad 4.15$$

Here, N is the total number of the points used in optimising the BIP and $\underline{i}$ stands for an individual data point.

4.5 Results and discussion

4.5.1 VLE measurement data

The VLE analysis of the HFC-32 + CO_2 binary system was conducted at three temperatures of (273, 238 and 223) K. Table 4.5 presents the average values for the measured temperature, pressure, and composition of the liquid and vapour phases at each equilibrium condition. Figure 4.7 shows the experimental pressure and composition data together with the predictions of the tuned Helmholtz energy model of Arami Niya et al. [13].

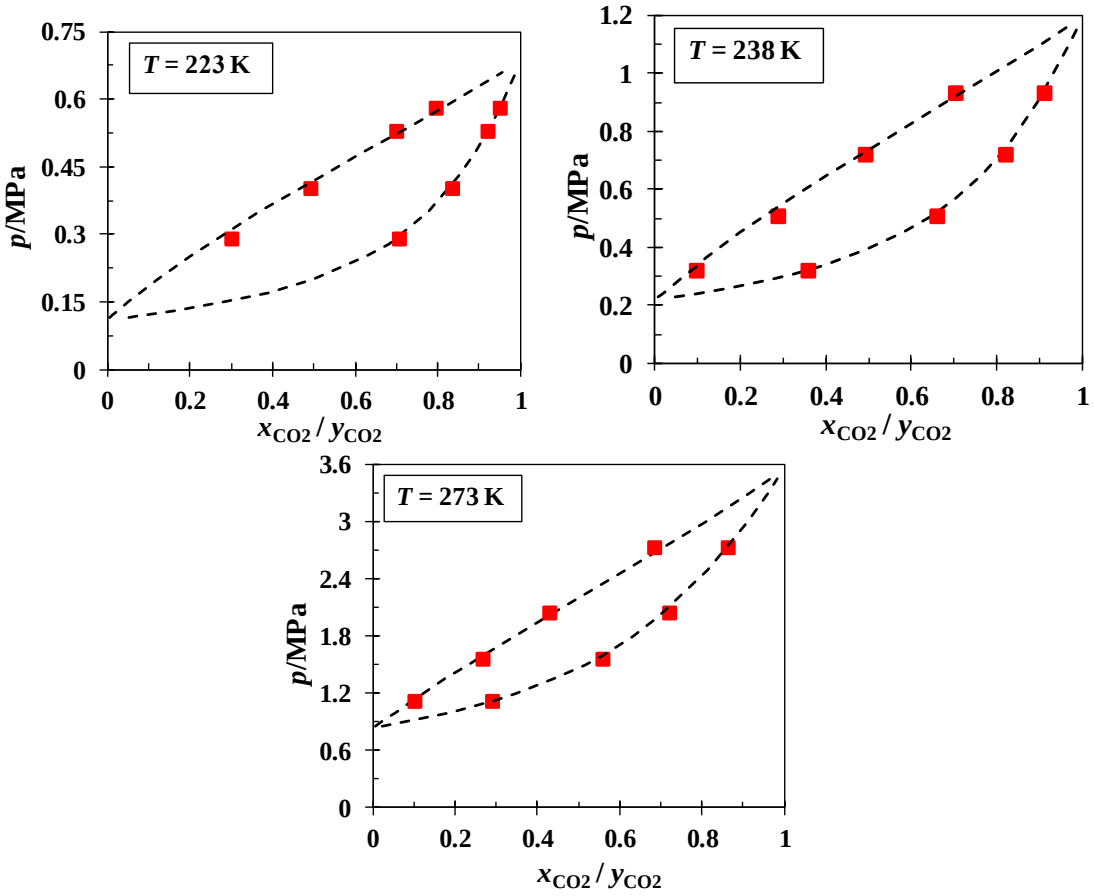

Figure 4.7: VLE results and phase envelopes of the HFC-32 + CO_2 binary system at (223, 238 and 273) K: (---) REFPROP (Helmholtz energy model [13]) predicted phase envelope, ■ experimental bubble and dew points.

Table 4.5: Experimental liquid (x_{exp}) and vapour (y_{exp}) phase mole fractions of CO_2 in binary mixtures with HFC-32 mixtures together with the calculated values (x_{calc} and y_{calc}) by the Helmholtz EOS [13] at equilibrium temperatures (T) and pressures (p)*.

T/K	p/MPa	x_{exp}	y_{exp}	$u(x)$**	$u(y)$**	x_{calc}	y_{calc}	x_{exp} - x_{calc}	y_{exp} - y_{calc}
274.0	1.112	0.1063	0.2935	0.0031	0.0071	0.0918	0.2805	0.0145	0.0130
273.9	1.558	0.2720	0.5617	0.0039	0.0046	0.2527	0.5406	0.0192	0.0211
273.8	2.036	0.4345	0.7265	0.0045	0.0034	0.4362	0.7043	-0.0017	0.0222
273.8	2.723	0.6895	0.8687	0.0046	0.0024	0.7052	0.8602	-0.0157	0.0085
238.2	0.318	0.0986	0.3582	0.0069	0.0209	0.0784	0.3391	0.0202	0.0191
238.2	0.505	0.2885	0.6621	0.0083	0.0090	0.2500	0.6401	0.0385	0.0220
238.2	0.718	0.4937	0.8206	0.0096	0.0052	0.4713	0.8029	0.0224	0.0177
238.3	0.929	0.7053	0.9110	0.0098	0.0037	0.7022	0.9022	0.0030	0.0088
223.2	0.288	0.3039	0.7080	0.0138	0.0134	0.2607	0.6932	0.0432	0.0148
223.3	0.400	0.4943	0.8389	0.0156	0.0076	0.4591	0.8248	0.0352	0.0141
223.2	0.527	0.7007	0.9246	0.0162	0.0051	0.7075	0.9188	-0.0068	0.0057
223.1	0.578	0.7987	0.9517	0.0159	0.0045	0.8123	0.9498	-0.0135	0.0019

* The standard uncertainties in temperature, $u(T)$, and pressure, $u(p)$, are 0.1 K and 0.008 MPa, respectively.
** The average experimental uncertainty for the VLE data measured analytic was a CO_2 mole fraction of 0.008.

4.5.1.1 Thermodynamic consistency

The measured VLE data for the HFC-32 + CO_2 binary system were assessed for thermodynamic consistency using the point test method described by Fredesnlund et al. [33–35]. The following statistics were calculated to determine the consistency of the VLE data:

$$\Delta y_i = (y_{\mathrm{exp},i} - y_{\mathrm{calc},i}) \tag{4.16}$$

$$\overline{\Delta y_i} = \frac{1}{N}\sum_{i=1}^{N} \Delta y_i \tag{4.17}$$

$$\mathrm{AAD}y_i = \frac{1}{N}\sum_{i=1}^{N} |\Delta y_i| \tag{4.18}$$

$$\mathrm{STD}\Delta y_i = \sqrt{\frac{1}{N}\sum_{i=1}^{N} [\Delta y_i - \overline{\Delta y_i}]^2} \tag{4.19}$$

The default Helmholtz energy model implemented in REFPROP 10 was used to calculate the values of y_{calc} based on the experimental temperature and liquid phase composition as the inputs to the model. Fredenslund et al. [34,35] used polynomial expansions to determine activity coefficients needed to estimate y_{calc} and consider a VLE data set thermodynamically consistent

if the AADy_i is less than or equal to 0.01 mole fraction of the component *i*. However, in this work, a Helmholtz EOS was used to calculate y_{calc} and AADy_i for each isotherm of the measured VLE data, presented in Table 4.6. The AADy_i is less or equal to 0.01 for all isothermal data sets. Additionally, thermodynamically consistent VLE data will have a smooth trend of deviation from the y_{calc} with pressure. The STDΔy_i values quantifies the dispersion of the data and their smoothness. For each isotherm, the STDΔy_i is less or comparable with the estimated experimental uncertainty, indicating that the measured VLE data all satisfy this thermodynamic consistency test.

Table 4.6: The thermodynamic consistency test results for the HFC-32 + CO_2 binary systems.

	Helmholtz energy EOS	
T/K	STDΔy_{CO2}	AADy_{CO2}
273	0.008	0.010
238	0.006	0.004
223	0.007	0.005
Average (all VLE data)	0.007	0.006

4.5.1.2 Comparison with Helmholtz energy EOS

Figure 4.8 (a)-(b) shows the differences between the experimental liquid and vapour compositions of the equilibrium HFC-32 + CO_2 mixtures measured in this work together with the data reported by Adams et al. [11], Rivollet et al. [12] and Arami Niya et al. [13] from the tuned Helmholtz energy EOS's calculated values [13]. The abscissa and ordinates in these plots are the experimental equilibrium pressure and the differences between the measured and predicted mole fractions of CO_2, respectively. The overall experimental composition of the binary mixture was used as input to perform the flash calculations at the corresponding measured temperature and pressure and compute the mole fractions for each phase. The average RMSD of all VLE points from the Helmholtz EOS calculations was around 0.02 CO_2 mole fraction, 2.5 times larger than the average experimental uncertainty. In general, the deviations from the model decrease with pressure. Additionally, the deviations are smaller for dew points than they are for bubble points. These deviations indicate a need to further optimise the predictions of the Helmholtz model to accurately describe this binary system's VLE at low temperatures. However, before such tuning is implemented, it would be advisable to acquire single-phase density data at similar low temperatures to ensure that any further adjustment of the BIPs do not cause a deterioration of the model's predictions for other properties.

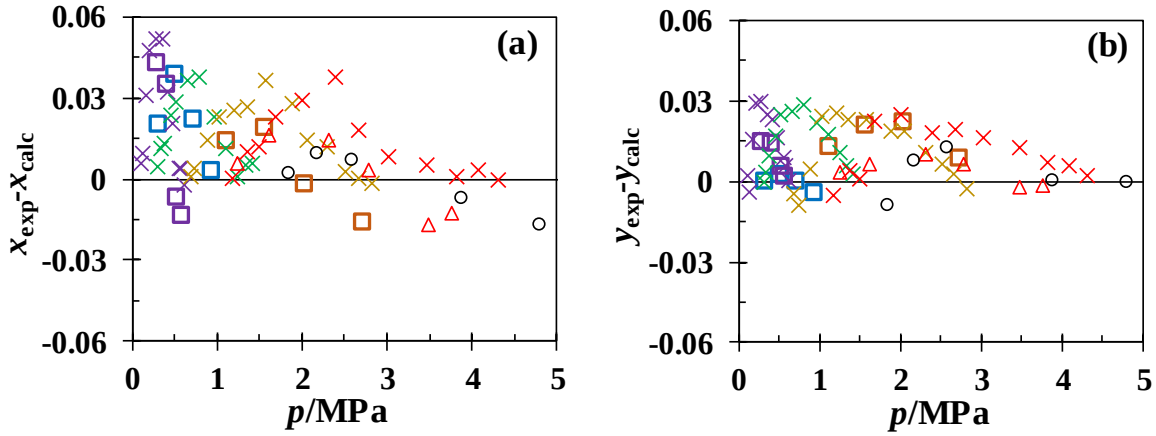

Figure 4.8: Absolute differences between the measured mole fraction (x_{exp}, y_{exp}) and the predicted values (x_{calc}, y_{calc}) by the tuned Helmholtz energy EOS [13] for the component (CO_2) of the HFC-32 + CO_2 binary system: □ this work, × Adams et al. [11], Δ Rivollet et al. [12] and ○ Arami Niya et al. [13]; equilibrium temperature: purple (T = 223 K), blue (T = 238 K), green (T = 244 K), gold (T = 266 K), brown (T = 273 K), red (T = 283 K) and black (T = 293 K).

4.5.2 SFE measurement data

The melting and freezing temperatures of the HFC-32 + CO_2 binary system were measured for mixtures with CO_2 compositions between (0 and 100) mol%. Table 4.7 presents the average freezing and melting temperatures and pressures at different overall compositions of the binary mixtures measured in this study.

Table 4.7: Measured SFE data for the HFC-32 + CO_2 binary mixtures at different CO_2 mole fractions and operating pressures*.

Phase	X_{HFC-32}	x_{CO2}	T_f /K	p_f /MPa	T_m /K	p_m /MPa
SLVE	0.00	1.00	216.0	0.518	216.6	0.53
SLVE	0.05	0.95	214.2	0.461	214.9	0.47
SLVE	0.10	0.90	212.1	0.405	212.6	0.41
SLVE	0.15	0.85	209.2	0.350	210.2	0.36
SLVE	0.20	0.80	207.1	0.299	208.0	0.31
SLVE	0.28	0.72	201.3	0.203	201.9	0.21
SLE	0.28	0.72	203.0	8.090	203.7	8.09
SLE	0.28	0.72	204.2	11.083	204.5	11.08
SLVE	0.49	0.51	186.2	0.060	187.5	0.07
SLE	0.49	0.51	187.7	8.083	189.2	8.09
SLE	0.49	0.51	187.3	11.063	189.7	11.07
SLVE	0.72	0.28	162.4	0.02**	165.5	0.02**
SLE	0.72	0.28	161.3	8.062	166.3	8.07
SLE	0.72	0.28	165.0	11.006	167.1	11.05
SLVE	0.89	0.11	128.9	0.02**	131.9	0.02**
SLE	0.89	0.11	129.9	8.062	132.7	8.09
SLE	0.89	0.11	130.9	11.064	133.0	11.07
SLVE	1.00	0.00	134.4	0.02**	135.3	0.02**

* The standard uncertainties in temperature, $u(T)$, pressure, $u(p)$, and CO_2 mole fractions, $u(z_{CO2})$, are 0.3 K, 0.02 MPa, and 0.01, respectively.

** The resolution limit of the pressure measurement is 0.02 MPa when performing cooling/heating ramps. The actual pressure is likely to be close to the vapour pressure of HFC-32.

At the SLVE, the freezing and melting temperatures were measured isochorically at the vapour pressure of the mixture, while at the SLE, the measurements were carried out isobarically at pressures of (8 and 11) MPa. Figure 4.9 (a)-(c) show the freezing and melting measurements for the HFC-32 + CO_2 (72:28 mol%) mixture at SLVE, and Figure 4.9 (d)-(f) shows the measurements at 8 MPa when the mixture was at SLE. The HFC-32 + CO_2 binary systems generally needed an average sub-cooling (cooling the sample below the melting temperature) of 1.7 K to initiate solid formation.

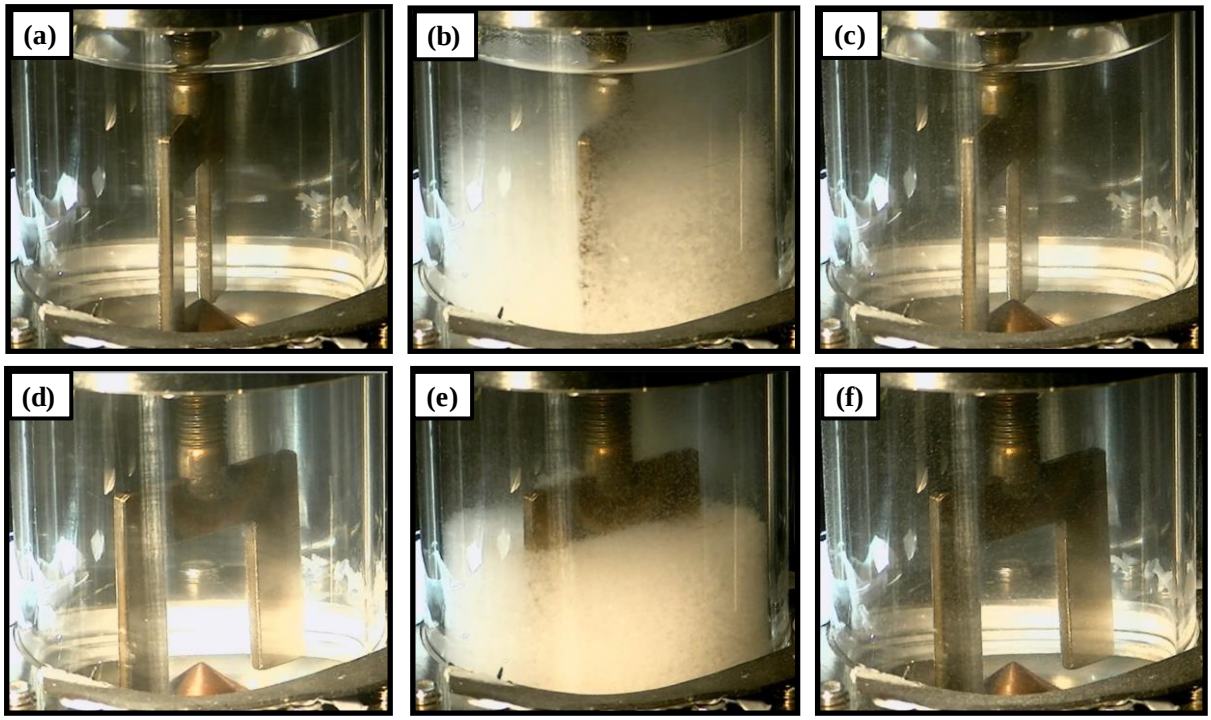

Figure 4.9: The freezing and melting points measurement for the HFC-32 + CO_2 (72:28 mol%) at the SLVE (a)-(c) and SLE (d)-(f) conditions: (a) sub-cooled VLE (p = 0.02 MPa, T = 162.4 K); (b) freezing point – SLVE (p = 0.02 MPa, T = 162.4 K); and (c) melting point – SLVE (p = 0.02 MPa, T = 165.5 K); (d) sub-cooled liquid (p = 8.1 MPa, T = 161.3 K); (e) freezing point – SLE (p = 8.1 MPa, T = 161.3 K); and (f) melting point – SLE (p = 8.1 MPa, T = 166.3 K).

Figure 4.10 shows the melting temperature of solids in the HFC-32 + CO_2 binary system against the different CO_2 compositions measured in this work, together with the reported data by Di Nicola et al. [7]. The melting temperature of CO_2 decreased from (216.6 to 165.5) K with the addition of 72 mol% HFC-32 to the pure CO_2 sample. Increasing the fraction of HFC-32 to 89 mol% resulted in complete freezing of the fluid phase at temperatures below 129 K, with complete melting of the solids achieved at 131.9 K under SLVE. This melting temperature is lower than pure HFC-32 (135.3 K) and CO_2 (216.6 K) melting temperatures, showing the presence of a eutectic [7].

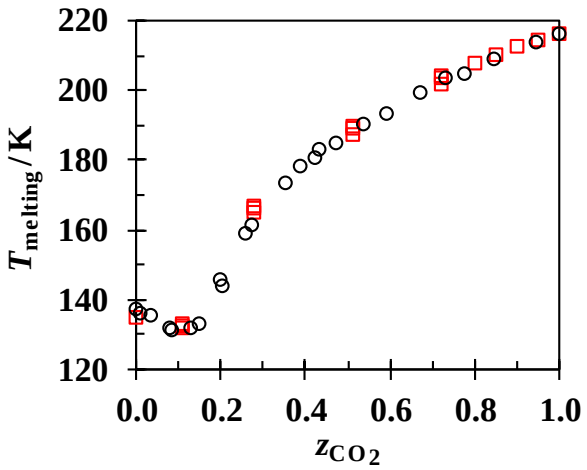

Figure 4.10: The temperature-composition (T-z_{CO2}) diagram for the experimental melting points of the CO_2 in the HFC-32 + CO_2 binary system: this work (□); Di Nicola et al. [7] (○).

4.5.2.1 Model tuning

Figure 4.11 (a) shows the measured melting points for the HFC-32 + CO_2 binary system, together with the predictions of the default ThermoFAST model. The melting data measured at SLVE (Figure 4.11 (b)) follow the pure CO_2 sublimation curve. Using its default BIP of zero in the PR-EOS for the HFC-32 + CO_2 binary system the untuned ThermoFAST model represented the measured melting points with an RMSD of 7.3 K. Additionally, the Helmholtz energy EOS [13] was used for the fluid phase calculations in the ThermoFAST model along with the Helmholtz EOS for the CO_2 solid phase [18], resulting in an RMSD of 9.1 K from the measured melting data. In this study, the ThermoFAST model with PR-EOS for the fluid phase was tuned to the measured SFE data (the melting temperatures). The measured freezing temperatures cannot be used for this purpose due to the stochastic nature of nucleation.

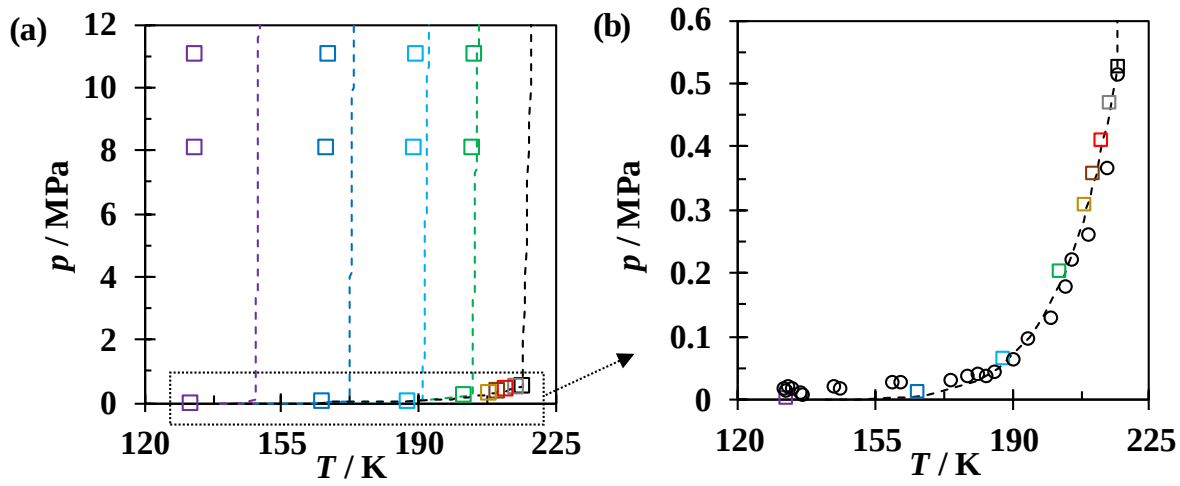

Figure 4.11: (a) The pressure-temperature (P-T) data for the melting points of the HFC-32 + CO_2 binary system. The insert (b) shows the SLVE data, together with the reported data by Di Nicola et al. [7]: this work (□), Di Nicola et al. [7] (○) --- melting temperature predicted by ThermoFAST using the default BIP of zero; compositions: black (100 mol% CO_2), grey (95 mol% CO_2), red (90 mol% CO_2), brown (85 mol% CO_2), yellow (80 mol% CO_2), green (72 mol% CO_2), light-blue (51 mol% CO_2), dark-blue (28 mol% CO_2), purple (11 mol% CO_2).

Tuning the model to the measured melting data by adjusting the BIP decreased the RMSD by 60 %, from (7.3 to 3) K, with an optimised BIP of (k_{ij} = -0.024). Figure 4.12 shows the differences between the experimental melting points and predicted values by the default and tuned ThermoFAST models. In this plot, the abscissa is the CO_2 mole fraction in the HFC-32 + CO_2 mixture and the ordinate is the difference between the measured and calculated equilibrium melting temperatures. For mixtures with the CO_2 fraction over 11 mole% (eutectic composition), the tuned model represents the melting point data with an RMSD of 0.5 K that is 87 % lower than the default model. For the eutectic composition (11 mol% CO_2), the tuned model correlated the melting temperature of the mixture with an RMSD of 7.6 K against the default model's RMSD of 16.3 K. Finally, the RMSD of the model calculations from the experimental melting point data reported by Di Nicola et al. [7] was improved by 46 %, from (9.1 to 4.9) K, by this optimisation.

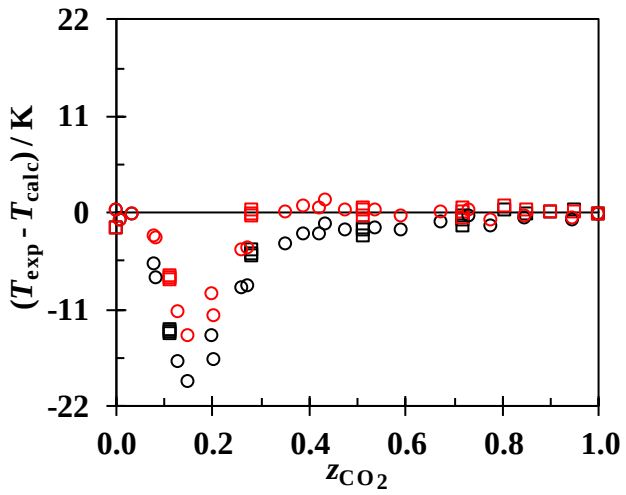

Figure 4.12: Absolute difference between the measured melting temperature (T_{exp}) and correlated values (T_{calc}) by the default (black) and tuned (red) ThermoFAST models for the HFC-32 + CO_2 binary system: this work (□), Di Nicola et al. [7] (○).

4.6 Conclusions

A new set of experimental vapour-liquid equilibrium (VLE) data for the HFC-32 + CO_2 binary system is reported at equilibrium temperatures between (223 and 273) K and pressures between (0.3 and 2.7) MPa. Data presented in this study and the literature data were compared with the predictions of a Helmholtz free energy model with the binary interaction parameters tuned by Arami-Niya et al. [13]. The tuned Helmholtz EOS represented dew point data better than the bubble points, with the deviations between the measured and calculated mole fractions for both phases being about 2.5 times larger than the average experimental uncertainty. These deviations decrease with increasing pressure and temperature.

New solid-fluid equilibrium (SFE) data for the HFC-32 + CO_2 binary system were also measured at CO_2 concentrations between (0 and 100) mol%. The experimental data reported in this study and the literature data show a eutectic composition of around 11 mol% CO_2 with a eutectic temperature of 131.9 K at an SLVE condition. The measured melting data were compared with the predictions of a thermodynamic model using the Peng-Robinson EOS with van der Waals one-fluid mixing rules for the fluid phase and a reference Helmholtz EOS for the CO_2 solid phase. The binary interaction parameter of the model was adjusted by fitting to the measured melting data. The tuned model represented the melting data with an RMSD of 3.2 K, 60 % better than the default model. The RMSD for the mixtures with the CO_2 fractions over 11 mol% was 0.5 K for the tuned model against an RMSD of 3.4 K for the default model. This work provides new VLE and SFE data for the HFC-32 + CO_2 binary system that will help

design refrigeration systems utilising eco-friendly refrigerant mixtures with up to 80 % less GWP than currently-used working fluids.

4.7 References

[1] Change IP on C. Anthropogenic and natural radiative forcing. In: Intergovernmental Panel on Climate Change, editor. Clim. Chang. 2013 Phys. Sci. Basis Work. Gr. I Contrib. to Fifth Assess. Rep. Intergov. Panel Clim. Chang., vol. 9781107057, Cambridge: Cambridge University Press; 2013, p. 659–740. doi:10.1017/CBO9781107415324.018.

[2] Sadaghiani MS, Arami-Niya A, Zhang D, Tsuji T, Tanaka Y, Seiki Y, et al. Minimum ignition energies and laminar burning velocities of ammonia, HFO-1234yf, HFC-32 and their mixtures with carbon dioxide, HFC-125 and HFC-134a. J Hazard Mater 2021;407:124781. doi:10.1016/j.jhazmat.2020.124781.

[3] Chernyak Y, Zhelezny P, Paulaitis M. Thermodynamic Properties of HFC-32 / HFC-125 Mixtures and an Estimation of Its Environmental Impact and Utility in Refrigeration. Int Refrig Air Cond Conf 1996;360. doi:http://docs.lib.purdue.edu/iracc/360.

[4] UNEP. The Kigali Amendment to the Montreal Protocol: HFC Phase-down. 28th Meet Parties to Montr Protoc 10-14 October, 2016, Kigali, Rwanda 2016:1–7.

[5] Span R, Wagner W. A new equation of state for carbon dioxide covering the fluid region from the triple-point temperature to 1100 K at pressures up to 800 MPa. J Phys Chem Ref Data 1996;25:1509–96. doi:10.1063/1.555991.

[6] Meyers C, Van Dusen M. The vapor pressure of liquid and solid carbon dioxide. Bur Stand J Res 1933;10:381–412.

[7] Di Nicola G, Giuliani G, Polonara F, Stryjek R. Solid-liquid equilibria for the CO2 + N2O, CO2 + R32, and N2O + R32 systems. Fluid Phase Equilib 2007;256:86–92. doi:10.1016/j.fluid.2006.11.015.

[8] Di Nicola G, Polonara F, Stryjek R. Burnett measurements for the difluoromethane + carbon dioxide system. J Chem Eng Data 2002;47:876–81. doi:10.1021/je015537m.

[9] Nicola G Di, Pacetti M, Polonara F, Stryjek R. Isochoric Measurements for CO 2 + R125 and CO 2 + R32 Binary Systems 2002. doi:10.1021/je015541y.

[10] Diefenbacher A, Türk M. (Vapour + liquid) Equilibria of binary mixtures of CO2, CH2F2, CHF3, and SF6. J Chem Thermodyn 2002;34:1361–75. doi:10.1016/S0021-9614(02)00123-4.

[11] Adams RA, Stein FP. Vapor-Liquid Equilibria for Carbon Dioxide-Difluoromethane System. J Chem Eng Data 1971;16:146–9. doi:10.1021/je60049a015.

[12] Rivollet F, Chapoy A, Coquelet C, Richon D. Vapor-liquid equilibrium data for the carbon dioxide (CO2) + difluoromethane (R32) system at temperatures from 283.12 to 343.25 K and pressures up to 7.46 MPa. Fluid Phase Equilib 2004;218:95–101. doi:10.1016/j.fluid.2003.12.002.

[13] Arami-Niya A, Xiao X, Al Ghafri SZS, Jiao F, Khamphasith M, Sadeghi Pouya E, et al. Measurement and modelling of the thermodynamic properties of carbon dioxide mixtures with HFO-1234yf, HFC-125, HFC-134a, and HFC-32: vapour-liquid equilibrium, density, and heat capacity. Int J Refrig 2020;118:514–28. doi:10.1016/J.IJREFRIG.2020.05.009.

[14] S. Sadaghiani M, Arami-Niya A, Marsh B, Z.S. Al Ghafri S, F. May E. Vapor–Liquid Equilibria for Carbon Dioxide + 3,3,3-Trifluoropropene Binary Mixtures at Temperatures between (288 and 348) K. J Chem & Eng Data 2021;0. doi:10.1021/acs.jced.1c00297.

[15] Lemmon EW, Bell IH, Huber ML, McLinden MO. NIST Standard Reference Database 23: Reference Fluid Thermodynamic and Transport Properties-REFPROP, Version 10.0; National Institute of Standards and Technology. Https://WwwNistGov/Srd/Ref 2018.

[16] Siahvashi A, Al Ghafri SZ, May EF. Solid-fluid equilibrium measurements of benzene in methane and implications for freeze-out at LNG conditions. Fluid Phase Equilib 2020;519:112609. doi:10.1016/j.fluid.2020.112609.

[17] Siahvashi A, Al Ghafri SZS, Yang X, Rowland D, May EF. Avoiding costly LNG plant freeze-out-induced shutdowns: Measurement and modelling for neopentane solubility at LNG conditions. Energy 2021;217:119331. doi:10.1016/j.energy.2020.119331.

[18] Martin Trusler JP. Equation of State for Solid Phase I of Carbon Dioxide Valid for Temperatures up to 800 K and Pressures up to 12 GPa. J Phys Chem Ref Data 2011;40. doi:10.1063/1.3664915.

[19] The University of Western Australia FS and R. ThermoFAST 1.2.1: thermodynamic calculator for natural gas properties. 2019.

[20] Siahvashi A, Al-Ghafri SZS, Oakley JH, Hughes TJ, Graham BF, May EF. Visual Measurements of Solid-Liquid Equilibria and Induction Times for Cyclohexane + Octadecane Mixtures at Pressures to 5 MPa. J Chem Eng Data 2017;62:2896–910. doi:10.1021/acs.jced.7b00171.

[21] Siahvashi A. Visual Measurements of Solid-Fluid Equilibria in Hydrocarbon Mixtures for Enhanced LNG Production 2019.

[22] Siahvashi A, Al Ghafri SZ, May EF. Solid-fluid equilibrium measurements of benzene in methane and implications for freeze-out at LNG conditions. Fluid Phase Equilib 2020;519:112609. doi:10.1016/j.fluid.2020.112609.

[23] Siahvashi A, Al Ghafri SZ, Hughes TJ, Graham BF, Huang SH, May EF. Solubility of p-xylene in methane and ethane and implications for freeze-out at LNG conditions. Exp Therm Fluid Sci 2019;105:47–57. doi:10.1016/J.EXPTHERMFLUSCI.2019.03.010.

[24] Guilbot P, Valtz A, Legendre H, Richon D. Rapid on-line sampler-injector: A reliable tool for HT-HP sampling and on-line GC analysis. Analusis 2000;28:426–31. doi:10.1051/analusis:2000128.

[25] Richon D. Method and device for taking micro samples from a pressurized fluid contained in a container. Organisation Mondiale De La Propriete Intellectuelle (Bureau International), Publication No FR2853414B1, 2003.

[26] Davis RS. Equation for the determination of the density of moist air (1981/91). Metrologia 1992;29:67–70. doi:10.1088/0026-1394/29/1/008.

[27] Lemmon, E. W.; Bell, I. H.; Huber, M. L.; McLinden, M. O. NIST Standard Reference Database 23: Reference Fluid Thermodynamic and Transport Properties-REFPROP, Version 10.0; National Institute of Standards and Technology, 2018; https://www.nist.gov/srd/ref n.d.

[28] Joint Committee For Guides In. Evaluation of measurement data — Guide to the expression of uncertainty in measurement. Int Organ Stand Geneva ISBN 2008;50:134. doi:10.1373/clinchem.2003.030528.

[29] Arami-Niya A, Xiao X, Al Ghafri SZS, Jiao F, Khamphasith M, Sadeghi Pouya E, et al. Measurement and modelling of the thermodynamic properties of carbon dioxide mixtures with HFO-1234yf, HFC-125, HFC-134a, and HFC-32: vapour-liquid equilibrium, density, and heat capacity. Int J Refrig 2020;118:514–28. doi:10.1016/j.ijrefrig.2020.05.009.

[30] Tillner-Roth R, Yokozeki A. An International Standard Equation of State for Difluoromethane (R-32) for Temperatures from the Triple Point at 136.34 K to 435 K and Pressures up to 70 MPa. J Phys Chem Ref Data 1997;26:1273–328. doi:10.1063/1.556002.

[31] Souza LFS, Al Ghafri SZS, Trusler JPPM. Measurement and modelling of the vapor–liquid equilibrium of (CO2 + CO) at temperatures between (218.15 and 302.93) K at pressures up to 15 MPa. J Chem Thermodyn 2018;126:63–73. doi:10.1016/j.jct.2018.06.022.

[32] Peng D-Y, Robinson DB. A New Two-Constant Equation of State. Ind Eng Chem Fundam 1976;15:59–64. doi:10.1021/i160057a011.

[33] Wisniak J, Ortega J, Fernández L. A fresh look at the thermodynamic consistency of vapour-liquid equilibria data. J Chem Thermodyn 2017;105:385–95. doi:10.1016/J.JCT.2016.10.038.

[34] Fredenslund A, Gmehling J, Rasmussen P. Vapor-liquid Equilibria Using UNIFAC. Elsevier Ltd; 1977. doi:https://doi.org/10.1016/B978-0-444-41621-6.50009-0.

[35] Christiansen LJ, Fredenslund A. Thermodynamic consistency using orthogonal collocation or computation of equilibrium vapor compositions at high pressures. AIChE J 1975;21:49–57. doi:10.1002/aic.690210105.

[36] Nicola G Di, Brandoni C, Nicola C Di, Giuliani G. Triple point measurements for alternative refrigerants. J Therm Anal Calorim J Therm Anal Calorim 2012;108:627–31. doi:10.1007/s10973-011-1944-4.

[37] Lüddecke TO, Magee JW. Molar heat capacity at constant volume of difluoromethane (R32) and pentafluoroethane (R125) from the triple-point temperature to 345 K at pressures to 35 MPa. Int J Thermophys 1996;17:823–49. doi:10.1007/bf01439192.

5 Chapter 5 | Prediction of Solid Formation Conditions in Mixed Refrigerants with iso-Pentane and Methane at High Pressures and Cryogenic Temperatures

Forward – The full text of this chapter has been published in the *International Journal of Energy* in 2022 (DOI: https://doi.org/10.1016/j.energy.2022.123789). It has been reformatted with minor amendments to fit the style and structure of this thesis.

5.1 Abstract

High boiling-point components in mixed refrigerants can improve the performance of natural gas and hydrogen liquefaction facilities. However, such heavy compounds can freeze out from the refrigerant mixture, posing blockage and plant shutdown risks for cryogenic heat exchangers. To improve the predictions of these conditions, freezing and melting temperatures of pure iso-pentane and (methane + iso-pentane) binary systems were measured at temperatures down to 87.5 K and pressures up to 13 MPa. The iso-pentane melting data are compared with predictions of a thermodynamic model embedded in the ThermoFAST software package. Adjusting the model's fusion molar volume change parameter to force agreement with the measurements reduced the deviations of the experimental data from the model by over 90 % relative to the default parameter value. The measured melting data for binary mixtures were used to confirm solubility predictions for iso-pentane in mixed refrigerants. Adding 20 mol% iso-pentane to a methane-rich refrigerant increases the available duty for cooling natural gas or hydrogen from (313 to 123) K by a factor of three. This improvement outweighs the risk of freeze-out in this refrigerant with the melting temperature being 98 K, which is 15 K lower than the minimum temperature needed for LNG production.

5.2 Introduction

Liquefied natural gas (LNG) can help drive global decarbonisation efforts by displacing emissions from coal, particularly as hydrogen and green technologies are developed commercially and at scale [1]. The increased global demand for cleaner energy carriers has considerably enhanced LNG's potential to overtake coal in the overall market by 2035 [2,3]. However, the liquefaction process is energy-intensive with a large amount of power required

for treatment, compression and, particularly, refrigeration processes [4]. Mixed refrigerant (MR) liquefaction systems have high thermodynamic efficiencies because their composition can be adjusted to match closely system cooling curves [5]. Using high boiling-point components like iso-butane and iso-pentane in mixed refrigerants can also increase the refrigerant mixture's enthalpy of vaporisation and promote latent heat transfer from the gas to the coolant over wider ranges of temperature, reducing the refrigerant circulation rate. This can result in smaller equipment size, higher liquefaction efficiency, and ultimately reduced operating and capital costs [6–10]. In sophisticated applications, mixed refrigerants may start as a single-phase fluid which is then flashed through several stages of the liquefaction process, delivering heavy and light mixtures with tuneable boiling points [11]. This dynamic control of the cooling curve inside the primary heat exchanger improves the energy efficiency and decreases the LNG production costs.

However, the presence of high-boiling components such as iso-pentane in the MR inherently poses a potential risk of freeze-out and/or blockage in the cryogenic sections of the heat exchanger, with the potential for inefficient operations, unwanted plant shutdowns or even equipment damage. Such risks are similar to those caused by the freeze-out of trace impurities such as heavy hydrocarbons, water, and CO_2 [12–16] within the process stream during natural gas liquefaction. To understand and thereby avoid these risks in both cases, accurate thermodynamic models are crucial for estimating heavy compound concentration limits at cryogenic pressures and temperatures [17]. Reliable and relevant solid−fluid equilibrium (SFE) data for pure and multi-component mixtures (including MR systems) are needed to verify and/or improve the prediction of the thermodynamic models used for such calculations.

Table 5.1 presents a literature survey of the fusion and melting property data for pure iso-pentane. These data give an average normal melting temperature for pure iso-pentane of 113.1 K with a standard deviation of 0.4 K, which reflects the experimental uncertainty of such measurements.

Table 5.1: Summary of the literature data for fusion and melting properties of pure iso-pentane.

T / K	p / MPa	ΔH / J·mol^{-1}	Reference
112.05 [a]	-	-	[18]
112.65 [a]	0.1	5105 ± 100	[19]
113.15	-	-	[20], [21] & [22]
113.15	0.1	-	[23]
113.2	-	-	[24]
113.25	-	5150	[25]
113.25	-	5146.84	[26]
113.26	0.1	-	[27]
113.3	-	5200	[28]
113.37	0.1	5155.5 ± 4.2	[29]
113.39	0.1	5134 ± 2.1	[30]
120.15	50	-	[23]
126.15	100	-	[23]
133.15	150	-	[23]
139.65	200	-	[23]
145.15	250	-	[23]
151.15	300	-	[23]
119.3	80.4	-	[31]
141.4	273.7	-	[31]
158.7	431.4	-	[31]
176.4	610.7	-	[31]
185.9	700.3	-	[31]
206.6	962.6	-	[31]

[a] Triple point

A literature survey found limited data available for the thermophysical properties of pure iso-pentane at pressures relevant to mixed refrigerant cycles. Furthermore, no experimental data are available for mixtures of methane and iso-pentane; this binary system will largely determine the solubility of iC5 in any mixed refrigerant of light hydrocarbons.

In this work, freezing and melting points for pure iso-pentane and binary mixtures of (methane + iso-pentane) were measured at cryogenic conditions relevant to LNG production. Below, experimental set-up, procedure and thermodynamic modelling are discussed, and then the measured melting temperature data are compared with the predictions of a thermodynamic model embedded in the ThermoFAST software package [32]. The measured data are then used to tune the model and its improved performance in predicting the melting temperatures is

shown. Finally, the addition of iso-pentane to methane-rich mixtures as a refrigerant is discussed in terms of its impact on the liquefaction capacity and specific energy consumption of the refrigeration system and solid formation risks.

5.3 Experimental

5.3.1 Apparatus overview

A visual high-pressure sapphire cell, as shown in Figure 5.1 and similar to those described in previous publications [14,16,33,34], was used in this work to conduct the freezing and melting temperature measurements. The measurement set-up included a gas mixing and dosing system, a high-pressure sapphire cell located inside an environmental cooling chamber and a data acquisition system. The environmental cooling chamber (M170J-13100) with a Thermal Solution Series controller (KTS6310AB) housed the equilibrium cell and had an operational temperature range of (87 to 473) K. A high-pressure Dewar supplied liquid nitrogen (LN_2) to the chamber, providing the required cooling load at cryogenic temperatures. A quartz-crystal pressure transducer (Digiquartz, Paroscientific) with a relative standard uncertainty of 0.01 % of the full scale (41 MPa) was used to measure the system's pressure. A stepper motor (Arun Microelectronics D42.2) drove a magnetic stirrer bar inside the equilibrium cell to ensure the thermal homogeneity of the sample during cooling and heating processes.

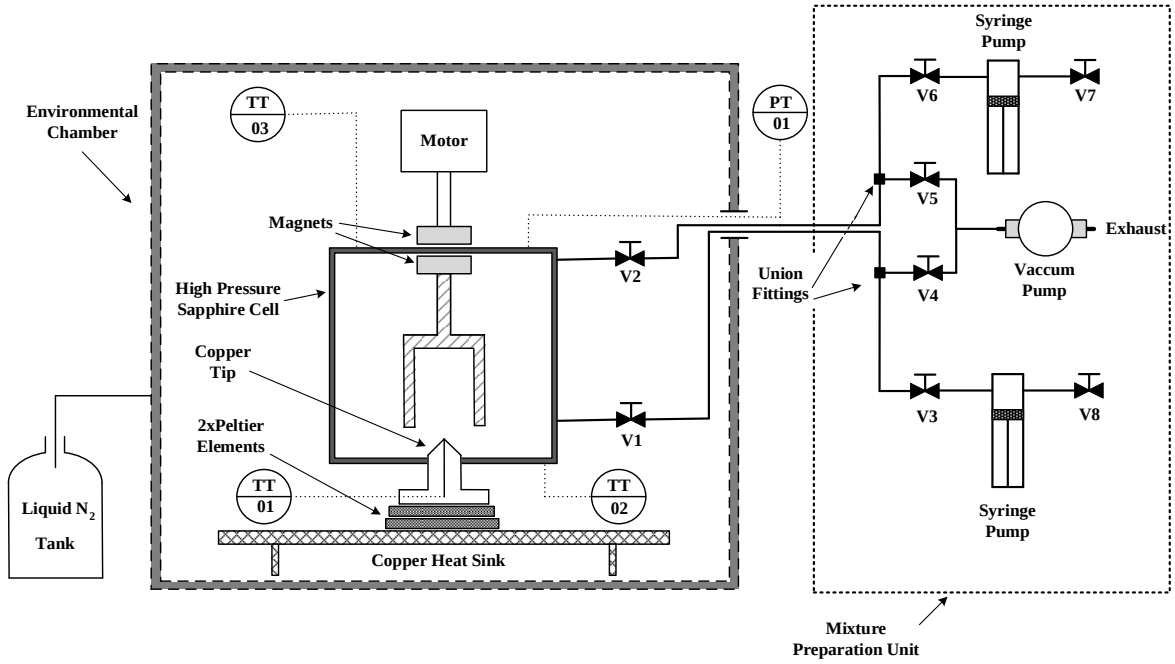

Figure 5.1: Schematic diagram of the CryoSolids apparatus (not to scale).

Figure 5.2 shows the visual high-pressure sapphire cell, which has a 75 mL internal volume and is capable of measurements at temperatures down to 85 K and pressures up to 30 MPa. Fast response 100 Ω platinum resistance thermometers (PRT NR-14, Netsushin) were employed to measure the cell temperature. All PRTs were calibrated against a reference standard PRT sensor (ASL-WIKA) with a standard uncertainty of 0.02 K over a temperature range of 100 - 273 K. The PRTs were placed into holes bored on the bottom and top flanges and the copper tip inside the equilibrium cell. In this study, the copper tip temperature was taken as the measure of the observed freezing and melting points.

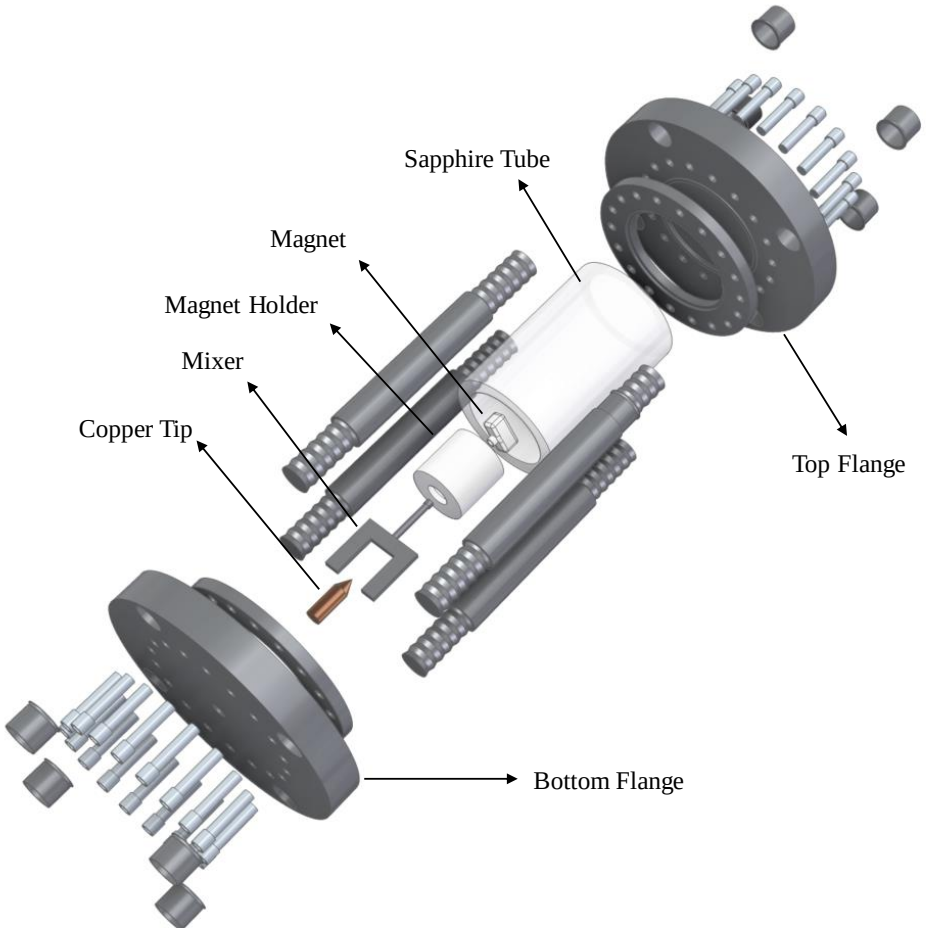

Figure 5.2: The visual cell assembly's exploded view. A photograph of the cell is shown in Siahvashi et al. [16].

The maximum cooling or heating rate applied to the CryoSolid apparatus was limited to 1 $K \cdot min^{-1}$ to minimise the risk of thermal shock or damage to the system, especially to the sapphire cell. Only the bulk fluid temperature was controlled and adjusted to determine the freezing and melting points in this work. Each experimental point was repeated three times to ensure the reliability of the measurements. A Panasonic high-definition (HD) camcorder (HCV 180) was employed to capture and record freezing and melting processes. In addition to the

chamber's built-in illumination, extra lights were used to achieve sufficient background lighting for high-quality imaging.

5.3.2 Materials and sample preparation procedure

Details of the pure fluids purchased directly from the suppliers are listed in Table 5.2, which were used without further purification.

Table 5.2: Details of the chemicals used

Chemical Name	Supplier	Purity Mole Fraction	Impurities	CAS Number
iso-pentane (2-Methylbutane)	Merck (Sigma Aldrich)	Anhydrous ≥0.995	<0.02 % Water	78-78-4
Methane	CoreGas Australia	Compressed Gas ≥0.999995	-	74-82-8

Binary mixtures of (methane + iso-pentane) were prepared in a custom mixing unit consisting of two high precision syringe pumps (Teledyne ISCO 260D) each with 260 mL volume. The syringe pumps were capable of injection at different flow rates ranging from 0.01 to 107 $mL \cdot min^{-1}$ under controlled pressures ranging from 0.07 to 52 MPa. The syringe pumps were loaded with pure iso-pentane and methane then connected to the bottom and top flanges, respectively, of the equilibrium cell. Six binary mixtures were prepared in situ using this synthesis technique. The pre-calculated amounts of each component were injected into the equilibrium cell at ambient temperature (measured by an independent 100 Ω PRT) and constant pressures. The actual injected volumes were recorded to determine the overall composition of the mixtures. First, iso-pentane was injected into the cell, and then methane was added to prepare the target mixture. Once inside the cell, the synthesised mixture was repeatedly stirred on an intermittent basis (20 seconds stirring at 300 rpm, 20 seconds of no stirring) to ensure the mixture remained homogenous throughout the measurement. At solid-liquid equilibrium (SLE) conditions, for both the pure iso-pentane as well as the methane + iso-pentane binary mixtures, sample pressure was controlled using the syringe pump. At solid-liquid-vapour equilibrium (SLVE) conditions, both the liquid and vapour phases were visually observed together with the solid, and the pressure of the sample was the vapour pressure of the fluid phase. At higher pressures, the fluid phase existed only as a liquid and as at SLE when the solid phase appeared.

5.3.3 Melting and freezing measurement procedures

Before commencing the measurements, the equilibrium cell was cleaned with appropriate solvents (including Toluene, Methanol, Ethanol and Acetone) and evacuated using a vacuum pump (Varian SH-110). After loading the cell, the cooling chamber temperature was decreased at a controlled rate of 0.8 $K \cdot min^{-1}$ while the sample inside the cell was stirred. The cooling chamber and the equilibrium cell temperatures were stabilised by control algorithms at the desired set-points and then reduced gradually at a rate between (0.3 and 0.8) $K \cdot min^{-1}$ until the first solid crystals formed. This point was recorded as the freezing point (T_f) of the fluid. Following the formation of solids in the cell, the temperature was first increased at a rate between (0.1 and 0.2) $K \cdot min^{-1}$ to about 2 K below the expected melting point. Then the temperature of the cooling chamber increased in steps of (0.5-1) K every 20 minutes until complete melting was observed. This temperature was recorded as the melting temperature (T_m) for the pure fluid and the liquidus temperature ($T_{liquidus}$) for the mixtures [35]. The term liquidus corresponds to the condition at which the last solid crystal melts into the bulk fluid of a mixture [36–39]. In this study, the melting temperature was used as an equivalent term for the liquidus temperature of the methane + iso-pentane binary mixtures.

5.3.4 Experimental Uncertainty

The uncertainty of the experimental melting properties was carried out in accordance with the "Guide to the Expression of Uncertainty in Measurement", developed by the National Institute of Standards and Technology (NIST) [40]. The experimental uncertainty assessment for the synthetic mixture composition, temperature and pressure measurements were detailed in the previous publications [34,41]. The standard uncertainty of the iso-pentane mole fraction (z_1) is calculated as follows:

$$u^2(z_1) = z_1(1 - z_1)[u_r^2(\rho_1) + u_r^2(\rho_2) + u_r^2(V_1) + u_r^2(V_2)] \quad 5.1$$

where ρ_1, ρ_2, V_1 and V_2 are the molar density and cumulative injected volumes for iso-pentane and methane samples, respectively, at the syringe pumps condition. The density standard relative uncertainty, $u_r(\rho)$, for each component is obtained from the equations of state embedded in the software package REFPROP 10 [42] with an estimated value of 1 % considering the uncertainties in temperature and pressure measurements in the syringe pumps.

The volume standard relative uncertainty, $u_r(V)$, was found to be 0.3 % for both syringe pumps [16]. The standard uncertainty in the measured melting temperature was estimated by considering the standard deviation of the three repeated measurements (± 0.3 K) together with the estimated standard uncertainty of the PRTs (0.05 K). The standard uncertainty in pressure measurements was estimated to be 0.02 MPa by considering fluctuations in temperature and pressure. The mole fraction uncertainty associated with the binary mixtures was estimated to be 0.01.

5.4 Thermodynamic Modelling

The ThermoFAST software package was used to predict the solid-fluid-equilibrium (SFE) for iso-pentane and (methane + iso-pentane) binary mixtures. At SFE, the fugacity of the individual component *i* that forms the solid phase is equal to the partial fugacity of the same component in the fluid phase as follows:

$$f_i^{\text{solid}}(p,T) = f_i^{\text{fluid}}(p,T,x_i) \qquad 5.2$$

Here, *p* and *T* are the melting pressure and temperature, respectively, and x_i represents the mole fraction of component *i* in the fluid phase. The partial fugacity of the fluid phase can be calculated using thermodynamic models such as cubic or Helmholtz energy equations of state. The Peng-Robinson cubic equation of state (PR EOS) implemented in ThermoFAST was used to calculate the partial fugacity of iso-pentane in the fluid phase at melting conditions. The PR EOS correlates temperature, pressure and molar specific volume as follows [17,43]:

$$p = \frac{RT}{v-b} - \frac{a}{\left[v+(1+\sqrt{2})b\right]\left[(v+(1-\sqrt{2})b)\right]} \qquad 5.3$$

Here, the symbol *R* is the universal molar gas constant, and v is the molar specific volume. Parameters *a* and *b* represent the temperature-dependent energy and co-volume constants. The PR EOS can be used for both pure fluids and mixtures by employing mixing functions like the van der Waals one-fluid mixing rules that incorporate a single binary interaction parameter (BIP). In this study, a temperature-independent BIP (k_{ij}) was used for (methane + iso-pentane) binary mixtures as follows:

$$a = \sum_i \sum_j x_i x_j \left[(1 - k_{ij})\sqrt{a_i a_j}\right]$$

$$b = \sum_i x_i b_i \qquad 5.4$$

ThermoFAST has a default BIP of (k_{ij} = 0.0286) for the SFE calculations involving (methane + iso-pentane) binary systems, which was determined by regression to the available experimental thermodynamic data available in the literature [17].

The fugacity of the pure solid was calculated using a standard model implemented ThermoFAST and described by Prausnitz et al. [38]:

$$\frac{f_i^s}{\varphi_{pure,i}^L p} = exp\left[\left(-\frac{\Delta H_i^{fus}}{RT_{m,i}}\right)\left(\frac{T_{m,i}}{T} - 1\right) + \frac{\Delta c_{P,i}^{fus}}{R}\left(\frac{T_{m,i}}{T} - 1 + \ln(\frac{T}{T_{m,i}})\right) - \frac{\Delta v_i^{fus}(p - p_{m,i})}{RT}\right] \qquad 5.5$$

Here, f_i^s and $\varphi_{pure,i}^L$ stand for the fugacity and fugacity coefficient of the pure solid and liquid phases of component *i*, respectively, while $T_{m,i}$ and $p_{m,i}$ are the normal melting point temperature and the reference pressure for the given melting temperature, respectively. The constants $\Delta c_{P,i}^{fus}$, ΔH_i^{fus} and Δv_i^{fus} are the molar heat capacity, molar enthalpy and molar volume changes upon fusion at the melting point of component *i*, respectively. The term Δv_i^{fus} reflects the effect of the pressure on the solid fugacity and melting temperature of the pure component *i*. In this work, the iso-pentane molar volume change upon fusion (Δv_{iC5}^{fus}) was treated as an adjustable parameter to improve the agreement between the model predictions and the melting temperature data for pure iso-pentane. Table 5.3 lists the parameters for iso-pentane used in ThermoFAST's default solid fugacity model together with the optimised value of Δv_{iC5}^{fus} determined in this work.

Table 5.3: Pure iso-pentane fusion parameters used in the ThermoFAST model.

Parameter →	T_{iC5}^{fus} / K	ΔH_{iC5}^{fus} / J·mol^{-1}	$\Delta c_{P,iC5}^{fus}$ / J·(mol·K)$^{-1}$	Δv_{iC5}^{fus*} / m^3·mol^{-1}
Default value	113.2	5147	32.194	1.34E-5
Reference	[24]	[30,44]	[30]	[45,46]
Optimised value (this work)				(5.6 ± 0.7**)E-6

* The default molar volume change on fusion is calculated using the solid [45] and liquid [46] density differences at the melting point temperature.

** The uncertainty for the optimised Δv_{iC5}^{fus} was estimated by considering the standard deviation of three Δv_{iC5}^{fus} determined separately by tuning the model to each melting point dataset reported in this work, Würflinger [23] and Reeves et al. [31].

5.5 Results and Discussion

5.5.1 Pure iso-pentane

Figure 5.3 (a)-(d) show observations of solid formation in pure iso-pentane. In liquid alkanes like iso-pentane, the molecules are bound together by the van der Waals (London dispersion) intermolecular forces [47]. These intermolecular forces generally become stronger with a higher molecular mass and colder operating conditions, at which the molecules are frozen and locked in positions relative to their neighbours [48]. On the other hand, the energy penalty associated with forming new interfaces between the bulk liquid and the more stable solid phase represents an activation energy barrier to nucleation. Sub-cooling of the fluid phase is needed to overcome the activation energy required to form the solid phase. Figure 5.3 (a) shows the iso-pentane liquid sub-cooled by up to 7 K below the melting point without freezing, even with the liquid being stirred. Figure 5.3 (b) shows the first solid iso-pentane forming at a sub-cooling of 7 K, followed by Figure 5.3 (c) and (d) with further conversion of the bulk liquid into solid. In this study, an average sub-cooling temperature ($T_f - T_m$) of (6 to 8) K was observed in part as a result of using an average cooling rate of 0.8 K·min^{-1} to induce the solid formation for the pure iso-pentane and its binary mixtures with methane. The cooling rate adapted in this study was close to the average cooling rate of 0.6 K·min^{-1} used by Di Nicola et al. [49] to measure the triple point of CO_2, which was resulted in an average sub-cooling temperature of 10 K. Unlike the melting (equilibrium) data points, different freezing points were obtained for repeat measurements at the same pressure condition due to the stochastic nature of nucleation [50].

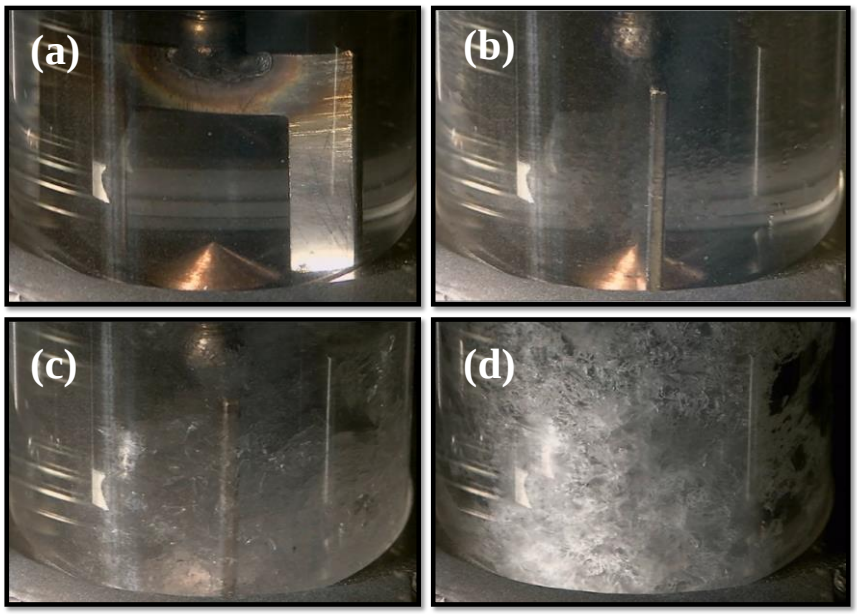

Figure 5.3: Freezing process of the pure iso-pentane at (p = 13 MPa, T = 108.3 K): (a) 7 K sub-cooled iso-pentane liquid (no solids); (b) and (c) SLE mixtures of iso-pentane;(d) solid iso-pentane.

The freezing and melting temperatures of the pure iso-pentane samples were measured isobarically at pressures between (0.25 and 13.06) MPa, as presented in Figure 5.4. The average cooling and heating rates to obtain the freezing and melting temperatures were $\beta_{f,ave}$= 0.8 K·min^{-1} and $\beta_{m,ave}$= 0.2 K·min^{-1}, respectively. Figure 5.4 (a) shows that the freezing and melting temperatures increased linearly with pressure; however, their pressure sensitivity was insignificant with slopes of 0.28 K·MPa^{-1} and 0.14 K·MPa^{-1}, respectively, as expected given the incompressible nature of liquids.

Table 5.4: Measured freezing and melting temperature ($T_{f,}$ and T_m) and pressure (p_f and p_m) data together with the differences between the experimental and calculated melting temperatures by the default (def) and optimised (opt) ThermoFAST model for pure iso-pentane.

p_f / MPa	T_f / K	p_m / MPa	T_m / K	$(T_{m,exp} - T_{m,calc})_{def}$ / K	$(T_{m,exp} - T_{m,calc})_{opt}$ / K
0.25	104.5	0.27	113.4	0.2	0.2
1.88	105.2	1.89	113.6	-0.1	0.2
5.05	106.1	5.06	114.0	-0.7	0.2
7.04	106.7	7.06	114.3	-1.0	0.2
13.04	108.3	13.06	115.2	-1.9	0.3

* The overall uncertainties in the temperature, $u(T)$, and pressure, $u(p)$, measurements were 0.3 K and 0.02 MPa, respectively.

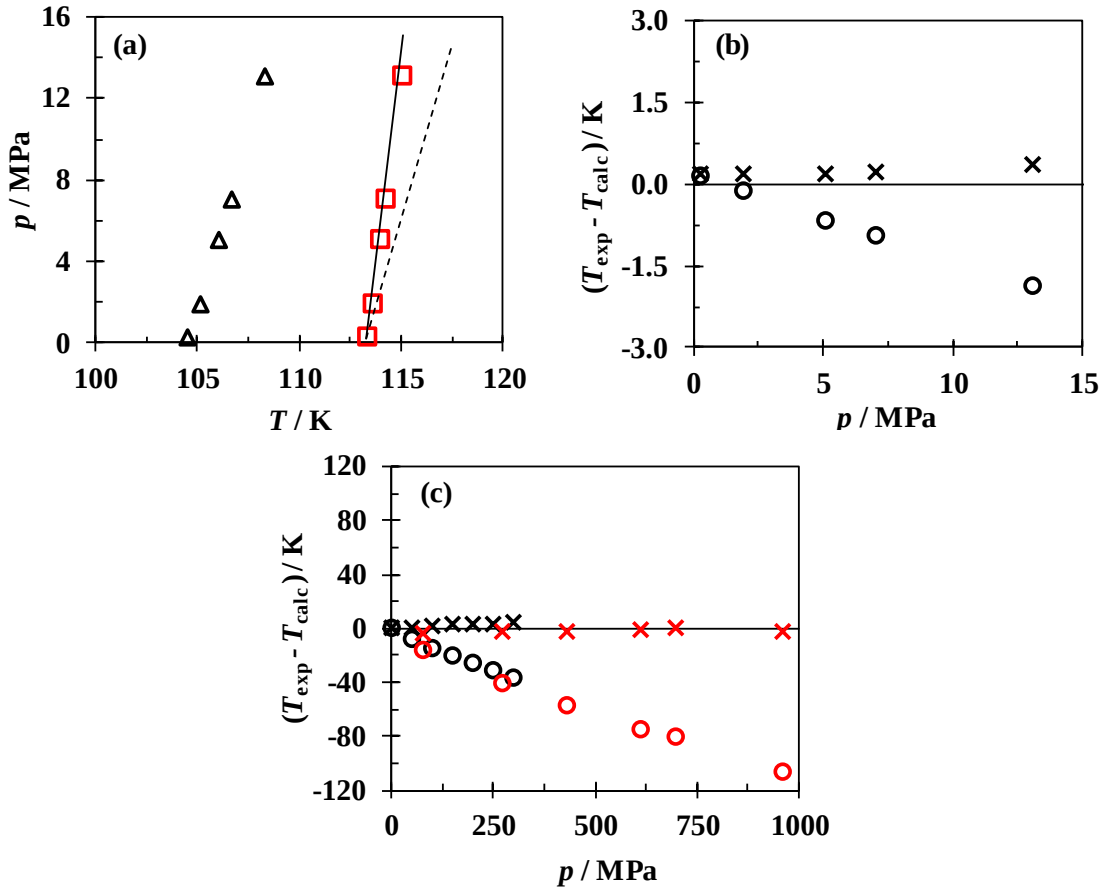

Figure 5.4: (a) Phase diagram showing the freezing and melting temperatures measured for pure iso-pentane: (Δ, black) experimental freezing temperature, (□, red) experimental melting temperature, (---) melting temperature predicted by default ThermoFAST model and (—) melting temperature predicted by the optimised ThermoFAST model. (b) Deviations of the measured melting temperatures (T_{exp}) from the predictions of ThermoFAST, (T_{calc}), with the default and optimised solid fugacity models, Equation 5.5, as a function of pressure (p); (c) Deviations of the measured melting temperatures by Würflinger [23] (black) and Reeves et al. [31] (red) from the predictions of ThermoFAST with the (○) default and (×) optimised models.

The reported triple point of iso-pentane in the literature varies between 112.65 K and 113.39 K [24,30,51,52]. Extrapolating the data obtained in this work beyond the lowest measured pressure (0.27 MPa) resulted in a triple point temperature estimate of (113.4 ± 0.4) K, which is in good agreement with the value of 112.65 K reported by Parks and Huffman [19,52].

The measured melting temperature data were also compared with the predictions of ThermoFAST. Figure 5.4 (b) and (c) show the deviations of the experimental data measured in this study (0.3-13 MPa) and by Würflinger [23] and Reeves et al. [31], which were acquired over the pressure range of (0.1-300) MPa and (80.4-962.6) MPa from the prediction of the default ThermoFAST SFE model, respectively. The default model systematically deviated from the experimental melting temperature data with average root mean square deviations

(RMSDs) of (1.0, 22.7 and 69.1) K, respectively, for the melting data measured in this study, by Würflinger [23] and by Reeves et al. [31]. These systematic deviations suggested that the default molar volume change on fusion for the pure iso-pentane in the freeze-out model (Δv_{iC5}^{fus} = 13.4×10^{-6} m^3.mol^{-1}) was inaccurate and needed adjustment. Tuning the model to the experimental melting points of this work and those of Würflinger [23] and Reeves et al. [31] considerably decreased the RMSDs between the calculated and the reported melting data: from (1 to 0.2) K for this work, and from (22.7 to 2.7) K and (69.1 to 2.1) K for the data of Würflinger [23] and Reeves et al. [31], respectively. The optimised value obtained for the fusion molar volume change, Δv_{iC5}^{fus} = (5.6 ± 0.1)×10^{-6} m^3.mol^{-1}, was in a good agreement with Würflinger's reported value based on the Clausius-Clapeyron equation [23,53].

5.5.2 Methane + iso-pentane binary mixtures melting points

The melting temperatures of iso-pentane in a binary mixture with methane were measured and compared with predictions of the default and optimised ThermoFAST models. Figure 5.5 (a)-(f) show the solid formation and melting processes of the (methane + iso-pentane) (61:39 mol%) binary mixture. The mixture was cooled to 94 K to induce solid formation. The binary mixture was then heated until all solids had been melted at 99.6 K.

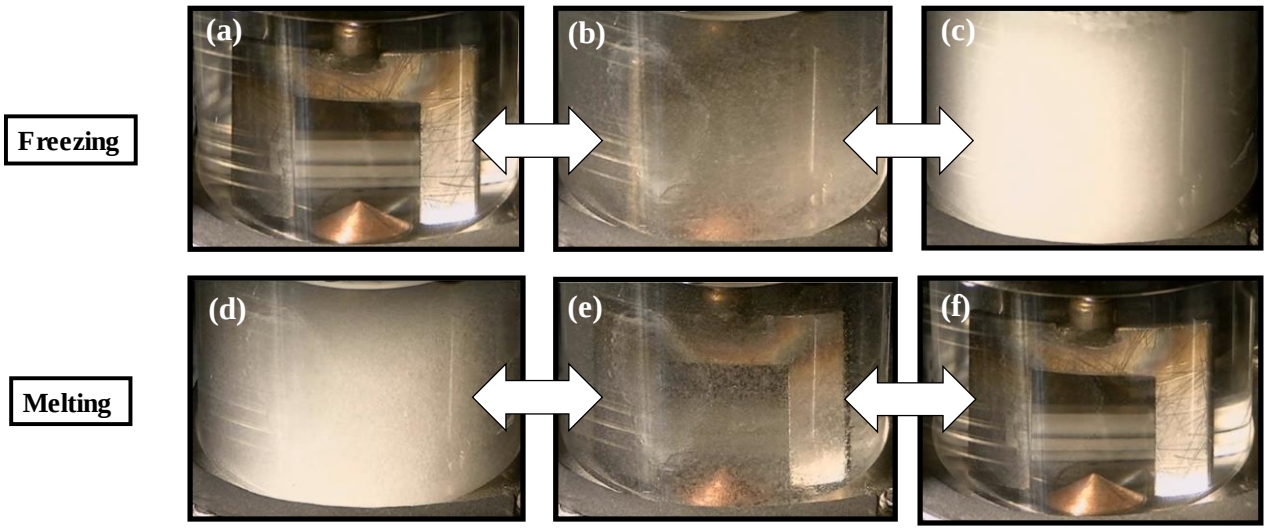

Figure 5.5: Solid formation and melting processes of (methane + iso-pentane) binary mixture (61:39 mole%) at 0.03 MPa and: (a) T = 94.2 K (sub-cooled mixture); (b) T = 93.9 K (SLVE); (c) T = 93.5 K; (d) T = 98.8 K; (e) T = 99.3 K; (f) T = 99.6 K (no solids). A clear phase boundary between vapour and liquid phases was observed for the fluid phase within the cell, which is not shown in these photos due to the angular view of the camera. The minimum particle size for the visual detection of the solid phase was estimated to be over 50 microns.

The measured freezing and melting temperatures, pressures and overall compositions of the (methane + iso-pentane) binary systems studied in this work are presented in Table 5.5

and Figure 5.6 (a). The iso-pentane melting temperature decreased from (114 to 101) K with the addition of approximately 60 mol% methane to the pure iso-pentane sample. Increasing the fraction of methane to 85 mol% decreased the melting temperature further to 96 K.

Table 5.5: Measured freezing and melting temperatures for binary mixtures of (methane + iso-pentane)*.

z_{iC5}	Equilibrium Type	p_f / MPa	T_f / K	p_m / MPa	T_m / K
0.15	SLVE	0.02	92.5	0.04	96.3
0.20	SLE	10.05	93.3	10.07	98.2
0.24	SLE	7.55	92.8	7.57	98.5
0.25	SLVE	0.04	93.1	0.11	96.9
0.39	SLVE	0.03	94.1	0.04	99.6
0.41	SLE	6.05	95.4	6.07	100.6

* The overall uncertainties in the temperature, $u(T)$, pressure, $u(p)$, and iso-pentane mole fraction, $u(z_{iC5})$, were 0.3 K, 0.02 MPa and 0.01, respectively.

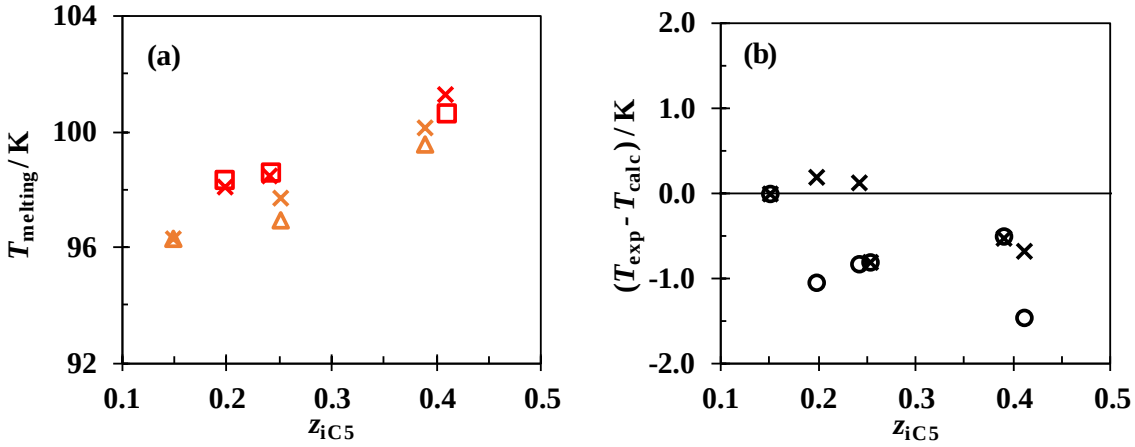

Figure 5.6: (a) The temperature-composition (T-z) phase diagram for the melting temperatures of (iso-pentane + methane) binary mixtures: (Δ, orange) experimental SLVE data, (□, red) experimental SLE data, (×) melting temperatures calculated using the optimised model. (b) Deviations of the experimental melting temperatures (T_{exp}) from the calculations of the default and optimised ThermoFAST models (T_{calc}) as a function of iso-pentane mole fraction: (○) default model and (×) optimised model.

The experimental melting data for the (methane + iso-pentane) binary systems were compared with values calculated using the default and optimised ThermoFAST models. The default model had an RMSD of 0.9 K which decreased to 0.5 K with the optimised model. Figure 5.6 (b) illustrates the deviation of the experimental melting points from the predicted values using the default and optimised freeze-out models. The pressure dependence of the solid iso-pentane's fugacity is more accurately represented by the optimised model and this is reflected

by the better representation of the measured melting temperatures at (10, 7.6 and 6) MPa, with an RMSD of 0.4 K that is 64 % less than that for the default model. No further improvement in the agreement between the model and experimental data could be achieved by adjusting the default BIP used in ThermoFAST (k_{ij} = 0.0286) for solid-fluid equilibrium calculations.

5.5.3 Operational impact of iso-pentane addition to cooling performance in MR systems

High boiling-point components like iso-butane and iso-pentane have been used previously in mixed refrigerants to reduce LNG production operating and capital costs [6–10,54]. However, limited information is available for the associated iso-pentane freeze-out risk in such MR systems. In this section, the freeze-out risk and impact of adding iso-pentane to a single mixed refrigerant (SMR) used as the working fluid in a simulated LNG liquefaction cycle was investigated using VMGSim^{TM} simulation software with the PR EOS fluid package [55]. Methane and iso-pentane binary mixtures were considered as simple representations of the refrigerant mixtures used in industrial liquefaction processes because experimental melting data are available. The SMR process, shown in Figure 5.7 and similar to the LNG processes described in [56,57], was used to simulate the liquefaction of a natural gas feed at 305 K and 8 MPa, with an effluent condition of 123 K prior to expansion across a Joule-Thomson valve (JT-NG). The minimum approach temperature and pressure drop of the main cryogenic heat exchanger (MCHE) were set to 4 K and 0.01 MPa, respectively. The refrigerant (MR-1) with a flow rate of 10 kg·s^{-1} left the air-cooled condensers (AC-2) at 313 K and 5 MPa and was pre-cooled to 123 K by also passing through the MCHE. Upon flashing to 0.13 MPa via the Joule-Thomson valve (JT-MR), a two-phase refrigerant was produced to provide the necessary cooling duty. After leaving the MCHE, the refrigerant entered the compression train consisting of a trim heater (to ensure full vaporisation), two dynamic compressors (CM-1 and CM-2) and two inter-coolers (AC-1 and AC-2), which returns the refrigerant to 5 MPa. The adiabatic

efficiencies of the compressors were considered to be 80 % and a pressure drop of 0.01 MPa was assumed across the inter-coolers and the trim heater.

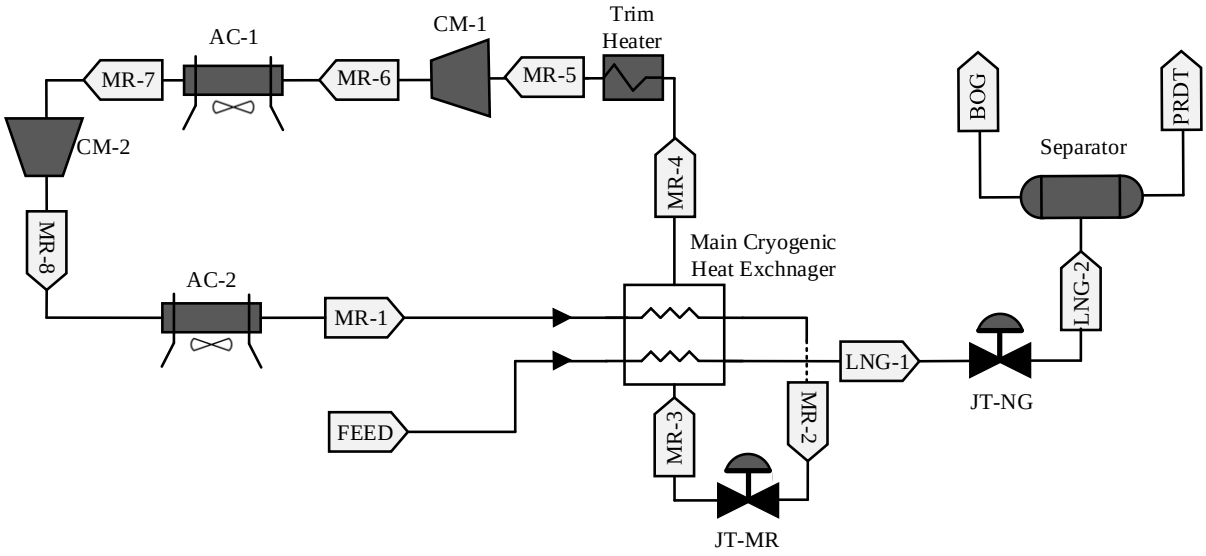

Figure 5.7: Process flow diagram of the SMR process.

In this study, specific energy consumption (SEC) was used to evaluate the liquefaction process performance at different iso-pentane fractions, which can be expressed as follows:

$$SEC = \frac{Total\ power\ consumed}{LNG\ flow\ rate} = \frac{\dot{W}_{\mathrm{CM-1}} + \dot{W}_{\mathrm{CM-2}} + \dot{W}_{\mathrm{TH}}}{\dot{m}_{\mathrm{PRDT}}} \quad 5.6$$

Here, $\dot{m}_{\mathrm{PRDT}}$ is the produced LNG flow rate, while parameters $\dot{W}_{\mathrm{CM-1}}$, $\dot{W}_{\mathrm{CM-2}}$ and $\dot{W}_{TH}$ represent the power consumptions of the compressor 1 (CM-1), compressor 2 (CM-2) and the trim heater.

Figure 5.8 (a)-(b) shows the impact of adding iso-pentane to the refrigerant (initially pure methane) on the cooling performance of the liquefaction process when all other process factors were kept constant. Adding 15 mol% iso-pentane to the refrigerant increased $\dot{m}_{\mathrm{PRDT}}$ from (0.5 to 1.4) kg·s^{-1}. This improvement derives primarily from four factors: an increase in the refrigerant dew point temperature with the addition of iso-pentane ($T_{\mathrm{dew,\ iC5}}$ = 308.2 K, $T_{\mathrm{dew,\ C1}}$ = 114.7 K and $T_{\mathrm{dew,\ 15\%\ iC5,\ bal.\ C1}}$ = 259.8 K – calculated by ThermoFAST [32]) at 0.13 MPa (after the Joule-Thomson valve); a better match between hot and cold temperature-heat flow composite curves in the MCHE (Figure 5.9), where the average temperature difference between the hot and cold streams decreased by 33 %, from (44.5 to 29.8) K; the iso-

pentane's higher latent heat of vaporisation ($\Delta H_{vap,\ iC5}$ = 25 kJ·mol^{-1} [30], $\Delta H_{vap,\ C1}$ = 8.5 kJ·mol^{-1} [58] and $\Delta H_{vap,\ 15\%\ iC5,\ bal.\ C1}$ = 17.5 kJ·mol^{-1} [42]); and improved overall heat transfer coefficient by 36 % compared with pure methane. Additionally, the higher molar mass of iso-pentane improved the compressibility characteristics of the refrigerant and decreased the overall SEC by about 80 % from (5.7 to 1.2) kWh·kg$_{LNG}^{-1}$. The lowest SEC of 1.1 kWh·kg$_{LNG}^{-1}$ was achieved with 20 mol% iso-pentane in the refrigerant. The melting temperature measured for a 20 mol% iso-pentane in a methane mixture in this work was 98.2 K, which is still 12 K lower than the coldest temperature experienced by the refrigerant in the LNG cycle.

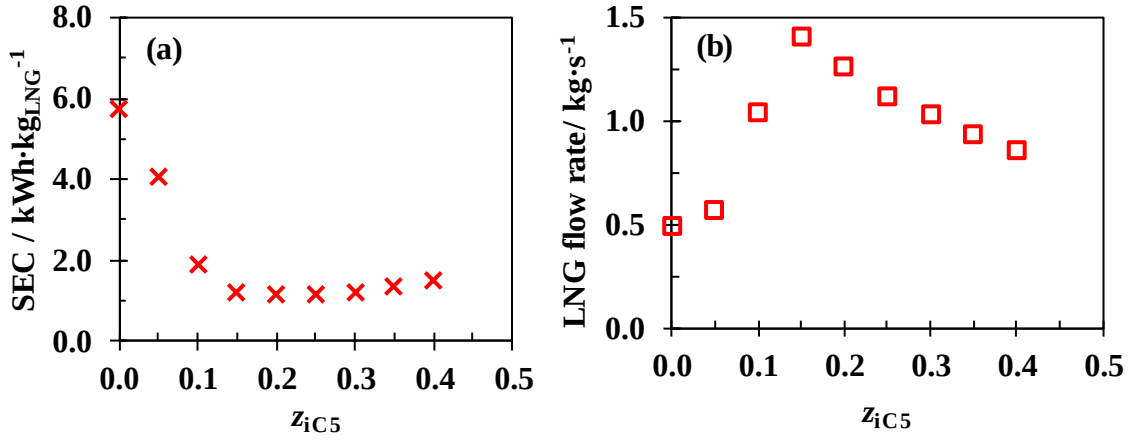

Figure 5.8: (a) The variation of the specific energy consumption (SEC) as a function of iso-pentane mole fraction in a binary mixture with methane. (b) The impact of iso-pentane mole fraction on the produced LNG flow rate ($\dot{m}_{PRDT}$).

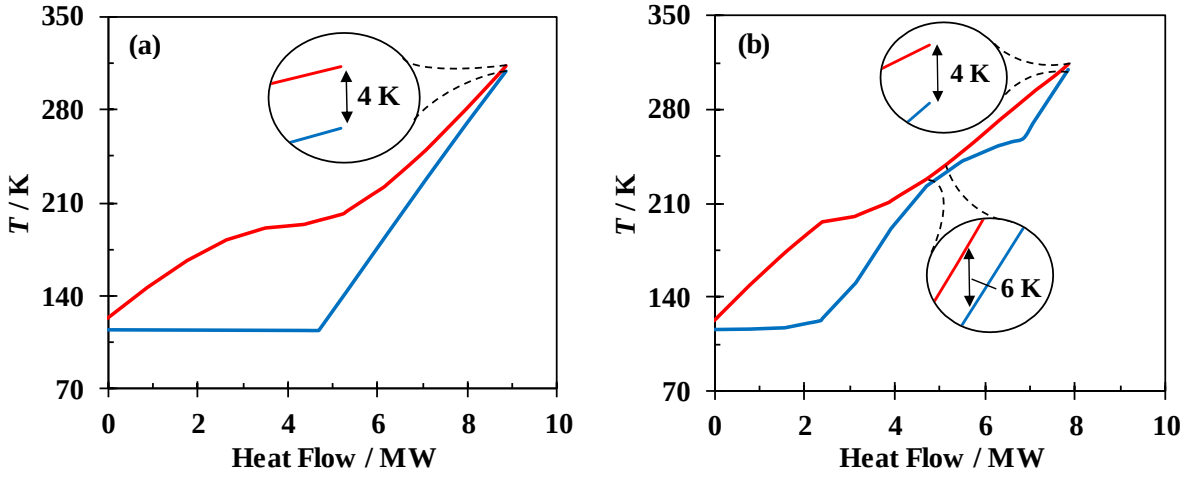

Figure 5.9: Temperature – heat flow diagram of the hot and cold composite curves (THCC) of (a) pure methane refrigerant and (b) iso-pentane + methane (15:85 mol%) refrigerant mixture (b). The pinch points were adjusted to be in the warm end of the heat exchangers as recommended by Venkatarathnam [59].

However, increasing the iso-pentane concentration to 40 mol% decreased $\dot{m}_{\mathrm{PRDT}}$ by 50 % relative to that achieved at 20 mol%. This reduction in produced LNG flow rate determines the optimum fraction of iso-pentane to use in the refrigerant, rather than the melting temperature which remains below 101 K at 40 mol%. These results illustrate the advantage of using iso-pentane in mixed refrigerant cycles and confirm that the risk of freeze-out associated with its use is negligible.

5.6 Conclusions

New experimental freezing and melting point data for pure iso-pentane and (methane + iso-pentane) binary systems are reported for the purpose of more accurately assessing freeze-out risk in mixed refrigerants that may be used in LNG production or potentially the pre-cooling stage of liquid hydrogen production. The data measured in this study were compared with the predictions of the ThermoFAST software package and used to improve the model's accuracy. The optimised ThermoFAST model was able to represent iso-pentane melting temperatures measured in this work and reported in the literature with an RMSD of 0.2 K for the pressure range between (0.1 and 300) MPa. The melting temperatures measured for the (methane + iso-pentane) binary systems showed that adding 85 mol% methane to iso-pentane reduced the melting temperature from (114 to 96) K.

A simulation of a single mixed refrigerant (SMR) natural gas liquefaction process investigated the effect of adding iso-pentane to mixed refrigerants together with the associated freeze-out risks on the cycle's energy consumption and LNG production rate. Binary mixtures of iso-pentane + methane were chosen as simple representations of the mixed refrigerant in the liquefaction processes because relevant experimental melting data for this binary are available. An iso-pentane fraction around 15-20 mol% produced an optimum in both quantities, while having no significant risk of freeze-out. Further melting data for rich iso-pentane binary mixtures with methane and multi-component mixtures containing components with high-boiling points should be measured to ensure that predictions made with models are reliable over this extended range of composition.

5.7 References

[1] Fioriti D, Baccioli A, Pasini G, Bischi A, Migliarini F, Poli D, et al. LNG regasification and electricity production for port energy communities: Economic profitability and thermodynamic performance. Energy Convers Manag 2021;238:114128. doi:10.1016/J.ENCONMAN.2021.114128.

[2] Kumar S, Kwon H-T, Choi K-H, Lim W, Cho JH, Tak K, et al. LNG: An eco-friendly cryogenic fuel for sustainable development. Appl Energy 2011;88:4264–73. doi:https://doi.org/10.1016/j.apenergy.2011.06.035.

[3] BP Statistical Review of World Energy 2019.

[4] Pospíšil J, Charvát P, Arsenyeva O, Klimeš L, Špiláček M, Klemeš JJ. Energy demand of liquefaction and regasification of natural gas and the potential of LNG for operative thermal energy storage. Renew Sustain Energy Rev 2019;99:1–15. doi:https://doi.org/10.1016/j.rser.2018.09.027.

[5] Khan MS, Lee S, Rangaiah GP, Lee M. Knowledge based decision making method for the selection of mixed refrigerant systems for energy efficient LNG processes. Appl Energy 2013;111:1018–31. doi:https://doi.org/10.1016/j.apenergy.2013.06.010.

[6] Qyyum MA, Duong PLT, Minh LQ, Lee S, Lee M. Dual mixed refrigerant LNG process: Uncertainty quantification and dimensional reduction sensitivity analysis. Appl Energy 2019;250:1446–56. doi:https://doi.org/10.1016/j.apenergy.2019.05.004.

[7] He T, Lin W. Design and optimization of integrated single mixed refrigerant processes for coproduction of LNG and high-purity ethane. Int J Refrig 2020;119:216–26. doi:https://doi.org/10.1016/j.ijrefrig.2020.06.033.

[8] Xu X, Liu J, Jiang C, Cao L. The correlation between mixed refrigerant composition and ambient conditions in the PRICO LNG process. Appl Energy 2013;102:1127–36. doi:https://doi.org/10.1016/j.apenergy.2012.06.031.

[9] Pham TN, Long NVD, Lee S, Lee M. Enhancement of single mixed refrigerant natural gas liquefaction process through process knowledge inspired optimization and modification. Appl Therm Eng 2017;110:1230–9. doi:https://doi.org/10.1016/j.applthermaleng.2016.09.043.

[10] Krishnamurthy G, Roberts MJ, Ott CM. Precooling strategies for efficient natural gas liquefaction. Gas Process 2017;September/:19–29.

[11] Qyyum MA, He T, Qadeer K, Mao N, Lee S, Lee M. Dual-effect single-mixed refrigeration cycle: An innovative alternative process for energy-efficient and cost-effective natural gas liquefaction. Appl Energy 2020;268:115022. doi:https://doi.org/10.1016/j.apenergy.2020.115022.

[12] Hisazumi Y, Yamasaki Y, Sugiyama S. Proposal for a high efficiency LNG power-generation system utilizing waste heat from the combined cycle1Published in co-operation with the Japanese Society of Energy Resources.1. Appl Energy 1998;60:169–82. doi:https://doi.org/10.1016/S0306-2619(98)00034-8.

[13] Baccanelli M, Langé S, Rocco M V, Pellegrini LA, Colombo E. Low temperature techniques for natural gas purification and LNG production: An energy and exergy analysis. Appl Energy 2016;180:546–59. doi:https://doi.org/10.1016/j.apenergy.2016.07.119.

[14] Siahvashi A, Al Ghafri SZS, Yang X, Rowland D, May EF. Avoiding costly LNG plant freeze-out-induced shutdowns: Measurement and modelling for neopentane solubility at LNG conditions. Energy 2021;217:119331. doi:10.1016/j.energy.2020.119331.

[15] Sampson CC, Metaxas PJ, Siahvashi A, Stanwix PL, Graham BF, Johns ML, et al. Measurements of solidification kinetics for benzene in methane at high pressures and cryogenic temperatures. Chem Eng J 2020:127086. doi:https://doi.org/10.1016/j.cej.2020.127086.

[16] Siahvashi A, Al Ghafri SZ, May EF. Solid-fluid equilibrium measurements of benzene in methane and implications for freeze-out at LNG conditions. Fluid Phase Equilib 2020;519:112609. doi:10.1016/j.fluid.2020.112609.

[17] Baker C, Siahvashi A, Oakley J, Hughes T, Rowland D, Huang S, et al. Advanced predictions of solidification in cryogenic natural gas and LNG processing. J Chem Thermodyn 2019;137:22–33. doi:10.1016/j.jct.2019.05.006.

[18] Day RK. Variation of the Vapor Viscosities of Normal and Isopentane with Pressure by the Rotating Cylinder Method. Phys Rev 1932;40:281–90. doi:10.1103/PhysRev.40.281.

[19] Parks GS, Huffman HM. Some Fusion and Transition Data for Hydrocarbons. Ind Eng Chem 1931;23:1138–9. doi:10.1021/ie50262a018.

[20] Timmermans J. Recherches sur la théorie des solutions concentrées, XII: Application de l'analyse thermique à la détermination de la chaleur de fusion de quelques composés organiques. Bull La Société Chim Belgique 1934;43:626–38.

[21] Timmermans J, Naveau J. Recherches sur les Solutions Concentrées XVII Quelques courbes de congélation de mélanges binaires. Bull Des Sociétés Chim Belges 2010;67:560–5. doi:10.1002/bscb.19580670903.

[22] Labruyère-Verhavert MML. Recherches Stoechiométriques VI.-Contribution á l'étude des composés globulaires cyclaniques en C5 et C6. Bull Des Sociétés Chim Belges 2010;60:270–81. doi:10.1002/bscb.19510600503.

[23] Würflinger A. Differential thermal analysis under high pressure IV: Low-temperature DTA of solid-solid and solid-liquid transitions of several hydrocarbons up to 3 kbar. Berichte Der Bunsengesellschaft Für Phys Chemie 1975;79:1195–201. doi:10.1002/bbpc.19750791206.

[24] Preston GT, Funk EW, Prausnitz JM. Solubilities of hydrocarbons and carbon dioxide in liquid methane and in liquid argon. J Phys Chem 1971;75:2345–52. doi:10.1021/j100684a020.

[25] Acree WE. Thermodynamic properties of organic compounds: enthalpy of fusion and melting point temperature compilation. Thermochim Acta 1991;189:37–56. doi:10.1016/0040-6031(91)87098-H.

[26] Gmehling J, Krafczyk J, Ahlers J, Nebig S, Hunecker I, Eisel M, et al. Pure compound data from DDB. Dortmund Data Bank, 1983-2017 n.d.

[27] Glasgow AG, Murphy ET, Willingham CB, Rossini FD. Purification, purity, and freezing points of 31 hydrocarbons of the API-NBS series. J Res Natl Bur Stand (1934) 1946;37:141–5. doi:10.6028/jres.037.003.

[28] Hopfe D. Thermophysical data of Pure Substances. Data Compil FIZ CHEMIE Ger 1990;1.

[29] Guthrie GB, Huffman HM. Thermal data. 16. The heat capacity and entropy of

isopentane. the absence of a reported anomaly. J Am Chem Soc 1943;65:1139–43.

[30] Schumann SC, Aston JG, Sagenkahn M. The Heat Capacity and Entropy, Heats of Fusion and Vaporization and the Vapor Pressures of Isopentane. J Am Chem Soc 1942;64:1039–43. doi:10.1021/ja01257a007.

[31] Reeves LE, Scott GJ, Babb SE. Melting Curves of Pressure-Transmitting. J Chem Phys 1964;40.

[32] The University of Western Australia FS and R. ThermoFAST 1.2.1: thermodynamic calculator for natural gas properties. 2019.

[33] Siahvashi A, Al Ghafri SZS, Graham BF, May EF. Experimental study of impurity freeze-out in ternary methane + ethane + benzene mixtures with applications to LNG production. J Nat Gas Sci Eng 2021;90:103918. doi:10.1016/j.jngse.2021.103918.

[34] Siahvashi A, Al Ghafri SZ, Hughes TJ, Graham BF, Huang SH, May EF. Solubility of p-xylene in methane and ethane and implications for freeze-out at LNG conditions. Exp Therm Fluid Sci 2019;105:47–57. doi:10.1016/J.EXPTHERMFLUSCI.2019.03.010.

[35] Oakley JH, Hughes TJ, Graham BF, Marsh KN, May EF. Determination of melting temperatures in hydrocarbon mixtures by differential scanning calorimetry. J Chem Thermodyn 2017;108:59–70. doi:10.1016/j.jct.2016.12.030.

[36] Tiffin DL, Kohn JP, Luks KD. Solid Hydrocarbon Solubility in Liquid Methane-Ethane Mixtures along Three-Phase Solid-Liquid-Vapor Loci. J Chem Eng Data 1979;24:306–10. doi:10.1021/je60083a013.

[37] Tiffin DL, Kohn JP, Luks KD. Three-Phase Solid-Liquid-Vapor Equilibria of the Binary Hydrocarbon Systems Ethane-2-Methylnaphthalene, Ethane-Naphthalene, Propane-n-Decane, and Propane-n-Dodecane. J Chem Eng Data 1979;24:98–100. doi:10.1021/je60081a020.

[38] Prausnitz JM, Lichtenthaler RN, Azevedo EG de. Molecular Thermodynamics of Fluid-Phase Equilibria. Third. Upper Saddle River, N.J.: Prentice Hall PTR.; 1999.

[39] Smith JM, Van Ness HC, Abbott MM, Swihart MT. Introduction To Chemical Engineering Thermodynamics Eighth Edition. 2018.

[40] Joint Committee for Guides in Metrology. Evaluation of measurement data — Guide to the expression of uncertainty in measurement. Int Organ Stand Geneva ISBN 2008;50:134. doi:10.1373/clinchem.2003.030528.

[41] Al Ghafri SZS, Jiao F, Hughes TJ, Arami-Niya A, Yang X, Siahvashi A, et al. Natural gas density measurements and the impact of accuracy on process design. Fuel 2021;304:121395. doi:10.1016/j.fuel.2021.121395.

[42] Lemmon EW, Bell IH, Huber ML, McLinden MO. NIST Standard Reference Database 23: Reference Fluid Thermodynamic and Transport Properties-REFPROP 2018.

[43] Baker CJ, Oakley JH, Rowland D, Hughes TJ, Aman ZM, May EF. Rapid Simulation of Solid Deposition in Cryogenic Heat Exchangers To Improve Risk Management in Liquefied Natural Gas Production. Energy & Fuels 2018;32:255–67. doi:10.1021/acs.energyfuels.7b03057.

[44] Yaws CL, Lin S-C. Chapter 11 - Enthalpy of fusion at freezing point—Organic compounds. In: Yaws CLBT-TP of C and H, editor., Norwich, NY: William Andrew Publishing; 2009, p. 552–91. doi:https://doi.org/10.1016/B978-081551596-8.50016-X.

[45] Goodman BT, Wilding WV, Oscarson JL, Rowley RL. A note on the relationship between organic solid density and liquid density at the triple point. J Chem Eng Data 2004;49:1512–4. doi:10.1021/je034220e.

[46] Matsumoto T, Miyamoto H. PρT and saturation properties of isopentane at T=(280–440)K and up to 200MPa. J Chem Thermodyn 2016;101:150–6. doi:https://doi.org/10.1016/j.jct.2016.05.019.

[47] Gooch JW, editor. London dispersion forces (London forces) BT - Encyclopedic Dictionary of Polymers, New York, NY: Springer New York; 2007, p. 582. doi:10.1007/978-0-387-30160-0_6895.

[48] Arora A. Hydrocarbons (Alkanes, Alkenes And Alkynes). Discovery Publishing House; 2006.

[49] Di Nicola G, Giuliani G, Polonara F, Santori G, Stryjek R. Solid-liquid equilibria for the CO 2 + R23 and N 2O + R23 systems. Int J Thermophys 2010;31:1880–7. doi:10.1007/s10765-008-0511-0.

[50] Kashchiev D. Nucleation. Elsevier; 2000.

[51] Prodany NW, Williams B. Vapor-Liquid Equilibria in Methane-Hydrocarbon Systems. J Chem Eng Data 1971;16:1–6. doi:10.1021/je60048a015.

[52] Lemmon EW, Span R. Short Fundamental Equations of State for 20 Industrial Fluids. J Chem Eng Data 2006;51:785–850. doi:10.1021/je050186n.

[53] Würflinger A, Kreutzenbeck J. Differential thermal analysis at high pressures- VIII: Phase behaviour of solid cyclopentanone, cyclopentanol, and cyclohexanone up to 3 KBAR. J Phys Chem Solids 1978;39:193–6. doi:10.1016/0022-3697(78)90042-2.

[54] Swenson LK. Single mixed refrigerant, closed loop process for liquefying natural gas. US Pat 4,033,735 1977.

[55] Peng D-Y, Robinson DB. A New Two-Constant Equation of State. Ind Eng Chem Fundam 1976;15:59–64. doi:10.1021/i160057a011.

[56] Rehman A, Qyyum MA, Qadeer K, Zakir F, He X, Nawaz A, et al. Single mixed refrigerant LNG process: Investigation of improvement potential, operational optimization, and real potential for further improvements. J Clean Prod 2021;284:125379. doi:10.1016/j.jclepro.2020.125379.

[57] Khan MS, Lee M. Design optimization of single mixed refrigerant natural gas liquefaction process using the particle swarm paradigm with nonlinear constraints. Energy 2013;49:146–55. doi:10.1016/j.energy.2012.11.028.

[58] Hestermans P, White D. The Vapor Pressure, Heat Of Vaporization And Heat Capacity Of Methane From The Boiling Point To The Critical Temperature. J Phys Chem 1961;65:362–5. doi:10.1021/j100820a044.

[59] Venkatarathnam G. Cryogenic Mixed Refrigerant Processes. vol. 33. 2010. doi:10.1016/j.ijrefrig.2009.11.013.

6 Chapter 6 │ Conclusions and Future Work

6.1 Conclusions

International governments and organisations pledged to reduce greenhouse gases (GHGs) emissions to a level that will limit the global temperature rise by 1.5 ℃ above pre-industrial levels. Two significant contributors to global GHG emissions are fluorinated gases (F-gases) employed as the working fluid of cooling systems and massive CO_2 emitted by using high-emission fuels in industry. The main objective of this work was to improve the safety and thermodynamic knowledge for eco-friendly and energy-efficient refrigerant mixtures that can reduce the ecological footprint of domestic cooling systems and improve the viability of natural gas in replacing coal by reducing its liquefaction costs. To achieve this objective, this work investigated the thermophysical properties and flammability characteristics of alternative refrigerant mixtures and optimised the thermodynamic predictive models in REFPROP, Multiflash and ThermoFAST software packages. Additionally, the freeze-out risk of iso-pentane in mixed refrigerants used in LNG production was studied to fill some of the existing literature gaps for solid-fluid equilibrium data (SFE), which was accompanied by detailed uncertainty analysis and thermodynamic model optimisation. The research outcomes of this thesis will help the energy and refrigeration industries enhance the sustainability of their products and operations and develop reliable new domestic and cryogenic cooling systems compatible with efficient and eco-friendly refrigerant mixtures.

To investigate the flammability characteristics of alternative refrigerants, two pieces of new apparatus were designed, commissioned and deployed to measure the minimum ignition energy (MIE) and laminar burning velocity (BV) of Hydrofluorocarbons (HFCs), Hydrofluoroolefins (HFOs) and CO_2 mixtures. The MIEs of NH_3, HFC-32 and HFO-1234yf were measured to be (18.0 ± 1.4), (8.0 ± 1.5) and (510 ± 130) mJ at equivalence ratios of 0.9, 1.27 and 1.33, respectively. To reduce the ignition risk of HFC-32, HFO-1234yf and CO_2 were added to the HFC-32/air mixture, which increased the MIE of the mixture by 40 times relative to the pure HFC-32. To reduce the flammability of the refrigerant mixture, non-flammable refrigerants of HFC-134a, HFC-125 and CO_2 were added to HFC-32 and HFO-1234yf (an equimolar five-component mixture), where no ignition was observed with spark energies up to 8 J. The BV of HFC-32 was measured to be 6.4 $cm \cdot s^{-1}$ at an equivalence ratio of 1.1, while no propagating flame could be established for HFO-1234yf, precluding the determination of its BV. Adding 5

vol% of HFO-1234yf to the HFC-32/air mixture at a 1.1 equivalence ratio decreased the laminar burning velocity of the mixture by 0.8 $cm \cdot s^{-1}$ compared with the pure HFC-32. However, no propagating flames could be established for HFO1234yf + HFC-32 mixtures (10:90 vol%) indicating the laminar BV for binary mixtures with 10 vol% or more HFO-1234yf is below the measurable threshold of 5 $cm \cdot s^{-1}$. These results show that refrigerant mixtures rich with HFO-1234yf and CO_2 could provide safe and sustainable refrigerant solutions for domestic air-conditioners.

After observing the effectiveness of CO_2 in suppressing the flammability of HFOs, the vapour-liquid equilibrium (VLE) of CO_2 + HFO-1243zf binary mixtures was studied as the eco-friendliest HFO refrigerant that is available commercially. As the first experimental thermophysical property data in the open literature, the VLE data presented in this work were compared with the predictions of a Helmholtz free energy model that utilises the GERG-2008 mixing rule [2], implemented in the REFPROP software package [3], and the Peng-Robinson Advanced EOS with van der Waals one-fluid mixing rules, implemented in Multiflash software package [4]. Both models' binary interaction parameters (BIPs) were determined by fitting to the measured VLE data. The PRA-EOS with the tuned BIP represented the VLE data slightly better than the original untuned Helmholtz free energy EOS. However, the tuned Helmholtz energy EOS provided 33 % better representation of the experimental bubble and dew points than the tuned PRA-EOS and 45 % better than the untuned Helmholtz energy EOS. The comparison of the pressure-enthalpy diagrams of three equimolar mixtures of CO_2 with HFO-1234yf, HFO-1234ze(E) or HFO-1243zf showed that the latter binary mixture has a wider enthalpy difference between the saturated liquid and vapour curves (from 0.7 to 1.4 $kJ \cdot mole^{-1}$) in the pressure range of (5.7 to 0.3) MPa. The reported experimental VLE data and optimised thermodynamic models will aid in designing and simulating refrigeration processes utilising working fluids with low global warming potential.

HFC-32 has a lower GWP than other commonly used HFCs and is more compatible with current cooling systems than most HFOs. This makes it a suitable refrigerant for transitioning domestic and industrial applications towards lower environmental impact while HFO compatible cooling systems are being developed. HFC-32 can be blended with CO_2 to neutralise its flammability and further reduce the refrigerant's overall GWP with minor cooling performance reductions. New sets of experimental vapour-liquid equilibrium (VLE), solid-liquid-vapour equilibrium (SLVE) and solid-liquid equilibrium (SLE) data were measured for the HFC-32 + CO_2 binary system at temperatures between (131.9 and 273) K to test the

reliability of existing predictive models in representing the thermodynamic properties, in particular, solid formation points at low-temperature conditions. The VLE data presented in this study, together with the literature data [5–7] measured at similar temperatures, were compared with the predictions of a Helmholtz energy EOS [7]. This Helmholtz EOS [7], presented in Appendix B, represents the dew point data better than the bubble point data, with the deviations between the experimental and predicted mole fractions for the liquid and vapour phases being about (2.8 and 1.9) times larger than the average experimental uncertainty, respectively. The SLVE data reported in this study together with the literature data [8] showed a eutectic temperature of 131.9 K around 11 mol% CO_2 for this binary system. The SFE data were compared with the predictions of thermodynamic models using the Peng-Robinson EOS (PR-EOS) [9] and Helmholtz EOS [7] for the fluid phase and a reference Helmholtz EOS for the CO_2 solid phase [10], implemented in the ThermoFAST software package. The thermodynamic model with the default PR-EOS represented the SFE data with an RMSD of 7.3 K, while the model with the Helmholtz EOS [7] for the fluid phase had an RMSD of 9.1 K from the measured SFE data. In this study, the binary interaction parameter of the model with the PR-EOS was adjusted by fitting to the experimental data. The tuned model represented the experimental melting points for the binary mixtures with CO_2 concentrations of over 11 mol% with an RMSD of 0.5 K, 85 % better than the untuned model. The new VLE and SFE data for HFC-32 + CO_2 binary systems will help design refrigeration systems utilising refrigerant mixtures with up to 80 % less environmental impact compared to the conventional options.

New freezing and melting point data were measured for pure iso-pentane and (methane + iso-pentane) binary systems to verify and/or improve the prediction of the thermodynamic models used for MR systems containing iso-pentane fractions. The measured melting data in this study together with the literature data [11,12] were compared with the predictions of a thermodynamic model implemented in the ThermoFAST software package [13], using the Peng-Robinson EOS for the fluid phase and the classical pure substance fugacity correlation for the solid phase [14,15]. Melting point predictions of pure iso-pentane data were optimised by adjusting the fusion molar volume change within the solid fugacity model by fitting it to the pure iso-pentane experimental melting data. The optimised ThermoFAST model calculated the iso-pentane melting temperatures measured in this study together with the literature data [11,12] with an RMSD of 2.1 K at pressures between (0.1 and 962.6) MPa compared the RMSD of 69.1 K for the default model. The optimised model represented the binary mixture melting temperatures measured in this work with an RMSD of 0.5 K, 45 % less than the RMSD

of the default model. For mixed refrigerant applications, the effects of adding iso-pentane to methane as working fluid of a single mixed refrigerant (SMR) liquefaction system were investigated. Adding 15 mol% iso-pentane to methane increases the LNG production capacity of the SMR cycle by three times and reduces the specific energy consumption of the process by 80 %, relative to pure methane. The melting temperatures measured for the (methane + iso-pentane) binary systems showed that with the addition of 85 mol% methane to iso-pentane, the melting temperature decreased from (114 to 96) K. These new, accurate melting point data will aid in the design and simulation of cost-effective cryogenic refrigeration processes for natural gas and, potentially, hydrogen liquefaction facilities.

The measured flammability and phase equilibrium properties of eco-friendly refrigerants provide a better understanding of physical behaviour and safety hazards associated with these working fluids. The tuned thermodynamic models presented in this thesis will help air-conditioning industry design safe and compatible refrigeration systems with these eco-friendly refrigerants and accelerate the replacement of the current high GWP working fluids. The new experimental data on iso-pentane solubility in mixtures with light hydrocarbons like methane along with the optimised solid fugacity model for pure iso-pentane will enable improved predictions of the iso-pentane freeze-out points in cost-effective mixed refrigerants for efficient natural gas and hydrogen liquefaction processes.

6.2 Recommendations for future work

In general, further experimental investigations on the flammability characteristics and thermodynamic properties of alternative refrigerant mixtures are recommended. This information would improve the safety and technical knowledge of eco-friendly refrigerants and help them find global market acceptance. Additionally, further solubility measurements are recommended for high boiling-point components in mixed refrigerants at cryogenic temperatures to improve the solid formation predictions and reduce the blockage incidents in natural gas and potentially in hydrogen liquefaction plants. These general recommendations are discussed in more specific detail below.

6.2.1 Improved understanding of minimum ignition energy and burning velocities in HFOs with CO_2 at different temperatures and humidity levels

For the flammability characteristics measurement of HFOs, future research should focus on the minimum ignition energy (MIE) and burning velocity (BV) measurements of HFO-1243zf, which has the lowest GWP potential relative to other HFOs. Unfortunately, no experimental MIE and BV data are available in the open literature of this refrigerant. Also, the CO_2 concentration limits in binary mixtures with HFO-1243zf to neutralise the flammability characteristics of the refrigerant mixture need to be investigated. The flammability of HFOs like HFO-1234yf and HFO-1243zf varies significantly with temperature and humidity. In future work, threshold values for CO_2 within mixtures of HFO-1234yf/air or HFO-1243zf/air at different humidity levels and temperatures needs to be determined; a concentration above which the MIE energy is high enough for the mixture to be considered effectively non-flammable at various weather conditions across the globe. Also, the rate of pressure rise and its maximum value caused by the explosion for different scales of refrigerant mixtures should be investigated to address the effect of the confinement as well as the extent of the hazards in case of ignition.

6.2.2 Improved thermodynamic descriptions of HFO mixtures with CO_2 for further optimisation of engineering models.

For the thermodynamic property data of HFO-1243zf + CO_2 binary systems, more experimental data, in particular density, vapour-liquid equilibrium (VLE) and solid-fluid equilibrium (SFE), should be acquired in low-temperature conditions (down to the HFO-1243zf triple point of 122.8 K [16]) to enable verification and further improvements in the performance of engineering models with deviations similar in magnitude to the experimental uncertainties. Unfortunately, no experimental data are available for this binary mixture with exception of this thesis. Further optimisation of Helmholtz energy EOS would require more extensive experimental data for other properties such as density, speed of sound and heat capacity. For the solid freeze-out predictions and thermodynamic calculations including the solid phase, new experimental data should be provided to enable verification of the accuracy of predictive models and their optimisation if necessary.

6.2.3 Improved solid formation predictions in mixed refrigerants with heavy compounds used in cryogenic liquefaction systems

Further experimental melting data for multi-component mixtures of iso-pentane with lighter components like nitrogen, methane, ethane, propane and iso-butane, as the main components in the mixed refrigerants of an LNG production plant, should be measured to enable further improvement in the performance of the predictive models. While the effect of adding methane on the melting temperature of iso-pentane was investigated in this thesis, the impact of nitrogen, ethane, propane and iso-butane in a multi-component mixture has not been explored in the open literature. Such measurements can verify the accuracy of the solid formation predictions and improve the confidence in using iso-pentane in cryogenic refrigeration systems used for LNG production and the pre-cooling refrigeration cycles of liquid hydrogen production systems.

Similar to LNG, liquid hydrogen could a viable method to store and transport this clean energy carrier across wide ranges of locations. However, to produce liquid hydrogen, the liquefaction system must decrease the temperature of the hydrogen feed down to 20 K, which those cryogenic refrigeration cycles are extremely energy-intensive and expensive-to-operate systems. Adding high-boiling components like methane, ethane, propane and nitrogen to the refrigerant mixtures in different stages of the hydrogen liquefaction processes can improve the heat transfer properties of the coolant and decrease the overall power consumption while posing a freeze-out risk at extreme cryogenic temperatures. The mixed refrigerants including these heavy compounds in mixtures with lighter components like hydrogen, helium and neon should be investigated for the purpose of freeze-out risk assessments. These investigations will help verify the solid formation predictions of the thermodynamic models and ensure the reliability of cryogenic refrigeration cycles that can reduce the overall costs of liquid hydrogen production.

6.3 References

[1] Fuller LE, Parks DJ, Fletcher EA. Flat flames in tubes—easy fundamental flame speed measurements. Combust Flame 1969;13:455–60. doi:https://doi.org/10.1016/0010-2180(69)90084-4.

[2] Kunz O, Wagner W. The GERG-2008 Wide-Range Equation of State for Natural Gases

and Other Mixtures: An Expansion of GERG-2004. J Chem Eng Data 2012;57:3032–91. doi:10.1021/je300655b.

[3] Lemmon EW, Bell I, Huber ML, McLinden MO. NIST Standard Reference Database 23: Reference Fluid Thermodynamic and Transport Properties-REFPROP, Version 10.0 n.d.

[4] Infochem / KBC Advanced Technologies Ltd. MultiFlash User Guide for Models and Physical Properties. 2017.

[5] Adams RA, Stein FP. Vapor-Liquid Equilibria for Carbon Dioxide-Difluoromethane System. J Chem Eng Data 1971;16:146–9. doi:10.1021/je60049a015.

[6] Rivollet F, Chapoy A, Coquelet C, Richon D. Vapor-liquid equilibrium data for the carbon dioxide (CO2) + difluoromethane (R32) system at temperatures from 283.12 to 343.25 K and pressures up to 7.46 MPa. Fluid Phase Equilib 2004;218:95–101. doi:10.1016/j.fluid.2003.12.002.

[7] Arami-Niya A, Xiao X, Al Ghafri SZS, Jiao F, Khamphasith M, Sadeghi Pouya E, et al. Measurement and modelling of the thermodynamic properties of carbon dioxide mixtures with HFO-1234yf, HFC-125, HFC-134a, and HFC-32: vapour-liquid equilibrium, density, and heat capacity. Int J Refrig 2020;118:514–28. doi:10.1016/J.IJREFRIG.2020.05.009.

[8] Di Nicola G, Giuliani G, Polonara F, Stryjek R. Solid-liquid equilibria for the CO2 + N2O, CO2 + R32, and N2O + R32 systems. Fluid Phase Equilib 2007;256:86–92. doi:10.1016/j.fluid.2006.11.015.

[9] Peng D-Y, Robinson DB. A New Two-Constant Equation of State. Ind Eng Chem Fundam 1976;15:59–64. doi:10.1021/i160057a011.

[10] Martin Trusler JP. Equation of State for Solid Phase I of Carbon Dioxide Valid for Temperatures up to 800 K and Pressures up to 12 GPa. J Phys Chem Ref Data 2011;40. doi:10.1063/1.3664915.

[11] Würflinger A. Differential thermal analysis under high pressure IV: Low-temperature DTA of solid-solid and solid-liquid transitions of several hydrocarbons up to 3 kbar. Berichte Der Bunsengesellschaft Für Phys Chemie 1975;79:1195–201.

doi:10.1002/bbpc.19750791206.

[12] Reeves LE, Scott GJ, Babb SE. Melting Curves of Pressure-Transmitting. J Chem Phys 1964;40.

[13] The University of Western Australia FS and R. ThermoFAST 1.2.1: thermodynamic calculator for natural gas properties. 2019.

[14] Baker CJ, Oakley JH, Rowland D, Hughes TJ, Aman ZM, May EF. Rapid Simulation of Solid Deposition in Cryogenic Heat Exchangers To Improve Risk Management in Liquefied Natural Gas Production. Energy & Fuels 2018;32:255–67. doi:10.1021/acs.energyfuels.7b03057.

[15] Baker C, Siahvashi A, Oakley J, Hughes T, Rowland D, Huang S, et al. Advanced predictions of solidification in cryogenic natural gas and LNG processing. J Chem Thermodyn 2019;137:22–33. doi:10.1016/j.jct.2019.05.006.

[16] Di Nicola G, Brandoni C, Di Nicola C, Giuliani G. Triple point measurements for alternative refrigerants. J Therm Anal Calorim 2012;108:627–31. doi:10.1007/s10973-011-1944-4.

Glossary

Term	Definition
Average absolute deviation (AAD)	A statistical value showing the average distance between each data value and the mean of a particular data set.
Binary interaction parameter (BIP)	A BIP represents the nature of molecular interaction between various substances of a mixture in thermodynamic predictive models.
Burning velocity (BV)	The speed at which a flame propagates in comparison with the unburned gas.
Chlorofluorocarbons (CFCs)	Synthetic, non-toxic, non-flammable gases containing atoms of carbon, chlorine, and fluorine, which are used in the manufacture of aerosol sprays and former generation of refrigeration systems.
Equation of estate (EOS)	A thermodynamic expression or model that correlates pressure, temperature and volume.
Fluorinated gases (F-gases)	Synthetic gases including hydrofluorocarbons, hydrofluoroolefins, perfluorocarbons, sulphur hexafluoride, and nitrogen trifluoride that are emitted from a variety of household, commercial, and industrial applications and processes.
Gas Chromatograph (GC)	An analytical technique to separate the chemical substances of a sample mixture and determine their quantity (fraction in the sample mixture).
Global warming potential (GWP)	A measure of the amount of energy absorbed by the emissions of 1 ton of a gas relative to the emissions of 1 ton of Carbon Dioxide (CO2) over a specific period.
Greenhouse gases (GHGs)	Gases with the ability to absorb and emit radiant energy usually within the thermal infrared range that can cause the greenhouse effect.
Hydrochlorofluorocarbons (HCFCs)	Synthetic substances consisted of hydrogen, chlorine, fluorine, and carbon with 1-17 years of stay length in the atmosphere and are used as the working fluids of domestic refrigeration systems.

Hydrofluorocarbons (HFCs)	Synthetic gases with atoms of hydrogen, fluorine and carbon and are commonly used in refrigeration, air-conditioning (AC), building insulation, fire extinguishing systems.
Hydrofluoroolefins (HFOs)	Unsaturated organic gases composed of hydrogen, fluorine and carbon that are of interest to be used as the working fluid of modern refrigeration systems.
Liquefied Natural Gas (LNG)	Natural gas that has been cooled down to its liquid form for ease and safety of non-pressurized storage or global transport.
Minimum ignition energy (MIE)	The minimum amount of energy is needed to ignite a refrigerant/air mixture.
Mixed refrigerant (MR)	A mixture of various chemicals is employed as the working fluid of refrigeration systems.
Ozone depletion potential (ODP)	A measure of damage a refrigerant causes to the ozone layer compared with an identical amount of trichlorofluoromethane (CFC-11)
Root mean square deviation (RMSD)	A statistical value showing the square root of the sum of the squares of the deviations between the calculated and measured property divided by the number of the deviations.
Solid-fluid equilibrium (SFE)	A state at which both the fluid (including vapour/liquid) and solid phases of a mixture exist.
Thermal conductivity detector (TCD)	A universal, non-destructive, concentration-sensitive detector used in gas chromatography.
Vapour-liquid equilibrium (VLE)	A state at which both the liquid and vapour phases of a pure component or mixture exist.

Appendices

A Appendix A | Supplementary information for Chapter 2

Forward – The full text of this appendix has been published as the supporting information (SI) in the *Journal of Hazardous Materials* in 2021 (DOI: https://doi.org/10.1016/j.jhazmat.2020.124781). It has been reformatted with minor amendments to fit style and structure of this thesis.

A.1 Hartmann bomb

Figure A.1 shows a schematic of the Hartmann bomb apparatus as a recommended configuration for the minimum ignition energy measurement by EN 1839 [1], according to which a semi-closed tube can be used to measure the minimum ignition energy of a combustible mixture. The Hartmann bomb used in this work (Figure A.1) is a vertical cylindrical vessel with 1.4 L volume (70 mm diameter and 370 mm height) with perforated aluminium foil placed across the top end and closed bottom end of the cylinder. These holes ensure the pressure remains at atmospheric conditions.

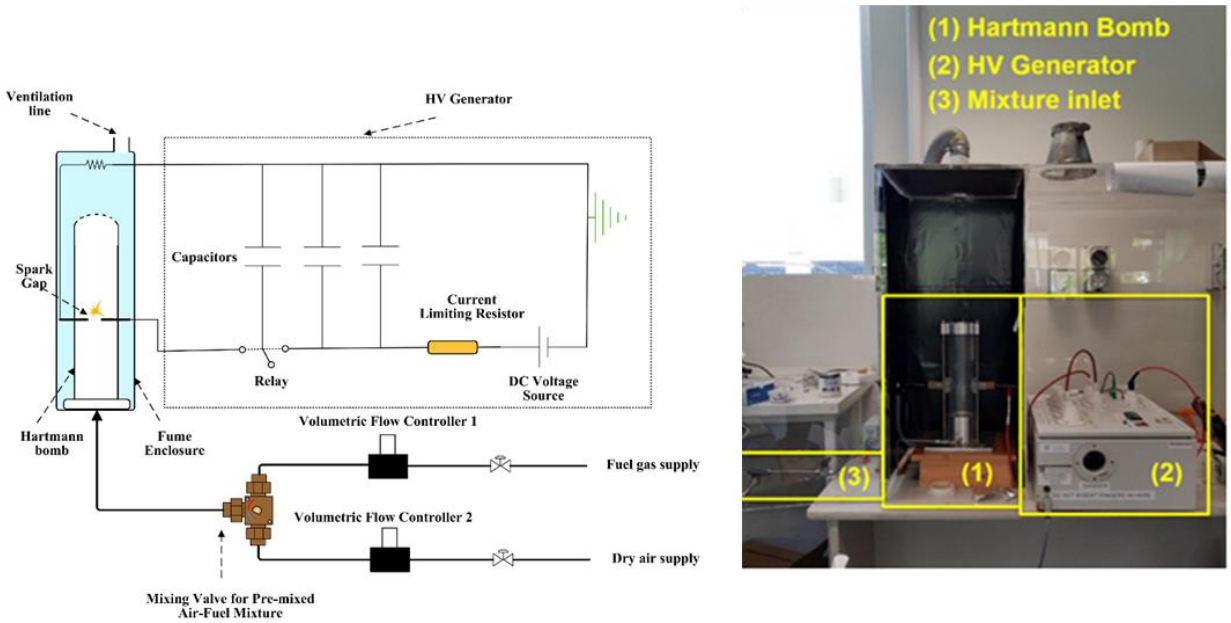

Figure A.1: A schematic of the Hartmann bomb apparatus configuration and photographs of the experimental set-up

A.2 Neutralising the combustion products

The combustion of either R32 or R1234yf generates hydrogen fluoride (HF) gas as one of the products. The combustion reaction of R32 with dry air is as follows:

$$CH_2F_2 + (O_2 + 3.77N_2) = CO_2 + 2HF + 3.77\ N_2$$

The combustion reaction of R1234yf is as follows:

$$CF_3CF{=}CH_2 + 2.5(O_2 + 3.77N_2) = 2CO_2 + COF_2 + 2HF + 9.425N_2$$

Thus the primary mitigation of the hazard required in this work was the containment and neutralisation of the hydrogen fluoride (HF) combustion product. The arrangement of the specific minimum ignition energy measurement configuration is shown in Figure 2.1. The flammable mixtures of R32, R1234yf, or their blends with air were prepared in the gas mixing section (located on a manifold in the lab outside the main enclosure), connected to the combustion tube. The cylindrical tube was located within a custom enclosure purged with a continuous stream of N_2 to ventilate any possible leak from the system that might occur during the experiment. The outlet stream from the cylindrical tube was vented to the expansion tank, followed by two cylinders containing a soda-lime tower and a sodium hydroxide (NaOH) solution. The volume combusted was 2 L, and thus, in each experiment with R32 up to 0.6 L of HF (0.72 g) was produced. For experiments with R1234yf, 0.3 L (0.33 g) HF and 0.14 L (0.43 g) carbonyl fluoride (COF_2) were produced. The local partial pressure of the HF or COF_2 in the gas phase did not exceed 35 kPa for either reaction, being well below the vapour pressures of these compounds at 20 °C (104 kPa and 5530 kPa, respectively). These products were neutralised by a Soda-Lime Tower and a NaOH solution through which the effluent gases were forced to flow. The combustion products left the cylindrical tube due to their expansion after combustion, the purging flow of nitrogen, and the presence of a vacuum pump connected

to the lower side of the soda-lime tower and NaOH solution. Soda Lime consisted of calcium hydroxide ($Ca(OH)_2$), and thus the neutralising reactions were:

$$NaOH + HF = NaF + H_2O$$

$$Ca(OH)_2 + 2HF = CaF_2 + 2H_2O$$

$$4NaOH + COF_2 = Na_2CO_3 + 2NaF + 2H_2O$$

To neutralise the combustion products of a single batch experiment, 1.33 g $Ca(OH)_2$ was needed. Therefore, the 2 L size of the soda-lime tower, containing 1500 g of soda-lime granules of 75 % $Ca(OH)_2$ had more than eight times the amount of material needed to complete 100 batch experiments. The purpose of the NaOH solution was to neutralise COF_2, which can pass through the soda-lime tower. To neutralise the amount of COF_2 produced in a single batch experiment, 0.71 g NaOH was needed. Thus 2 litres of the two molar NaOH solution was able to neutralise products from more than 210 experiments.

The CaF_2 product of the neutralisation reaction in the soda-lime tower was insoluble in water, posing no further health or environmental hazard and can be disposed of in the landfill. The NaF solution can be treated by combining it with additional soda-lime $Ca(OH)_2$ to form CaF_2. The corrosion rate of gaseous HF in continuous contact with carbon steel is less than 0.25 mm per year; furthermore, to achieve this, a continuous flow velocity of 1.5 m/s was required to remove the protective film of iron fluoride that would form on the carbon steel. Thus corrosion of the stainless steel tubing was highly unlikely.

A.3 Spark Generation System

Figure A.2 illustrates the electrical circuit employed to generate a spark within the ignition vessel. First, a high voltage power supply (GLOW 28720 Digit H.V Source Meter generator, up to 20 kV) charged a capacitor bank (ranged between 0.3 nF and 20 nF) to a requisite voltage

that would be sufficient to breakdown the dielectric barrier of the air gap between two electrodes in the cylindrical vessel (typically higher than 6 kV). In the second step, a relay connected the capacitor to the discharge circuit containing the electrodes, equipped with a known high-power resistor, R2 (in range of 0.35-27 Ω), an inductor (1 mH), a current probe (Pearson, Model 6595) and a voltage probe (Pintek, Model HVP-39pro) for measuring the current and high voltage present in the circuit. These probes were connected to a digital oscilloscope (Keysight, Model DSOX3022T). Resistance (R2) affected the oscillations of the spark voltage and current signals by damping them. Also, it reduced the energy and duration of the spark. The inductor increased the spark duration by order of magnitude relative to a circuit without any inductor and made the associated voltage and current oscillations more regular and easier to integrate. Figure A.3 indicates the voltage and current oscillations measured for a spark discharge with 8 mJ energy.

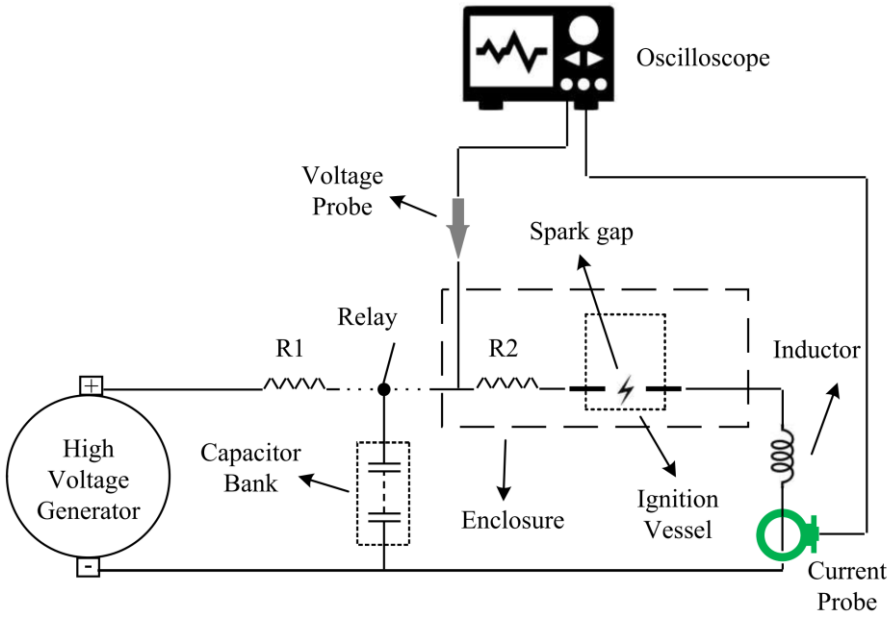

Figure A.2: The electrical circuit used to generate and monitor a spark in the Hartmann bomb.

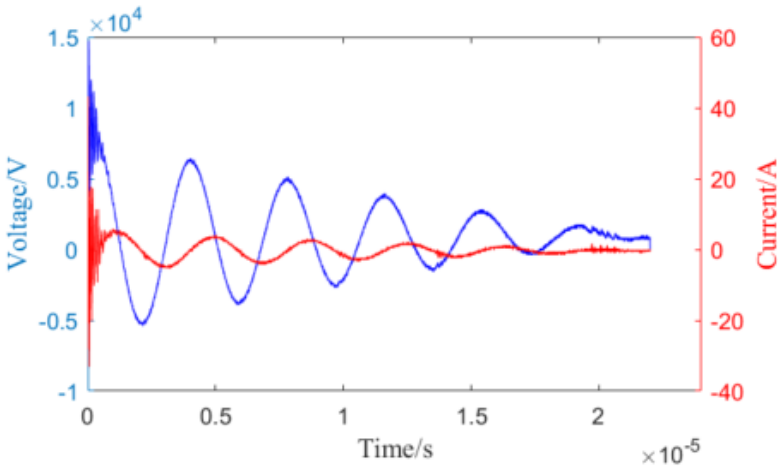

Figure A.3: The real-time voltage and current oscillations during a spark discharge with 8 mJ energy.

The spark is the energy dissipated during the electrical breakdown between electrodes. To calculate the spark energy, the time-dependent voltage $v(t)$ and current $i(t)$ needs to be monitored during the spark, from which the spark energy, E_{spark}, can be calculated [2]:

$$E_{Spark} = \int_0^t v(t)i(t)dt - E_{circuit} \quad \text{(A-1)}$$

Here E_{circuit} is the energy dissipated by the impedance in the circuit containing the electrodes. Given the resistance, R, of the circuit, the energy dissipated in it can be calculated by [3]:

$$E_{circuit} = \int_0^t Ri(t)^2 dt \quad \text{(A-2)}$$

Alicat Scientific mass flow controllers were used to prepare the mixture via an inline mixer. The uncertainty of these mass flow controllers is as below:

$$u_{flow} = (0.8\ \%\ \text{reading value} + 0.2\ \%\ \text{of Full Scale}) \quad \text{(A-3)}$$

Guide to the Expression of Uncertainty in Measurements (GUM) method was used for determining standard uncertainties for the experimental quantities [4]. The uncertainty

associated with the equivalence ratio determined by the mixture preparation is then derived from the uncertainties of the two mass flow controllers:

$$u^2(\varphi) = \left[\frac{\partial \varphi}{\partial v_{fuel}} \times u(v_{refrigerant})\right]^2 + \left[\frac{\partial \varphi}{\partial v_{air}} \times u(v_{air})\right]^2 \quad \text{(A-4)}$$

Here, v_{fuel}, v_{air} and φ stand for standard volumetric flow of the refrigerant, standard volumetric flow of air and the equivalence ratio. A similar expression can be written for standard uncertainty associated with the refrigerant concentration in a refrigerant/air mixture.

For spark energy measurements, a Pearson current monitor (Model 6595) and a Pintek high voltage probe (Model HVP-39pro) with a relative uncertainty of 1% in the measured value were used for the current and voltage measurements, respectively. The standard uncertainty in the spark power ($P_{spark} = VI$) is then given by:

$$u^2(P_{spark}) = \left[\frac{\partial P_{spark}}{\partial V} \times u(V)\right]^2 + \left[\frac{\partial P_{spark}}{\partial I} \times u(I)\right]^2 \quad \text{(A-5)}$$

from which the standard uncertainty in the spark energy can be obtained:

$$u(E_{Spark}) = \int u(P_{spark})dt \quad \text{(A-6)}$$

The final uncertainty for spark energy was either the calculated standard uncertainty or the standard deviation of the measured values, whichever was more significant. Fuller et al. [5] assumed a relative uncertainty of 4.25% to address the effect of the heat loss to the wall and upturned edge of the flat flame in the laminar burning velocity measurement. In this study, either a similar relative uncertainty or the standard deviation of the measured laminar burning velocities were used to determine the overall uncertainty, whichever was higher.

A.4 Bunsen Burner and Vertical Tube Burning Velocity Measurement Methods

In Bunsen burner method, a burner with a stainless steel tube with an ID of 10.3 mm and a length of 520 mm was coupled with a Z-type Schlieren imaging technique [6,7]. After maintaining a laminar flame on the tip of the burner, the volumetric flow rate of the refrigerant/air mixtures (Q) together with the flame surface area (A_u) were measured and the laminar burning velocity is calculated via:

$$S_U = \frac{Q}{A_u} \tag{A-7}$$

Figure A.4 shows a schematic diagram of the Vertical Tube configuration used in this work for the BV measurements, which is similar to the approach followed by Jabbour et al. [8]. The flame propagated from the bottom end of the 1.5 m long tube (50 mm ID) to the top end in an upward direction. The velocity of the flame (tip), S_{flame}, was then determined from data recorded with a high-speed camera. The observed flame tip velocity, however, was increased by the effects of buoyancy, causing it to propagate up the tube at a rate higher than the burning velocity, S_U. A correction for the effects of buoyancy must, therefore, be applied via [8]:

$$S_U = S_{flame}(\frac{a}{A_{flame}}) \tag{A-8}$$

Here A_{flame} is the flame's surface area, and a is the flame's cross-sectional area; these geometrical features of the flame were derived from images captured by the video camera, as shown in Figure A.5.

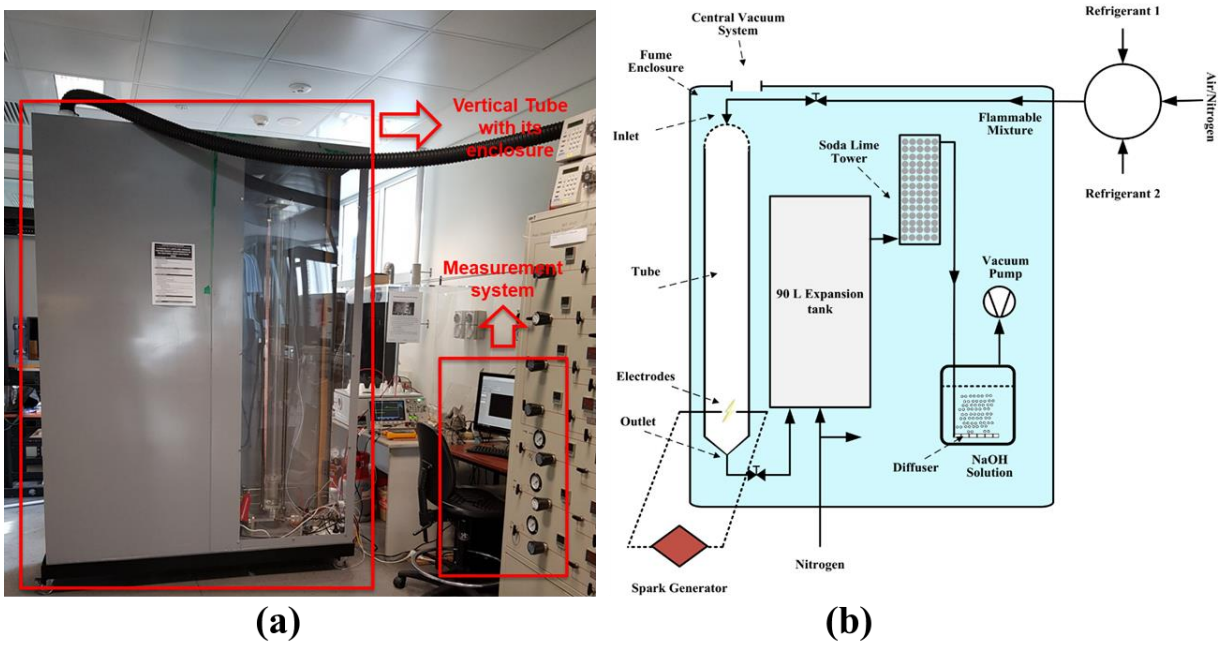

Figure A.4: photographs (a) and Schematic (b) of the Vertical Tube apparatus used for the burning velocity measurements.

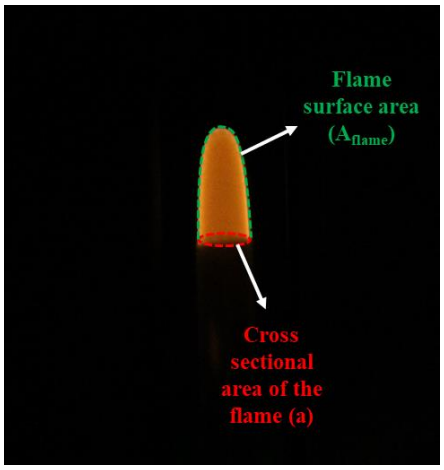

Figure A.5: Flame cross-sectional and surface area of the ammonia/air mixture.

A.5 Reference

[1] EN 1839. Determination of Explosion Limits of Gases and Vapours. Eur Comm Stand 2003;Brussels.

[2] Lee JJ, Shepherd JE. Spark Ignition Measurements in Jet A : part II. Test 2000.

[3] Alexander C, Sadiku M. Fundamentals of Electric Circuits. 4th ed. McGraw Hill Higher Education; 2008.

[4] Joint Committee for Guides in Metrology. Evaluation of measurement data — Guide to the expression of uncertainty in measurement. Int Organ Stand Geneva ISBN 2008;50:134. doi:10.1373/clinchem.2003.030528.

[5] Fuller LE, Parks DJ, Fletcher EA. Flat flames in tubes—easy fundamental flame speed measurements. Combust Flame 1969;13:455–60. doi:https://doi.org/10.1016/0010-2180(69)90084-4.

[6] Lesmana H, Zhu M, Zhang Z, Gao J, Wu J, Zhang D. Experimental and kinetic modelling studies of laminar flame speed in mixtures of partially dissociated NH3 in air. Fuel 2020;278:118428. doi:10.1016/j.fuel.2020.118428.

[7] Shang R, Zhang Y, Zhu M, Zhang Z, Zhang D, Li G. Laminar flame speed of CO2 and N2 diluted H2/CO/air flames. Int J Hydrogen Energy 2016;41:15056–67. doi:10.1016/j.ijhydene.2016.05.064.

[8] Clodic D, Jabbour T. Method of test for burning velocity measurement of flammable gases and results. HVAC R Res 2011;17:51–75. doi:10.1080/10789669.2011.543252.

B Appendix B │ Measurement and modelling of the thermodynamic properties of carbon dioxide mixtures with HFO-1234yf, HFC-125, HFC-134a, and HFC-32: vapour-liquid equilibrium, density, and heat capacity

Authors: Arami-Niya, A., Xiao, X., Al Ghafri, S. Z. S., Jiao, F., Khamphasith, M., Sadeghi Pouya, E., **Seyyedsadaghiani, M.**, Yang, X., Tsuji, T., Seiki, Y., May, E. F.

Forward – The full text of this chapter has been published in the *International Journal of Refrigeration* in 2020 (DOI: https://doi.org/10.1016/j.ijrefrig.2020.05.009). Mirhadi's contributions can be summarised as follows: Commissioned VLE measurement setups; Developed VLE measurement procedures; Calibrated the Gas Chromatograph detector; Executed VLE experimental work. The full text of the publication has been reformatted with minor amendments to fit style and structure of this thesis.

B.1 Abstract

Measurements of the thermodynamic properties for a series of more environmentally-friendly refrigerant mixtures containing hydrofluorocarbons (HFCs), hydrofluoroolefins (HFOs), and carbon dioxide (CO_2) were conducted. These new property data help increase confidence in the design and simulation of refrigeration processes that use CO_2 + HFO + HFC refrigerant mixtures. The HFCs of interest were R32, R125, and R134a and the HFO tested was R1234yf. The measurements collected were prioritised to fill gaps in the available literature data. Vapour-liquid equilibrium plus liquid-phase density and heat capacity data were collected for different binary mixtures containing HFCs, HFOs and CO_2, with the liquid phase measurements spanning (223 to 323) K and (1 to 5) MPa. The measured data, as well as data from the literature, were then used to tune the mixture parameters in the models used by NIST's REFPROP 10 software package to improve the prediction of thermodynamic properties for these fluids. To test the predictive capabilities of the models tuned to the binary mixtures, thermodynamic property data were also measured for four ternary mixtures and a five-component mixture of HFCs, HFOs and CO_2. The new models developed in this work significantly improved the root mean square deviations of the predicted properties for these multi-component mixtures: the most significant reductions were about a factor of two in density.

B.2 Nomenclature

A	the GC peak area	T_{step}	temperature step of calorimetry experiment
c_p	isobaric specific heat capacity	ρ	density
N_{tuned}	number of data points used in fitting of Helmholtz model binary interaction parameters		
k	GC response factor		
p	pressure		
R	GC peaks areas ratio of 2 components	**Subscripts**	
T	temperature		
u	absolute uncertainty	c	at the critical point
x	liquid mole fraction	cal	calculated
y	vapour mole fraction	i	integer counter representing a component number in a mixture
z	overall mole fraction	j	integer counter representing a component number in a mixture
α	the relative response factor in GC calibration	liq	liquid
β_v	Helmholtz energy model binary interaction parameter	n	integer counter for data point number
β_T	Helmholtz energy model binary interaction parameter	r	relative
γ_v	Helmholtz energy model binary interaction parameter	sat	under saturation
γ_T	Helmholtz energy model binary interaction parameter	vap	vapour

B.3 Introduction

The global warming potential (GWP) of dominant hydrofluorocarbon refrigerants (HFCs) such as R134a motivate the search for new refrigerants with a lower effect on climate that can efficiently work in current refrigeration cycles. Hydrofluoroolefins (HFOs) are a new generation of refrigerants with a much lower global warming potential than conventional HFC refrigerants. However, the performance of HFOs in existing refrigeration cycles is generally inferior, with a higher amount of energy required for the same cooling power. Another concern about HFOs relates to their Standard 34 classification by the American Society of Heating, Refrigerating and Air-Conditioning Engineers (ASHRAE) as “marginally flammable”[1,2]. Blending these new types refrigerants with existing ones offers a way to improve the performance and decrease the GWP of the working fluid simultaneously [3].

The low GWP and suitable phase behaviour of fluids such as carbon dioxide (R744), propane (R290), and ammonia (R717), make them promising candidates for reducing the environmental impact of industrial refrigerants. Among this class of refrigerants, R744 is more suitable for

use in HFO-containing refrigerant blends because of its lower flammability and toxicity compared with R290 and R717, respectively [4,5]. Non-ignitable HFC compounds such as R125 and R134a can also reduce the flammability of HFOs and improve the mixture's performance. Mixtures of HFOs, HFCs and CO_2 are thus promising candidates for refrigerants to be used in air conditioning and building cooling applications; these blends present high working capacity with low GWP and flammability. However, to design and simulate a refrigeration system, property data for the fluid mixtures need to be measured at relevant conditions of pressure, temperature and composition so that equations of state and transport property models can be anchored to them. Recently, Bobbo et al.[6] reviewed the state of the art for experimental thermophysical properties of low GWP halocarbon refrigerants, with May and co-workers [7,8] subsequently reporting data and tuned Helmholtz models for binary mixtures of HFOs and HFCs. Nevertheless, still there is still a significant need for new experimental data for a wide range of both properties and conditions to tune the models used by engineers for refrigerant design and optimisation.

The current study aims to provide the reference quality thermodynamic property data for the binary, ternary and multi-component mixtures of HFO-1234yf with HFC-32, HFC-125, HFC-134a and CO_2 (R744) listed in Table B.1. Vapour-liquid equilibrium, as well as density and heat capacity data in the liquid phase region of the refrigerant binaries, were measured at different temperatures and pressures. The acquired data, as well as available literature data, were then used to validate and, if required, improve the Helmholtz energy equations of state (EOS) available in the software package REFPROP 10 [9]. After improvement of the model's representation of the binary systems, the predictive capability of the model for the ternary (CO_2 + R1234yf + R32) and five-component (CO_2 + R1234yf + R32 + R125 + R134a) mixtures were tested against the new experimental data.

Table B.1: Details of the refrigerants used in the mixtures studied.

ASHRAE Refrigerant Number	IUPAC name	Chemical formula	CAS #	Refrigerant Type	Supplier	Supplier Purity (%)
R774	Carbon dioxide	CO_2 	124-38-9	Natural	Core gas	99.95
R32	Difluoromethane	CH2F2 	75-10-5	HFC	Core gas	99.5
R134a	1,1,1,2-Tetrafluoroethane	CH2FCF3 	811-97-2	HFC	Core gas	99.5
R125	Pentafluoroethane	C2HF5 	354-33-6	HFC	Core gas	99.95
R1234yf	2,3,3,3-Tetrafluoroprop-1-ene	C3H2F4 	754-12-1	HFO	Core gas	99.99

B.4 Material and methods

B.4.1 *Materials*

The refrigerants investigated in this study and their supplied purity are given in Table B.1. The reference Helmholtz-free energy equations of state (EOS) implemented in the REFPROP 10 software that were used to describe the thermodynamic properties of the pure refrigerants considered in this study are listed in Table B.2. The expected uncertainties of the reference EOS for each of these various thermodynamic properties are also included in Table B.2. In addition to being the basis of the mixture models, these reference EOS for the pure refrigerants were used for the necessary mixture-preparation calculations.

Table B.2: Components studied in this work, sources of their pure fluid equations of state (EOSs) in the software REFPROP 10 and expected standard relative uncertainties for thermodynamic properties as indicated by summary of the original reference given in REFPROP 10.

Component	***Reference equation of state***	***Expected relative uncertainty (%)***
CO_2	Span and Wagner, 1996 [10]	ρ = 0.03-0.05 p_{sat} = 0.012 $c_{p,liq}$ = 1.5
R1234yf	Richter et al., 2011 [1][11]	ρ_{vap} = 0.5 ρ_{liq} = 0.1 p_{sat} = 0.1 $c_{p,liq}$ = 5
R32	Tillner-Roth and Yokozeki, 1997 [12]	ρ = 0.05 p_{sat} = 0.02 $c_{p,liq}$ = 0.5-1
R134a	Tillner-Roth and Baehr, 1994 [13]	ρ = 0.05 p_{sat} = 0.02 $c_{p,liq}$ = 0.5-1
R125	Lemmon and Jacobsen, 2005 [14]	ρ = 0.04-0.5 p_{sat} = 0.2 $c_{p,liq}$ = 0.5

Al Ghafri et al. [7] described the procedure used to volumetrically prepare and transfer binary refrigerant mixtures into various apparatus that were also used here for the density and heat capacity measurements. In summary, the procedure consisted of transferring measured amounts of each pure component from one high-pressure syringe pump into another high-pressure syringe pump that also contained a mixing capability. Once all the components had been loaded, they were then mixed at high-pressure (5 MPa) under liquid phase conditions. This homogenous liquid mixture was then transferred into the apparatus at constant pressure by first back-filling and pressurising (to 5 MPa) the apparatus and lines connecting it to the mixing pump with a pure component contained in a third syringe pump. The mixing pump was then used to displace the pure component with the synthetically prepared mixture by injecting at a fixed, slow flow rate while the third syringe pump was maintained the system pressure by withdrawing the pure component as the mixture was injected. To ensure any impact on the composition of the mixture in the apparatus was negligible, the displaced volume was at least several times that of the apparatus volume. Specific details of the syringe pump arrangements and connections to the various apparatus are shown in Sections B.4.3 and B.4.4.

The formula provided by Al Ghafri et al. [7] for estimating the standard mole fraction uncertainty $u(x_i)$ of each component in the synthetic binary is extended here to the general case of a multi-component mixture preparation. For component i in an N component mixture, the standard uncertainty in the mole fraction of x_i is given by:

$$u(x_i) = x_i(1-x_i)\sqrt{u_r(n_i)^2 + u_r(N_k)^2}, \text{ where } N_k = \sum_{j \neq i} n_j \qquad \text{B.1}$$

Here u_r denotes the standard relative uncertainty of a quantity and n_i is the molar amount of component *i* added to the mixture. From Equation B.1 it apparent that in general, the uncertainty in x_i depends on the uncertainties in the amounts of all the components added to the mixture. For the special case of the binary mixture, it can be shown that Equation B.1 implies $u(x_1) = u(x_2)$. However, for a multi-component mixture, each component's mole fraction has an uncertainty that differs from those of the other components. For example, a ternary mixture with components *i, p* and *q* has $u(x_i)$ given by

$$u(x_i) = x_i(1-x_i)\sqrt{u_r(n_i)^2 + \left(\frac{n_p}{n_p+n_q}\right)^2 \cdot u_r(n_p)^2 + \left(\frac{n_q}{n_p+n_q}\right)^2 \cdot u_r(n_q)^2} \qquad \text{B.2}$$

In this work, the uncertainties in the amounts of each component transferred into an apparatus arise principally from the uncertainties in displacement volumes measured by the syringe pumps used in the preparation process.

B.4.2 *Vapour-liquid-equilibrium*

B.4.2.1 Apparatus overview

The vapour-liquid equilibrium (VLE) apparatus employed in this study is illustrated in Figure B.1. Two systems (called System 1 and System 2 henceforth) were used in parallel to improve the data collection rate. System 1 and System 2 shared one gas chromatograph (GC, Agilent 7890A) and were otherwise fundamentally the same as the system described by May and co-workers [7,15]. The main difference between the current set-up and those detailed previously was the use of a thermal conductivity detector (TCD) instead of a flame ionization detector for the GC measurements. The VLE cells were placed in Memmert ovens (UN110) with a normal operating temperature range from 5 °C above ambient to 300 °C. To achieve lower temperatures, a copper plate-spiral tubes-plate was designed, positioned under the cells and connected to refrigerated circulators following an approach to that of Efika et al. [16]. Two fans inside the ovens were also responsible for circulating the air, thereby making the temperature profile more uniform.

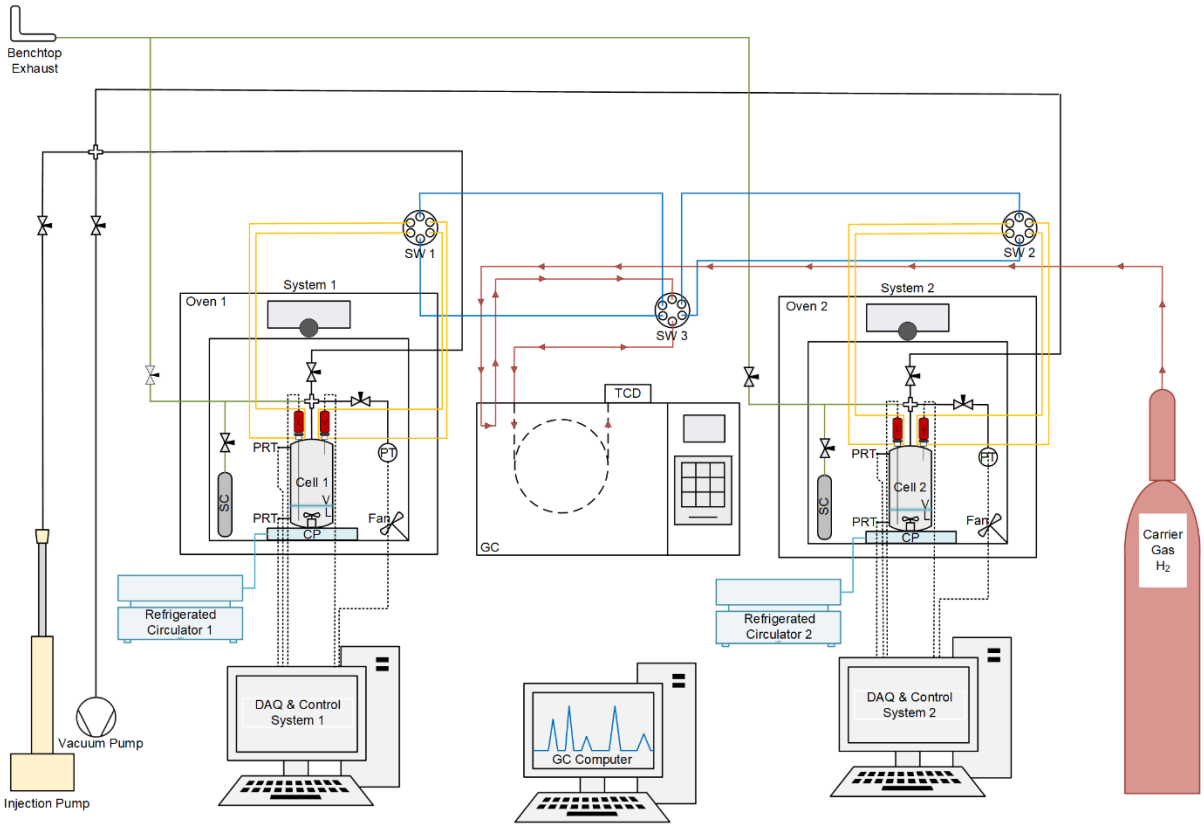

Figure B.1: Schematic diagram of the VLE apparatus (CP: Cooling plate; DAQ: Data acquisition; GC: Gas chromatograph, PRT: Platinum resistance thermometer; SC: Sample cylinder; SW: Switch valve; TCD: Thermal conductivity detector). SW 3 was used to shift from Cell 1 to Cell 2 (or vice versa). SWs 1 and 2 were used to shift from the vapour ROLSI® sampler [17,18] to the liquid ROLSI® sampler (or vice versa) for each cell.

For the VLE experiments, a capillary column (Agilent J&W HP/PLOT-U) was used to separate the components of the sample and adjust the requisite retention time between the GC peaks for most of the mixtures, except for five-component mixture and binary mixture of R32 + CO_2. In those cases, a packed column (Shinwa Express Sunpak-H 80/100 Glass) was employed to improve separation of the components.

B.4.2.2 GC calibration

To calibrate the GC, binary mixtures of the refrigerants with CO_2 as the common compound (i.e., CO_2 + the other refrigerant), were volumetrically prepared at different ratios in sample cylinders. Additionally, for the 5-component experiments, two ternary mixtures with R125 as the common compound (CO_2 + R32 + R125 and R134a + R1234yf + R125) were volumetrically prepared at different concentrations of the components. The exact composition of the prepared calibration mixtures was gravimetrically determined, as described in the Supporting Information section.

Each calibration mixture was transferred to the VLE cell after it was heated to the temperature at least 10 K above the mixture's calculated cricondentherm (T_{Heated}) to make sure there was only one phase in the cylinder. The VLE cell was also heated to T_{Heated} and after reaching a stable temperature and pressure, samples were taken from the single-phase mixture. Different opening times of the ROLSI® IV electromagnetic sampling valve [17,18] were selected to ensure that a broad enough range of GC peak areas was covered.

The average of the peak areas obtained for each component, A_i, were combined in a ratio A_i / A_j and plotted against the known mole fraction ratio z_i / z_j. The calibration data were fitted to a linear equation with the intercept constrained to zero:

$$(z_i/z_j) = k_{ij} \times (A_i/A_j) \qquad \text{B.3}$$

where k_{ij} denote the relative response factor for the two compounds. In Equation B.3 component j was CO_2 for binary and ternary experiments, while it was R125 for the 5-component experiments. To convert the integrated GC peak areas to mole fractions, Equation B.3 and the normalisation requirement, $\sum_{i=1}^{n} z_i = 1$, were solved simultaneously.

The GC calibration results (Figure B.10 and Figure B.11), the details of the GC temperature programs for the GC calibration and the VLE experiments (Table B.12), and the relative response factors (Table B.13) are reported in the Supporting Information.

B.4.2.3 Measurement procedure

After evacuating the VLE cell and the connection lines, the predetermined volumes of the pure refrigerant(s) were injected to the cell separately to achieve a target overall mixture composition. Then the cell was heated in the oven to a temperature 10 K above the predicted critical temperature of the injected mixture while the stirrer was on to produce a homogenous one-phase mixture. The overall composition of the mixture was confirmed by analysing samples taken from the top and bottom of the cell while it was still at the supercritical temperature. Then the oven's temperature was set to the desired measurement temperature with the stirrer on. Upon reaching an equilibrium condition, the vapour and liquid phases were sampled and the composition of each phase was determined by the GC.

B.4.2.4 Uncertainty calculation

The method used for the uncertainty estimation is similar to the method reported previously [7]. The only minor change was use of a relative calibration instead of an absolute calibration

for the GC's detector response. The combined uncertainty in the mole fraction is the sum of the contributions of the uncertainty in the temperature, pressure, GC's detector response factor and the area ratios used to determine each component molar fractions. Hence the following can be written for a binary system:

$$u^2(x_i) = \left(\frac{\partial x_i}{\partial T}\right)^2 u(T)^2 + \left(\frac{\partial x_i}{\partial p}\right)^2 u(p)^2 + \left(\frac{\partial x_i}{\partial k_{ij}}\right)^2 u\left(k_{ij}\right)^2 + \left(\frac{\partial x_i}{\partial R_{ij}}\right)^2 u\left(R_{ij}\right)^2 \qquad \text{B.4}$$

Here k_{ij} is the chromatographic response factor and $R_{ij} \equiv (A_i / A_j)$ is the area ratio of the chromatographic peaks for component *i* and component *j*. The uncertainty of the mole fraction arising from the peak area ratios and the detector calibration factor were determined from the standard deviation of the peak area ratios obtained during sampling, the uncertainties during calibration of both the peak area ratios, and the uncertainties of the measured pure substance masses from the gravimetric preparation. Although the manufacturer reported uncertainties for the PRTs and pressure transducers were 0.02 K and 0.01 % of the full-scale range (13.8 MPa), respectively, the thermal stability of the ovens meant these were increased to 0.1 K and 0.005 MPa, respectively.

B.4.3 *Density method*

B.4.3.1 Apparatus overview and experimental procedure

The density measurements were conducted with a commercial, high-pressure vibrating tube densimeter [7] (VTD), (Anton Paar, DMA HPM). The experimental setup was as described previously [7] except that the temperature control system was upgraded to a Weiss Environmental Chamber with a working temperature range of (203.15 to 453.15) K. A schematic of the entire system is shown in Figure B.2.

Before loading the mixtures prepared in ISCO Syringe Pump 1, the system up to V0 (Figure B.3) was flushed at least 3 times, evacuated and then pressurized with pure CO_2 to above the mixture's saturation pressure using ISCO Syringe Pump 3, with ISCO Syringe Pump 2 in an empty condition (minimum volume). To displace the mixture through the VTD and avoid any phase change or fractionation, ISCO Syringe Pump 3 was set in constant pressure mode, ISCO Syringe Pump 1 was placed in constant flow mode and set to a low flow rate (1 ml·min^{-1} or less), and valve V0 was opened. The displacement of the refrigerant mixture continued until at least three times the total volume of the VTD and transfer lines (V ≈ 10 ml) had been injected from ISCO Pump 1.

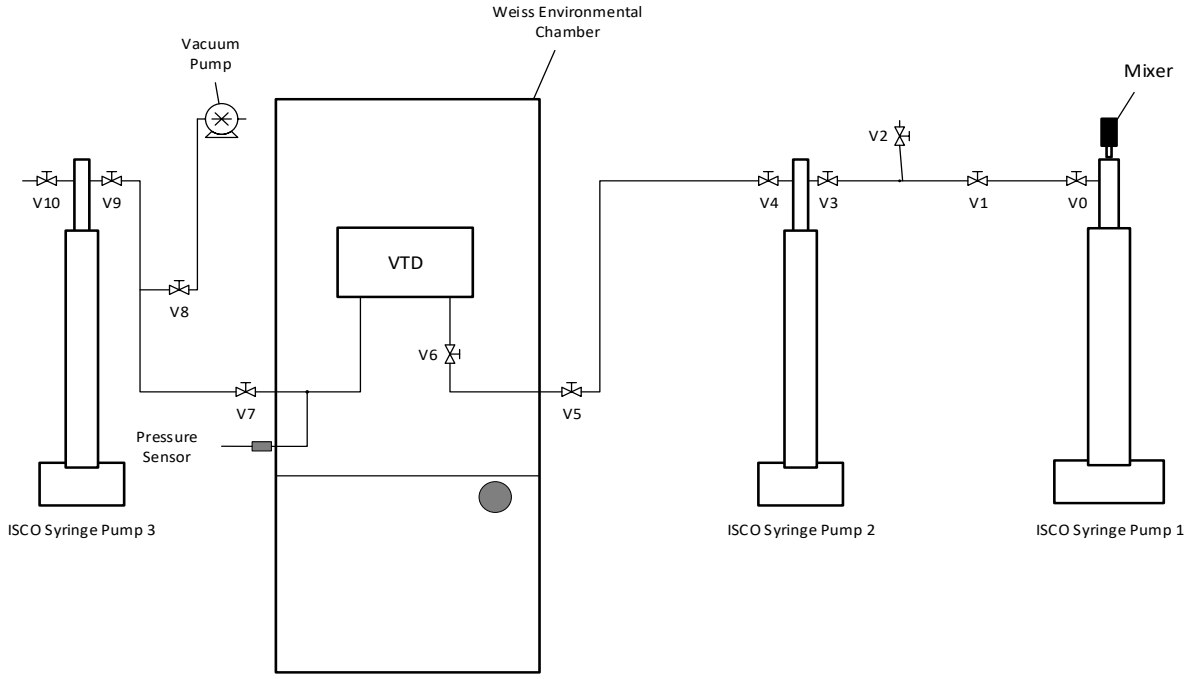

Figure B.2: Schematic diagram of the VTD assembly.

Once the displacement process was completed, V7 was closed and ISCO Pump 2 was set to refill at the same flowrate as ISCO Syringe Pump 1 (1 ml·min^{-1} or less) until the desired volume of mixture had been transferred into ISCO Syringe Pump 2. Then, V3 was closed and ISCO Syringe Pump 2 was set to constant pressure mode at the desired pressure for a few hours allowing the mixture inside the VTD to stabilize before the measurement was recorded.

The calibration of the VTD was extended to lower temperatures than previously reported for such instruments [19], and is detailed further by Jiao et al. [20]. The VTD was connected to a system controller (Anton Paar, Davis) which displayed the measured parameters including the pressure, p temperature and the tube's resonant period of oscillation (τ). These quantities were used to calculate the fluid mixture density (ρ_F) according to the model described by May et al. [21]:

$$\rho_F = \frac{(\rho_M / S_{00})}{(1+\alpha_V t+\beta_V p)} \times \left(\left(\frac{\tau}{\tau_{00}(1+\varepsilon_{\tau 1} t+\varepsilon_{\tau 2} t^2)}\right)^2 (1+\beta_\tau p)-1\right) \qquad \text{B.5}$$

Here t is the difference between the system temperature and a selected reference temperature (273.15 K); S_{00} is the geometric sensitivity factor of the evacuated tube at the reference temperature; τ_{00} is the resonance period of the evacuated tube at the reference temperature; $\varepsilon_{\tau 1}$

and $\varepsilon_{\tau 2}$ are the linear and quadratic temperature response coefficients of the spring constant, respectively; β_τ is the pressure response coefficient of the spring constant; and α_V and β_V are the linear temperature response and pressure response coefficients of tube volume, respectively.

The three parameters describing the vacuum resonance and its variation with temperature, τ_{00}, $\varepsilon_{\tau 1}$ and $\varepsilon_{\tau 2}$ were determined by linear least squares regression to data measured with the evacuated VTD while the remaining four parameters were determined by regression of pure methane and propane data measured over a wide range of pressure and temperature conditions, as shown in Figure B.12 of the SI section. The relative deviations between the fitted values and those predicted by the corresponding reference EOS implemented in REFPROP 10 [22,23] were between (-0.5 to 0.5) $kg \cdot m^{-3}$, respectively, which is excellent considering the wide temperature range considered in the calibration.

B.4.3.2 Uncertainty calculation

The combined standard uncertainty in density is estimated by Equation B.6:

$$u^2(\rho) = \left\{ \begin{array}{l} \left(\frac{\partial \rho}{\partial S_{00}}\right)^2 u^2(S_{00}) + \left(\frac{\partial \rho}{\partial \alpha_V}\right)^2 u^2(\alpha_V) + \left(\frac{\partial \rho}{\partial \beta_V}\right)^2 u^2(\beta_V) \\ + \left(\frac{\partial \rho}{\partial \tau_{00}}\right)^2 u^2(\tau_{00}) + \left(\frac{\partial \rho}{\partial \varepsilon_{\tau 1}}\right)^2 u^2(\varepsilon_{\tau 1}) + \left(\frac{\partial \rho}{\partial \varepsilon_{\tau 2}}\right)^2 u^2(\varepsilon_{\tau 2}) + \left(\frac{\partial \rho}{\partial \beta_\tau}\right)^2 u^2(\beta_\tau) \end{array} \right\}^{Calibration} \quad \text{B.6}$$

$$+ \left\{ \left(\frac{\partial \rho}{\partial p}\right)^2 u^2(p) + \left(\frac{\partial \rho}{\partial t}\right)^2 u^2(t) + \left(\frac{\partial \rho}{\partial \tau}\right)^2 u^2(\tau) \right\}^{Measurement} + \left\{ \left(\frac{\partial \rho}{\partial x}\right)^2 u^2(x) \right\}^{Composition}$$

The variables that contribute primarily to the overall uncertainties in the density measurements are uncertainties associated with calibration and the reproducibility of the measured period of oscillation. The effect of the temperature, pressure and mixture composition uncertainties on the density measurements were also considered when evaluating the combined uncertainty. The relative standard uncertainty associated with the calibration was estimated to be 0.3 %, based on the calibration and validation measurements conducted with pure methane and pure propane.

Partial derivatives of pressure and temperature were estimated using REFPROP 10 [9]. The overall standard uncertainty of the cell temperature was estimated to be 0.1 K, taking into account temperature gradients and fluctuations, while the global standard uncertainty of the

pressure measurement was estimated to be 0.01 MPa. The uncertainty in density attributed to the measured period of oscillation, τ, was estimated to be the difference between the density of the mixture calculated with exact measured period of oscillation, τ, and that calculated with $\tau+u(\tau)$; the standard uncertainty of the measured period of oscillation, $u(\tau)$, was previously estimated to be 0.02 μs [7]. The uncertainty in density due to the uncertainty in the composition of the sample was estimated to be the difference between the density of the mixture with the specified composition and that varied by its standard uncertainty, as estimated using the default models in REFPROP 10 [9]. Equation B.1 was used to estimate the standard uncertainties of the mixture mole fractions, which were 0.005 for the equimolar binary mixtures considering the contributions to the uncertainties in the amounts of each component added due to fluid injection, mixture preparation, mixture transfer, mixture purity and homogeneity. Taking all of this into account, the combined standard relative uncertainty of the measured densities ranges between (0.30 and 0.45) %, as shown Figure B.13 of the SI for all mixtures; the primary contribution to the final uncertainty being the quality of the calibration.

B.4.4 *Isobaric heat capacity method*

B.4.4.1 Apparatus overview and experimental procedure

Isobaric heat capacities, c_p, were measured via a commercialised differential scanning calorimeter (Setaram DSC BT 2.15) described previously [7]. For this work, liquid nitrogen was used instead of water as a coolant to cover the required temperature range of the measurements. Refrigerant mixtures were loaded into the DSC following the procedure described by Al Ghafri et al. [7] Pure CO_2 was used to backfill the DSC measurement cell up to valve 7 in Figure B.3, at a pressure of 10 MPa or more. To flush the mixture through the cell, pump 2 was set to maintain constant pressure (10 MPa). ISCO Pump 1 (Floxlab, BTs605/606-0 / SS / 500cc / SN 4342) was then set to constant flow mode at a low flow rate (2 ml·min^{-1} or less) and valves 7 and 8 were simultaneously opened. This ensured the displacement of the mixture through the DSC cell without any inadvertent phase change, thereby avoiding fractionation of the mixture. The displacement continued until at least 40 ml of volume passed through the cell, which is much larger than the volume of the DSC cell (≈ 9 ml). Once the displacement process was complete, valve 2 was closed and pump 1 was set to constant pressure mode at the desired pressure of the measurement.

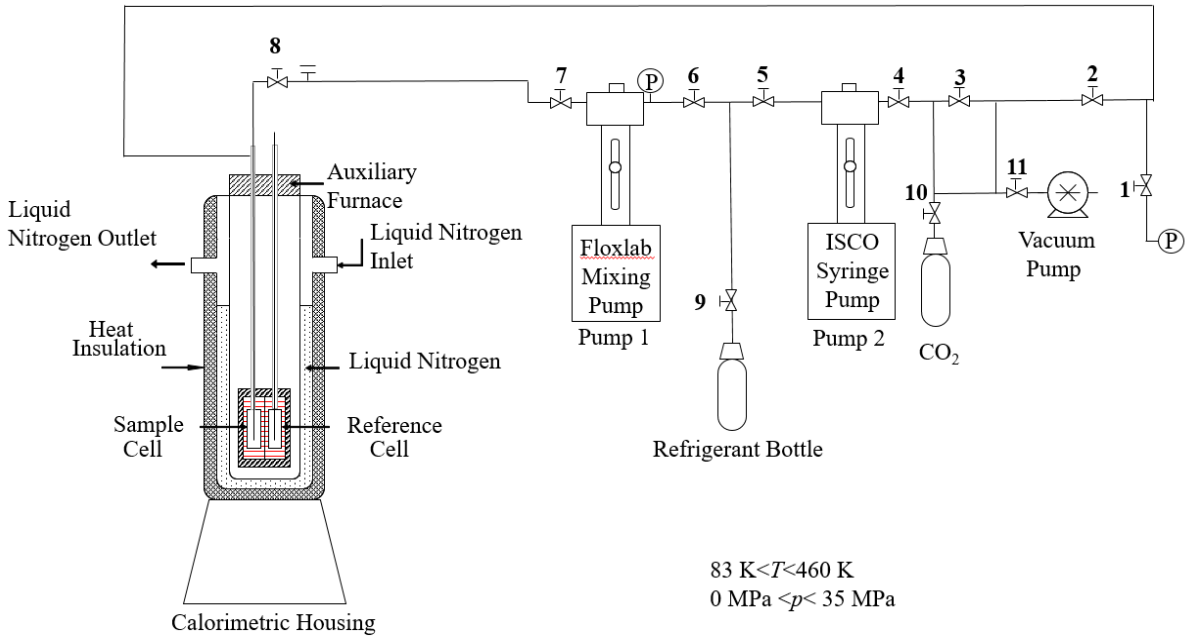

Figure B.3: Differential scanning calorimeter (Setaram DSC BT 2.15) used for measurements of the isobaric heat capacity of refrigerant mixtures.

The isobaric heat capacity was measured by the step method with the DSC's reference cell filled with dry nitrogen at atmospheric pressure. Following an initial isothermal equilibration period of 4 h, the DSC furnace temperature was increased by 10 K at a constant rate of 0.15 K·min^{-1}. A final isothermal period of 6 h followed the temperature ramp. To account for the heat capacity of the DSC cell itself, a series of blank experiments with dry nitrogen gas under atmospheric pressure in the measurement cell were also performed. The isobaric heat capacities were then calculated from

$$c_p = \frac{\int \Phi_s \mathrm{d}t - \int \Phi_b \mathrm{d}t}{\rho V_{\mathrm{cell}} \Delta T_{\mathrm{step}}} \qquad \text{B.7}$$

where $\int \Phi_s \mathrm{d}t$ is the integrated heat flow difference between the measurement cell filled with sample and the reference cell containing dry N_2 at atmospheric pressure over the temperature step (scan), $\int \Phi_b \mathrm{d}t$ is the integrated heat flow difference for the calibration scans where both the measurement and reference cells were filled with dry N_2, ρ is the fluid density (tuned in this work for the refrigerant mixtures), V_{cell} is the volume of the cell and ΔT_{step} is the temperature step (10 K). The volume of the cell was determined to be (8.947 ± 0.043) cm^3 using propane at a pressure of 2 MPa as a reference fluid.

B.4.4.2 Uncertainty calculation

The uncertainty of a heat capacity measurement was estimated via the GUM method [24] from the following equation:

$$u^2(c_p) = \sum_{i=1}^{n}\sum_{j=1}^{n} \frac{\partial f}{\partial y_i}\frac{\partial f}{\partial y_j} u(y_i, y_j) \qquad \text{B.8}$$

where y_i and y_j are the input variables, $(\partial f/\partial y_i)$ is the sensitivity coefficient for y_i, $u(y_i, y_j)$ is the covariance ($i \neq j$) or the variance ($i = j$) of variables y_i and y_j, and $u^2(y)$ is the variance of y.

The measurement of heat capacity is also dependent on temperature, pressure and mixture composition. With $Q = \int \Phi_s \mathrm{d}t - \int \Phi_b \mathrm{d}t$, Equation B.8 becomes:

$$u^2(c_p) = \left(\frac{\partial c_p}{\partial Q}\right)^2 u^2(Q) + \left(\frac{\partial c_p}{\partial \rho}\right)^2 u^2(\rho) + \left(\frac{\partial c_p}{\partial V}\right)^2 u^2(V) + \left(\frac{\partial c_p}{\partial \Delta T}\right)^2 u^2(\Delta T) + \left(\frac{\partial c_p}{\partial T}\right)^2 u^2(T) + \left(\frac{\partial c_p}{\partial p}\right)^2 u^2(p) + \left(\frac{\partial c_p}{\partial x}\right)^2 u^2(x) \qquad \text{B.9}$$

where $\frac{\partial c_p}{\partial Q} = \left(\frac{1}{V\rho\Delta T}\right)^2$, $\frac{\partial c_p}{\partial V} = \left(\frac{Q}{V^2\rho\Delta T}\right)^2$, $\frac{\partial c_p}{\partial \rho} = \left(\frac{Q}{\rho^2 V\Delta T}\right)^2$, and $\frac{\partial c_p}{\partial \Delta T} = \left(\frac{Q}{\Delta T^2 V\rho}\right)^2$, and $u_B(c_p)$ is any Type-B uncertainty. The Type-B uncertainty is an estimate of the systematic uncertainty compared with independent measurements or a well-defined equation of state of lower uncertainty as discussed by Tay and Trusler [25]. In this work, pure methane [26] was measured for the validation of the Type-B uncertainty with a Helmholtz energy EOS from Setzmann and Wagner [23]. No systematic error was observed and thus the Type-B uncertainty was taken to be negligible. For each term in Equation B.9, a summary of the method of estimation and a representative value are listed in Table B.3.

Table B.3 List of the estimation method and representative values for the uncertainties and the derivative terms in Equation B.9.

Term	Estimation method	Value
$u(Q)$	The standard deviation of Joule-effect calibration measurement from the fitted 4th polynomial curve	0.30 J
$u(\rho)$	The estimated uncertainty in the new regressed equation of state	0.5 %$\cdot \rho$
$u(V)$	The standard deviation in the three effective cell volume measurements	0.028 mL
$u(\Delta T)$ and $u(T)$	The standard deviation for temperature in the melting point measurement	0.15 K
$u(p)$	Combined from pressure stability in the measurement and the pressure transducer calibration	$\sqrt{\left(0.005 \cdot \left(\frac{p}{\mathrm{MPa}}\right)\right)^2 + 0.005^2}$ MPa
$u(x)$	Combined from all the factors in the fluid injection, mixture preparation, density obtained from REFPROP 10, mixture transfer and mixture homogeneity	0.005
$\frac{\partial c_p}{\partial T}$, $\frac{\partial c_p}{\partial p}$ and $\frac{\partial c_p}{\partial x}$	Estimated by the EOS implemented in REFPROP 10	
$u_B(c_p)$	The systematic uncertainty of pure methane measurements compared with the reference equation of state	0

B.4.5 *Helmholtz energy mixture method*

The state-of-the-art approach for predicting the thermodynamic properties of refrigerant mixtures is based on fundamental Helmholtz equations of state. As part of this work, the capability of existing models to predict the experimentally-determined data for refrigerant mixtures was assessed, and then these models were tuned to data available for binary mixtures where applicable. The multi-component mixture data were used to verify the predictions of the models with the tuned binary interaction parameters.

The mixing rules for Helmholtz equations describing refrigerant mixtures are the same as those utilized in the GERG-2008 EOS [27] To describe binary mixture thermodynamic properties, reducing functions containing binary interaction parameters are used to tune to available experimental data:

$$\frac{1}{\rho_{c,ij}} = \beta_{v,ij}\gamma_{v,ij}\frac{x_i + x_j}{\beta_{v,ij}^2 x_i + x_j} \cdot \frac{1}{8}\left(\frac{1}{\rho_{c,i}^{1/3}} + \frac{1}{\rho_{c,j}^{1/3}}\right)^3 \quad \text{B.10}$$

$$T_{c,ij} = \beta_{T,ij}\gamma_{T,ij}\frac{x_i + x_j}{\beta_{T,ij}^2 x_i + x_j}\left(T_{c,i}T_{c,j}\right)^{1/2} \quad \text{B.11}$$

The parameters $\rho_{c,i}$ and $T_{c,i}$ are the critical density and critical temperature of pure fluid i, $\beta_{v,ij}$, $\gamma_{v,ij}$, $\beta_{T,ij}$ and $\gamma_{T,ij}$ are binary interaction parameters (BIPs) between fluids i and j, and x_i is the mole fraction of component i in the mixture. The BIPs can be set to unity for binaries with very few or no data. In cases where large numbers of accurate data are available or the BIPs alone cannot describe the available thermodynamic data well, a departure function (linked with an adjustable factor, F_{ij}) might be used. Mixtures with more than 2 components are calculated using the binary interaction models with no further terms incorporated.

In this work, only the binary interaction parameters within the reducing functions were tuned; no departure functions were adjusted. The binary interaction parameters were tuned by minimising the root mean square (RMS) deviations between the selected experimental data and the model. The RMS deviations were calculated via the following equations for the three types of thermodynamic properties considered:

$$\mathrm{RMS(VLE)} = \left(\frac{1}{N}\sum_{n=1}^{N}\left[\left(x_{1,n} - x_{1,\mathrm{calc},n}\right)^2 + \left(y_{1,n} - y_{1,\mathrm{calc},n}\right)^2\right]\right)^{\frac{1}{2}} \quad \text{B.12}$$

$$\mathrm{RMS}(\rho) = 100\left(\frac{1}{N}\sum_{n=1}^{N}\left(\frac{\rho_n - \rho_{\mathrm{calc},n}}{\rho_n}\right)^2\right)^{\frac{1}{2}} \quad \text{B.13}$$

$$\mathrm{RMS}(c_p) = 100\left(\frac{1}{N}\sum_{n=1}^{N}\left(\frac{c_{p,n} - c_{p,\mathrm{calc},n}}{c_{p,n}}\right)^2\right)^{\frac{1}{2}} \quad \text{B.14}$$

where x_1 and y_1 are the mole fraction of component 1 in the liquid and in the vapour at equilibrium, respectively. Values of x_i and y_i were obtained from the specified overall composition of the mixture z_i by calculating the properties of the equilibrium liquid and vapour phases, respectively, at the experimental temperature and pressure (flash calculation).

In this work the number of thermodynamic data available for a given binary mixture was limited. Thus, it was only necessary to tune two BIPs from their standard value (unity) to achieve acceptable fits to the data. Weighting factors were given to different properties following a method similar to that detailed by Kunz et al. [28]. The tuning procedure minimised the following objective function:

$$\chi^2 = W_1 \mathrm{RMS(VLE)}^2 + W_2 \mathrm{RMS}(\rho)^2 + W_3 \mathrm{RMS}\left(c_p\right)^2 \qquad \text{B.15}$$

where W_1 to W_3 are the weighting factors applied to the different properties as considered in Equations (B.12)-(B.14). The values of the weighting factors are empirical and are determined by the scale of the RMS deviation, the uncertainty of the experimental data, and the importance (or sensitivity) of each property. The tuning of each binary used slightly different weighting factors according to the available data situation but typically W_2 was 2-5 times larger than W_1 and 5-10 times larger than W_3. This reflects the fact that density data have the both the smallest uncertainty and the greatest influence on EOS tuning [29]. Heat capacity data have relatively large uncertainties and limited influence on EOS predictions, although they can provide good checks of mixing rule formulations as demonstrated by Syed et al. [30] and Rowland et al. [31].

For completeness, it is noted that Jaubert and co-workers [32] recently added six fluorinated groups to the well-known Enhanced-PPR78 model [33] allowing for the estimation of the temperature-dependent binary interaction parameters $k_{ij}(T)$ in the Peng-Robinson equation of state. While not as accurate as Helmholtz models that are adequately anchored to experimental data, the group-contribution approach allows for the prediction of the phase behaviour and thermodynamic properties for systems that are not yet measured and can thus be extremely useful to the design of very new processes and/or products. It would be interesting to apply and compare the recent extension of this group contribution scheme to the prediction of the mixture properties measured in this work.

B.5 Results

B.5.1 *Experimental measurements*

The experimental data measured in this work are presented in both Tables and Figures either in this Section or in the Supporting Information.

B.5.1.1 Vapour-liquid equilibrium

Measurement of four binary systems of (CO_2 + R32), (CO_2 + R134a), (CO_2 + R1234yf), and (CO_2 + R125) were made at constant temperatures around 293 K. Five different composition of CO_2 from (8 to 81) % were studied in each binary system. After the preparation of each mixture, the overall composition of the mixture was examined at a temperature at least 10 K above the mixture's calculated cricondentherm to ensure the presence of a single phase. For the isothermal measurements, the mixture was stabilized at a temperature of around 293 K and then the composition of the vapour (y_i) and liquid (x_i) phases were measured by sampling each more than ten times, with the average reported here. The initial composition, the saturation pressure (p^{sat}) and the equilibrium liquid and vapour compositions (x, y) for each binary at the experimental temperature (T) are listed in Table B.14. The (p-x,y) phase envelopes of the binary mixtures are presented in Figure B.4 (a) –(d), where the mole fraction of CO_2 (1) in the liquid, x_1, and vapour phases, y_1, respectively, are plotted versus the saturation pressure.

The results were compared to values reported in the literature and those that are calculated with the default Helmholtz equation of state (EOS) as implemented in REFPROP 10 [9], based on the experimental pressure, temperature and overall composition using the method described by May et al. [15]. The deviations between the data and model predictions are shown in the form of mole fraction deviation plots in Figure B.16 to Figure B.19 of the SI. In these plots, the abscissa is the measured saturation pressure and the ordinates are the deviation of the measured mole fraction of CO_2 ($x_{1,exp}$, $y_{1,exp}$) from the value calculated with the default Helmholtz equation of state (EOS) for that component ($x_{1,cal}$, $y_{1,cal}$).

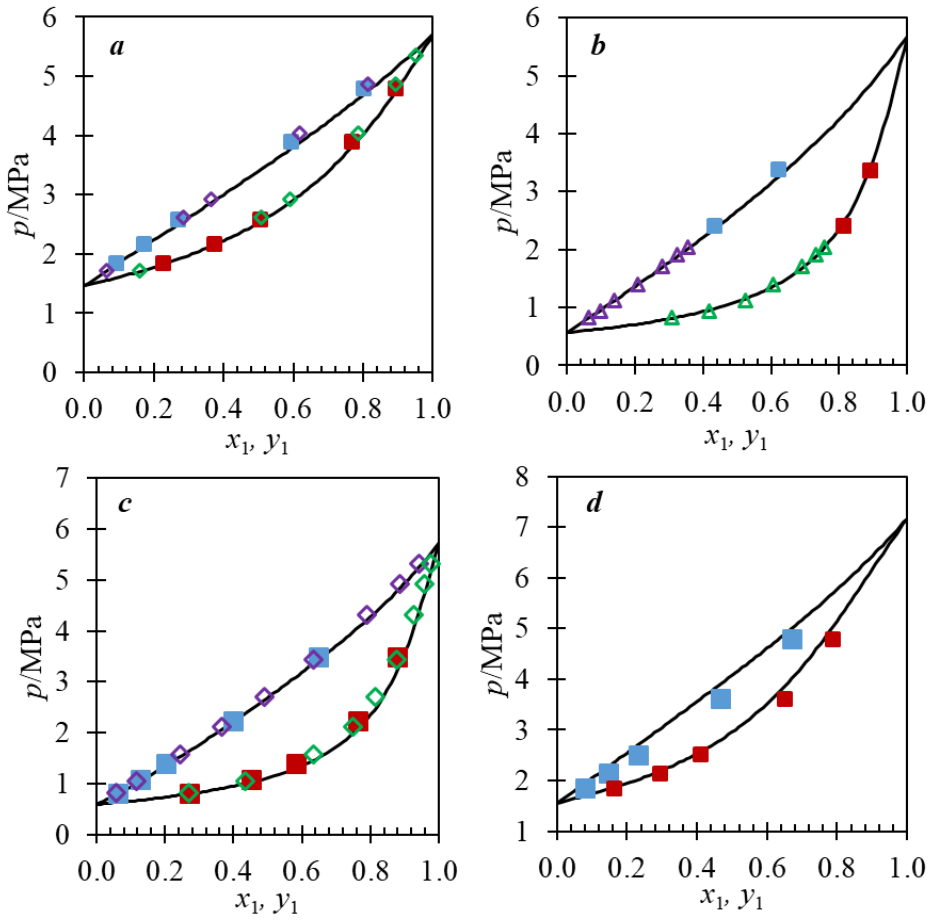

Figure B.4: VLE results and phase envelope of (a) CO_2 (1) + R32 (2) at 292.98 K, (b) CO_2 (1) + R134a (2) 292.88 K, (c) CO_2 (1) + R1234yf (2) at 293.13 K, (d) CO_2 (1) + R125 (2) at 302.89 K from available experimental data and the EOS in REFPROP 10 using the default binary interaction parameters (BIPs). Symbols refer to the measurements at different pressures, and the solid curves refer to the model predictions. Symbol list: (■, blue) Bubble point measured in this work (■, red) Dew point measured in this work (◇, purple) Bubble point from Rivollet et al.[34] (◇, green) Dew point from Rivollet et al. [34] (Δ, purple) Bubble point from Duran-Valencia et al. [35] (Δ, green) Dew point from Duran-Valencia et al. [35] (○, purple) Bubble point from Juntarachat et al. [36] (○, green) Dew point from Juntarachat et al [36].

The ternary mixture of (CO_2 + R1234yf + R32) was prepared by the addition of CO_2 to a near equimolar mixture of R1234yf + R32 with $z_{R1234yf}/z_{R32}$=0.45. The VLE measurements were made at four different mixture compositions and two temperatures near 284 and 312 K. The results are presented in Figure B.5 and Figure B.20 and tabulated in Table B.14 of the SI. Before commencing each measurement, the overall composition of the mixture was measured by GC at the single gas phase condition (Table B.14). Similar comparisons to values calculated with the default Helmholtz EOS implemented in REFPROP 10 are shown for the ternary mixture in Figure B.21 of the SI. Comparisons of the ternary mixture VLE data with predictions made using the EOS tuned to the binary data are presented in Figure B.5.

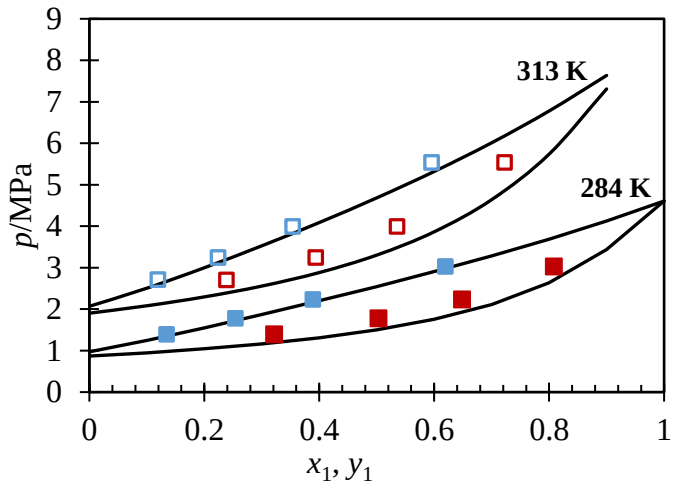

Figure B.5: Measured (symbols) and predicted (curves) bubble and dew pressures at T=284 K and T=313 K for the CO_2 (1) + R1234yf (2) + R32 (3) ternary systems ($z_{R1234yf}/z_{R32}$=0.45) as a function of the measured liquid and vapour mole fractions of each component: (■, blue) Bubble point measured in this work (■, red) Dew point measured in this work (filled symbols for *T*=284 K, and empty symbols for *T*=313 K). The dew and bubble curve predictions were made with the EOS in REFPROP 10 using the default binary interaction parameters.

A near-equimolar mixture of five-components, [CO_2 (1) + R1234yf (2) + R32 (3) + R125 (4) + R134a (5)], was prepared gravimetrically then injected to the VLE cell under single-phase conditions. The overall composition of the mixture was confirmed by GC analysis. Three VLE measurements at (273, 312 and 333) K were made (Table B.4) and the deviations of the results from the prediction of the default Helmholtz energy mixture model are shown in Figure B.6.

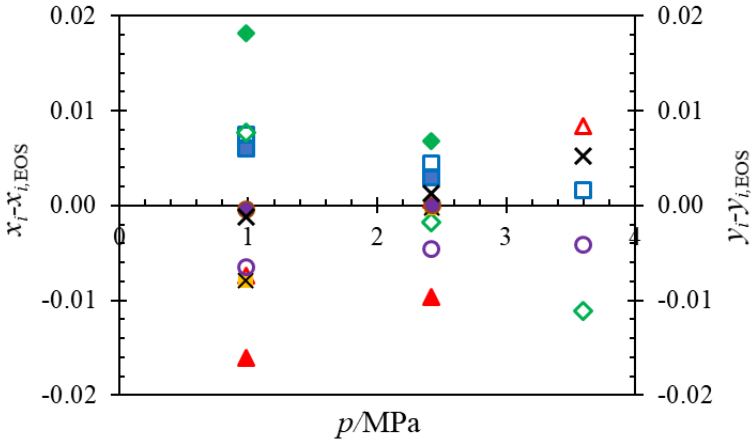

Figure B.6: Deviations (x_i-$x_{i,EOS}$) and (y_i-$y_{i,EOS}$) of the measured compositions from those predicted with the default Helmholtz energy mixture model for [CO_2 (1, ◆, green)+ R1234yf (2, ▲, red)+ R32 (3, ■, blue) + R125 (4, ●, purple) + R134a (5, ×, black)] system. Left axis: filled symbols, deviations for liquid; Right axis: empty symbols, deviations for vapour.

Table B.4: Measured *p*, *T*, *x* and *y* data for a five component mixture of CO_2 (1) + R1234yf (2) + R32 (3) + R125 (4) + R134a (5) with the global composition of z_1=0.1994 ± 0.0045, z_2=0.2002 ± 0.0045, z_3=0.2015 ± 0.0045, z_4=0.2016 ± 0.0045, z_5=0.1974 ± 0.0009.

***T*/K**	***p*/MPa**	x_1	$u(x_1)$	y_1	$u(y_1)$	x_2	$u(x_2)$	y_2	$u(y_2)$	x_3	$u(x_3)$	y_3	$u(y_3)$	x_4	$u(x_4)$	y_4	$u(y_4)$	x_5	$u(x_5)$	y_5	$u(y_5)$
273.48	0.98	0.1812	0.0022	0.4916	0.0036	0.1974	0.0011	0.0826	0.0014	0.2066	0.0008	0.1971	0.0015	0.2068	0.0008	0.149	0.0015	0.2081	0.0012	0.0797	0.0014
312.79	2.42	0.1607	0.0055	0.3425	0.0022	0.2112	0.0055	0.1311	0.0011	0.1989	0.0054	0.2155	0.0009	0.2065	0.0005	0.1807	0.001	0.2227	0.0055	0.1303	0.0011
333.5	3.6	N/A*		0.2644	0.0018	N/A*		0.1663	0.001	N/A*		0.213	0.0008	N/A*		0.1915	0.0008	N/A*		0.1648	0.001

*At 333.5 K, a liquid phase was present but the volume available was insufficient to reliably sample and analyse its composition

B.5.1.2 Density

Single-phase densities for the binary mixtures (0.50 CO_2 + 0.50 R125), (0.50 CO_2 + 0.50 R1234yf), (0.50 CO_2 + 0.50 R32), and (0.50 CO_2 + 0.50 R134a), a ternary mixture (0.09 CO_2 + 0.48 R1234yf + 0.43 R32) and a 5-component mixture (0.20 CO_2 + 0.20 R1234yf + 0.20 R32 + 0.20 R125 + 0.20 R134a) were measured at temperatures between (223 and 323) K over the pressure range of 1.0 MPa to 5.0 MPa. A total of 58 density data were acquired, ranging from (892 to 1404) $kg \cdot m^{-3}$. A summary of the measurement pressure and temperature conditions is shown in Figure B.14, along with the phase envelope for each mixture predicted using the default reference model implemented in the software REFPROP 10 [9]. For every isotherm, density measurements were performed for a minimum duration of 3 hours at every pressure. A repetition of one pressure value was also conducted to check the measurement reproducibility.

Single-phase densities measured for the binary mixtures (0.50 CO_2 + 0.50 R32), (0.50 CO_2 + 0.50 R134a), (0.50 CO_2 + 0.50 R125) and (0.50 CO_2 + 0.50 R1234yf) at pressures between (1.5 and 5.0) MPa are shown in Table B.5 and Figure B.22 to Figure B.25 of the SI. As an example of the binary results, Figure B.7shows (0.5 CO_2 + 0.5 R1234yf) density results and the deviations of the results from the prediction of the default Helmholtz energy mixture model. In all cases the measured values follow the same trend as the calculated values. The relative deviations between the present measurements and the values predicted with the default EOS for each system span the range (-1.77 to +1.65) %, with the relative deviations being systematically dependent on temperature.

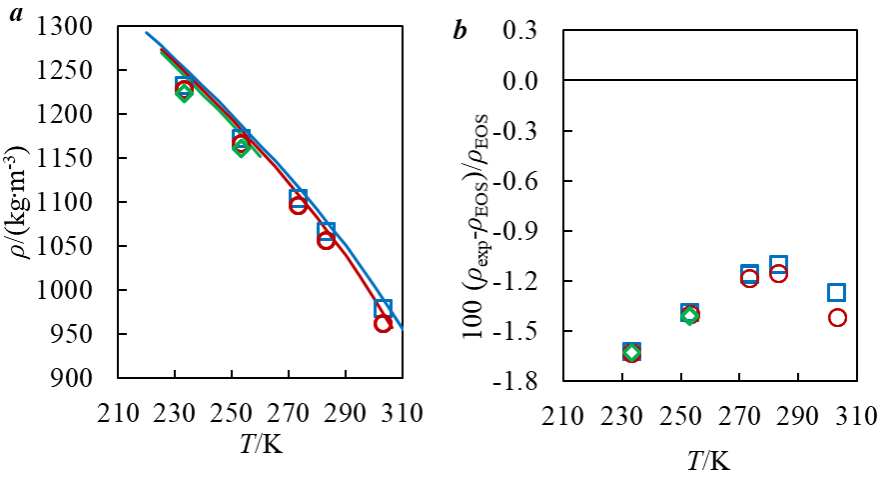

Figure B.7: Comparisons of 0.5 CO_2 + 0.5 R1234yf density results for the experimental data measured in this work and various models from default binary interaction parameters (BIPs). Deviations are shown of experimental data from those calculated with the default BIPs. Symbols refer to the measurements at different pressures (□ 5.09 MPa, ○ 3.56 MPa and ◇ 2.04 MPa), and the solid curves refer to the model prediction.

Table B.5: Measured density data for the refrigerant equimolar binary mixtures (CO_2 + R32), (CO_2 + R134a), (CO_2 + R125) and (CO_2 + R1234yf) and combined standard uncertainty $u_c(\rho)$ as a function of temperature and pressure. The standard uncertainties in the mole fractions of the binary mixtures were $u(z_1) = u(z_2) = 0.005$.

T/K	$u(T)$/K	p/MPa	$u(p)$/MPa	z_1	z_2	ρ/ kg·m^{-3}	$u_c(\rho)$/ kg·m^{-3}
			CO_2 (1) + R32 (2)				
293.3	0.1	5.11	0.01	0.501	0.499	921.2	3.0
273.3	0.1	5.03	0.01	0.501	0.499	1019.5	3.2
223.3	0.1	4.98	0.01	0.501	0.499	1195.0	3.6
273.3	0.1	3.51	0.01	0.501	0.499	1012.6	3.1
253.2	0.1	3.58	0.01	0.501	0.499	1093.8	3.3
243.3	0.1	3.46	0.01	0.501	0.499	1127.8	3.4
243.3	0.1	1.26	0.01	0.501	0.499	1122.0	3.4
243.3	0.1	1.50	0.01	0.501	0.499	1123.2	3.4
223.3	0.1	1.53	0.01	0.501	0.499	1186.8	3.6
			CO_2 (1) + R134a (2)				
283.3	0.1	5.05	0.01	0.500	0.500	1137.1	3.9
303.1	0.1	5.06	0.01	0.500	0.500	1045.5	3.9
253.2	0.1	3.56	0.01	0.500	0.500	1242.5	4.0
273.3	0.1	3.54	0.01	0.500	0.500	1168.4	3.9
233.3	0.1	3.98	0.01	0.500	0.500	1310.0	4.2
253.2	0.1	2.23	0.01	0.500	0.500	1238.1	4.0
233.3	0.1	2.31	0.01	0.500	0.500	1306.0	4.2
283.3	0.1	5.05	0.01	0.500	0.500	1137.1	3.9
303.1	0.1	5.06	0.01	0.500	0.500	1045.5	3.9
			CO_2 (1) + R125 (2)				
293.2	0.1	5.10	0.01	0.500	0.500	1098.3	4.2
273.3	0.1	5.10	0.01	0.500	0.500	1201.9	4.2
253.1	0.1	5.06	0.01	0.500	0.500	1289.7	4.3
243.2	0.1	5.09	0.01	0.500	0.500	1328.4	4.4
223.3	0.1	5.13	0.01	0.500	0.500	1404.6	4.6
293.3	0.1	3.60	0.01	0.500	0.500	1070.1	4.3
273.3	0.1	3.59	0.01	0.500	0.500	1190.9	4.1
253.1	0.1	3.61	0.01	0.500	0.500	1283.7	4.3
243.2	0.1	3.57	0.01	0.500	0.500	1323.9	4.4
223.3	0.1	3.72	0.01	0.500	0.500	1402.6	4.5
243.2	0.1	1.41	0.01	0.500	0.500	1314.9	4.3
223.2	0.1	1.73	0.01	0.500	0.500	1396.7	4.5
223.2	0.1	1.52	0.01	0.500	0.500	1396.1	4.5
			CO_2 (1) + R1234yf (2)				
303.1	0.1	5.10	0.01	0.501	0.499	978.0	3.4
283.2	0.1	5.07	0.01	0.501	0.499	1066.4	3.5
273.3	0.1	5.09	0.01	0.501	0.499	1104.2	3.5
253.2	0.1	5.08	0.01	0.501	0.499	1172.4	3.7
233.2	0.1	5.10	0.01	0.501	0.499	1233.5	3.8
303.1	0.1	3.58	0.01	0.501	0.499	961.0	3.5
283.2	0.1	3.55	0.01	0.501	0.499	1056.3	3.5
273.3	0.1	3.56	0.01	0.501	0.499	1096.1	3.5
253.2	0.1	3.58	0.01	0.501	0.499	1166.9	3.7
233.2	0.1	3.55	0.01	0.501	0.499	1229.3	3.8
253.2	0.1	2.11	0.01	0.501	0.499	1161.3	3.6
233.2	0.1	1.97	0.01	0.501	0.499	1224.8	3.8

Single-phase densities at pressures of (1.7, 3.0, and 4.5) MPa were measured for the ternary mixture (0.09 CO_2 + 0.48 R1234yf + 0.43 R32), and the data are shown in Table B.6. As it was shown in Figure B.26 in the SI, the measured values follow the same trend as the calculated values. The relative deviations between the present measurements and the values predicted with the default EOS span (-2.77 to -0.78) %, with the relative deviations systematically dependent on temperature.

Table B.6: Measured density data for the CO_2 (1) + R1234yf (2) + R32 (3) ternary systems with the global composition of z_1=0.093 ± 0.010, z_2=0.477 ± 0.008, z_3=0.430 ± 0.009 and combined standard uncertainty $u_c(\rho)$ as a function of temperature and pressure.

T/K	*u*(*T*)/K	*p*/MPa	*u*(*p*)/MPa	*z*(CO_2)	*z*(R32)	*z*(R1234yf)	ρ/ kg·m^{-3}	$u_c(\rho)$/ kg·m^{-3}
324.1	0.1	4.53	0.01	0.092	0.434	0.474	891.1	3.7
303.5	0.1	4.53	0.01	0.092	0.434	0.474	1001.3	3.5
303.5	0.1	3.00	0.01	0.092	0.434	0.474	987.1	3.5
282.9	0.1	3.03	0.01	0.092	0.434	0.474	1070.2	3.6
275.2	0.1	3.09	0.01	0.092	0.434	0.474	1101.3	3.6
273.3	0.1	1.75	0.01	0.092	0.434	0.474	1109.6	3.6
253.2	0.1	1.70	0.01	0.092	0.434	0.474	1175.1	3.7

Single-phase densities at pressures of (1.5, 3.5 and 5.0) MPa were measured for the 5-component mixture (0.20 CO_2 + 0.20 R1234yf + 0.20 R32 + 0.20 R125 + 0.20 R134a) and the data are tabulated in Table B.7 and shown in Figure B.27. The measured values follow the same trend as the calculated values. The relative deviations between the present measurements and the values predicted with the default EOS span (-1.09 to -0.57) %, with the relative deviations systematically dependent on temperature.

Table B.7: Measured density data for the refrigerant a five component mixture of CO_2 (1) + R1234yf (2) + R32 (3) + R125 (4) + R134a (5) with the global composition of z_1=0.200 ± 0.007, z_2=0.200 ± 0.004, z_3=0.200 ± 0.007, z_4=0.200 ± 0.005, z_5=0.200 ± 0.006. and combined standard uncertainty $u_c(\rho)$ as a function of temperature and pressure.

T/K	*u*(*T*)/K	*p*/MPa	*u*(*p*)/ MPa	*z*(CO_2)	*z*(R32)	*z*(R1234yf)	*z*(R134a)	*z*(R125)	ρ/ kg·m^{-3}	$u_c(\rho)$/ kg·m^{-3}
323.1	0.1	5.06	0.01	0.200	0.200	0.200	0.200	0.200	971.1	4.35
303.1	0.1	5.07	0.01	0.200	0.200	0.200	0.200	0.200	1079.5	3.97
283.3	0.1	5.04	0.01	0.200	0.200	0.200	0.200	0.200	1162.7	3.95
243.3	0.1	5.02	0.01	0.200	0.200	0.200	0.200	0.200	1298.8	4.14
243.3	0.1	5.07	0.01	0.200	0.200	0.200	0.200	0.200	1299.0	4.14
303.1	0.1	3.53	0.01	0.200	0.200	0.200	0.200	0.200	1065.1	4.01
283.3	0.1	3.54	0.01	0.200	0.200	0.200	0.200	0.200	1154.1	3.95
243.3	0.1	3.51	0.01	0.200	0.200	0.200	0.200	0.200	1294.3	4.13
263.2	0.1	1.43	0.01	0.200	0.200	0.200	0.200	0.200	1219.8	4.01
243.3	0.1	1.45	0.01	0.200	0.200	0.200	0.200	0.200	1287.9	4.12

B.5.1.3 Isobaric heat capacity

Heat capacity data for the binary refrigerant mixtures are reported in Table B.8. The deviations of the measurements from the default model implemented in REFPROP 10[9] which are shown in Figure B.28 to Figure B.31 are within the estimated experimental uncertainties for (CO_2 + R125) and for most of the (CO_2 + R1234yf) data. Figure B.8 illustrates an example of heat capacity measurements results of (0.5 CO_2 + 0.5 R1234yf) and their deviations from the REFPROP 10 predictions. Relatively large deviations (up to 4.9%) were observed for (CO_2 + R32) and (CO_2 + R134a). For the mixture of (CO_2 + R32), the data were all 3% higher than the predictions. All the measured data follow the same trends with temperature and pressure predicted by the default model in REFPROP 10.

For the ternary and five-component mixtures, the measured data still follow the same trend as the values predicted by REFPROP 10. The relative deviations of the experimental data from the REFPROP 10 models vary from (-4.0 to 2.0) %, which is within the experimental uncertainty for most of the points (given the increased uncertainty from the mixture composition). As shown in Figure B.32 and Figure B.33 of the SI, the binaries involved in these multi-component mixtures show positive and negative deviations from the default model predictions. These positive and negative differences among the different binaries mostly cancel out when the components are combined; thus, the relative deviations turn out to be relatively small for the multi-component refrigerant mixtures.

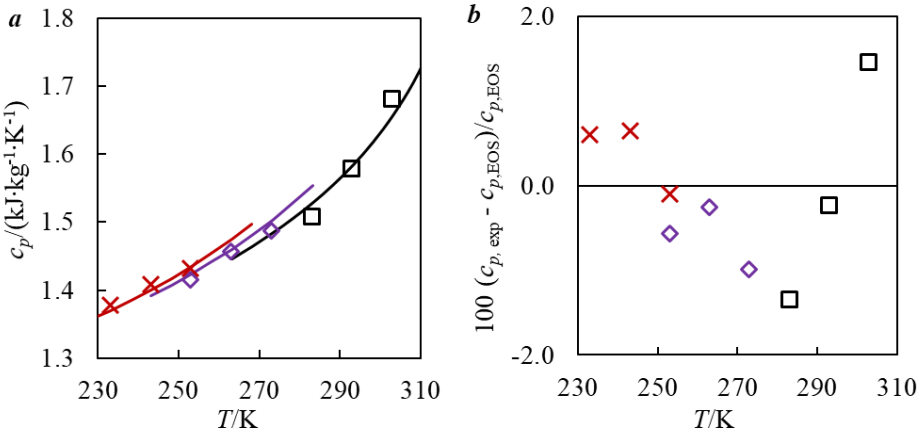

Figure B.8: Heat capacity measurements of 0.5 CO_2 + 0.5 R1234yf. a: Absolute c_p as a function of T (temperature), symbols correspond to the measured values (☐ 5.09 MPa, ◇ 3.50 MPa and ×2.07 MPa) and the solid coloured lines correspond to the predictions from REFPROP 10. b: Relative deviations of the measured c_p (using average fitted cell volume) from that calculated using the default model in REFPROP 10 ($c_{p,\mathrm{cal}}$) at different pressures (☐ 5.09 MPa, ◇ 3.50 MPa and ×2.07 MPa) as a function of temperature.

Table B.8: Heat capacity c_p, and its combined standard uncertainty $u_c(c_p)$ as a function of temperature T and pressure p. At all temperatures, $u(T)$ = 0.2 K, $u(x)$ = 0.005 for binary components, and the $u(x)$ for multi-component mixtures are given in the table.

T/K	p/MPa	$u(p)$/MPa	c_p/ (kJ·kg^{-1}·K^{-1})	$u_c(c_p)$/(kJ·kg^{-1}·K^{-1})
0.500 CO_2 + 0.500 R32				
272.98	5.00	0.03	1.989	0.036
282.96	5.00	0.03	2.098	0.038
292.93	5.00	0.03	2.257	0.041
253.05	3.52	0.02	1.898	0.034
263.00	3.52	0.02	1.937	0.035
272.98	3.52	0.02	2.013	0.036
223.13	1.50	0.01	1.803	0.033
233.09	1.50	0.01	1.833	0.033
243.06	1.50	0.01	1.871	0.034
0.501 CO_2 + 0.499 R134a				
283.08	5.00	0.03	1.682	0.030
293.02	5.00	0.03	1.744	0.031
303.02	5.00	0.03	1.833	0.033
253.01	3.50	0.02	1.567	0.028
263.00	3.50	0.02	1.581	0.028
233.07	2.00	0.01	1.504	0.027
243.02	2.00	0.01	1.526	0.027
253.02	2.00	0.01	1.567	0.028
0.500 CO_2 + 0.500 R125				
272.99	5.10	0.03	1.531	0.028
282.93	5.10	0.03	1.587	0.029
292.90	4.92	0.03	1.732	0.032
253.04	3.52	0.02	1.440	0.026
263.00	3.52	0.02	1.487	0.027
272.97	3.52	0.02	1.541	0.028
223.13	1.50	0.01	1.352	0.024
233.08	1.58	0.01	1.370	0.025
243.05	1.60	0.01	1.421	0.025
0.499 CO_2 + 0.501 R1234yf				
282.94	5.10	0.03	1.508	0.027
292.92	5.10	0.03	1.579	0.029
302.89	5.08	0.03	1.681	0.031
253.02	3.50	0.02	1.416	0.025
262.99	3.50	0.02	1.456	0.026
272.95	3.50	0.02	1.487	0.027
233.06	2.07	0.01	1.378	0.025
243.04	2.07	0.01	1.409	0.025
253.02	2.07	0.01	1.433	0.026
(0.093 ± 0.010) CO_2 + (0.477 ± 0.008) R1234yf + (0.430 ± 0.008) R32				
302.98	4.50	0.02	1.610	0.030
322.90	4.55	0.02	1.817	0.036
283.04	2.98	0.02	1.502	0.028
293.04	2.98	0.02	1.560	0.029
242.69	1.55	0.01	1.361	0.025
252.64	1.55	0.01	1.379	0.025
(0.200 ± 0.007) CO_2 + (0.200 ± 0.004) R1234yf + (0.200 ± 0.008) R32 + (0.200 ± 0.006) R125 + (0.200 ± 0.006) R134a				
302.79	5.00	0.03	1.564	0.030
322.73	4.90	0.03	1.773	0.035
272.88	3.58	0.02	1.409	0.026
302.80	3.58	0.02	1.531	0.029
252.95	1.50	0.01	1.351	0.025
262.91	1.50	0.01	1.384	0.026

B.5.2 *Modelling*

B.5.2.1 Parameter tuning results

In this work the number of thermodynamic data available for a given binary mixture was limited. Thus, it was only necessary to tune two BIPs from their standard value (unity) to achieve acceptable fits to the data. A summary of binary mixture tuning is shown in Table B.9. The results of reviewing the literature for the thermodynamic properties of the refrigerant mixtures investigated in this work are shown in Table B.10. Almost all of the reported literature data were included in the new model fitting. Significant improvements were achieved for the mixtures of (R32 + CO_2) and (R134a + CO_2): the RMS deviations decreased for all the properties. For the mixtures of (R125 + CO_2) and (R1234yf + CO_2), the regression mainly been focused on density as the default model was only fit to the VLE data available at the time. For all the mixtures, the heat capacity predictions were insensitive to changes in the BIPs.

Table B.9: Overview of the binary interaction parameters from the Helmholtz energy models tuned in this work and implemented as the default in REFPROP 10. The adjustable parameter F_{ij} associated with the departure function was not varied for any binary.

	Default in REFPROP 10					Values after tuning in this work				
System	$\beta_{T,ij}$	$\gamma_{T,ij}$	$\beta_{v,ij}$	$\gamma_{v,ij}$	F_{ij}	$\beta_{T,ij}$	$\gamma_{T,ij}$	$\beta_{v,ij}$	$\gamma_{v,ij}$	F_{ij}
CO_2 + R32	1	0.99782	1	1.0059	0	1	0.992	1	0.9786	0
CO_2 + R134a	1	1.008	1	1	0	1	1	1.016	1.027	0
CO_2 + R125	1.0115	0.96741	1	1	0	1	0.9871	1	1.0311	0
CO_2 + R1234yf	1.017	1	1	1.015	-0.657	1	1	1.125	1.051	-0.657

The quality of the literature VLE data was checked via comparisons of the vapour-liquid equilibrium ratio K_i. As a result, not all the literature data were used in the regression process. In Figure B.16 and Figure B.18, the tuned models from this work represent the VLE of (CO_2 + R32) and (CO_2 + R125) with small deviations. Fewer outliers can also be observed in the corresponding isotherms. In Figure B.17 and Figure B.19 of the SI, for the binaries of (CO_2 + R134a) and (CO_2 + R1234yf), the tuned models exhibit the same quality as the default REFPROP 10 models in the isotherms and the deviation plots. For these two mixtures, better performance in VLE was not achieved because the default models were tuned to VLE data only, while in this work, the models were also tuned to density data.

Table B.10: Sources of data for mixtures with the type of reported data, the number of measured data (N), the (percentage) RMS deviations between the default and tuned Helmholtz energy mixture models calculated using Equations (B.12)-(B.14), and the number of data used for tuning in this work (N_{tuned}).

Reference	Type	N	RMS (default)	N_{tuned}	RMS (tuned)
CO_2 + R32					
Diefenbacher and Türk[37]	VLE	9	0.018	8	0.012
Rivollet et al.[34]	VLE	45	0.018	43	0.008
Stein and Adams [38]	VLE	48	0.009	0	0.019
Di Nicola et al. [39]	VLE	5	0.45	0	0.27
This work	ρ	9	1.08	9	0.15
Di Nicola et al. [39]	ρ	65	1.17	0	0.77
This work	c_p	9	3.20	9	2.90
This work	VLE	5	0.018	4	0.008
CO_2 + R134a					
Duran-Valencia et al.[35]	VLE	27	0.007	27	0.007
Lim et al.[40]	VLE	37	0.026	36	0.024
Silva-Oliver and Galicia-Luna [41]	VLE	23	0.017	23	0.016
This work	ρ	7	1.67	7	0.34
This work	c_p	8	3.94	8	3.80
This work	VLE	5	0.010	5	0.008
CO_2 + R125					
Di Nicola et al. [39]	VLE	5	0.052	3	0.008
Jeong et al. [42]	VLE	19	0.019	15	0.018
This work	ρ	13	1.19	13	0.55
Di Nicola et al. [39]	ρ	65	1.08	65	0.42
This work	c_p	9	1.18	9	2.10
This work	VLE	5	0.031	5	0.010
CO_2 + R1234yf					
Juntarachat et al.[36]	VLE	65	0.028	54	0.032
Di Nicola et al. [43]	VLE	110	0.20	0	0.21
This work	ρ	12	1.38	12	0.18
Di Nicola et al. [43]	ρ	73	0.91	0	1.02
This work	c_p	9	0.83	9	0.84
This work	VLE	5	0.018	5	0.021

Figure B.22 to Figure B.25 in the SI show that the density measurements are not well-represented by the REFPROP 10 default model. Systematic offsets occur between the measurements and the model mainly due to a lack of available density data for the binary mixtures during the default model's development. In this work, for almost all the measurements, the density RMS deviations are within the experimental uncertainties because density had the highest weighting of all the properties. Significant improvements were achieved with deviations having been reduced from (54 to 87) %.

For the mixture of (CO_2 + R1234yf), the RMS deviation in heat capacity is smaller than the experimental uncertainty (1.8 %). A modification in the departure function might significantly decrease the deviations in heat capacity. However, there are not enough data to reliably tune the departure function and all the adjustable parameters (F_{ij}) remains unchanged from the value used in the default model.

B.5.2.2 Validation of the model

The thermodynamic models were regressed to the binary data detailed above and used without further adjustment to predict the properties of the ternary and five-component mixtures at the measurement conditions. Interaction parameters have been tuned for most of the other binary subsystems by Akasaka (R32 + R1234yf) [44], Al Ghafri et al. (R125 + R1234yf) [7] and Lemmon and Jacobsen (R134a + R125, R134a + R32 and R125 + R32) [45]. For the mixture of (R134a + R1234yf) there are no thermodynamic property data available in the literature to the authors' knowledge and the default BIPs in REFPROP [9] were used. The statistical results of these predictive comparisons are shown in Table B.11.

Table B.11: Summary for the multi-component mixture comparisons, the number of measured data, the RMS deviations between the default and tuned Helmholtz energy mixture models calculated using Equations. (B.12)-(B.14).

Property	Data points	RMS (default)	RMS (tuned)
Ternary mixture			
ρ	6	1.67	0.85
VLE	8	0.05	0.02
c_p	6	1.15	1.08
Five-component mixture			
ρ	6	0.79	0.42
VLE	3	0.005	0.004
c_p	6	1.65	1.68

Compared with the default parameters set used in REFPROP, the densities predicted for the multi-component mixtures are significantly improved using the tuned BIPs determined in this work. As shown in Table B.11, the deviations decrease by 49 % and 47 % for the ternary and five-component mixtures, respectively. The same applies to the VLE results for the ternary mixture, where the deviations have decreased by 60 %. The RMS deviation of the VLE results was calculated by Equation B.12, where the composition of R32 was used as x_1 and y_1. The deviation of the VLE results from the predictions of default Helmholtz energy mixture model

with tuned BIPs are shown in Figure B.9 (a). As can be seen by comparing Figure B.6 and Figure B.9 (b) for the five component mixture, the deviations between the VLE data and the default model predictions are similar to those between the data and the optimised model. There is not much change in the heat capacity predictions, which reflects the situation for the binary mixtures that this property is relatively insensitive to the change in BIPs over the measured conditions, and it lacks sufficient data to alter the departure functions.

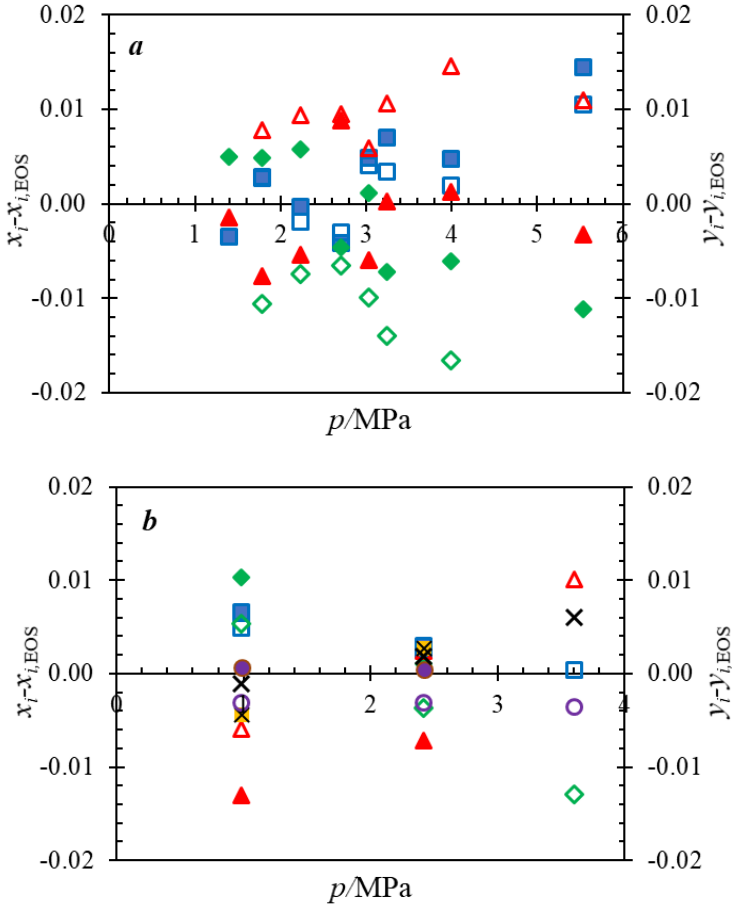

Figure B.9: Deviations (x_i-$x_{i,EOS}$) and (y_i-$y_{i,EOS}$) of the measured compositions from those predicted with the Helmholtz energy mixture model using the tuned binary interaction parameters (BIPs) for (a) the ternary mixture of (CO_2 + R1234yf + R32) and (b) the five-components mixture of [CO_2 + R1234yf + R32 + R125 + R134a]: CO_2 (◆), R1234yf (▲), R32 (■), R125 (●), R134a (×). Left axis: filled symbols, deviations for liquid; Right axis: empty symbols, deviations for vapour.

B.6 Conclusion

In this work, new data for the thermodynamic properties of carbon dioxide mixtures with HFCs (R32, R125, and R134a) and HFO-1234yf were reported. In summary, the following properties were measured:

1. Vapour-liquid equilibria (VLE) for twenty binary mixtures of CO_2 + [R1234yf, R32, R125, R134a] with molar compositions of (10, 20, 30, 50 and 70) % CO_2 measured by the analytic method (sampling with gas chromatography) at 20 ºC and pressures from (0.82 to 4.80) MPa.
2. Liquid densities of four equimolar mixtures CO_2 + [R1234yf, R32, R125, R134a] measured by vibrating tube densimetry at temperatures between (-50 and 30) °C and pressures from (1.52 to 5.11) MPa.
3. Liquid heat capacity of four equimolar mixtures CO_2 + [R1234yf, R32, R125, R134a] by differential scanning calorimetry at temperatures between (-50 and 30) °C and pressures between (1.50 and 5.08) MPa.

In addition to the data collected in this work, literature data for VLE, density, and heat capacities were used to tune the mixture parameters in REFPROP 10 and improve the prediction of these thermodynamics properties. There were significant improvements in the prediction of thermodynamic properties, particularly the density where, for example, the root-mean-square (RMS) of the relative deviation between the model and the experimental data for the (CO_2 + R1234yf) mixture was decreased from (1.38 to 0.18) %. The tuned REFPROP models were then evaluated in terms of their ability to predict the thermodynamic properties of several ternaries and a five-component mixture of HFCs, an HFO, and CO_2. The following mixtures and properties were measured:

1. Vapour-liquid equilibria (VLE) of four ternary mixtures of CO_2 + R1234yf + R32 with respective component compositions of (10, 45, 45) mass%, (20, 40, 40) mass%, (30, 35, 35) mass%, and (50, 25, 25) mass% at T = (10, 40) ℃ and an equimolar five-component mixture of CO_2 + R1234yf + R32 + R125 + R134a at T = (0, 40, 60) ℃.
2. Liquid densities of a ternary mixture of CO_2 + R1234yf + R32, with respective component compositions of (5, 67, 28) mass % and an equimolar five-component mixture of CO_2 + R1234yf + R32 + R125 + R134a at temperatures between (-30 and 50) °C and pressures between (1.43 and 5.07) MPa.
3. Liquid heat capacities of a ternary mixture of CO_2 + R1234yf + R32, with respective component compositions of (5, 67, 28) mass % and an equimolar five-component mixture of CO_2 + R1234yf + R32 + R125 + R134a at temperatures between (-30 and 50) °C and pressures between (1.50 and 5.00) MPa.

The multi-component mixture measurements showed that the tuned REFPROP models give significantly better predictions of the refrigerant mixtures' thermodynamic properties. Density predictions were improved by a factor of 2. These improved thermodynamic models will help make simulations of refrigeration processes involving these mixtures more reliable.

B.7 Supporting Information

B.7.1 *Experimental method*

B.7.1.1 GC calibration

For the GC calibration experiments and also for the five-component VLE experiments, a typical gravimetric method was used to find the exact composition of the mixtures prepared volumetrically. For this purpose, sample cylinders were used for the preparation of the mixtures. As the first step, the sample cylinders were put under vacuum overnight (to reach a vacuum level lower than 100 Pa). This was followed by weighing each cylinder 10 times using a three-digit balance, leaving them for 24 h, and weighing them again 10 other times. After, the desired volume of the first refrigerant (the heavier one) in its subcooled condition was injected into the sample cylinder by Teledyne ISCO pumps (260D). The sample cylinder was then left for 24 h for temperature and pressure stability, weighed 10 times, left for 24 h, and weighed again 10 other times. Subsequently, the second refrigerant was injected into the cylinder and the cylinder was weighed using the same process as for the first refrigerant (the same procedure was followed for the next refrigerants if there was any). Calculating the average weight of each refrigerant injected and using the molar mass of the refrigerant, the composition of the fluid in mole percentage was calculated.

The weights recorded by the balance were also corrected by the air buoyancy effect using the following equation:

$$W_{\mathrm{Actual}} = W_{\mathrm{Balance}} + V_{\mathrm{Cylinder}} \times \rho_{\mathrm{Air}} \qquad \text{B.16}$$

In Equation B.16, W_{Actual} is the corrected weight, W_{Balance} is the weight shown by the balance, V_{Cylinder} is the volume of the cylinder and ρ_{Air} is the density of humid air. V_{Cylinder} was calculated by the water displacement method and an average value of three measurements was used as the volume of the cylinder. The laboratory conditions, including temperature, atmospheric pressure, and relative humidity, were recorded during weighing and used to calculate ρ_{a} by the method reported in P. Giacomo [46].

Table B.12: The GC temperature program for the VLE experiments.

Experiment	GC column	GC temperature program	
VLE CO_2 + R32	Sunpak-H 80/100 Glass	Heater Temperature (Inlet)	220 ºC
		Pressure (Inlet)	10 psi
		Total Flow (Inlet)	52 mL/min
		Septum Purge Flow (Inlet)	1 mL/min
		Split Ratio	Splitless
		Column Flow	ml/min
		Temperature (Oven)	220 ºC
		Equilibration Time (Oven)	0 min
		Heater Temperature (Detector)	260 ºC
		Reference Flow (Detector)	30 mL/min
		Makeup Flow	2 mL/min
VLE CO_2 + R134a VLE CO_2 + R1234yf VLE CO_2 + R125	HP/PLOT-U	Heater Temperature (Inlet)	150 ºC
		Pressure (Inlet)	4.98 psi
		Total Flow (Inlet)	152.5 mL/min
		Septum Purge Flow (Inlet)	1.5 mL/min
		Split Ratio	100/1
		Column Flow	1.5 ml/min
		Temperature (Oven)	60 ºC
		Equilibration Time (Oven)	0 min
		Heater Temperature (Detector)	180 ºC
		Reference Flow (Detector)	15 mL/min
		Makeup Flow	3 mL/min

VLE and GC Calibration Ternary Mixtures	HP/PLOT-U	Heater Temperature (Inlet)	150 ºC
		Pressure (Inlet)	4.98 psi
		Total Flow (Inlet)	152.5 mL/min
		Septum Purge Flow (Inlet)	1.5 mL/min
		Split Ratio	100/1
		Column Flow	1.5 ml/min
		Temperature (Oven)	60 ºC
		Equilibration Time (Oven)	0 min
		Heater Temperature (Detector)	180 ºC
		Reference Flow (Detector)	15 mL/min
		Makeup Flow	3 mL/min

VLE and GC calibration 5-Component Mixture	Sunpak-H 80/100 Glass	Heater Temperature (Inlet)	220 ºC
		Pressure (Inlet)	10 psi
		Total Flow (Inlet)	52 mL/min
		Septum Purge Flow (Inlet)	1 mL/min
		Split Ratio	Splitless
		Column Flow	ml/min
		Temperature (Oven)	220 ºC
		Equilibration Time (Oven)	0 min
		Heater Temperature (Detector)	260 ºC
		Reference Flow (Detector)	30 mL/min
		Makeup Flow	2 mL/min

Table B.13: The relative response factors for the GC calibration.

Experiment	Component	α_i
Binary / Ternary Mixtures	R32	0.9594
	R134a	0.7047
	R1234yf	0.6239
	R125	0.6612
5-Component Mixture	CO_2	1.4191
	R32	1.4087
	R134a	1.0319
	R1234yf	1.0070

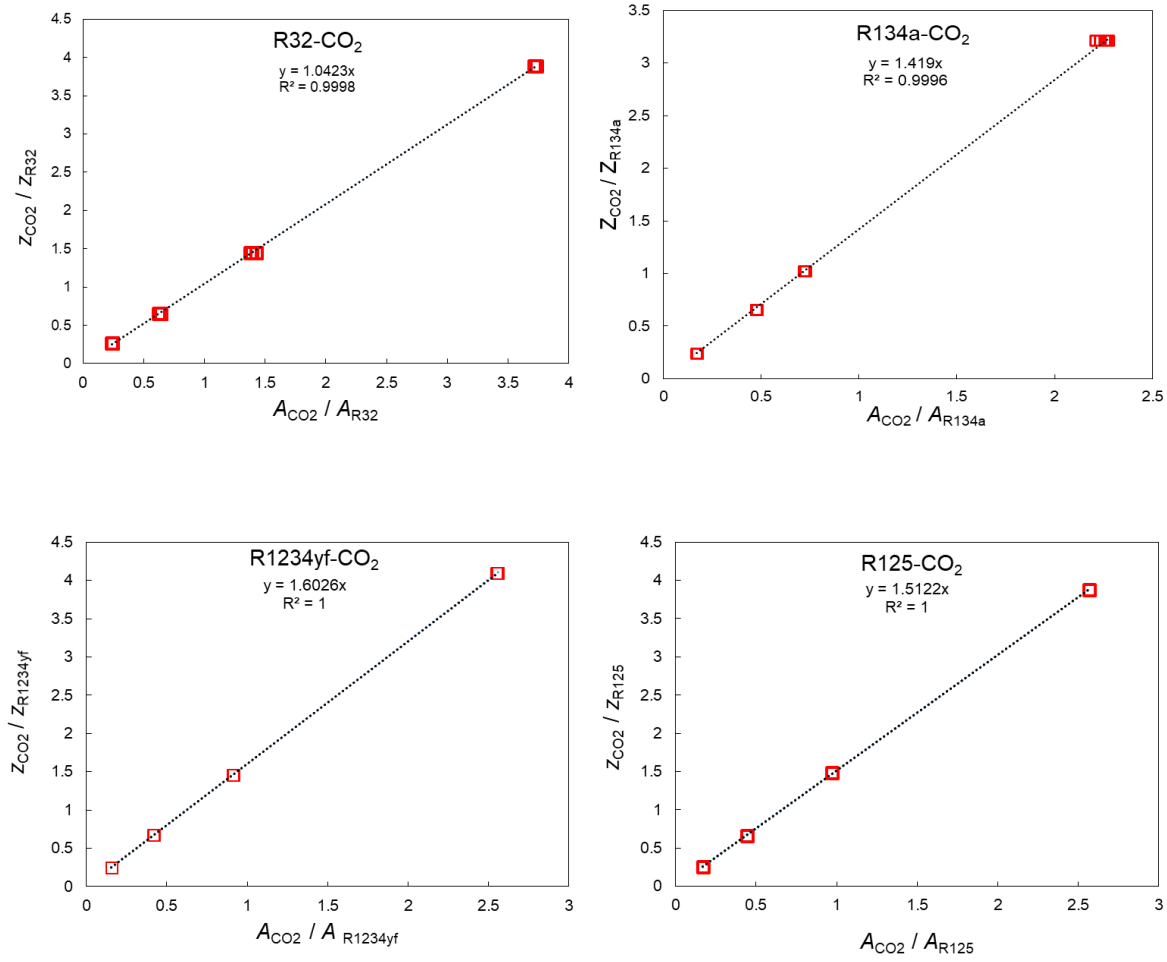

Figure B.10: The calibration results used for VLE binary / ternary experiments.

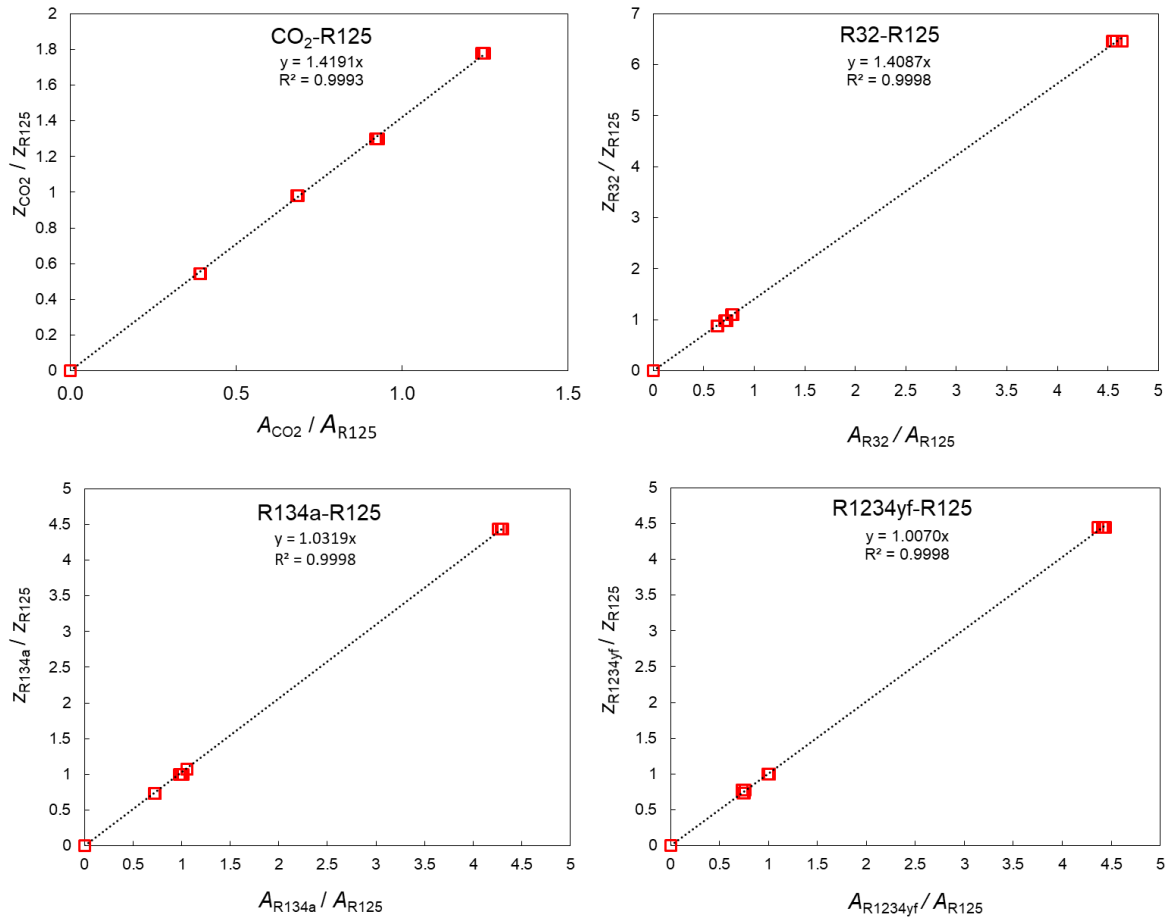

Figure B.11: The calibration results used for VLE five-component experiments.

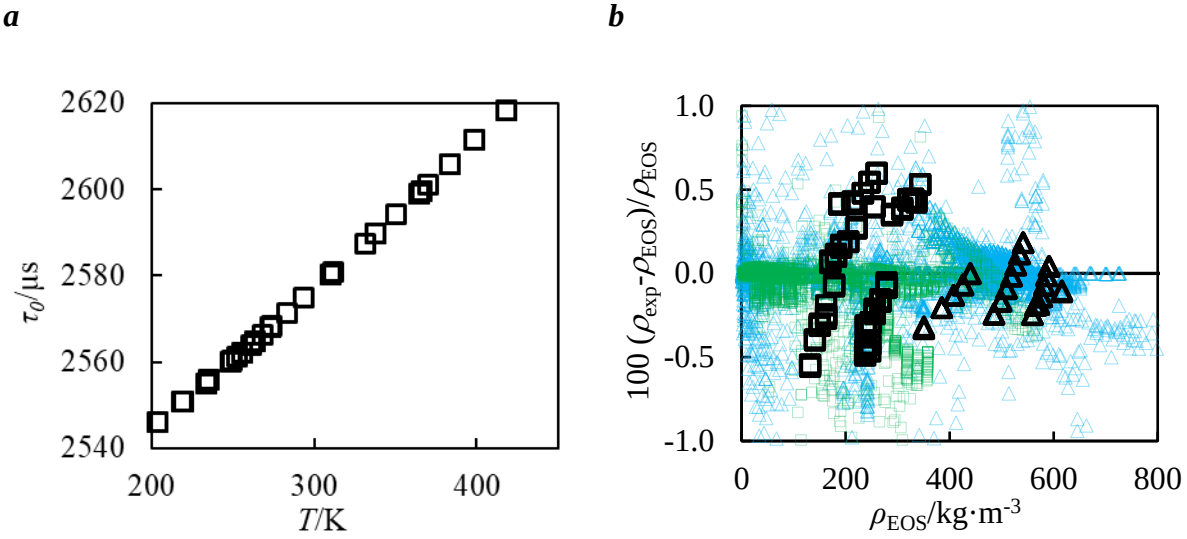

Figure B.12: (a) Resonance period of the evacuated tube (τ_0) at different temperatures and (b) deviations of the measured densities for ☐, methane and △, propane in this study; and literature densities (☐, methane and △, propane) from those calculated using reference EOS implemented in REFPROP 10 [39,47–77].

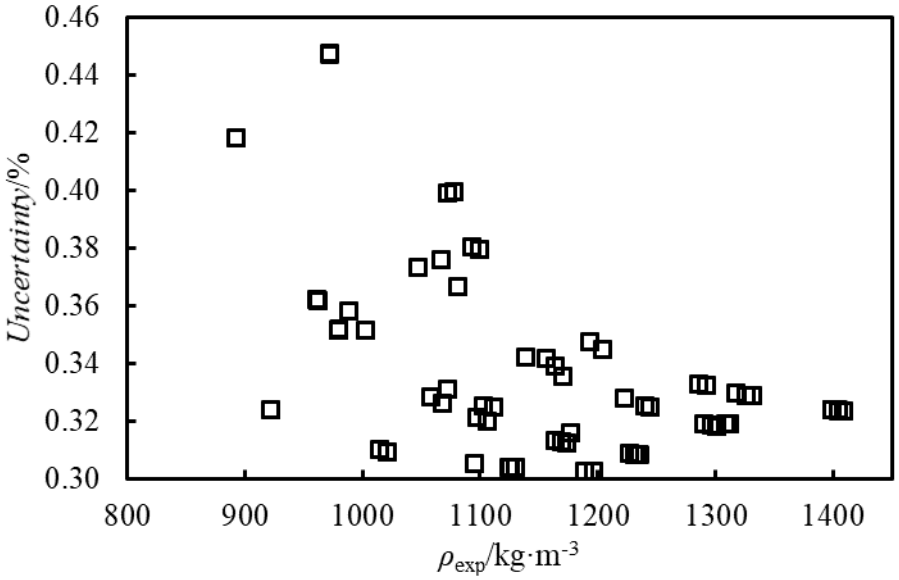

Figure B.13: Combined uncertainty with experimental measured densities

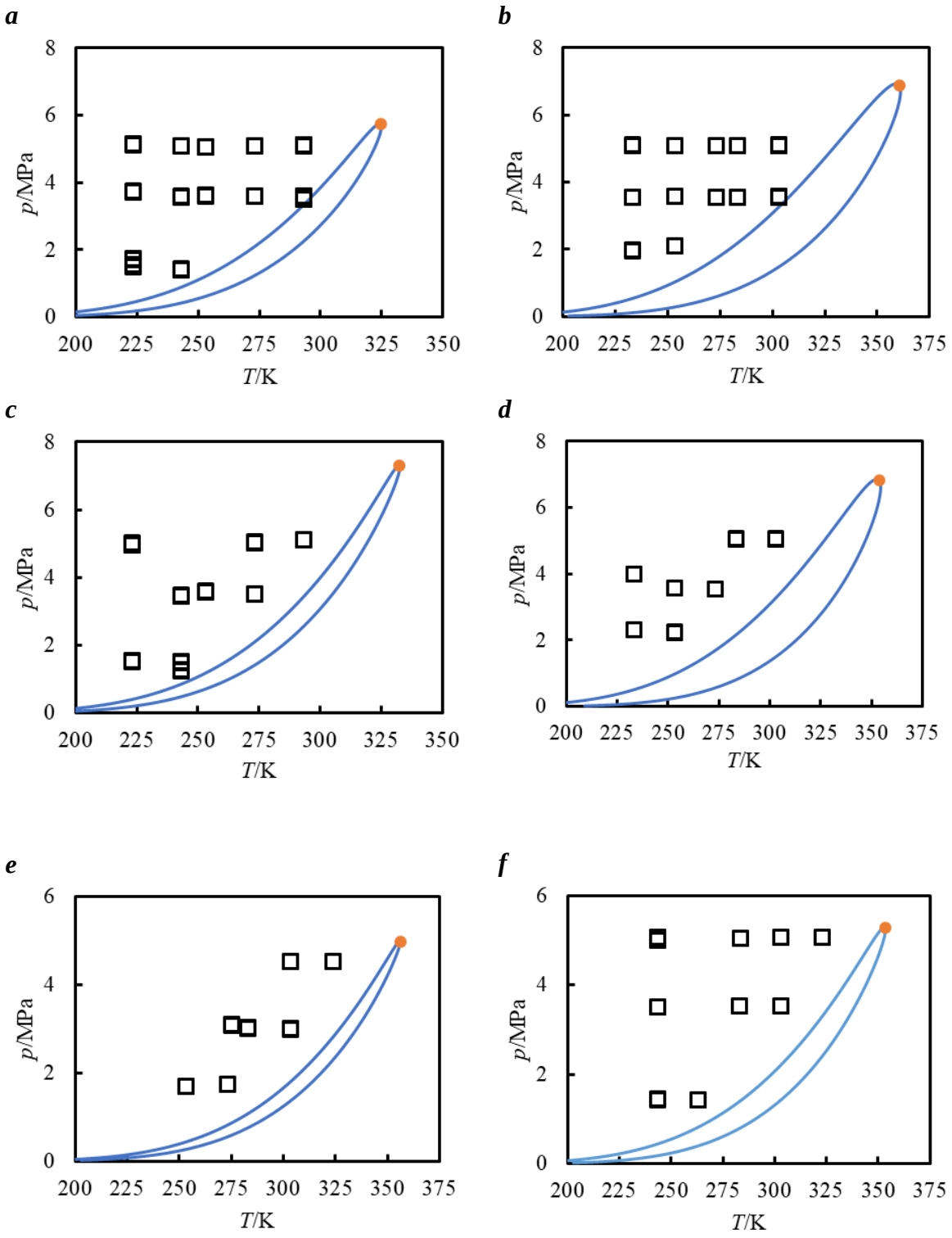

Figure B.14: Pressure and temperature conditions of (a) binary mixture (0.50 R32 + 0.50 CO_2), (b) binary mixture (0.50 R134a + 0.50 CO_2), (c) binary mixture (0.50 R125 + 0.50 CO_2), (d) binary mixture (0.50 R1234yf + 0.50 CO_2), (e) ternary mixture (0.09 CO_2 + 0.43 R32 + 0.48 R1234yf) and (f) 5-component mixture (0.20 CO_2 + 0.20 R32 + 0.20 R1234yf + 0.20 R134a + 0.20 R125) at which the density data were measured. Phase envelopes calculated using the default EOS implemented in REFPROP 10 [9] are also shown for each mixture. Symbols correspond to: ☐ experimental data; ● predicted critical point; ▬ predicted phase envelope.

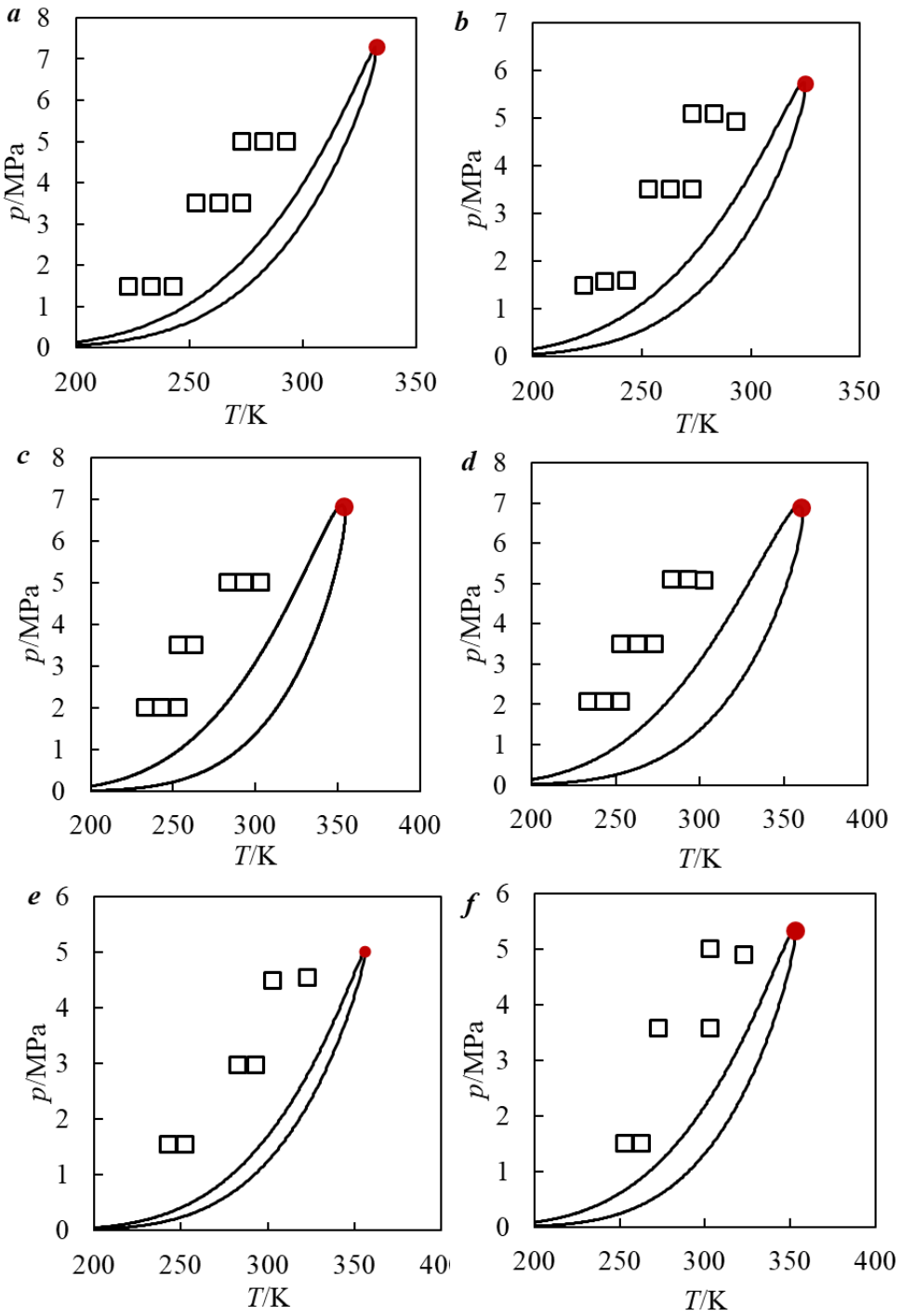

Figure B.15: Pressure and temperature conditions of (*a*) binary mixture (0.50 R32 + 0.50 CO_2), (*b*) binary mixture (0.50 R134a + 0.50 CO_2), (*c*) binary mixture (0.50 R125 + 0.50 CO_2), (*d*) binary mixture (0.50 R1234yf + 0.50 CO_2), (*e*) ternary mixture (0.09 CO_2 + 0.43 R32 + 0.48 R1234yf) and (*f*) 5-component mixture (0.20 CO_2 + 0.20 R32 + 0.20 R1234yf + 0.20 R134a + 0.20 R125) at which the heat capacity data were measured. Phase envelopes calculated using the default EOS implemented in REFPROP 10 [9] are also shown for each mixture. Symbols correspond to: □ experimental data; ● predicted critical point; ▬ predicted phase envelope.

B.7.2 ***Results***

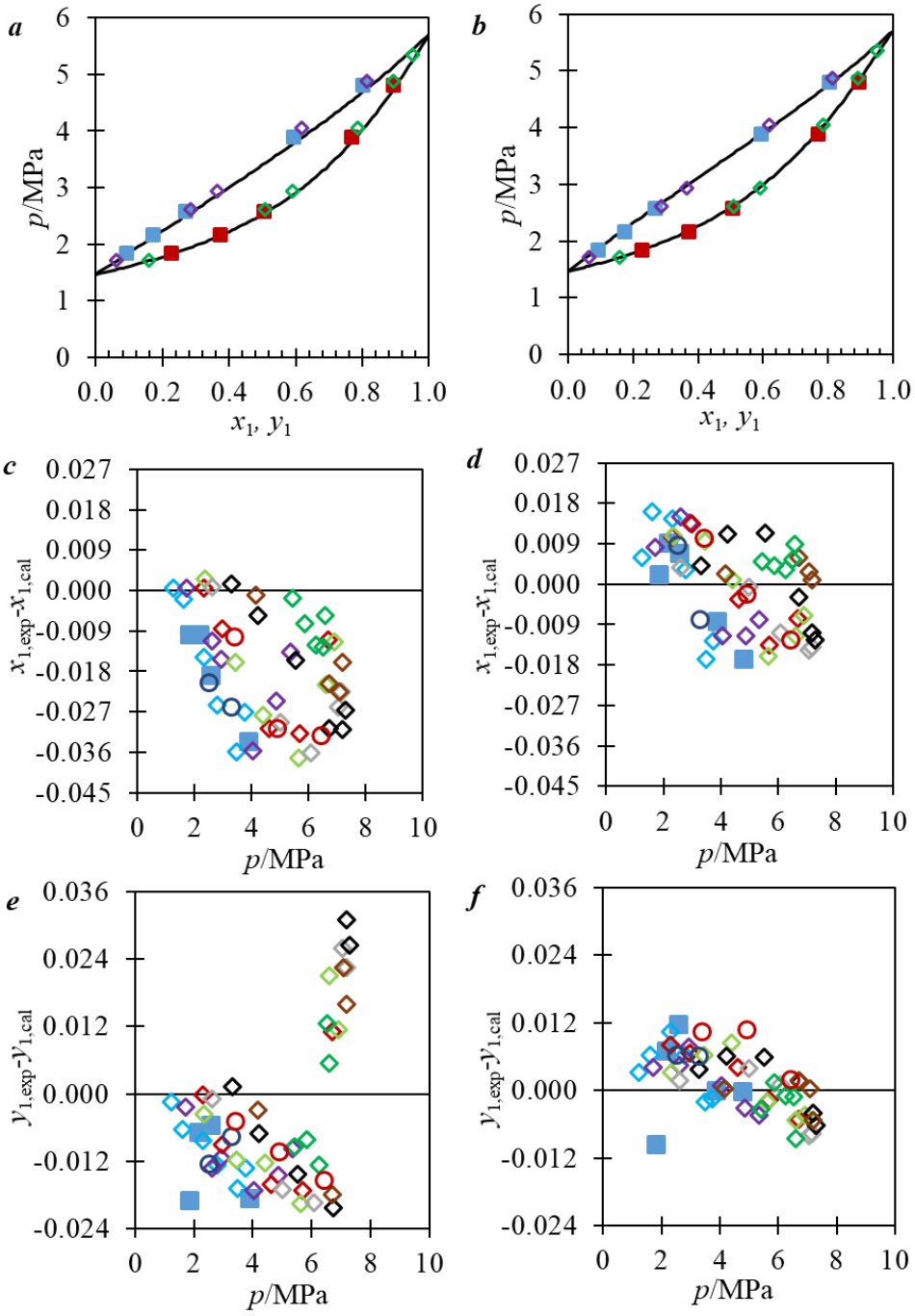

Figure B.16: Comparisons of CO_2 (1) + R32 (2) VLE results from available experimental data and various models: Data and phase envelope at 293.0 K from the EOS in REFPROP 10 [9] using the (*a*) default and (*b*) tuned binary interaction parameters (BIPs). Deviations are shown of the measured x_1 from those calculated with the default (*c*) and tuned (*d*) BIPs. Deviations are shown of the measured y_1 from those calculated with the default (*e*) and tuned (*f*) BIPs. Symbols refer to the measurements at different pressures, and the solid curves refer to the model predictions. Symbol list: (*a*) and (*b*), (■, blue) Bubble point measured in this work, (■, red) Dew point measured in this work (◇, purple) Bubble point from Rivollet et al. [34] (◇, green) Dew point from Rivollet et al. [34]; (*c*), (*d*), (*e*) and (*f*): (■, blue) This work (293 K), (◇, blue) (283 K), (◇, purple) (293 K), (◇, red) (303 K), (◇, light-green) (305 K), (◇, grey) (313 K), (◇, black) (323 K), (◇, brown) (333 K), (◇, green) (343 K) of Rivollet et al. [34], (○, blue) (280 K), (○, green) (295 K), (○, red) (310 K) of Diefenbacher and Türk [78].

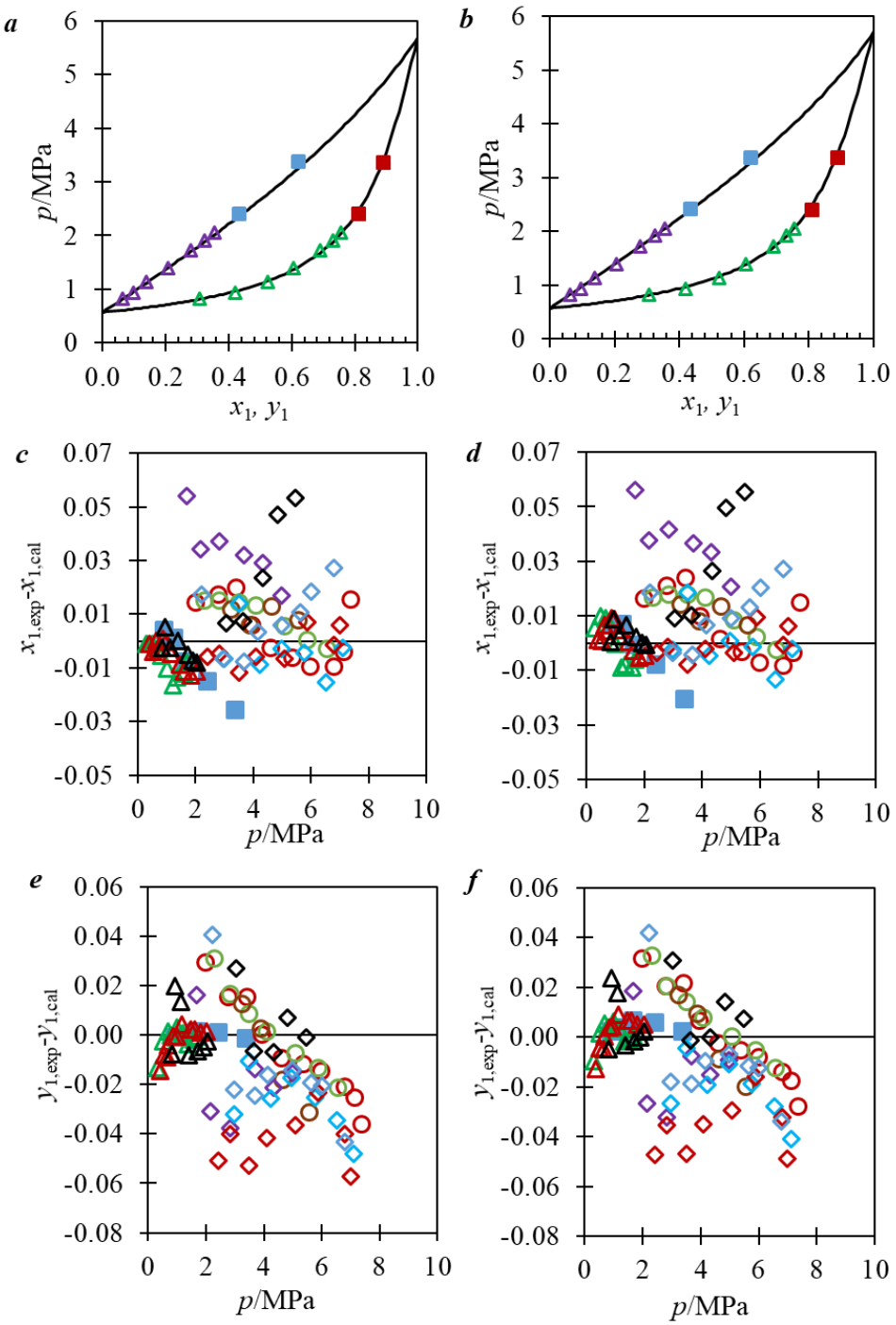

Figure B.17: Comparisons of CO_2 (1) + R134a (2) VLE results from available experimental data and various models: Data and phase envelop at 292.9 K from the EOS in REFPROP 10 [9] using the (*a*) default and (*b*) tuned binary interaction parameters (BIPs). Deviations are shown of the measured x_1 from those calculated with the default (*c*) and tuned (*d*) BIPs. Deviations are shown of the measured y_1 from those calculated with the default (*e*) and tuned (*f*) BIPs. Symbols refer to the measurements at different pressures, and the solid curves refer to the model predictions. Symbol list: (*a*) and (*b*) (■, blue) Bubble point measured in this work (■, red), Dew point measured in this work (Δ, purple) Bubble point from Duran-Valencia et al. [35] (Δ, green) Dew point from Duran-Valencia et al. [35]; (*c*), (*d*), (*e*) and (*f*): (■, blue) this work (294 K), (○, red) (330 K), (○, green) (339 K), (○, brown) (354 K) of Silva-Oliver and Galicia-Luna [41], (◇, pruple) (323 K), (◇, light blue) (328 K), (◇, red) (333 K), (◇, blue) (338 K), (◇, black) (343 K) of Lim et al. [40], (Δ, green) (253 K), (Δ, red) (273 K), (Δ, black) (293 K) of Duran-Valencia et al. [35].

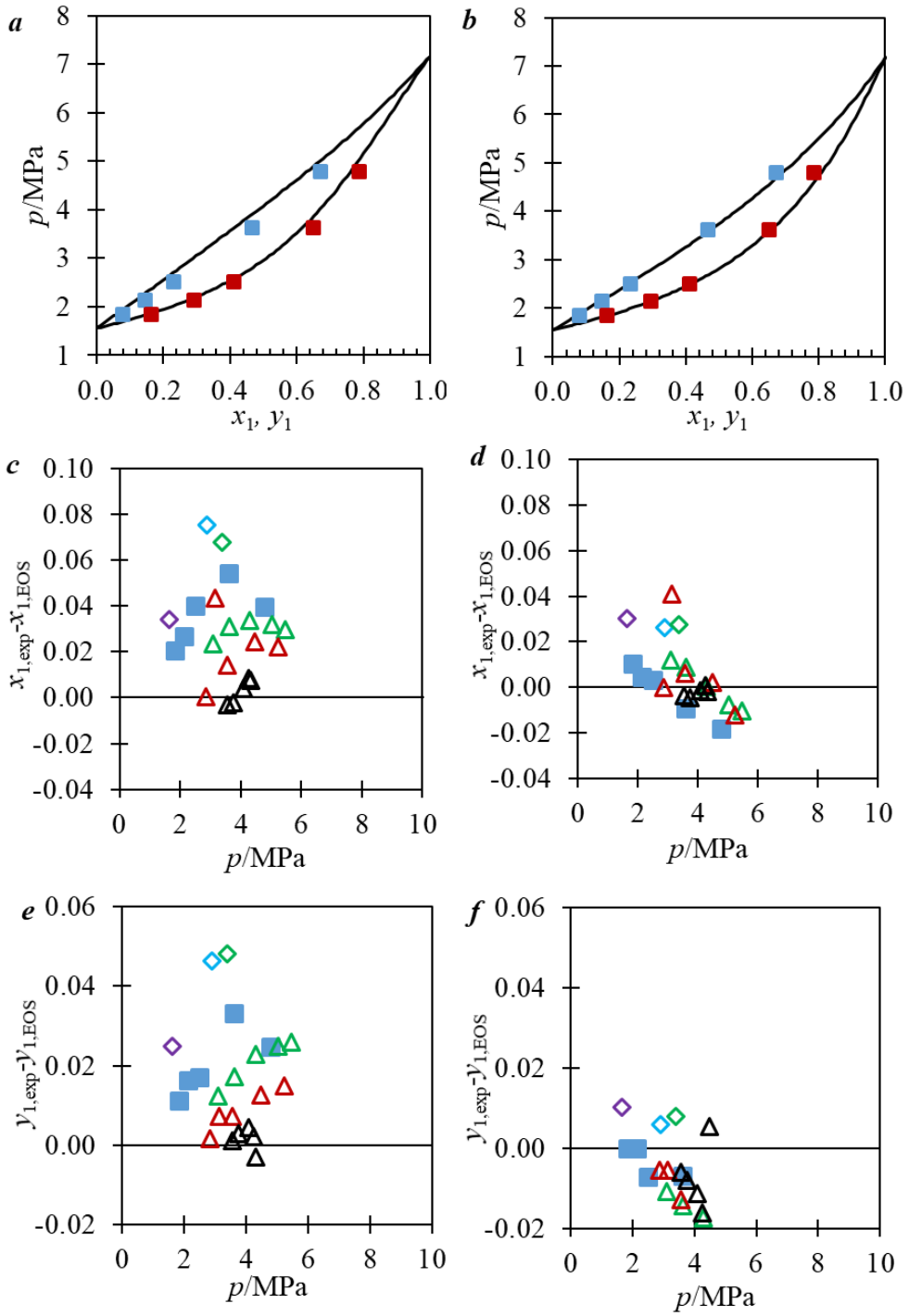

Figure B.18: Comparisons of CO_2 (1) + R125 (2) VLE results from available experimental data and various models: Data and phase envelop at 302.9 K from the EOS in REFPROP 10 [9]using the (*a*) default and (*b*) tuned binary interaction parameters (BIPs). Deviations are shown of the measured x_1 from those calculated with the default (*c*) and tuned (*d*) BIPs. Deviations are shown of the measured y_1 from those calculated with the default (*e*) and tuned (*f*) BIPs. Symbols refer to the measurements at different pressures, and the solid curves refer to the model predictions. Symbol list: (*a*) and (*b*) (■, blue) Bubble point measured in this work (■, red) Dew point measured in this work; (*c*), (*d*), (*e*) and (*f*): (■, blue) This work (303 K), (◇, light blue) (283 K), (◇, purple) (293 K), (◇, green) (299 K) of Di Nicola et al. [36], (Δ, green) (313 K), (Δ, red) (323 K), (Δ, black) (333 K) of Jeong et al. [42].

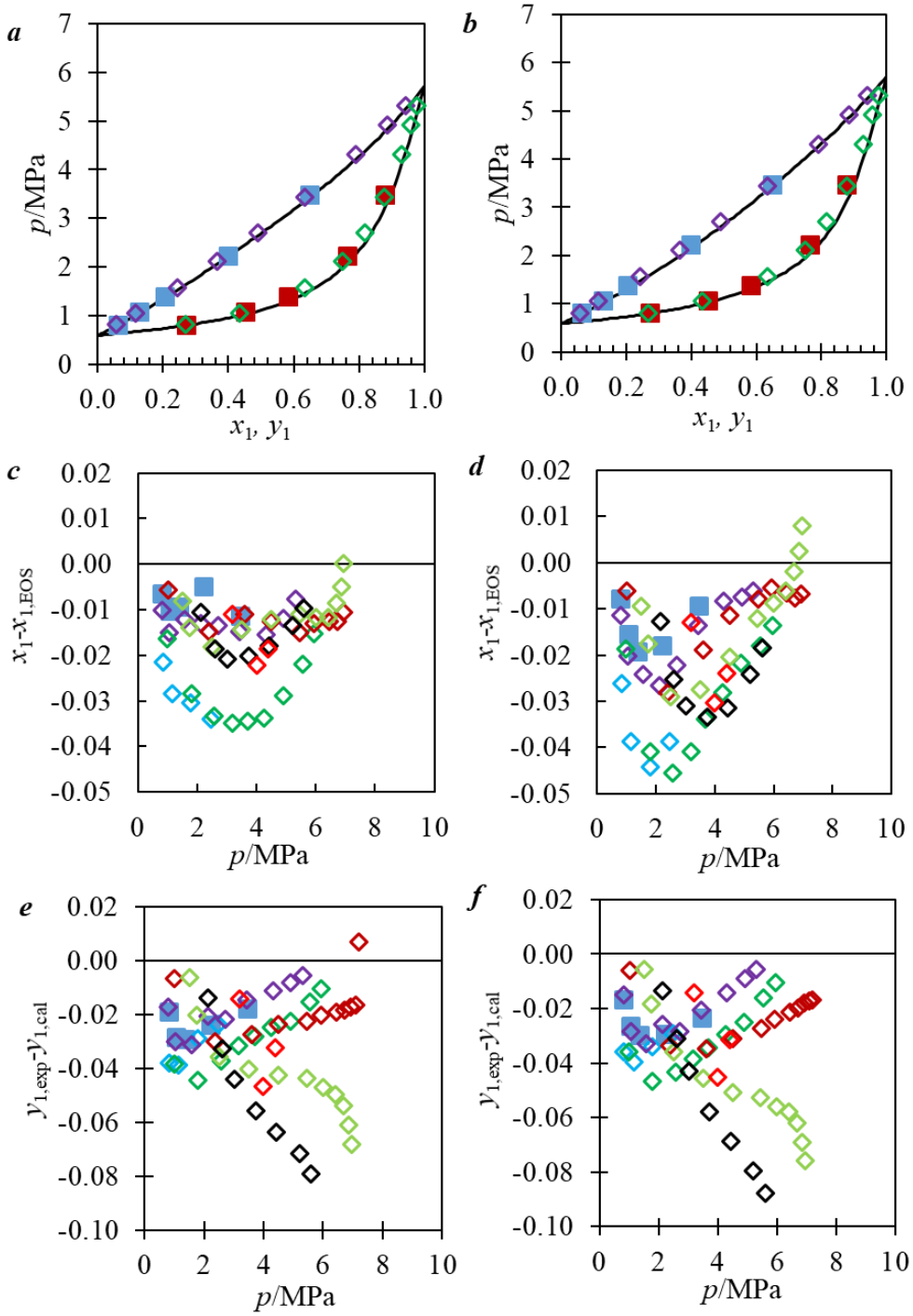

Figure B.19: Comparisons of CO_2 (1) + R1234yf (2) VLE results from available experimental data and various models: Data & phase envelope at 293.13 K from the EOS in REFPROP 10 [9] using the (*a*) default and (*b*) tuned binary interaction parameters (BIPs). Deviations are shown of the measured x_1 from those calculated with the default (*c*) and tuned (*d*) BIPs. Deviations are shown of the measured y_1 from those calculated with the default (*e*) and tuned (*f*) BIPs. Symbols refer to the measurements at different pressures, and the solid curves refer to the model predictions. Symbol list: (*a*) and (*b*) (■, blue) Bubble point measured in this work, (■, red) Dew point measured in this work, (◇, purple) Bubble point from Juntarachat et al. [36], (◇, green) Dew point from Juntarachat et al. [36]; (*c*), (*d*), (*e*) and (*f*): (■, blue) This work (293 K), (◇, light blue) (283 K), (◇, purple) (293 K), (◇, green) (298 K), (◇, red) (308 K), (◇, light green) (323 K), (◇, black) (338 K), (◇, red) (353 K) of Juntarachat et al. [36].

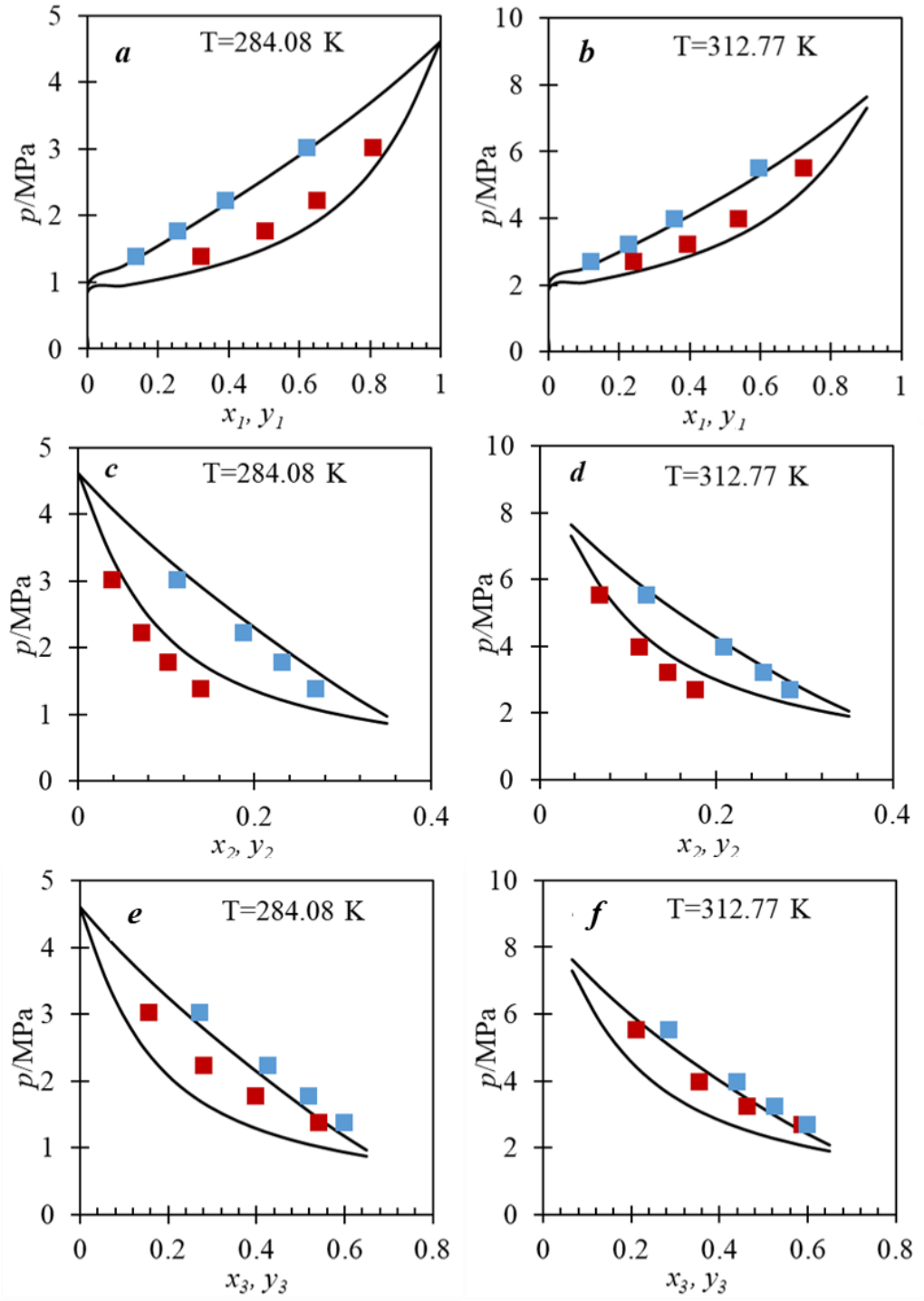

Figure B.20: Measured (symbols) and predicted (curves) bubble and dew pressures at T=284.1 K and T=312.8 K for the CO_2 (1) + R1234yf (2) + R32 (3) ternary systems ($z_{R1234yf}/z_{R32}$=0.45) as a function of the measured liquid and vapour mole fractions of each component: (■, blue) Bubble point measured in this work, (■, red) Dew point measured in this work. The dew and bubble curve predictions were made with the EOS in REFPROP 10 using the default binary interaction parameters.

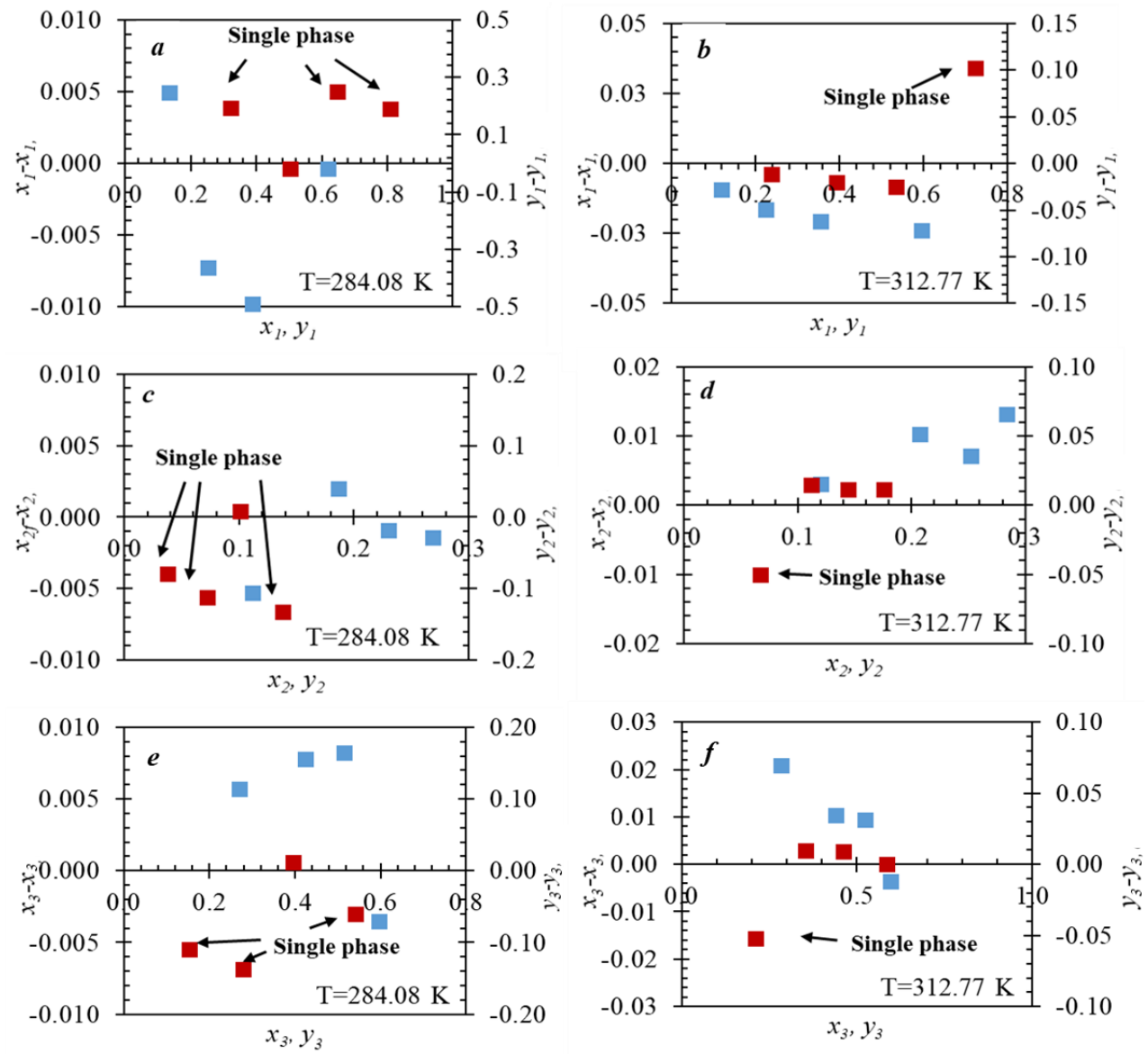

Figure B.21: Deviations ($x_i - x_{i,EOS}$) and ($y_i - y_{i,EOS}$) from the default Helmholtz energy mixture model for the CO_2 (1) + R1234yf (2) + R32 (3) ternary systems plotted against the liquid and vapour mole fraction of each component. Left axes: (■, blue), deviations for liquid; Right axes:, (■, red) deviations for vapour. Experimental points with an arrow indicating "single phase" are points where the model predicts a single phase, but two-phases were measured in this work.

Table B.14: Measured VLE data and the estimated uncertainty for the refrigerant mixtures

CO_2 (1) + R32 (2)						
Global composition	***T*/K**	***p*/MPa**	x_i	$u(x_i)$	y_i	$u(y_i)$
z_1 = 0.1089 ±0.0010	292.53	1.84	0.0931	0.0018	0.2269	0.0041
z_1 = 0.2000 ±0.0020	293.06	2.17	0.1729	0.0023	0.3721	0.0034
z_1 = 0.3116 ±0.0025	293.21	2.58	0.2687	0.0032	0.5059	0.0044
z_1 = 0.6360 ±0.0024	292.67	3.89	0.5945	0.0046	0.7681	0.0040
z_1 = 0.8099 ±0.0017	292.66	4.80	0.8023	0.0016	0.8934	0.0010
CO_2 (1) + R1234yf (2)						
Global composition	***T*/K**	***p*/MPa**	x_i	$u(x_i)$	y_i	$u(y_i)$
z_1 = 0.0828 ±0.0008	293.08	0.82	0.0619	0.0017	0.2718	0.0054
z_1 = 0.1799 ±0.0011	293.00	1.08	0.1274	0.0018	0.4514	0.0037
z_1 = 0.2836 ±0.0014	292.99	1.39	0.2043	0.0018	0.5835	0.0027
z_1 = 0.4907 ±0.0016	293.02	2.23	0.3992	0.0025	0.7632	0.0016
z_1 = 0.6996 ±0.0013	293.12	3.48	0.6492	0.0024	0.8782	0.0012
CO_2 (1) + R134a (2)						
Global composition	***T*/K**	***p*/MPa**	x_i	$u(x_i)$	y_i	$u(y_i)$
z_1 = 0.0864 ±0.0006	295.39	0.92	0.0779	0.0015	0.3376	0.0047
z_1 = 0.1856 ±0.0011	293.35	1.24	0.1668	0.0018	0.5528	0.0037
z_1 = 0.2821 ±0.0017	294.52	1.66	0.2497	0.0023	0.6681	0.0025
z_1 = 0.4696 ±0.0018	292.53	2.41	0.4334	0.0027	0.8102	0.0016
z_1 = 0.6939 ±0.0020	292.73	3.38	0.6213	0.0026	0.8884	0.0010
CO_2 (1) + R125 (2)						
Global composition	***T*/K**	***p*/MPa**	x_i	$u(x_i)$	y_i	$u(y_i)$
z_1 = 0.1073 ±0.0007	302.89	1.84	0.0787	0.0018	0.1641	0.0036
z_1 = 0.2028 ±0.0011	302.85	2.14	0.1456	0.0021	0.2943	0.0038
z_1 = 0.3090 ±0.0014	302.88	2.51	0.2332	0.0024	0.4109	0.0032
z_1 = 0.5485 ±0.0018	302.88	3.62	0.4656	0.0027	0.6495	0.0024
z_1 = 0.7234 ±0.0014	302.91	4.79	0.6720	0.0025	0.7865	0.0018

CO2 + R1234yf + R32														
Global composition	***T*/K**	***p*/MPa**	x_{CO2}	$u(x_{CO2})$	y_{CO2}	$u(y_{CO2})$	x_{R32}	$u(x_{R32})$	y_{R32}	$u(y_{R32})$	$x_{R1234yf}$	$u(x_{R1234yf})$	$y_{R1234yf}$	$u(y_{R1234yf})$
z_{CO2} = 0.1292 ±0.0011 z_{R32} = 0.6006 ±0.0030 $z_{R1234yf}$ = 0.2702 ±0.0025	284.03	1.39	0.1342	0.0011	0.3212	0.0031	0.5971	0.0027	0.5409	0.0027	0.2688	0.0022	0.1379	0.0014
z_{CO2} = 0.2688 ±0.0025 z_{R32} = 0.5042 ±0.0032 $z_{R1234yf}$ = 0.2270 ±0.0022	284.42	1.78	0.2539	0.0029	0.5028	0.0046	0.5160	0.0029	0.3963	0.0030	0.2301	0.0025	0.1009	0.0011
z_{CO2} = 0.3985 ±0.0033 z_{R32} = 0.4172 ±0.0027 $z_{R1234yf}$ = 0.1843 ±0.0017	284.19	2.23	0.3888	0.0038	0.6483	0.0039	0.4250	0.0029	0.2799	0.0025	0.1861	0.0018	0.0718	0.0010
z_{CO2} = 0.6195 ±0.0033 z_{R32} = 0.2634 ±0.0023 $z_{R1234yf}$ = 0.1171 ±0.0011	283.70	3.03	0.6191	0.0043	0.8083	0.0023	0.2691	0.0030	0.1539	0.0017	0.1118	0.0015	0.3265	0.0006
z_{CO2} = 0.1292 ±0.0011 z_{R32} = 0.6006 ±0.0030 $z_{R1234yf}$ = 0.2702 ±0.0025	312.88	2.71	0.1197	0.0015	0.2383	0.0032	0.5970	0.0026	0.5857	0.0029	0.2834	0.0024	0.1760	0.0022
z_{CO2} = 0.2688 ±0.0025 z_{R32} = 0.5042 ±0.0032 $z_{R1234yf}$ = 0.2270 ±0.0022	312.68	3.24	0.2243	0.0022	0.3936	0.0040	0.5233	0.0027	0.4624	0.0028	0.2522	0.0020	0.1440	0.0013
z_{CO2} = 0.3985 ±0.0033 z_{R32} = 0.4172 ±0.0027 $z_{R1234yf}$ = 0.1843 ±0.0017	312.78	3.99	0.3538	0.0032	0.5353	0.0040	0.4387	0.0026	0.3526	0.0025	0.2076	0.0016	0.1121	0.0010
z_{CO2} = 0.6195 ±0.0033 z_{R32} = 0.2634 ±0.0023 $z_{R1234yf}$ = 0.1171 ±0.0011	312.74	5.54	0.5954	0.0037	0.7221	0.0028	0.2844	0.0023	0.2110	0.0018	0.1203	0.0011	0.0669	0.0006

CO_2 + R1234yf + R32 + R125 + R134a

			R125				CO_2				R32			
Global composition	***T*/K**	***p*/MPa**	x_i	$u(x_i)$	y_i	$u(y_i)$	x_i	$u(x_i)$	y_i	$u(y_i)$	x_i	$u(x_i)$	y_i	$u(y_i)$
z_{R134a}=0.2015 ± 0.0045	273.48	0.98	0.2068	0.0008	0.1490	0.0015	0.1812	0.0022	0.4916	0.0036	0.2066	0.0008	0.1971	0.0015
$z_{R1234yf}$=0.2002±0.0045 z_{R125}=0.2016 ± 0.0045	312.79	2.42	0.2065	0.0005	0.1807	0.0010	0.1607	0.0055	0.3425	0.0022	0.1989	0.0054	0.2155	0.0009
z_{R32}=0.1994 ± 0.0045 z_{CO2}=0.1974 ± 0.0009	333.50	3.60	N/A*		0.1915	0.0008	N/A*		0.2644	0.0018	N/A*		0.2130	0.0008

			R134a				R1234yf			
Global composition	***T*/K**	***p*/MPa**	x_i	$u(x_i)$	y_i	$u(y_i)$	x_i	$u(x_i)$	y_i	$u(y_i)$
z_{R134a}=0.2015 ± 0.0045	273.48	0.98	0.2081	0.0012	0.0797	0.0014	0.1974	0.0011	0.0826	0.0014
$z_{R1234yf}$=0.2002±0.0045 z_{R125}=0.2016 ± 0.0045	312.79	2.42	0.2227	0.0055	0.1303	0.0011	0.2112	0.0055	0.1311	0.0011
z_{R32}=0.1994 ± 0.0045 z_{CO2}=0.1974 ± 0.0009	333.50	3.60	N/A*		0.1648	0.0010	N/A*		0.1663	0.0010

*At 333.5 K, a liquid phase was present but the volume available was insufficient to reliably sample and analyse its composition.

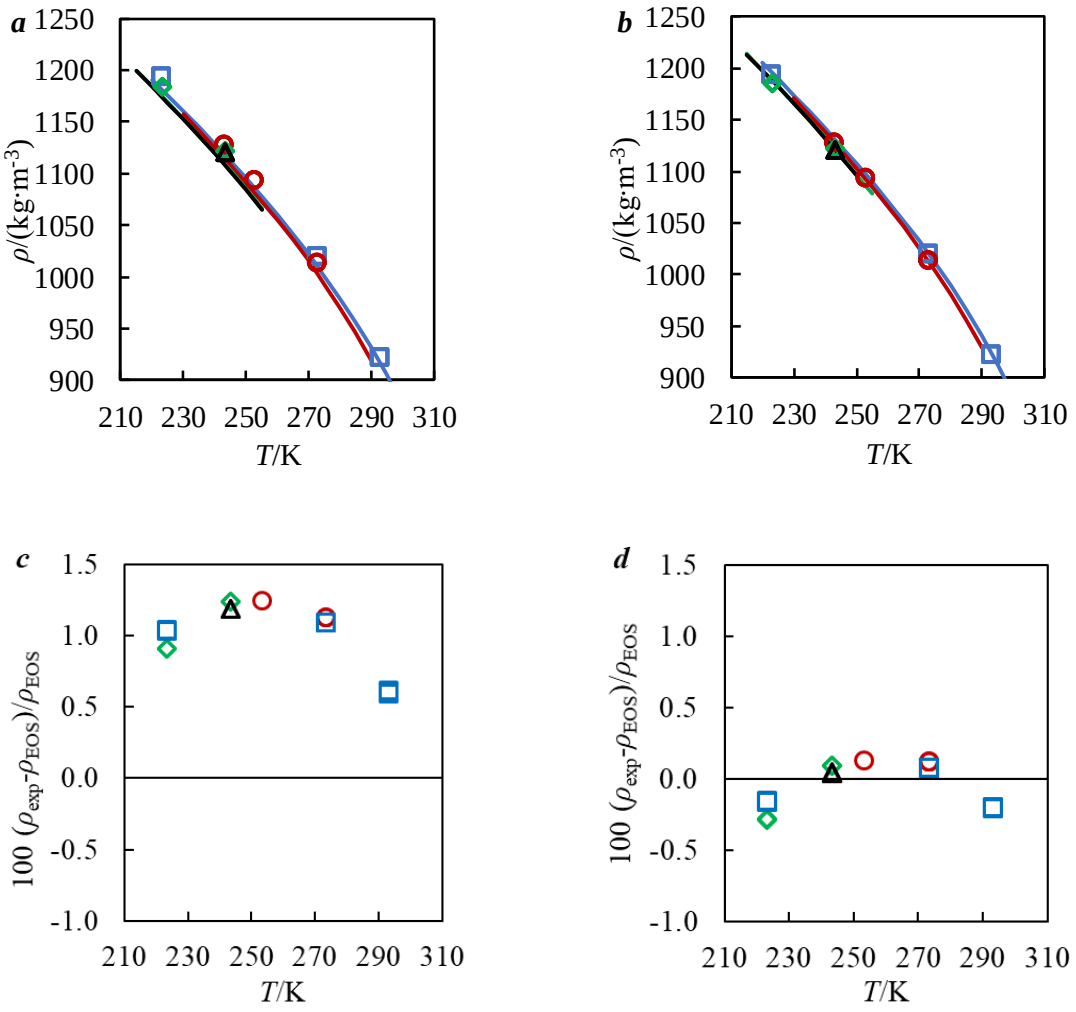

Figure B.22: Comparisons of 0.5 CO_2 + 0.5 R32 density results for the experimental data measured in this work and various models from (*a*) default and (*b*) tuned binary interaction parameters (BIPs). Deviations are shown of experimental data from those calculated with the default (*c*) and tuned (*d*) BIPs. Symbols refer to the measurements at different pressures (□ 5.00 MPa, ○ 3.50 MPa, ◇ 1.50 MPa and Δ 1.25 MPa), and the solid curves refer to the model prediction.

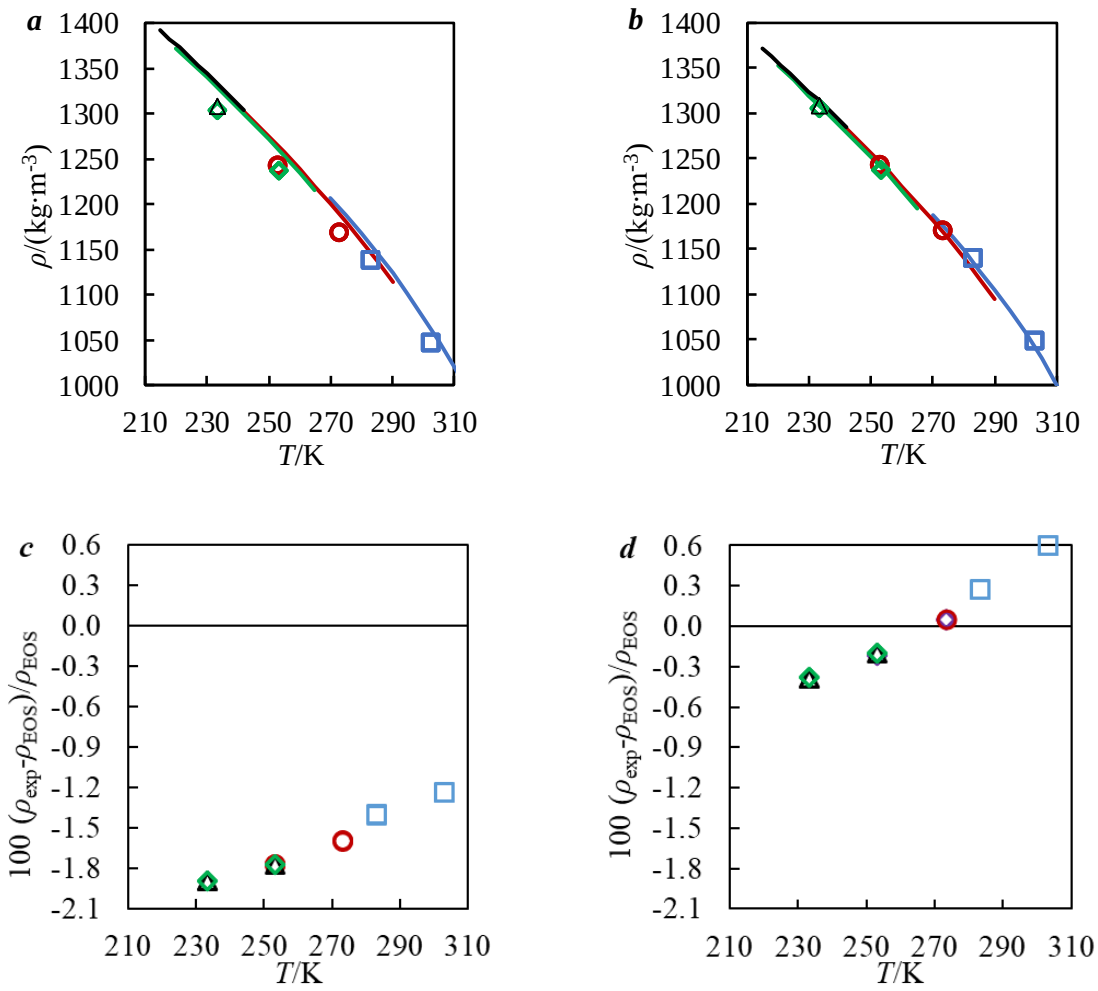

Figure B.23: Comparisons of 0.5 CO_2 + 0.5 R134a density results for the experimental data measured in this work and various models from (*a*) default and (*b*) tuned binary interaction parameters (BIPs). Deviations are shown of experimental data from those calculated with the default (*c*) and tuned (*d*) BIPs. Symbols refer to the measurements at different pressures (□ 5.05 MPa, Δ 3.98 MPa, ○ 3.55 MPa and ◇ 2.27 MPa), and the solid curves refer to the model prediction.

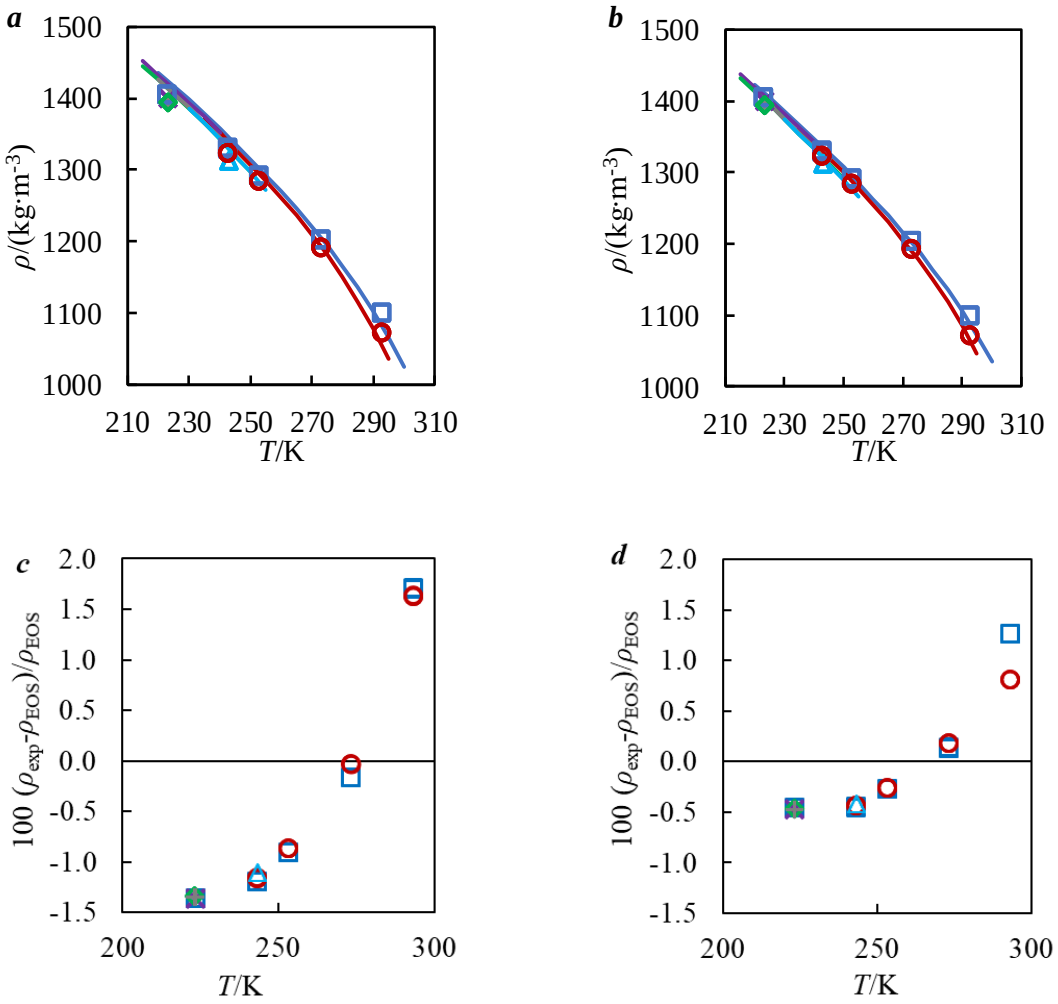

Figure B.24: Comparisons of 0.5 CO_2 + 0.5 R125 density results for the experimental data measured in this work and various models from (*a*) default and (*b*) tuned binary interaction parameters (BIPs). Deviations are shown of experimental data from those calculated with the default (*c*) and tuned (*d*) BIPs. Symbols refer to the measurements at different pressures (□ 5.10 MPa, ×3.72 MPa, ○ 3.59 MPa, + 1.73 MPa, ◇1.52 MPa and Δ 1.41 MPa), and the solid curves refer to the model prediction.

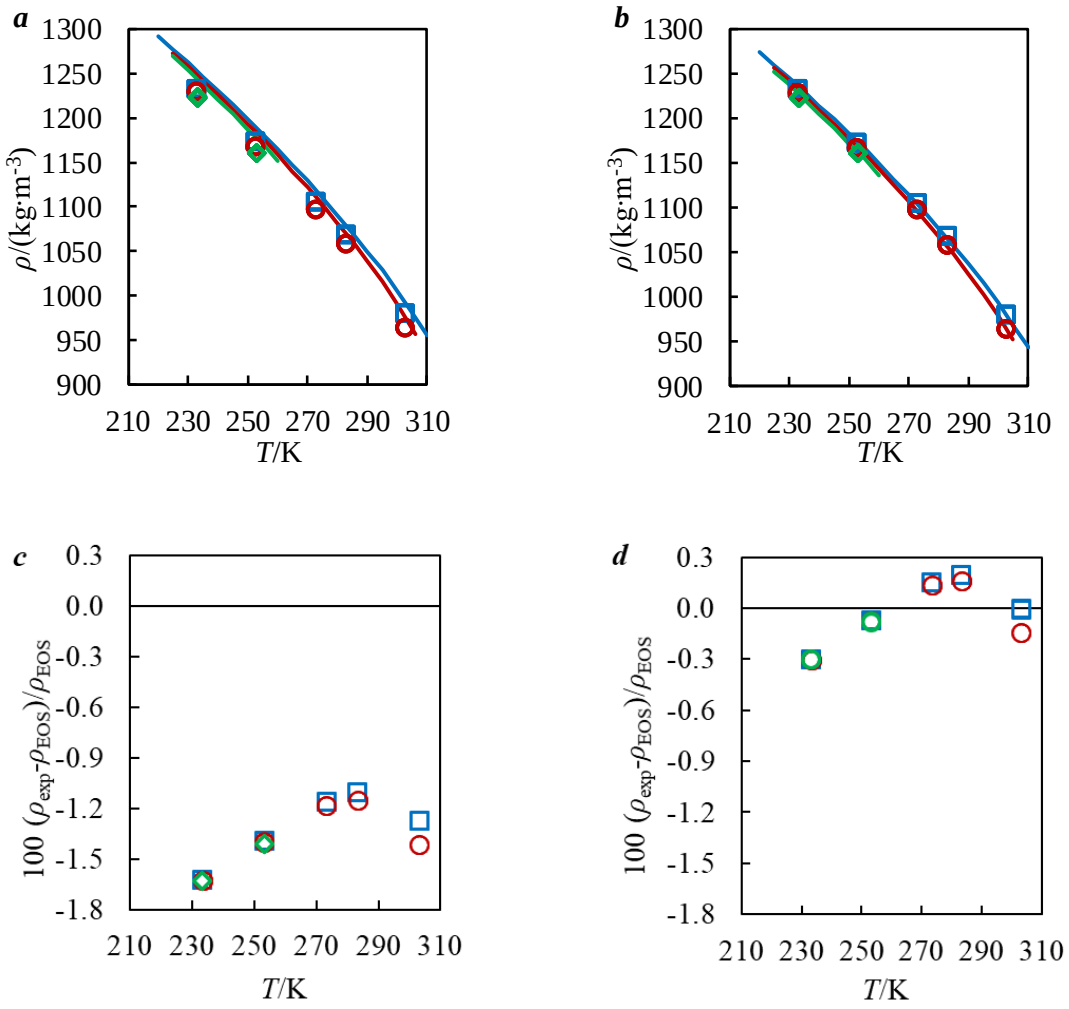

Figure B.25: Comparisons of 0.5 CO_2 + 0.5 R1234yf density results for the experimental data measured in this work and various models from (*a*) default and (*b*) tuned binary interaction parameters (BIPs). Deviations are shown of experimental data from those calculated with the default (*c*) and tuned (*d*) BIPs. Symbols refer to the measurements at different pressures (□ 5.09 MPa, ○ 3.56 MPa and ◇ 2.04 MPa), and the solid curves refer to the model prediction.

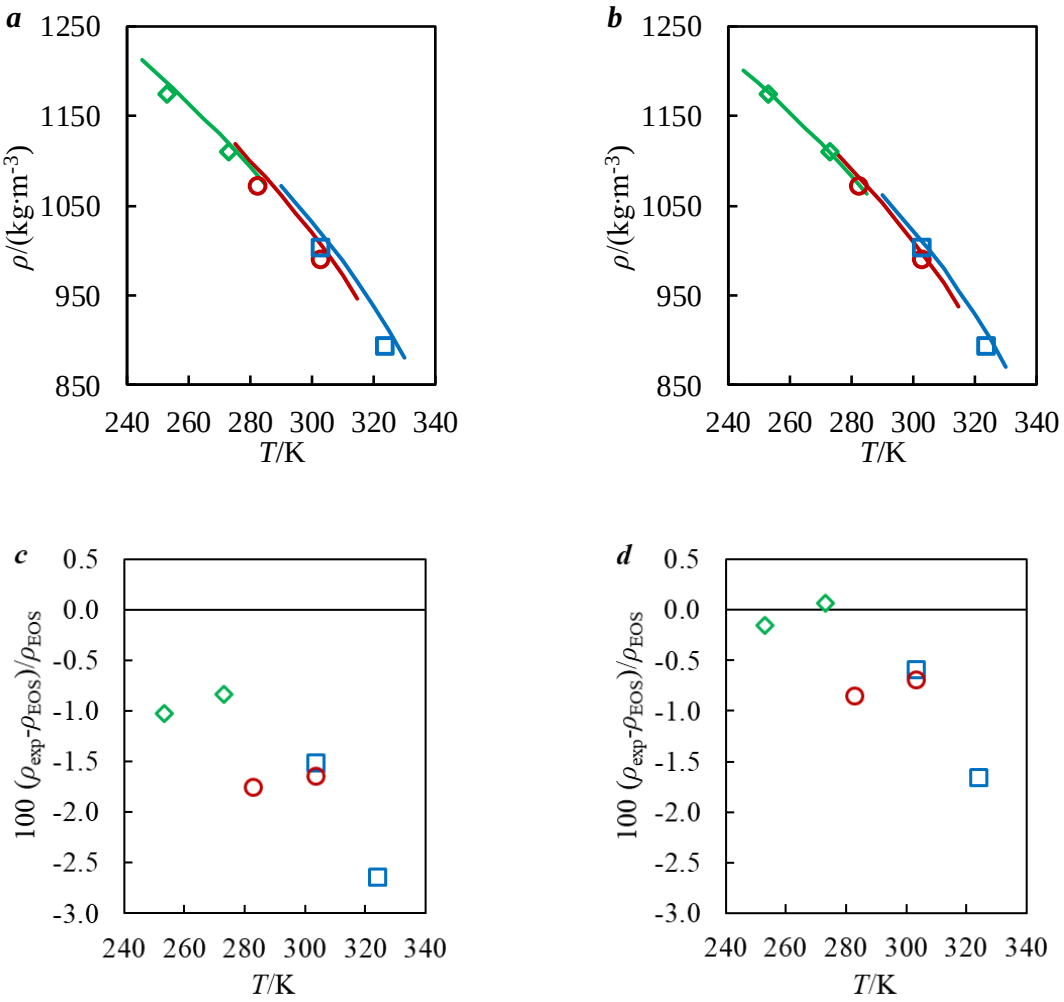

Figure B.26: Comparisons of 0.09 CO_2 + 0.48 R1234yf + 0.43 R32 density results for the experimental data measured in this work and various models from (*a*) default and (*b*) tuned binary interaction parameters (BIPs). Deviations are shown of experimental data from those calculated with the default (*c*) and tuned (*d*) BIPs. Symbols refer to the measurements at different pressures (□ 4.53 MPa, ○ 3.01 MPa and ◇1.72 MPa), and the solid curves refer to the model prediction.

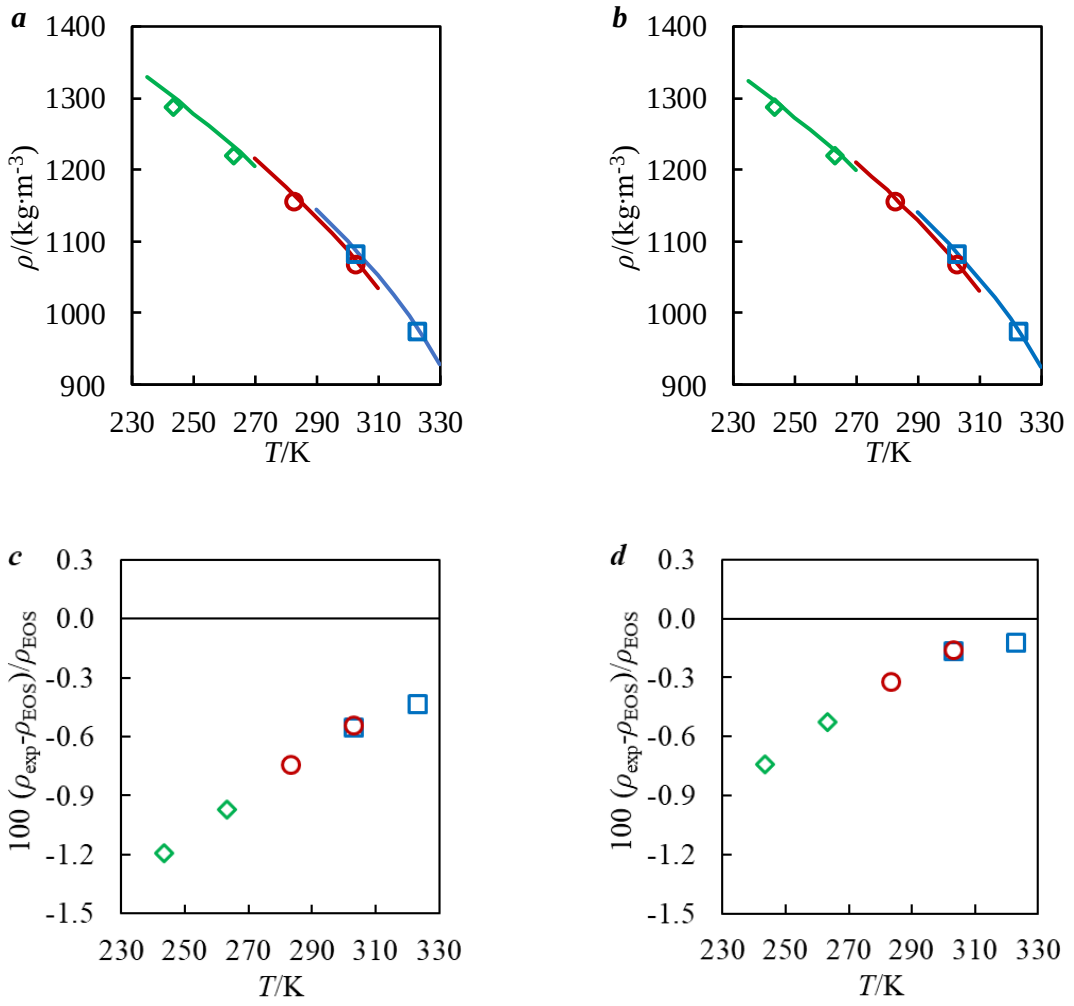

Figure B.27: Comparisons of (0.20 CO_2 + 0.20 R1234yf + 0.20 R32 + 0.20 R125 + 0.20 R134a) density results for the experimental data measured in this work and various models from (*a*) default and (*b*) tuned binary interaction parameters (BIPs). Deviations are shown of experimental data from those calculated with the default (*c*) and tuned (*d*) BIPs. Symbols refer to the measurements at different pressures (□ 5.06 MPa, ○ 3.53 MPa and ◇1.44 MPa), and the solid curves refer to the model prediction.

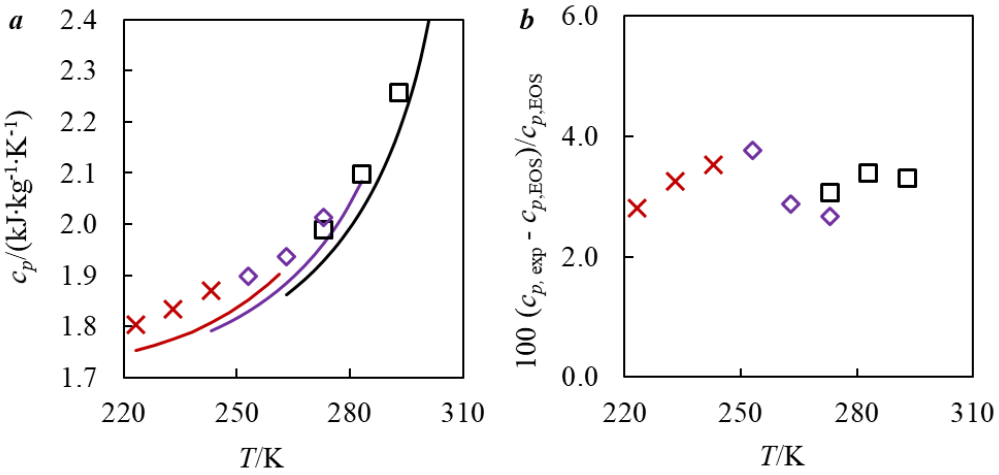

Figure B.28: Heat capacity measurements of 0.5 CO_2 + 0.5 R32. *a*: absolute c_p as a function of T (temperature), symbols corresponds to the measured values (☐ 5.00 MPa, ◇ 3.52 MPa and ×1.50 MPa), and the solid coloured lines correspond to the prediction from REFPROP 10 [9]. *b*: relative deviations of measured c_p (using average fitted cell volume) from that calculated using the default model in REFPROP 10 [9] ($c_{p,\mathrm{EOS}}$) at different pressures (☐ 5.00 MPa, ◇ 3.52 MPa and ×1.50 MPa) as a function of temperature.

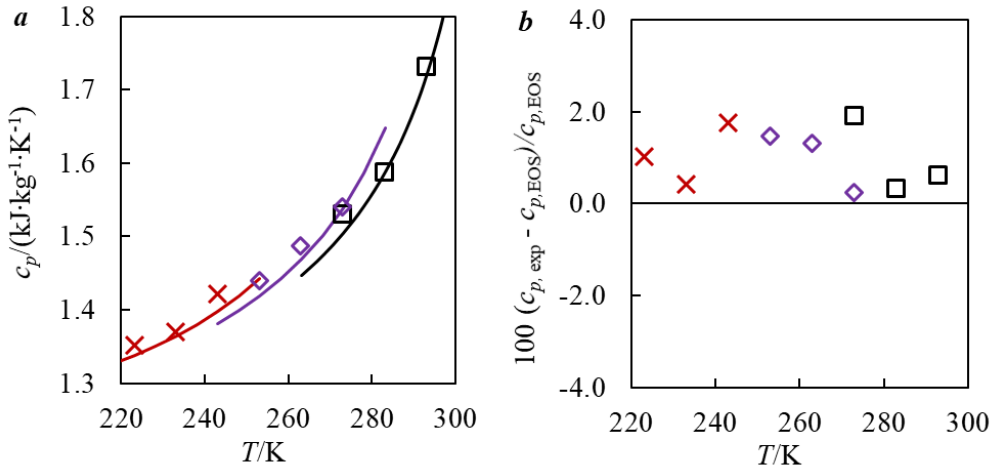

Figure B.29: Heat capacity measurements of 0.5 CO_2 + 0.5 R125. *a*: absolute c_p as a function of T (temperature), symbols corresponds to the measured values (☐ 5.04 MPa, ◇ 3.52 MPa and ×1.56 MPa), and the solid coloured lines correspond to the prediction from REFPROP 10 [9]. *b*: relative deviations of measured c_p (using average fitted cell volume) from that calculated using the default model in REFPROP 10 [9] ($c_{p,\mathrm{EOS}}$) at different pressures (☐ 5.04 MPa, ◇ 3.52 MPa and ×1.56 MPa) as a function of temperature.

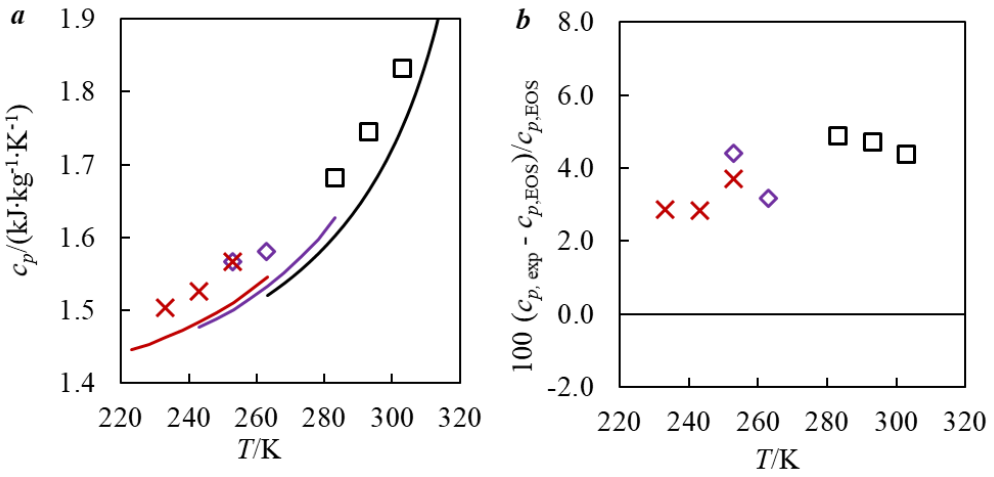

Figure B.30: Heat capacity measurements of 0.5 CO_2 + 0.5 R134a. *a*: absolute c_p as a function of T (temperature), symbols corresponds to the measured values (☐ 5.00 MPa, ◇ 3.50 MPa and ×2.00 MPa), and the solid coloured lines corresponds to the prediction from REFPROP 10 [9]. *b*: relative deviations of measured c_p (using average fitted cell volume) from that calculated using the default model in REFPROP 10 [9] ($c_{p,\mathrm{EOS}}$) at different pressures (☐ 5.00 MPa, ◇ 3.50 MPa and ×2.00 MPa) as a function of temperature.

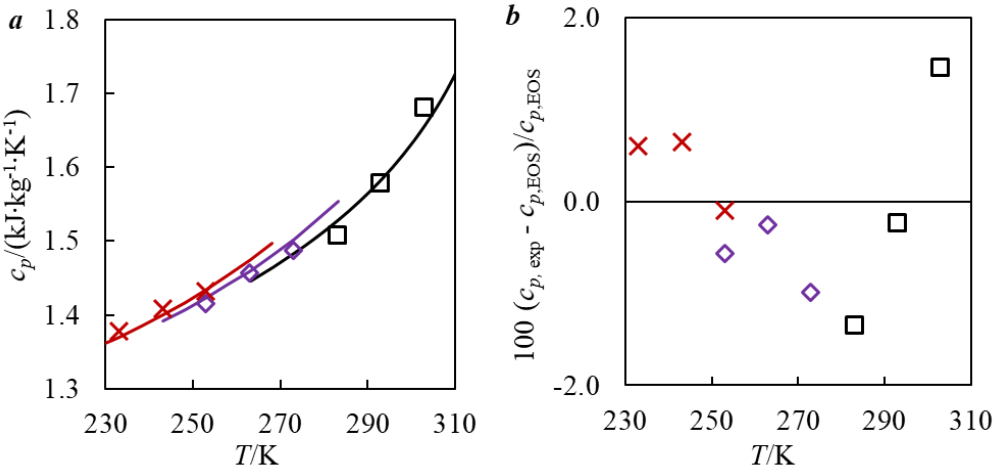

Figure B.31: Heat capacity measurements of 0.5 CO_2 + 0.5 R1234yf. *a*: Absolute c_p as a function of T (temperature), symbols correspond to the measured values (☐ 5.09 MPa, ◇ 3.50 MPa and ×2.07 MPa) and the solid coloured lines correspond to the predictions from REFPROP 10 [9]. *b*: Relative deviations of the measured c_p (using average fitted cell volume) from that calculated using the default model in REFPROP 10 [9] ($c_{p,\mathrm{EOS}}$) at different pressures (☐ 5.09 MPa, ◇ 3.50 MPa and ×2.07 MPa) as a function of temperature.

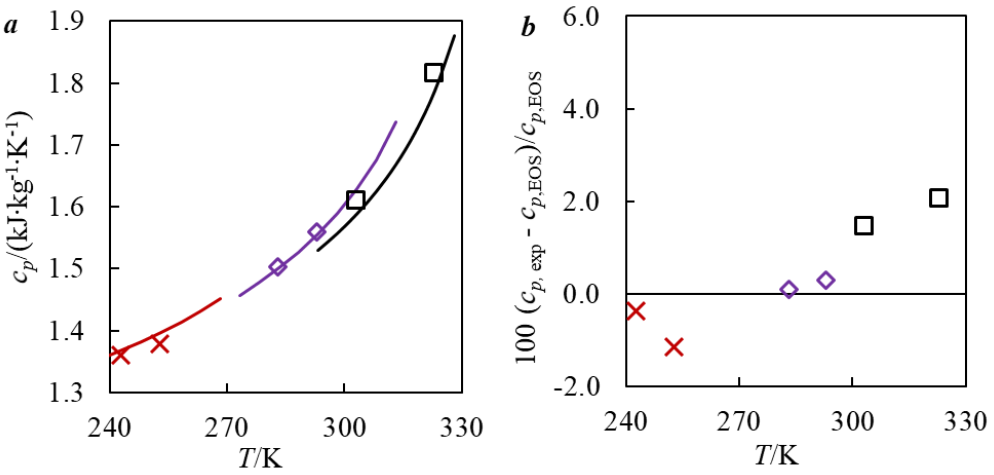

Figure B.32: Heat capacity measurements of 0.09 CO_2 + 0.48 R1234yf + 0.43 R32. *a*: absolute c_p as a function of *T* (temperature), symbols corresponds to the measured values (☐ 4.52 MPa, ◇ 2.98 MPa and ×1.55 MPa), and the solid coloured lines correspond to the prediction from REFPROP 10 [9]. *b*: relative deviations of measured c_p (using average fitted cell volume) from that calculated using the default model in REFPROP 10 [9] ($c_{p,\mathrm{EOS}}$) at different pressures (☐ 4.52 MPa, ◇ 2.98 MPa and ×1.55 MPa) as a function of temperature.

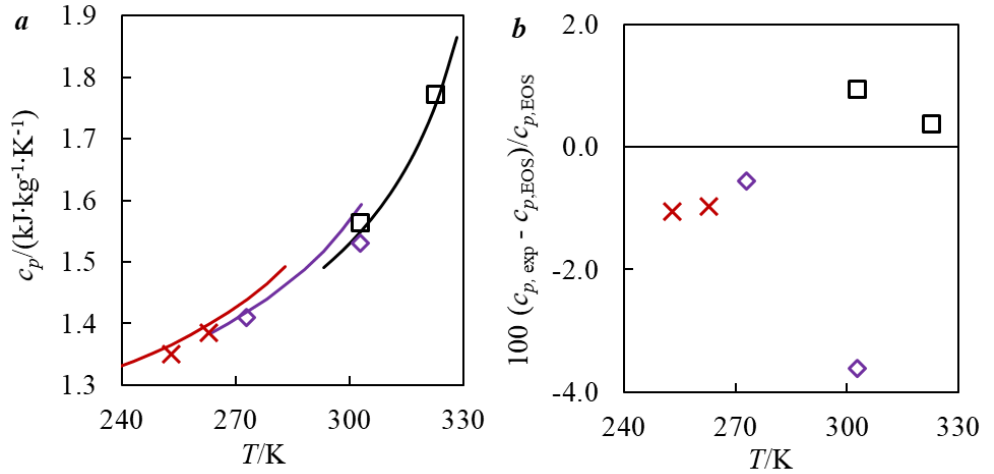

Figure B.33: Heat capacity measurements of (0.20 CO_2 + 0.20 R1234yf + 0.20 R32 + 0.20 R125 + 0.20 R134a). *a*: absolute c_p as a function of *T* (temperature), symbols corresponds to the measured values (☐ 4.95 MPa, ◇ 3.58 MPa and ×1.50 MPa), and the solid coloured lines corresponds to the prediction from REFPROP 10 [9]. *b*: relative deviations of measured c_p (using average fitted cell volume) from that calculated using the default model in REFPROP 10 [9] ($c_{p,\mathrm{EOS}}$) at different pressures (☐ 4.95 MPa,◇ 3.58 MPa and×1.50 MPa) as a function of temperature.

B.8 References

[1] Jabbour T, Clodic DF, Terry J, Kondo S. Burning velocity and refrigerant flammability classification. ASHRAE Trans 2004;110 PART I:522–33.

[2] Clodic D, Jabbour T. Method of test for burning velocity measurement of flammable gases and results. HVAC R Res 2011;17:51–75. doi:10.1080/10789669.2011.543252.

[3] Bell IH, Domanski PA, McLinden MO, Linteris GT. The hunt for nonflammable refrigerant blends to replace R-134a. Int J Refrig 2019. doi:10.1016/j.ijrefrig.2019.05.035.

[4] Bellos E, Tzivanidis C. A comparative study of CO2 refrigeration systems. Energy Convers Manag X 2019;1:100002. doi:https://doi.org/10.1016/j.ecmx.2018.100002.

[5] Wu X, Dang C, Xu S, Hihara E. State of the art on the flammability of hydrofluoroolefin (HFO) refrigerants. Int J Refrig 2019;108:209–23. doi:https://doi.org/10.1016/j.ijrefrig.2019.08.025.

[6] Bobbo S, Nicola G Di, Zilio C, Brown JS, Fedele L. Low GWP halocarbon refrigerants: A review of thermophysical properties. Int J Refrig 2018;90:181–201. doi:https://doi.org/10.1016/j.ijrefrig.2018.03.027.

[7] Al Ghafri SZS, Rowland D, Akhfash M, Arami-Niya A, Khamphasith M, Xiao X, et al. Thermodynamic properties of hydrofluoroolefin (R1234yf and R1234ze(E)) refrigerant mixtures: Density, vapour-liquid equilibrium, and heat capacity data and modelling. Int J Refrig 2019;98:249–60. doi:https://doi.org/10.1016/j.ijrefrig.2018.10.027.

[8] Akhfash M, Al Ghafri SZS, Rowland D, Hughes TJ, Tsuji T, Tanaka Y, et al. Liquid and Vapor Viscosities of Binary Refrigerant Mixtures Containing R1234yf or R1234ze(E). J Chem Eng Data 2019;64:1122–30. doi:10.1021/acs.jced.8b01039.

[9] Lemmon EW, Bell IH, Huber ML, McLinden MO. NIST Standard Reference Database 23: Reference Fluid Thermodynamic and Transport Properties-REFPROP, Version 10.0; National Institute of Standards and Technology. Https://WwwNistGov/Srd/Ref 2018.

[10] Span R, Wagner W. A new equation of state for carbon dioxide covering the fluid region from the triple-point temperature to 1100 K at pressures up to 800 MPa. J Phys Chem

Ref Data 1996;25:1509–96.

[11] Richter M, McLinden MO, Lemmon EW. Thermodynamic properties of 2,3,3,3-tetrafluoroprop-1-ene (R1234yf): Vapor pressure and p - φ - T Measurements and an Equation of State. J Chem Eng Data 2011;56:3254–64. doi:10.1021/je200369m.

[12] Tillner-Roth R, Yokozeki A. An International Standard Equation of State for Difluoromethane (R-32) for Temperatures from the Triple Point at 136.34 K to 435 K and Pressures up to 70 MPa. J Phys Chem Ref Data 1997;26:1273–328. doi:10.1063/1.556002.

[13] Tillner-Roth R, Baehr HD. An international standard formulation for the thermodynamic properties of 1, 1, 1, 2-Tetrafluoroethane (HFC-134a) for temperatures from 170 K to 455 K and pressures up to 70 MPa. J Phys Chem Ref Data 1994;23:657–729.

[14] Lemmon EW, Jacobsen RT. A new functional form and new fitting techniques for equations of state with application to pentafluoroethane (HFC-125). J Phys Chem Ref Data 2005;34:69–108.

[15] May EF, Guo JY, Oakley JH, Hughes TJ, Graham BF, Marsh KN, et al. Reference quality vapor-liquid equilibrium data for the binary systems methane + ethane, + propane, + butane, and + 2-methylpropane, at temperatures from (203 to 273) K and pressures to 9 MPa. J Chem Eng Data 2015;60:3606–20. doi:10.1021/acs.jced.5b00610.

[16] Efika EC, Hoballah R, Li X, May EF, Nania M, Sanchez-Vicente Y, et al. Saturated phase densities of (CO2 + H2O) at temperatures from (293 to 450) K and pressures up to 64 MPa. J Chem Thermodyn 2016;93:347–59. doi:https://doi.org/10.1016/j.jct.2015.06.034.

[17] Guilbot P, Valtz A, Legendre H, Richon D. Rapid on-line sampler-injector: A reliable tool for HT-HP sampling and on-line GC analysis. Analusis 2000;28:426–31. doi:10.1051/analusis:2000128.

[18] Richon D. Method and device for taking micro samples from a pressurized fluid contained in a container. FR2853414A1, 2003.

[19] Outcalt S. Calibration Fluids and Calibration Equations: How Choices May Affect the Results of Density Measurements Made with U-Tube Densimeters. J Res Natl Inst Stand

Technol 2018;123. doi:10.6028/jres.123.017.

[20] Jiao F, Al Ghafri SZS, Hughes TJ, May EF. Extended calibration of a vibrating tube densimeter and new reference density data for a methane-propane mixture at temperatures from (203 to 423) K and pressures to 35 MPa. J Mol Liq 2020:113219. doi:https://doi.org/10.1016/j.molliq.2020.113219.

[21] May EF, Tay WJ, Nania M, Aleji A, Al-Ghafri S, Martin Trusler JP. Physical Apparatus Parameters and Model for Vibrating Tube Densimeters at Pressures to 140 MPa and Temperatures to 473 K. Rev Sci Instrum 2014;85:95111. doi:doi:http://dx.doi.org/10.1063/1.4894469.

[22] Lemmon EW, McLinden MO, Wagner W. Thermodynamic Properties of Propane. III. A Reference Equation of State for Temperatures from the Melting Line to 650 K and Pressures up to 1000 MPa. J Chem Eng Data 2009;54:3141–80. doi:10.1021/je900217v.

[23] Setzmann U, Wagner W. A New Equation of State and Tables of Thermodynamic Properties for Methane Covering the Range from the Melting Line to 625 K at Pressures up to 100 MPa. J Phys Chem Ref Data 1991;20:1061–155. doi:10.1063/1.555898.

[24] JCGM (Joint Committee for Guides in Metrology)100:2008 (GUM 1995 with minor corrections), Evaluation of measurement data – Guide to the expression of uncertainty in measurement 2008.

[25] Tay WJ, Trusler JPM. Density, sound speed and derived thermophysical properties of n-nonane at temperatures between (283.15 and 473.15) K and at pressures up to 390 MPa. J Chem Thermodyn 2018;124:107–22. doi:https://doi.org/10.1016/j.jct.2018.04.019.

[26] Syed TH, Hughes TJ, Marsh KN, May EF. Isobaric Heat Capacity Measurements of Liquid Methane, Ethane, and Propane by Differential Scanning Calorimetry at High Pressures and Low Temperatures. J Chem Eng Data 2012;57:3573–80. doi:10.1021/je300762m.

[27] Kunz O, Wagner W. The GERG-2008 Wide-Range Equation of State for Natural Gases and Other Mixtures: An Expansion of GERG-2004. J Chem Eng Data 2012;57:3032–91. doi:10.1021/je300655b.

[28] Kunz O, Klimeck R, Wagner W, Jaeschke M. The GERG-2004 wide-range equation of state for natural gases and other mixtures. GERG Tech Monogr 2007;15.

[29] Span R, Lemmon EW. Chapter 5: Volumetric Properties from Multiparameter Equations of State. Vol. Prop. Liq. Solut. Vapours, The Royal Society of Chemistry; 2015, p. 125–51. doi:10.1039/9781782627043-00125.

[30] Syed TH, Hughes TJ, Marsh KN, May EF. Isobaric Heat Capacity Measurements of Liquid Methane + Propane, Methane + Butane, and a Mixed Refrigerant by Differential Scanning Calorimetry at High Pressures and Low Temperatures. J Chem Eng Data 2014;59:968–74. doi:10.1021/je4007019.

[31] Rowland D, Hughes TJ, May EF. Extending the GERG-2008 equation of state: Improved departure function and interaction parameters for (methane+butane). J Chem Thermodyn 2016;97:206–13. doi:https://doi.org/10.1016/j.jct.2016.01.005.

[32] Jaubert J-N, Coniglio L. The Group Contribution Concept: A Useful Tool To Correlate Binary Systems and To Predict the Phase Behavior of Multicomponent Systems Involving Supercritical CO2 and Fatty Acids. Ind Eng Chem Res 1999;38:5011–8. doi:10.1021/ie990544d.

[33] Qian J-W, Privat R, Jaubert J-N, Coquelet C, Ramjugernath D. Fluid-phase-equilibrium prediction of fluorocompound-containing binary systems with the predictive E-PPR78 model. Int J Refrig 2017;73:65–90. doi:https://doi.org/10.1016/j.ijrefrig.2016.09.013.

[34] Rivollet F, Chapoy A, Coquelet C, Richon D. Vapor–liquid equilibrium data for the carbon dioxide (CO2) + difluoromethane (R32) system at temperatures from 283.12 to 343.25 K and pressures up to 7.46 MPa. Fluid Phase Equilib 2004;218:95–101. doi:https://doi.org/10.1016/j.fluid.2003.12.002.

[35] Duran-Valencia C, Pointurier G, Valtz A, Guilbot P, Richon D. Vapor−Liquid Equilibrium (VLE) Data for the Carbon Dioxide (CO2) + 1,1,1,2-Tetrafluoroethane (R134a) System at Temperatures from 252.95 K to 292.95 K and Pressures up to 2 MPa. J Chem Eng Data 2002;47:59–61. doi:10.1021/je010075y.

[36] Juntarachat N, Valtz A, Coquelet C, Privat R, Jaubert JN. Experimental measurements and correlation of vapor-liquid equilibrium and critical data for the CO2 + R1234yf and CO2 + R1234ze(E) binary mixtures. Int J Refrig 2014;47:141–52.

doi:10.1016/j.ijrefrig.2014.09.001.

[37] Diefenbacher A, Türk M. (Vapour + liquid) Equilibria of binary mixtures of CO2, CH2F2, CHF3, and SF6. J Chem Thermodyn 2002;34:1361–75. doi:10.1016/S0021-9614(02)00123-4.

[38] Stein FP, Adams RA. Vapor-liquid equilibriums for carbon dioxide-difluoromethane system. J Chem Eng Data 1971;16:146–9.

[39] Di Nicola G, Pacetti M, Polonara F, Stryjek R. Isochoric Measurements for CO2 + R125 and CO2 + R32 Binary Systems. J Chem Eng Data 2002;47:1145–53. doi:10.1021/je015541y.

[40] Lim JS, Jin JM, Yoo K-P. VLE measurement for binary systems of CO2+1,1,1,2-tetrafluoroethane (HFC-134a) at high pressures. J Supercrit Fluids 2008;44:279–83. doi:https://doi.org/10.1016/j.supflu.2007.09.025.

[41] Silva-Oliver G, Galicia-Luna LA. Vapor–liquid equilibria for carbon dioxide + 1,1,1,2-tetrafluoroethane (R-134a) systems at temperatures from 329 to 354 K and pressures upto 7.37 MPa. Fluid Phase Equilib 2002;199:213–22. doi:https://doi.org/10.1016/S0378-3812(01)00816-0.

[42] Jeong K, Im J, Lee S, Kim H. (Vapour+liquid) equilibria of the {carbon dioxide+pentafluoroethane (HFC-125)} system and the {carbon dioxide+dodecafluoro-2-methylpentan-3-one (NOVEC^{TM}1230)} system. J Chem Thermodyn 2007;39:531–5. doi:https://doi.org/10.1016/j.jct.2006.09.010.

[43] Di Nicola G, Di Nicola C, Arteconi A, Stryjek R. PVTx measurements of the carbon dioxide+ 2, 3, 3, 3-Tetrafluoroprop-1-ene binary system. J Chem Eng Data 2012;57:450–5.

[44] Akasaka R. Thermodynamic property models for the difluoromethane (R-32)+ trans-1, 3, 3, 3-tetrafluoropropene (R-1234ze (E)) and difluoromethane+ 2, 3, 3, 3-tetrafluoropropene (R-1234yf) mixtures. Fluid Phase Equilib 2013;358:98–104.

[45] Lemmon EW, Jacobsen RT. Equations of state for mixtures of R-32, R-125, R-134a, R-143a, and R-152a. J Phys Chem Ref Data 2004;33:593–620.

[46] Giacomo P. Equation for the Determination of the Density of Moist Air (1981).

Metrologia 1982;18:33–40. doi:10.1088/0026-1394/18/1/006.

[47] Seitz JC, Blencoe JG, Bodnar RJ. Volumetric properties for {(1− x) CO2+ xCH4},{(1− x) CO2+ xN2}, and {(1− x) CH4+ xN2} at the pressures (9.94, 19.94, 29.94, 39.94, 59.93, 79.93, and 99.93) MPa and temperatures (323.15, 373.15, 473.15, and 573.15) K. J Chem Thermodyn 1996;28:521–38.

[48] Vennix AJ, Leland Jr TW, Kobayashi R. Low-temperature volumetric properties of methane. J Chem Eng Data 1970;15:238–43.

[49] Ito T, Nagata Y, Miyamoto H. Measurement of the (p, $$\rho $$, T) Pro perties for Pure Hydrocarbons at Tem peratures up to 600 K and Pressures up to 200 MPa. Int J Thermophys 2014;35:1636–46.

[50] Glos S, Kleinrahm R, Wagner W. Measurement of the (p, ρ, T) relation of propane, propylene, n-butane, and isobutane in the temperature range from (95 to 340) K at pressures up to 12 MPa using an accurate two-sinker densimeter. J Chem Thermodyn 2004;36:1037–59.

[51] Abdulagatov IM, Bazaev AR, Gasanov RK, Ramazanova AE. Measurements of the (p, ρ, T) properties and virial coefficients of pure water, methane, n-hexane, n-octane, benzene, and of their aqueous mixtures in the supercritical region. J Chem Thermodyn 1996;28:1037–57.

[52] Händel G, Kleinrahm R, Wagner W. Measurements of the (pressure, density, temperature) relation of methane in the homogeneous gas and liquid regions in the temperature range from 100 K to 260 K and at pressures up to 8 MPa. J Chem Thermodyn 1992;24:685–95.

[53] Galicia-Luna LA, Richon D, Renon H. New loading technique for a vibrating tube densimeter and measurements of liquid densities up to 39.5 MPa for binary and ternary mixtures of the carbon dioxide-methanol-propane system. J Chem Eng Data 1994;39:424–31.

[54] Reamer HH, Sage BH, Lacey WN. Phase equilibria in hydrocarbon systems. Volumetric and phase behavior of the propane-carbon dioxide system. Ind Eng Chem 1951;43:2515–20.

[55] Francesconi AZ, Lentz H, Franck EU. Phase equilibriums and PVT data for the methane-methanol system to 300 MPa and 240. degree. C. J Phys Chem 1981;85:3303–7.

[56] Robertson SL, Babb Jr SE. PVT Properties of Methane and Propene to 10 kbar and 200° C. J Chem Phys 1969;51:1357–61.

[57] Deschner WW. P–V–T Relations for Propane. Ind Eng Chem 1940;32:836–40.

[58] Hoover AE. Virial coefficients of methane and ethane. 1966.

[59] Prasad DHL. PVT relations of propane in the range 373. 15-423. 15K and 0. 2-4. 0 Mpa. AIChE J;(United States) 1982;28.

[60] Miyamoto H, Uematsu M. Saturated liquid densities of propane at T=(280 to 365) K. J Chem Thermodyn 2007;39:225–9.

[61] Seibt D, Voß K, Herrmann S, Vogel E, Hassel E. Simultaneous Viscosity− Density Measurements on Ethane and Propane over a Wide Range of Temperature and Pressure Including the Near-Critical Region. J Chem Eng Data 2011;56:1476–93.

[62] Olson JD. The refractive index and Lorenz–Lorentz function of fluid methane. J Chem Phys 1975;63:474–84.

[63] Roe DR. Thermodynamic properties of gases and gas mixtures at low temperatures 1972.

[64] McLinden MO. Thermodynamic Properties of Propane. I. p− ρ− T Behavior from (265 to 500) K with Pressures to 36 MPa. J Chem Eng Data 2009;54:3181–91.

[65] Burgoyne JH. Two-phase equilibrium in binary and ternary systems-IV. The thermodynamic properties of propane. Proc R Soc London Ser A Math Phys Sci 1940;176:280–94.

[66] Cristancho DE, Mantilla ID, Ejaz S, Hall KR, Atilhan M, Iglesia-Silva GA. Accurate P ρ T Data for Methane from (300 to 450) K up to 180 MPa. J Chem Eng Data 2009;55:826–9.

[67] Fenghour A, Wakeham WA, Scott AC, Watson JTR. Amount-of-substance density of CH4at temperatures from 322.5 K to 700 K and pressures up to 35 MPa. J Chem

Thermodyn 1995;27:213–8.

[68] Evers C, Lösch HW, Wagner W. An absolute viscometer-densimeter and measurements of the viscosity of nitrogen, methane, helium, neon, argon, and krypton over a wide range of density and temperature. Int J Thermophys 2002;23:1411–39.

[69] Huang ETS, Swift GW, Kurata F. Viscosities of methane and propane at low temperatures and high pressures. AIChE J 1966;12:932–6.

[70] Baidakov VG, Gurina TA. An experimental study of the equation of state of superheated liquid methane. J Chem Thermodyn 1989;21:1009–16.

[71] Defibaugh DR, Moldover MR. Compressed and saturated liquid densities for 18 halogenated organic compounds. J Chem Eng Data 1997;42:160–8.

[72] Ely JF, Kobayashi R. Isochoric pressure-volume-temperature measurements for compressed liquid propane. J Chem Eng Data 1978;23:221–3.

[73] Trappeniers NJ, Wassenaar T, Abels JC. Isotherms and thermodynamic properties of methane at temperatures between 0° and 150° C and at densities up to 570 amagat. Phys A Stat Mech Its Appl 1979;98:289–97.

[74] Babb Jr SE, Robertson SL. Isotherms of ethylene and propane to 10 000 bar. J Chem Phys 1970;53:1097–9.

[75] Sinor JE, Kurata F. Liquid Phase Volumetric Behavior of the Helium-Methane System. J Chem Eng Data 1966;11:1–6.

[76] Kayukawa Y, Hasumoto M, Kano Y, Watanabe K. Liquid-phase thermodynamic properties for propane (1), n-butane (2), and isobutane (3). J Chem Eng Data 2005;50:556–64.

[77] Vennix AJ. Low temperature volumetric properties and the development of an equation of state for methane. Rice University, 1966.

[78] Diefenbacher A, Türk M. (Vapour+liquid) Equilibria of binary mixtures of CO2, CH2F2, CHF3, and SF6. J Chem Thermodyn 2002;34:1361–75. doi:https://doi.org/10.1016/S0021-9614(02)00123-4.